

INFORMATION TO USERS

This manuscript has been reproduced from the microfilm master. UMI films the text directly from the original or copy submitted. Thus, some thesis and dissertation copies are in typewriter face, while others may be from any type of computer printer.

The quality of this reproduction is dependent upon the quality of the copy submitted. Broken or indistinct print, colored or poor quality illustrations and photographs, print bleedthrough, substandard margins, and improper alignment can adversely affect reproduction.

In the unlikely event that the author did not send UMI a complete manuscript and there are missing pages, these will be noted. Also, if unauthorized copyright material had to be removed, a note will indicate the deletion.

Oversize materials (e.g., maps, drawings, charts) are reproduced by sectioning the original, beginning at the upper left-hand corner and continuing from left to right in equal sections with small overlaps. Each original is also photographed in one exposure and is included in reduced form at the back of the book.

Photographs included in the original manuscript have been reproduced xerographically in this copy. Higher quality 6" x 9" black and white photographic prints are available for any photographs or illustrations appearing in this copy for an additional charge. Contact UMI directly to order.

UMI

A Bell & Howell Information Company
300 North Zeeb Road, Ann Arbor MI 48106-1346 USA
313/761-4700 800/521-0600

**FRACTURE AND SHAKEDOWN OF PAVEMENTS UNDER
REPEATED TRAFFIC LOADS**

**A
THESIS**

**Presented to the Faculty
of the University of Alaska Fairbanks
in Partial Fulfillment of the Requirements
for the Degree of**

DOCTOR OF PHILOSOPHY

**By
Tinggang Zhang, B. S., M. S.**

Fairbanks, Alaska

May 1998

UMI Number: 9838841

**UMI Microform 9838841
Copyright 1998, by UMI Company. All rights reserved.**

**This microform edition is protected against unauthorized
copying under Title 17, United States Code.**

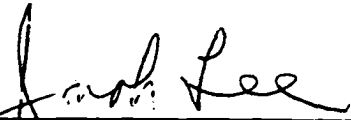
UMI
300 North Zeeb Road
Ann Arbor, MI 48103

FRACTURE AND SHAKEDOWN OF PAVEMENTS UNDER
REPEATED TRAFFIC LOADS

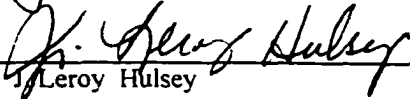
By

Tinggang Zhang

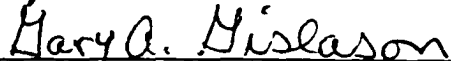
RECOMMENDED:



Dr. Jonah H. Lee




Dr. Leroy Hulsey




Dr. Gary A. Gislason



Dr. David Corey

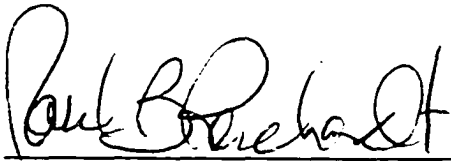


Dr. Lutfi Raad, Chairman, Advisory Committee

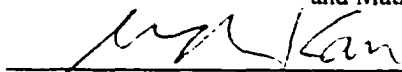


Dr. Lutfi Raad, Head, Department of Civil and
Environmental Engineering

APPROVED:



Dr. Paul Reichardt, Dean, College of Science, Engineering
and Mathematics



Dr. Joseph Kan, Dean of the Graduate School

4-13-48

Date

ABSTRACT

Under repeated external loads, engineering structures or objects may fail by large plastic deformation or fatigue. Shakedown will occur when the accumulation of plastic deformation ceases under repeated loads; the response of the system is then purely elastic. Fatigue and shakedown have been individually studied for decades and no attempt has been made to couple these two mechanisms in the mechanics analysis. In this study, an attempt is made to couple shakedown and fatigue in pavement mechanics analysis using numerical simulation.

The study covers three main areas: fatigue, static shakedown, and kinematic shakedown analysis. A numerical approach to fatigue analysis is proposed based on elastic-plastic fracture mechanics. The amount of the crack growth during each load cycle is determined by using the J-integral curve and R_curve. Crack propagation is simulated by shifting the R_curve along the crack growth direction. Fatigue life is predicted based on numerically established fatigue equation. The numerical results indicate that the algorithm can be applied to fatigue analyses of different materials. A numerical algorithm based on the finite element method coupled with the nonlinear programming is proposed in static shakedown analysis. In this algorithm, both the inequality and equality constraints are included in the pseudo-objective function. These constraints are normalized by the material yield stress and the reference load, respectively. A multidirectional search algorithm is used in the optimization process. The influence of finite element mesh on shakedown loads is investigated. An algorithm that utilizes eigen-modes to construct the arbitrary admissible plastic deformation path is proposed in kinematic shakedown analysis. This algorithm converts the shakedown theorem into a convex optimization problem and can be solved by using a multidirectional search algorithm. Fatigue behavior of a two-layer full-depth pavement system of asphalt concrete is analyzed using the proposed numerical algorithm. Fatigue crack growth rate is estimated and fatigue life is predicted for the system. Shakedown analyses are also carried out for the same pavement system. The comparison between the shakedown load and the fatigue failure load with respect to the same crack length indicates that the shakedown dominates the response of the pavement system under traffic loads.

TABLE OF CONTENTS

	PAGE
SIGNATURE	i
TITLE	ii
ABSTRACT	iii
TABLE OF CONTENTS	iv
LIST OF FIGURES	v
LIST OF TABLES	x
ACKNOWLEDGMENTS	xi
 CHAPTER	
I INTRODUCTION	1
II REVIEW OF FATIGUE AND FRACTURE	14
III REVIEW OF SHAKEDOWN THEORY	39
IV A NUMERICAL APPROACH TO FATIGUE	65
V NUMERICAL ALGORITHM FOR STATIC SHAKEDOWN ANALYSIS	107
VI AN ALGORITHM OF KINEMATIC SHAKEDOWN ANALYSIS	142
VII APPLICATIONS	190
VIII SUMMARY AND CONCLUSIONS	212
REFERENCES	215
 APPENDIX	
A TABLES USED IN CHAPTER IV	227
B VARIABLE DEFINITION IN FATIGUE LIFE ANALYSIS PROGRAM	245
C VARIABLE DEFINITION IN STATIC SHAKEDOWN ANALYSIS PROGRAM	267
D VARIABLE DEFINITION IN KINEMATIC SHAKEDOWN ANALYSIS PROGRAM	272

LIST OF FIGURES

FIGURE	PAGE	
1.1	Nomograph for Predicting Fatigue Life of Bituminous Mixes(After Bonnaure et al. (1980).)	13
2.1	Stress Components on a Three-Dimensional Element Referred to Cartesian Coordinate System.	15
2.2	An Infinite Plate Containing a Crack of Length $2a$ and Subjected to a Remote Tensile Stress σ .	17
2.3	An Infinite Plate Containing a Crack of Length $2a$ and Subjected to a Remote Shearing Stress τ .	17
2.4	An Infinite Plate Containing a Crack of Length $2a$ and Subjected to a Remote Shearing Stress τ along x_3 .	18
2.5(a)	Elastic Stress Distribution around Crack Tip.	21
2.5(b)	Irwin's Plastic Zone Model by Considering Stress Redistribution around Crack Tip.	21
2.6	Dugdale's Model for an Infinite Cracked Plate.	22
2.7	Crack Tip Coordinate System and Typical Line Integral Contour.	23
2.8	Comparison of Two Notched Elastic Bodies of Identical Shape, Composition, and Loading, but the Notches of the Two Bodies.	24
2.9	Flat Surface Notch in Two-dimensional Deformation Field.	25
2.10	Illustration of Work to a Given Displacement.	26
3.1	A Two-Span Beam Subjected to Cyclic Loading.	41
3.2	Plastic Deformation in Shakedown Analysis of Two-span Beam.	48
3.3	A Solid Body Subjected to Arbitrary Repeated Loads.	49
3.4	Illustration of Load Variation with Time.	49
4.1	Crack Tip Coordinate System and Typical Line Integral Contour.	67
4.2	An Alternative Interpretation of J-integral.	68
4.3	Illustration of Discretized Key Curve with N Divisions.	70
4.4	Illustration of Crack Increments Calculation and Shifting R_curve.	73
4.5	Plastic Zone Size Notation.	76
4.6	Denotation of Terms in Condition of J-controlled Crack Growth.	80
4.7	Geometry of ASTM Standard Compact Tension Specimen.	84
4.8	Stress-Strain Curve for A533B Steel at 200F and Its Representation by the Ramberg-Osgood Law.	85

4.9	J-integral versus Crack Length Curves with Load as the Parameter for Plane Strain Compact Tension Specimen of A533B Steel.	86
4.10	R _c curve for Compact Specimen of A533B Steel at 200F.	87
4.11	Fatigue Crack Growth Rate as a Function of Cyclic J-integral for A533B Steel at 200F(Current Study) and 97F(Dowling Fatigue Test).	88
4.12	Numerical Prediction of Fatigue Life at Different Load Levels for Compact Specimen of A533B Steel at 200F.	89
4.13(a)	Four-Point Beam Used in Fatigue Analysis	90
4.13(b)	Finite element Mesh for half of the Four-point beam.	91
4.14	Load as Function of Load-Line Displacement for Bending Beam of Soil-Cement Material with Cohesion C=2.586 Mpa and Internal Friction Angle $\phi=42^\circ$.	93
4.15	J-Resistance Curve for Bending Beam of Soil-Cement Material.	94
4.16	Fatigue Crack Growth Rate Changes with Cyclic J-integral for Bending Beam of Soil-Cement Material.	95
4.17	Fatigue Life Changes with Internal Flexural Stress for Bending Beam($\phi = 42^\circ$).	96
4.18	Fatigue of Flexural Specimens of Soil-Cement Material with Cohesion C=2.586 Mpa and Internal Friction Angle $\phi = 42^\circ$.	97
4.19	Normal Stress as a Function of Fatigue Life for Bending Beam of Asphalt Cement Material at 10° F and 68° F.	100
4.20	Numerical Predicted Fatigue Life Variations with Initial Flexural Stress (S-N curve) for Bending Beam of Asphalt Cement Material at 10° F($\phi = 48^\circ$).	101
4.21	Numerical Predicted Fatigue Life Variations with Initial Flexural Stress (S-N curve) for Bending Beam of Asphalt Cement Material 68° F($\phi = 17^\circ$).	104
5.1	The Three-Possible Steps Given the Simplex S with Vertices $\langle v_0, v_1, v_2 \rangle$.	116
5.2	A Beam with One Fixed End and One Roller Supported End.	121
5.3	Finite Element Mesh for Fixed End Beam with 18 Elements and 28 Nodes.	122
5.4	Finite Element Mesh for Fixed End Beam with 36 Elements and 52 Nodes.	123
5.5	Finite Element Mesh for Fixed End Beam with 48 Elements and 65 Nodes.	124
5.6	Finite Element Mesh for Fixed End Beam with 64 Elements and 85 Nodes.	125
5.7	Finite Element Mesh Influence on Lower Bound Shakedown Load.	126
5.8	Finite Element Mesh Influence on Shakedown Load for Load Applied at L/2.	127
5.9	Finite Element Mesh for Thin Biaxial Tension Square Plate with a Central Hole.	131

5.10	Lower Bound Shakedown Analysis Results of Thin Plate with Central Hole.	132
5.11	Finite Element Mesh and Numerical Results of Mesh Influence Analysis.	133
5.12	Finite Element Mesh Size Influence on Lower Bound Shakedown Load for a Thin Plate with Circular Central Hole and is Subjected Biaxial Tension Stress.	134
5.13	Finite Element Mesh Size Influence on Shakedown Load for a Thin Plate with Circular Central Hole and is Subjected Biaxial Tension Stress.	135
5.14	Finite Element Mesh for Two-Layer Pavement System in Shakedown Analysis.	136
5.15	The Variation of Shakedown Load with Elastic Modulus of Surface Layer with Different Cohesion.	137
5.16	The Variation of Shakedown Load with Thickness of Surface Layer for Stiff Sub-grade.	138
6.1	Drucker-Prager and Mohr-Coulomb Criteria.	147
6.2	A Beam with One Fixed End and One Roller Supported End.	158
6.3	Finite Element Mesh for Fixed End Beam with 18 Elements and 28 Nodes.	159
6.4	Finite Element Mesh for Fixed End Beam with 36 Elements and 52 Nodes.	160
6.5	Finite Element Mesh for Fixed End Beam with 48 Elements and 65 Nodes.	161
6.6	Finite Element Mesh for Fixed End Beam with 64 Elements and 85 Nodes.	162
6.7	Finite Element Mesh Influence on Shakedown Load(Upper Bound).	163
6.8	A Step by Step Finite Element Analysis of Collapse Load of Fixed End Beam with Load Applied at L/3 Location.	166
6.9	A Step by Step Finite Element Analysis of Collapse Load of Fixed End Beam with Load Applied at L/2 Location.	167
6.10	A Step by Step Finite Element Analysis of Collapse Load of Fixed End Beam with Load Applied at 2L/3 Location.	168
6.11	A Thin Plane Stress Plate with a Circular Hole and Subjected to Biaxial Tension Stress σ .	169
6.12	Elastic Shakedown and Limit Load Domain for a Thin Plate with a Circular Hole Subjected to Biaxial Tension Along its Edges.	170
6.13	Elastic Shakedown and Limit Load Domain for a Thin Plate with a Circular Hole Subjected to Biaxial Tension Along its Edges.	171
6.14	A Finite Element Mesh for Thin Biaxial Tension Square Plate with a Central Hole.	172
6.15	Shakedown Analysis Results of a Thin Plate with Central Hole.	173
6.16	Finite Element Mesh and Numerical Results of Mesh Influence Analysis.	174
6.17	Finite Element Mesh Size Influence on Shakedown Load Factor for a Thin Plate with Circular Central Hole and is Subjected to Biaxial Tension Stress.	176

6.18	A Stratum Supported by Rigid Sub-layer Subjected to Uniformly Distributed Strip Load and Its Finite Element Mesh.	177
6.19	Loading Program Used in Upper Bound Shakedown Analysis of A Stratum Supported by Rigid Sub-layer.	179
6.20	A Step by Step Finite Element Analysis of Collapse Load of a Stratum Supported by Rigid Sub-layer and Subjected to Uniformly Distributed Strip Load.	180
6.21	The Variation of Shakedown Load with Elastic Modulus of Surface Layer with Different Cohesion.	183
6.22	The Variation of Shakedown Load with Elastic Modulus of Surface Layer with Different Cohesion.	184
6.23	The Variation of Shakedown Load with The Thickness of Surface Layer for Stiff Sub-grade.	185
6.24	The Variation of Shakedown Load with The Thickness of Surface Layer for Soft Sub-grade.	186
6.25	The Variation of Shakedown Load with The Thickness of Surface Layer for Stiff Sub-grade.	187
7.1	Dimension of Two-Layered Pavement System.	194
7.2	Finite Element Mesh of Two-Layered Pavement System in Fatigue Analysis.	195
7.3	Fatigue Crack Growth Rate for a Two-Layered Pavement System.	197
7.4	Fatigue Life versus Applied Load Level Curve for Two-Layered Pavement System.	198
7.5	Finite Element Mesh of Two-Layered Pavement System in Shakedown Analysis.	199
7.6	Shakedown Load Variation with Notch Size of Two-Layered Pavement System.	201
7.7	Stress Distribution around Notch Tip of Two-Layered Pavement System.	202
7.8	Fatigue Failure Load Variation with Crack Length of Two-Layered Pavement System.	203
7.9	Dimension and Finite Element Mesh of Three-Layered Pavement System in Shakedown Analysis.	204
7.10	Shakedown Load Variation with Different Thickness of Surface Layer of Three-Layered Pavement System.	205
7.11	Lower Bound Shakedown Load Variation with Base Layer Friction Angle for Three-Layered Pavement System.	206
7.12	Upper Bound Shakedown Load Variation with Base Layer Friction Angle for Three-Layered Pavement System.	207

7.13	Comparison of Shakedown Load Variation with Base Layer Friction Angle for Three-Layered Pavement System Between Lower Bound and Upper Bound Value under Axisymmetric Condition with $C = 0.0345$ Mpa.	208
7.14	Comparison of Shakedown Load Variation with Base Layer Friction Angle for Three-Layered Pavement System between Lower Bound and Upper Bound Value under Axisymmetric Condition with $C = 0.069$ Mpa.	209
7.15	Comparison of Shakedown Load Variation with Base Layer Friction Angle for Three-Layered Pavement System between Lower Bound and Upper Bound Value under Plane Strain Condition with $C = 0.0345$ Mpa.	210

LIST OF TABLES

TABLE	PAGE
3.1 Elastic Bending Moments at the cross-section in the Two-Span Beam.	46
3.2 Elastic-Plastic Moments at the cross-section in the Two-Span Beam.	46
3.3 Elastic-Plastic Moments at the cross-section in the Two-Span Beam(Incremental Collapse).	47
5.1 Shakedown Analysis for Fixed End Beam.	128
5.2 Material Properties in Two-Layerd Pavement System Shakedown Analysis.	139
6.1 Shakedown Analysis for Fixed End Beam(Upper Bound)	164
6.2 Shakedown Analysis for a Thin Plate with a Circular Hole.	175
6.3 Collapse Loads for the Stratum	181
7.1 Material Properties of Three-Layered Pavement System.	211
7.2 Shakedown Load for Three-Layered Pavement System.	211
A.1 Function h1 for the Compact Specimen in Plane Strain Condition.	228
A.2 J_curve Data in Fatigue Analysis.	229
A.3 R_curve Data in Fatigue Analysis.	230
A.4 Crack Increments Data in Fatigue Analysis.	231
A.5 Modified Crack Increments Data in Fatigue Analysis.	232
A.6 J-integral Increments Data in Fatigue Analysis.	233
A.8 Crack Increment Data in Fatigue Analysis.	234
A.9 Modified Crack Increment Data in Fatigue Analysis.	235
A.10 Cyclic J-integral Data in Fatigue Analysis.	236
A.11 Pretorius Fitting Equation of Fatigue Test.	237
A.12 Asphalt Cement Material Mechanical Properties.	238
A.13 Crack Increment Data in Fatigue Analysis.	239
A.14 Modified Increment Data in Fatigue Analysis.	240
A.15 Cyclic J-integral Data in Fatigue Analysis.	241
A.16 Crack Increment Data in Fatigue Analysis(68° F)	242
A.17 Modified Increment Data in Fatigue Analysis(68° F).	243
A.18 Cyclic J-integral Data in Fatigue Analysis(68° F).	244

ACKNOWLEDGMENTS

The author wishes to express his appreciation to Professor L. Raad who proposed the topic of this study. His inspiration, constructive criticisms and encouragement were invaluable throughout the work.

Appreciation is equally extended to professors D. Weichert, Jonah H. Lee, J. Leroy Hulsey, Gary A. Gislason, Antorius Otto, who also reviewed the manuscript. Their comments and suggestions were critical and helpful.

Valuable recommendation in optimization algorithm provided by Dr. Covey was also appreciated.

The author wishes to thank Arctic Region Supercomputing Center for providing great computing resource to complete his study.

Specially, the author wishes to thank his wife, Zuobing, and child, Mingrui, for their understanding and support.

CHAPTER I

INTRODUCTION

1.1 PROBLEM DEFINITION

A scientific approach to pavement design has been pursued by engineers for many decades. Early pavement design consisted of rule-of-thumb procedures based on past experience. The total pavement thickness was estimated based on the classification of subgrade soil without a strength test. In an effort to characterize the strength of the soil, the CBR method was developed to relate the pavement thickness to the California Bearing Ratio of subgrade soil. The CBR method has been extensively studied and widely adapted both in airfield and highway pavement design. Another method relates the design of pavement thickness to the strength of the materials and is called limiting shear failure method [1]. This method considers the cohesion and internal friction angle of pavement components and subgrade soil as major material properties. The design of pavement thickness is based on its bearing capacity. To control large deformation of a pavement caused by heavy traffic load, the limiting deflection method is used to determine the thickness of pavements so that the vertical deflection is below an allowable limit [1]. To well understand the effects of traffic load, material, and environment on pavement performance, a large number of test-roads were constructed and tested under various conditions. Based on the results of road tests, regression equations for pavement design were developed by The American Association of State Highway Officials. The AASHO method uses the regression equations based on the results of road tests for pavement design [1]. This design procedure takes into account factors such as type and volume of traffic, pavement performance and serviceability, fatigue, and the environment.

All these methods are based on extensive road tests and past experience in pavement design. They are simple and easy to implement in practice. However, these methods are directly related to a given regional environment, material, load condition and experience. The application to different environmental, material, and load conditions cannot be made without extensive correlation. Based on some mathematical models such as half-space solid and multilayer theory, mechanistic-empirical methods of design are gradually developed. The mechanistic-empirical method of design is based on the physical requirements of a structure to withstand the anticipated external loads, postulated deformations and stresses in the elements, and satisfies the mechanical behavior of materials and meets the basic laws of mechanics governing motion

and force. With the development of computer techniques, various computer programs based on mechanistic-empirical methods have been developed and have gained popular acceptance in pavement analysis.

The ever-increasing transportation demands outgrew the advancement of pavement design and research. As indicated in [2, 3], current design procedures are not adequately meeting expectations and pavement life predictions are often inaccurate. Data from the Asphalt Institute's report on pavement thickness design [3] shows that under current design procedures, pavements might, in some cases, be oversized. Data from Brazil [2] indicates that the majority of the pavements studied may have been undersized. Therefore, developing a systematic, practical mechanistic pavement design procedure to provide an optimum reliable pavement structure and accurate service life prediction seems critical.

It is believed that uncertainties inherited from current pavement design practice are the major causes of inaccuracy in service life prediction and thickness design. With increasing tire pressure, roughness, truck loads and traffic volume as well as new vehicle configurations, it can be expected that current design practice will lead to higher inaccuracies in estimated pavement life and serviceability.

1.2 BACKGROUND

Fatigue and rutting are considered major distress modes in flexible pavement design. Repeated traffic loading is responsible for these two distress modes. Many models have been proposed to utilize stress, strain, or deflection related parameters to estimate "fatigue life" or "permanent deformation" accumulated under repeated traffic loading.

1.2.1 FATIGUE

The phenomenological characterization of fatigue in bituminous mixtures is utilized by Hveem [4] who developed a strong correlation between deflection measurements and pavement performance based on field observations. Since then, extensive laboratory modeling of the fatigue process has been studied by Monismith [5], Pell [6], Deacon [7], and Majidzadeh [8].

The stress-strain-based approach to fatigue relates the fatigue life of a flexible pavement to the maximum tensile stress σ_{Tmax} or tensile strain ϵ_{Tmax} developed in the under-side of the bituminous layer by semi-empirical relationship. A variety of specimen configurations and test setups have been developed for the fatigue testing of bituminous mixtures. But most fatigue tests employ the bending beams. This is because

the transverse deformation develops across the pavement and traffic loads are applied only at the wheel path. A simple supported beam with third-point [7], trapezoidal-shaped cantilever beam [9,10,11], center-point loading beam [12] or cantilever beam with rotating bending [6] has been used in laboratory investigations. The bending plate has also been used [13,14].

There are two types of loading modes that are generally selected in laboratory fatigue tests: controlled stress or controlled strain. In a controlled stress test, the stress remains constant, while the strain increases with the number of repetitions. In a controlled strain test, the strain is kept constant, while the load or stress decreases with the number of repetitions. When compared with the same initial nominal stress, available experimental results [15,5,16] have indicated that controlled stress tests are more conservative than controlled strain tests for predicting fatigue life. For a better simulation of fatigue response of pavements in service, the loading mode has to be selected according to the pavement thickness and other geometrical considerations [17]. Hung [1] concluded that the controlled stress test was applicable to thicker pavements, wherein the HMA (Hot Mix Asphalt or Asphalt Concrete) was more than 6 in. (152mm) thick and was the main load-carrying component. As the HMA becomes weaker under repeated loads, the strain should increase with the number of repetitions. The controlled strain test was applicable to thin pavements with HMA less than 2 in. (55mm) thick because the strain in the asphalt layer was governed by the underlying layers and was not affected by the decrease in stiffness of HMA. For intermediate thickness, a combination of controlled stress and controlled strain testing was desired.

Based on extensive fatigue test results, various fatigue equations have been developed. These equations relate the allowable number of load repetitions to the tensile strain at the bottom of the asphalt layer. In the Asphalt Institute and Shell design methods, the allowable number of repetitions, N_f , to cause fatigue cracking is related to the tensile strain, ϵ_t , at the bottom of the HMA and the HMA modulus, E_t , by

$$N_f = f_1 (\epsilon_t)^{f_2} (E_t)^{-f_3} \quad (1.1)$$

while other agencies [1] use the following fatigue equations in the design procedure,

$$N_f = f_1 (\epsilon_t)^{-f_2} \quad (1.2)$$

Laboratory fatigue tests have shown that the exponent, f_2 , of the fatigue equations varies from 3 to 6, but the coefficient, f_1 , varies over an order of magnitude from 5×10^{-6} to 1×10^{-4} . The exponents, f_2 and f_3 , are usually determined from fatigue tests on laboratory specimens, while f_1 must be shifted from laboratory to field values by calibration. Pell [18] indicated that the shift factor might range from 5 to 700.

Laboratory fatigue tests are time-consuming. Based on 146 fatigue tests covering a wide range of mixes, bituminous and testing conditions, Shell [19] developed separate equations and a nomograph for controlled stress and strain tests. The nomograph of the solutions of these equations is presented in Fig. 1.1. However, the accuracy of the equations for constant stress tests was reported within $\pm 40\%$ for 90% of the results and within $\pm 50\%$ for controlled strain tests.

Most of the previous stress-strain based investigations of fatigue response of asphalt mixes have been conducted using a simple loading history, in which the load or strain amplitude for each cycle was constant. Compound loadings have also been attempted by Deacon and Monismith [20] to study their effects on fatigue response.

Frequency of load application in fatigue tests has also been considered as an important testing variable. Monismith, et al [16] reported that the frequency of load application in the range of 3.0 to 30.0 cycles per minute had no effect on the specimen's fatigue behavior. The subsequent work of Deacon and Monismith [20] had shown that the increase in the rate of loading significantly decreased the fracture life for the type of test employed at rates ranging between 30 and 100 applications per minute.

But Raithby and Sterling [21,22] showed that rest periods between successive loading cycles had a beneficial effect on fatigue performance both by increasing the resistance to cracking and by reducing the rate of loss of dynamic stiffness due to repeated loading. When compared with fatigue life under continuous sinusoidal cyclic loading, rest periods on the order of one second increases the number of cycles to fatigue by a factor of up to 5. The improvement in fatigue life was less at high temperatures; it also appeared to be influenced by the magnitude of the applied cyclic stress, although this effect was not clearly established. A comparison of fatigue performance under square, sinusoidal and triangular waveforms indicated the same significant differences, but these were small compared to the effects of rest periods. The effect of rest periods on the crack growth process was also investigated by Majidzadeh and Kauffman [23] by testing beams on elastic foundations with rest periods of 0.0, 0.4 and 0.8 seconds. They reported that for such test conditions, there were no significant effects of rest period on the crack growth process.

The stress-strain-based approach to study fatigue behavior has gained universal acceptance and has been adopted by various organizations in their design practice. However, as pointed out in a previous section, a

fatigue equation from laboratory tests has to be shifted or calibrated to account for field behavior. In addition, the stress-strain-based approach cannot take into account crack initiation and propagation.

Fracture mechanics methods have been used to study the fracture behavior of pavement components including asphalt cement and cement-treated layers, particularly in relation to crack initiation and propagation. Fracture and fatigue behaviors of asphalt concrete materials were studied by Salam [24]. In his study, fracture toughness for different material compositions was measured at different temperatures. A fatigue equation for asphalt concrete beams at 10° F and 68° F was established based on laboratory fatigue test data. A fracture-mechanics based approach was also developed at Ohio State University [25,26,27] to study fatigue behavior of pavement systems. The research at Ohio State University [25,26,27] and the theoretical development of fracture mechanics at other institutes has provided various methods for the solution of crack problems. A computer program and analysis procedure was also developed for the design of pavement systems [23,26]. The results of the research at Ohio State University led to the following general conclusions:

- (1) The crack propagation law, $dc/dn = AK^n$ satisfactorily explains the fatigue performance of bituminous material with the stress intensity factor being the dominant parameter controlling the crack growth. Depending upon the material characteristics such as asphalt content, gradation, etc. the constant n varies.
- (2) The fatigue life of pavement slabs subjected to loads of variable amplitude can be predicted from tests on beams resting on an elastic solid. The sequence of load application has a significant effect on the fatigue life of asphalt materials, causing a delay in the rate of crack propagation. The rest period has little or no effect on the fatigue life of pavements.
- (3) The concept of linear elastic fracture mechanics is applicable in predicting the fatigue life of pavements.

As indicated in [25,26,27], bituminous mixtures could be brittle or ductile depending on temperature, loading conditions, hardening or softening induced factors, and inherited properties. The existence of crack-like imperfections or flaws creates a plastic zone around the crack tip when a body is subjected to alternating low stress levels. In addition, during each loading cycle the sharp aggregate corners transmit point-loading conditions to the asphalt cement with a stress singularity. Hence, even before crack formation, a plastic zone existed at each contact, and energy was dissipated through cyclic plasticity. Once a crack is initiated, then at the tip of the crack, stress distribution goes to infinity according to linear

fracture mechanics. However, the material can only tolerate stress up to its yield point, then a plastic zone around the crack tip forms and blunts the crack advance. The size of this plastic zone is critical in fatigue life analysis. If the formed plastic zone is small compared to the crack size and the geometry of the continuum, linear elastic fracture mechanics will favorably approximate fracture failure. On the other hand, if the size of the plastic zone cannot be ignored, a nonlinear fracture mechanics approach is more appropriate.

It has been found [25,26,27] that in bituminous mixtures, cracks usually develop at the bottom of the asphalt layer due to tensile stresses exceeding a threshold yield stress value. This provides an opening mode fracture, defined as Mode I. Furthermore, the crack propagates vertically but in a zigzag path, indicating either an aggregate obstruct or a crack contribution of Mode II loading type. However, for all practical purposes, Mode I can be considered a dominating crack propagation mode.

Based on these analyses, a fatigue fracture model was developed [26]. The model includes a crack initiation, a fatigue crack propagation and an ultimate failure. The fatigue life of the pavement system is the summation of the number of load cycles of the three stages.

1.2.2 RUTTING

Rut depth has a major influence on pavement design and performance. Current mechanistic based thickness design procedures limit the rut depth within allowable values. This is done by choosing the thickness of the surface layer according to a certain critical strain value. Many investigations have been conducted to establish a functional relationship between the permanent strain and loading repetitions for various materials. The functional relationship may be generalized in the following form [28],

$$\varepsilon_p = f(\sigma, N, T, A, B, E) \quad (1.3)$$

where

- ε_p - permanent strain
- σ - cyclic stress level
- N - number of repeated load applications
- T - temperature
- E - resilient modulus
- A and B – experimentally determined coefficients.

Current design procedures limit rut depth within an allowable value. However, a proper layer thickness determined by this approach will not guarantee the rut depth does not exceed a given value. From Eq. (1.3), it can be seen that for a given load level, temperature, and material properties, load repetition numbers are finite for a given ϵ_p . Permanent deformation will continually accumulate after N repetitions. Furthermore, the repeated load may vary in magnitude and sense, which will make the estimate much more uncertain. On the other hand, permanent deformation may stabilize after several load repetitions, and the response to further repeated loads is purely elastic. This phenomenon is explained by the shakedown theory.

The shakedown concept with regards to the reliability of the collapse loads calculated according to limit analysis theory in the case of variable repeated loads was first discussed by Grüning [29]. Later Bleich [30] established a necessary and sufficient shakedown condition for a simply indeterminate structure. Based on Bleich's work, Melan [31] presented a general shakedown theorem for structures and extended it to the elastic-perfectly-plastic continuum. Much the same as in limit theory, the kinematic shakedown theorem, a dual of Melan's static theorem, was established by Koiter [32] for elastic-perfectly plastic materials.

These two fundamental theorems known as the static and the kinematic shakedown theorems are based on a number of assumptions such as elastic-perfectly-plastic material, small deformation and quasi-static loads. However, in engineering practice, for most cases these assumptions cannot always be satisfied. Therefore, classical shakedown theorems have to be extended to include the effects of relaxation on one or more constraints of these assumptions.

By directly including thermal stresses in the shakedown formulation, Prager [33] and Rosenblum [34] extended Melan's static theorem to account for thermal loading effects in addition to mechanical loading effects. The kinematic shakedown theorem that accounts for thermal loading and mechanical loading was presented in [35,36,37]. When elastic moduli of the considered material also varies with temperature, the formulation for static shakedown theorem becomes rather complicated. The plastic strain field, ϵ_{ij}^p , does not define uniquely the residual stress field, ρ_{ij} . The static theorem has to be formulated in terms of steady plastic strains rather than in terms of residual stresses. König and Maier [37] presented the static shakedown theorem including thermal stresses. Based on König and Maier's work, Cazzani et al [38] proposed a numerical procedure to obtain a kinematic shakedown load factor. Ceradini [39] established

shakedown formulations to account for inertia and damping effects under dynamic loading. In these formulations, it was assumed that the actual history of external actions was known along with the initial conditions and that the fictitious elastic response was calculated from a dynamic analysis. This fictitious elastic stress field was superimposed with a time-independent residual stress field to determine the shakedown load factor. A shakedown theorem for systems with nonlinear kinematic hardening materials was first formulated by Neal [40]. Neal used a Masing [41] one-dimensional overlay model to describe the nonlinear kinematic behavior of material. Stein et al [42] extended the Masing's overlay model to a three-dimensional model in order to describe the nonlinear kinematic behavior of materials and formulated a corresponding shakedown theorem. The 'second order' geometrical effects were taken into account in Maier's [43] formulation of shakedown theorem for discretized systems in terms of the 'geometric stiffness' matrix. Weichert [44] discussed the effect of geometric nonlinearity on shakedown within the framework of continuum mechanics and proposed practicable methods in the prediction of the shakedown behavior for particular situations.

The classical shakedown theorems were reconsidered by Polizzotto et al [45] with the objective of extending it to a quite general constitutive law for rate-insensitive elastic-plastic material models endowed with dual internal variables and thermodynamic potential. A non-associated flow rule was considered in Maier's early work on shakedown theorem, which was concerned with perfect plasticity with piecewise linear yield functions. It was centered on the concept of a reduced elastic domain as a basis for a sufficient shakedown condition. Recently, this notion was re-proposed in a more general constitutive context under the name of elastic sanctuary by Nayroles and Weichert [46], who suggested its experimental determination. The article deals with an extension of the static shakedown theorem to a fairly general class of elastic-plastic material constitutive models and aims at unifying the above mentioned approaches.

By means of matrix description of the mechanical behavior based on the finite element discretization and the piecewise linearization of yield function, Maier [47] formulated Melan's shakedown theorem into a linear programming problem, which, in principle, permits the evaluation of the shakedown load for a general continuum. This shakedown matrix theory has been employed to extend shakedown theory to a broader area and has been applied widely to discretized structures such as truss and beams. Belytschko [48] presented the first numerical solution for shakedown analysis in continuum problems. Belytschko formulated the shakedown problem by using the equilibrated finite element formulation coupled with the sequential unconstrained minimization technique to obtain the shakedown load. The shakedown analysis was carried out for an elastic-perfectly-plastic square plate with a circular hole subjected to biaxial variable

repeated loading under plane stress condition. Corradi and Zavelani [49] proposed an alternative linear programming approach to reduce the number of constraints in Maier's approach while retaining the linear nature of the problem. The procedure is mainly based on expressing the yield condition by means of the coordinates of the vertices of the yield polyhedron instead of the direction cosines and the plastic capacity of each yield plane. The major advantage of this approach is the efficiency in computing time and the avoidance of computational difficulties with the nonlinear programming approach.

Hung and König [50] established a compatible finite element formulation for static shakedown theorem with a nonlinear mathematical programming formulation, based on the 'yield criterion of the mean'. By way of the 'yield criterion of the mean', the number of discrete nonlinear yield constraints in Belytschko's formulation was reduced by averaging the yield function over each element and make shakedown analysis for continuum problem more applicable in practice.

Application of shakedown theory to soil mechanics began in 1975 when Rowe [51] carried out an experimental model to study circular surface foundations, resting on saturated clays and subjected to inclined, eccentric static and cyclic loads to model an offshore gravity platform. The results of measured pore pressure showed that equilibrium was associated with the 'equilibrium of shakedown.' While studying wave effect on the foundations of offshore structures, Zienkiewicz et al [52] observed that 'Progressive deformation' at loading levels was much smaller than those resulted from the static collapse. Shakedown behavior is further illustrated by examples of a footing under plane strain condition subjected to a vertical steady loading and a cyclic bending moment due to horizontal loads. The results showed that the magnitude of settlement increased either due to the increase of the vertical load, or the decrease of the strain hardening parameter or the angle of internal friction. Shakedown analysis of a footing underlined by dry soil and subjected to a variable repeated loading was carried out by Aboustit and Reddy [53] under a plane strain condition. Shakedown load parameters for different angles of internal friction of the material were computed.

The possible application of the static shakedown theory in pavement design is first made by Sharp [54] and then illustrated by Sharp and Brooker [55]. The pavement is modeled as a multilayer system of an elastic-perfectly plastic solid subjected to a trapezoidal distributed load. The shakedown analysis of pavements was carried out by two approaches: a linear programming method and a conic section method. In the first approach, they followed the same procedure proposed by Maier [43] and transformed Melan's shakedown theorem into a linear programming problem by employing piecewise linearized Mohr-Coulomb yield

function. A conventional linear programming technique was then used to determine the shakedown limit of a layered continuum subjected to repeated moving surface loads under plane strain condition. In the second approach, the conic section method was used to find a shakedown load factor. By substituting stresses into Mohr-Coulomb yield function, a quadratic form in load factor and residual stresses was obtained, which defines a conic section for each point (x, z) in the half-space. The shakedown limit value was obtained by finding the largest load factor (λ) satisfying (a) $\lambda > 0$; (b) lie inside or on all of these conics; (c) residual stress field ρ must be larger than the tensile strength, $-\rho_t$, and smaller than the compressive strength, ρ_c .

Several layered pavements were analyzed by the proposed approaches. From these results, it was found that at a given value of strength, there exists an optimal value of relative stiffness that maximizes the shakedown limit. A higher value of E/E_0 results in the fatigue failure at the bottom of the top layer, while a lower value of E/E_0 results in the fatigue failure at the top of the subgrade. At a given value of stiffness, increasing the relative strength causes an increase in shakedown limit.

By case study, Sharp and Brooker [55] demonstrated that the shakedown limit of a pavement provides a convenient predictor of the performance for design purposes. The relationship between the shakedown limit, material properties, and the thickness developed from shakedown analysis may provide various combinations of relative strength, relative stiffness, and surface layer thickness. These may be chosen to give a standard of performance. Therefore, design tools may be readily developed based on shakedown analysis results.

A finite element method in conjunction with the nonlinear mathematical programming approach was employed by Raad et al. [56-58] in the shakedown analysis of pavement system. For the discretized system that consists of numbers of four node elements, Melan's shakedown theorem was formulated into a nonlinear programming problem. The equilibrium condition of the residual stress field is satisfied by incorporating the resultant forces caused by the residual stress at every node into the objective function. A pattern search algorithm originated by Hooke and Jeeves [59] was used to solve the optimization problem. The influence of compaction stress on shakedown limit value was investigated. It was found that compaction stresses would increase the predicted shakedown loads for both pavements with soft and stiff subgrade and the increase is most significant for granular base with low cohesion and for base overlaying stiff subgrade. The influence of the cohesion and friction of a granular base on shakedown load was also

studied. The numerical results show that increase in the strength of a granular base would significantly increase the shakedown capacity of the pavement. However, the cohesion of a base seems to be more a significant parameter on shakedown capacity than the friction angle.

Sharp's conic section method was re-examined by Collins et al [60]. Based on Koiter's [32] kinematic shakedown theorem, and the assumption that failure mechanism is similar to upper bound limit analysis, an upper bound physical interpretation was given to the conic method and the shakedown analysis was extended to a three dimensional half-space problem with elastic-perfectly plastic material following Mohr-Coulomb yield condition. Later, the same approach was extended to a layered pavement system shakedown analysis [61, 62], in which permanent deformations along the traffic direction were taken into account through a shakedown load formulation. Shakedown behavior for a two-dimensional plane strain problem under a trapezoidal distributed surface load and three-dimensional problem under a circular distributed load were investigated. The results showed that shakedown load from a two-dimensional analysis was consistently lower than that from a three-dimensional analysis, which means plane strain analysis gives a conservative estimation.

The advantage of Belytschko's shakedown analysis formulation is that equilibrium conditions of residual stresses need not be included in the optimization process. But the nonlinear optimization technique is rather complicated. The optimizer has to find the parameters of stress functions of residual stress field that minimize the objective function. Corradi and Zavelani's linear programming approach greatly reduce the numbers of variables used in the optimization process. However, only an upper bound shakedown load can be computed by using duality formulations. On the other hand, considering the plastic deformation defined in Eq. (5.8) in Ref [49], it only represents one instance within one admissible strain cycle. Therefore, the "total dissipated energy" may not be for one admissible strain cycle. Sharp and Booker's elegant 'method of conics' based on the assumption that residual stress distribution is uniformly distributed within a plane (x, y) and is dependent solely on the depth z . This assumption greatly simplifies the shakedown formulation and leads to 'method of conics,' but it may not be the case in actual loading situations, especially for the problem they considered. Raad et al's[56] approach does not include yield constraints in the objective function, although an alternative procedure was used to satisfy these conditions. Also the optimization algorithm is rather time consuming.

1.3 SCOPE OF STUDY

The objectives of the current study are:

1. Establish a numerical algorithm to simulate fatigue crack growth behavior, to determine unstable crack growth, and to predict fatigue life for engineering materials and objects.
2. Based on current numerical algorithms of shakedown analysis, develop a general numerical algorithm and optimization procedure to evaluate both the lower and upper bound shakedown loads for a given system accurately and efficiently.
3. Discuss the possibility to couple the fatigue failure mechanism with shakedown behavior.

There are seven major topics included in this thesis. The problem definition, general introduction, and objective of the study are included in the first chapter. Literature review of fatigue and shakedown and their current development is given in Chapter II and III. A numerical algorithm to simulate fatigue crack growth and to predict fatigue life is proposed in Chapter IV. The fatigue behavior of several simple problems is analyzed. The fatigue crack growth rates are established and fatigue lives are predicted for these problems. A general numerical algorithm to evaluate lower bound shakedown load is described in Chapter V. A multidimensional search algorithm adopted as an optimizer in finding lower bound shakedown load. An eigen-mode method is proposed in chapter VI to construct the arbitrary plastic deformation paths in evaluating the upper bound shakedown load. Several examples are presented to illustrate the applicability of the proposed method. Applications of these proposed numerical algorithms and methods are given in chapter VII. The fatigue behavior is analyzed and the lower and upper bound shakedown loads are evaluated for a two-layered pavement system. The lower and upper bound shakedown loads for a three-layered pavement system are also calculated. The possibility of interaction between fatigue failure mechanism and shakedown behavior is discussed. Summary and conclusions are given in chapter VIII.

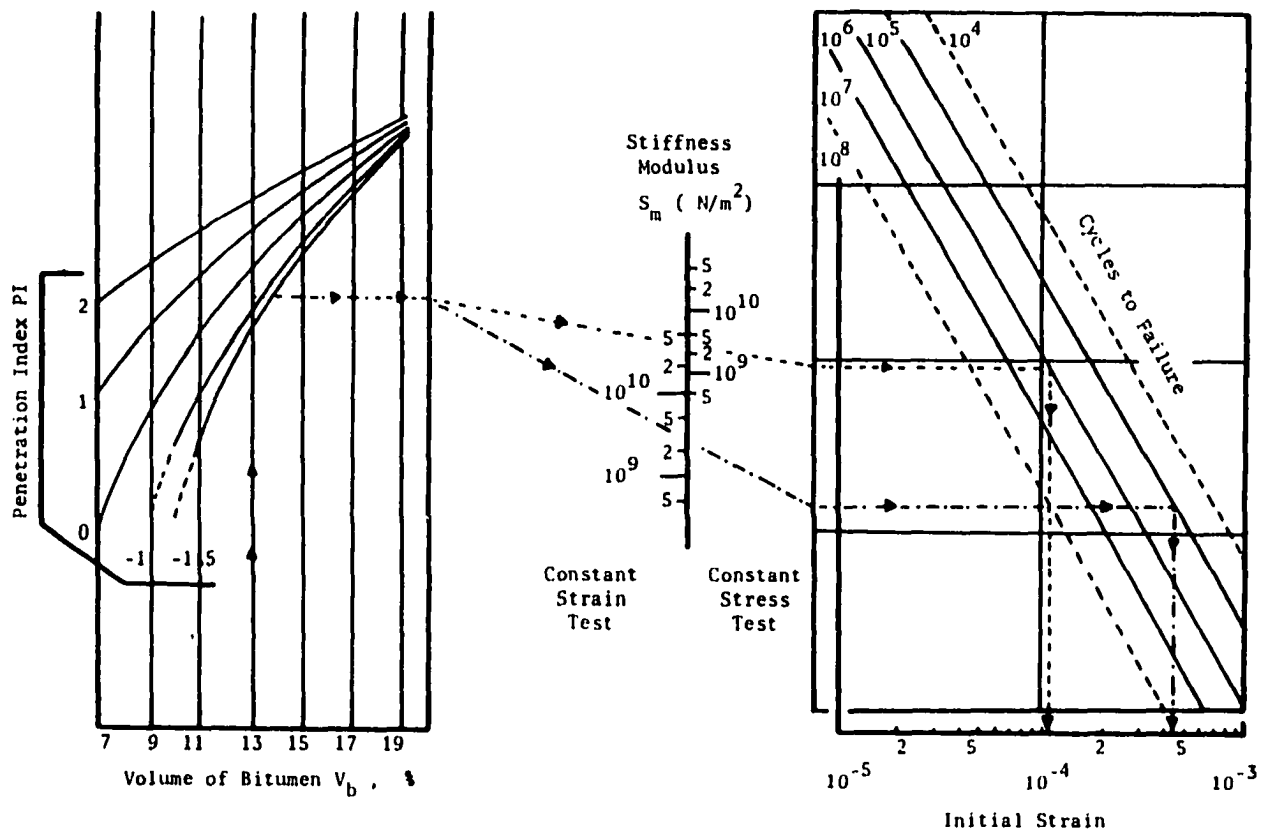


Figure 1.1 Nomograph for Predicting Fatigue Life of Bituminous Mixes.
(After Bonnaure et al. (1980).)

CHAPTER II

REVIEW OF FRACTURE AND FATIGUE

2.1 INTRODUCTION

Fracture and fatigue have great importance in engineering object design with regard to both reliability and economies. Engineering objects such as structural components and mechanical parts may fail in different ways under applied loads. The mechanical failure modes mostly concerned in engineering design may be classified as follows:

- Instability failure both in tension (plastic necking) and compression (buckling)
- Failure by yielding with large plastic deformation
- Failure by fracture (cracking)
- Failure by load cycling (fatigue).

The traditional design approach that is based on the selection of a limiting applied stress as compared with the material yield stress, σ_y , might not always guarantee a fail-safe design strategy. On the other hand, imperfection always exists in engineering materials and leads to local stress concentration. Hence, fracture and fatigue play more and more important roles in engineering object design. The concepts of fracture and fatigue are reviewed in this chapter. Fracture characteristic and fatigue behavior of engineering materials will be addressed in the following chapter.

2.2 BASIC EQUATIONS

The equilibrium state of the volume element of a loaded three-dimensional body as shown in Fig. 2.1 can be determined in terms of six stress components, σ_{ij} ($i, j=1,2,3$) acting on the element, as follows by ignoring any body forces

$$\sigma_{ij,j} = 0 \quad (2.1a)$$

where $\sigma_{ij,j}$ denotes partial differentiation of stress components, σ_{ij} , with respect to the coordinates x_j .

The elastic continuity requires the strain components, ϵ_{ij} , corresponding to the stress components satisfy the compatibility equation,

$$\epsilon_{ij,kk} + \epsilon_{kl,ij} - \epsilon_{ik,jl} - \epsilon_{jl,ik} = 0 \quad (2.2)$$

where $\epsilon_{ij} = \frac{1}{2}(u_{i,j} + u_{j,i})$ and $u_{i,j}$ denotes partial differentiation of displacement components u_i with respect to x_j . The relationship between stresses and strains for an isotropic, elastic material satisfies the generalized Hooke's law

$$\sigma_{ij} = 2\mu\epsilon_{ij} + \lambda\epsilon_{kk}\delta_{ij} \quad (2.3)$$

in which $\epsilon_{kk} = \epsilon_{11} + \epsilon_{22} + \epsilon_{33}$, $\mu = E/2(1+\nu)$ shear modulus of elasticity and $\lambda = 2\mu\nu/(1-2\nu)$ is Lamé constant. The equilibrium equation Eq. (2.1a) can be expressed in terms of displacements, which is known as Navier's displacement equations

$$u_{i,jj} + \frac{1}{1-2\nu}u_{j,ji} = 0 \quad (2.1b)$$

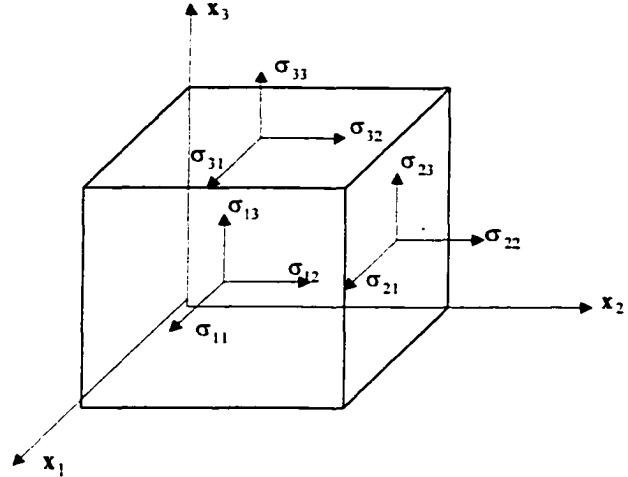


Figure 2.1 Stress Components on a three-dimensional Element Referred to Cartesian Coordinate System.

For plane strain problem, Hook's law can be simplified as

$$\begin{aligned} \epsilon_{11} &= \frac{1-\nu^2}{E}(\sigma_{11} - \frac{\nu}{1-\nu}\sigma_{22}) \\ \epsilon_{22} &= \frac{1-\nu^2}{E}(\sigma_{22} - \frac{\nu}{1-\nu}\sigma_{11}) \\ \epsilon_{12} &= \frac{1+\nu}{E}\sigma_{12} \end{aligned} \quad (2.4)$$

For plane stress problem, Hook's law becomes

$$\begin{aligned} \epsilon_{11} &= \frac{1}{E}(\sigma_{11} - \nu\sigma_{22}) \\ \epsilon_{22} &= \frac{1}{E}(\sigma_{22} - \nu\sigma_{11}) \\ \epsilon_{12} &= \frac{1+\nu}{E}\sigma_{12} \end{aligned} \quad (2.5)$$

2.3 LINEAR ELASTIC FRACTURE MECHANICS

2.3.1 Westergaard's Stress Function

In linear elasticity theory, Westergaard's stress function [63] is often used to solve two-dimensional problems of cracked bodies or components in structures. Considering a complex stress function Φ :

$$\Phi = R_e \bar{\bar{\phi}}(z) + x_2 \text{Im} \bar{\phi}(z) \quad (2.6)$$

$$\nabla^2 (\nabla^2 \phi) = 0$$

where $z=x+iy$ is a complex variable, $\phi(z)$ is a harmonic function and $\phi'(z)$, $\phi''(z)$, $\bar{\phi}(z)$ and $\bar{\bar{\phi}}(z)$ are denoted as its first and second derivatives and integrals, respectively, the state of stress can be determined by

$$\begin{aligned} \sigma_{22} &= \frac{\partial^2 \Phi}{\partial x_1^2} = R_e \phi(z) + \text{Im} \phi'(z) \\ \sigma_{11} &= \frac{\partial^2 \Phi}{\partial x_2^2} = R_e \phi(z) - x_2 \text{Im} \phi'(z) \\ \sigma_{12} &= \frac{\partial^2 \Phi}{\partial x_1 \partial x_2} = -x_2 R_e \phi'(z) \end{aligned} \quad (2.7)$$

The displacements are given by

$$\begin{aligned} 2\mu u_1 &= \frac{1}{2}(\kappa - 1)R_e \bar{\phi}(z) - x_2 \text{Im} \phi(z) \\ 2\mu u_2 &= \frac{1}{2}(\kappa + 1)\text{Im} \bar{\phi}(z) - x_2 R_e \phi(z) \end{aligned} \quad (2.8)$$

For three particular boundary conditions, specific stress functions were constructed respectively and the stress field near crack tip then is determined by Eq. (2.7).

A. Crack under Tension [64]

Consider an infinite plate containing a crack of length $2a$ subjected to a remote tensile stress, σ , as shown in Fig. 2.2. From the analysis of the boundary conditions, the complex stress function can be represented by [64]

$$\phi(z) = \frac{\sigma z}{\sqrt{z^2 - a^2}} \quad (2.9)$$

To obtain the stress state around the crack tip, it is more convenient to substitute the variable $\eta=z-a$ and $\eta = re^{i\theta}$ into Eq. (2.9) and make the first order approximation. Then the stress function can now be rewritten as

$$\phi = \frac{\sigma\sqrt{a}}{\sqrt{2r}} = \frac{\sigma\sqrt{a}}{\sqrt{2r}} e^{-i\theta/2} \quad (2.10)$$

From stress function Eq. (2.9), the stress field near crack tip can be obtained by

$$\begin{aligned} \sigma_{11} &= \sigma\sqrt{\frac{a}{2r}} \cos\frac{\theta}{2} (1 - \sin\frac{\theta}{2} \sin\frac{3\theta}{2}) + \dots \\ \sigma_{22} &= \sigma\sqrt{\frac{a}{2r}} \cos\frac{\theta}{2} (1 + \sin\frac{\theta}{2} \sin\frac{3\theta}{2}) + \dots \\ \sigma_{12} &= \sigma\sqrt{\frac{a}{2r}} \sin\frac{\theta}{2} \cos\frac{\theta}{2} \cos\frac{3\theta}{2} + \dots \end{aligned} \quad (2.11)$$

and the near tip displacement field is given by

$$\begin{aligned} u_1 &= \frac{\sigma}{\mu} \sqrt{\frac{ar}{2}} \cos\frac{\theta}{2} \left[\frac{1}{2}(\kappa - 1) + \sin^2\frac{\theta}{2} \right] \\ u_2 &= \frac{\sigma}{\mu} \sqrt{\frac{ar}{2}} \sin\frac{\theta}{2} \left[\frac{1}{2}(\kappa + 1) - \cos^2\frac{\theta}{2} \right] \end{aligned} \quad (2.12)$$

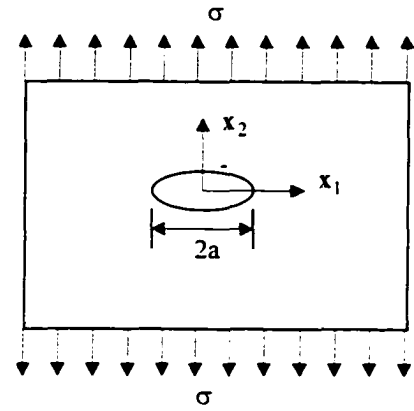


Figure 2.2 An Infinite Plate Containing a Crack of Length $2a$ Subjected to a Remote Tensile Stress σ .

B. Crack under Shear [64]

For the cracked plate subjected to a remote shear stress $\sigma_{21} = \tau$ as shown in Fig. 2.3, the stress function is expressed by

$$\Phi_{II} = -x_2 R_e \bar{\phi}_{II}(z) \quad (2.13a)$$

where $\phi_{II}(z)$ is a function of z , which is properly chosen to satisfy all the given boundary conditions. The stress field is then expressed by the stress function,

$$\begin{aligned} \sigma_{11} &= 2 \operatorname{Im} \phi_{II}(z) + x_2 R_e \phi'_{II}(z) \\ \sigma_{22} &= -x_2 R_e \phi''_{II}(z) \\ \sigma_{21} = \sigma_{12} &= R_e \phi_{II}(z) - x_2 \operatorname{Im} \phi'_{II}(z) \end{aligned} \quad (2.13b)$$

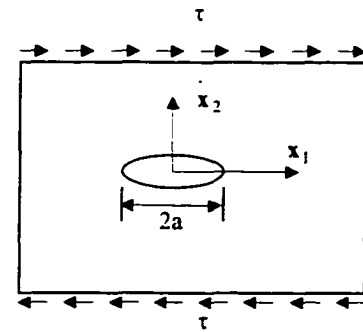


Figure 2.3 An Infinite Plate Containing a Crack of Length $2a$ Subjected to a Remote Shear Stress τ

Through the analysis of boundary conditions, the following specific stress function is obtained

$$\phi_{II} = \frac{\tau}{\sqrt{(1-a^2/z^2)}} \quad (2.14a)$$

Similar to the tensile situation, the stress field is given by

$$\begin{aligned} \sigma_{11} &= -\tau \sqrt{\frac{a}{2r}} \sin \frac{\theta}{2} \left(2 + \cos \frac{\theta}{2} \cos \frac{3\theta}{2}\right) \\ \sigma_{22} &= \tau \sqrt{\frac{a}{2r}} \sin \frac{\theta}{2} \cos \frac{\theta}{2} \cos \frac{3\theta}{2} \\ \sigma_{12} &= \tau \sqrt{\frac{a}{2r}} \cos \frac{\theta}{2} \left(1 - \sin \frac{\theta}{2} \sin \frac{3\theta}{2}\right) \end{aligned} \quad (2.14b)$$

The displacement field is given by

$$\begin{aligned} u_1 &= \frac{\tau}{\mu} \sqrt{\frac{ar}{2}} \sin \frac{\theta}{2} \left[\frac{1}{2}(\kappa+1) + \cos^2 \frac{\theta}{2}\right] \\ u_2 &= \frac{\tau}{\mu} \sqrt{\frac{ar}{2}} \cos \frac{\theta}{2} \left[\frac{1}{2}(1-\kappa) - \sin^2 \frac{\theta}{2}\right] \end{aligned} \quad (2.14c)$$

C. Crack under Antiplane Shear [64]

Another possible shear model is remote shear stress $\sigma_{23} = \tau$ applied along the direction perpendicular to the plate plane as illustrated in Fig. 2.4. In this situation, displacement occurs only in the x_3 direction. Therefore, we have

$$\frac{\partial u_3}{\partial x_1} = \frac{\sigma_{13}}{\mu}, \quad \frac{\partial u_3}{\partial x_2} = \frac{\sigma_{23}}{\mu} \quad (2.15a)$$

The equilibrium equation Eq. (2.1a) becomes

$$\frac{\partial \sigma_{13}}{\partial x_1} + \frac{\partial \sigma_{23}}{\partial x_2} = 0 \quad (2.15b)$$

Introducing Eq. (2.15a) into Eq. (2.15b), we obtain,

$$\frac{\partial^2 u_3}{\partial x_1^2} + \frac{\partial^2 u_3}{\partial x_2^2} = \nabla^2 u_3 = 0 \quad (2.15c)$$

By choosing the following displacement function

$$u_3 = \frac{1}{\mu} \text{Im} \phi_{III}(z) \quad (2.15d)$$

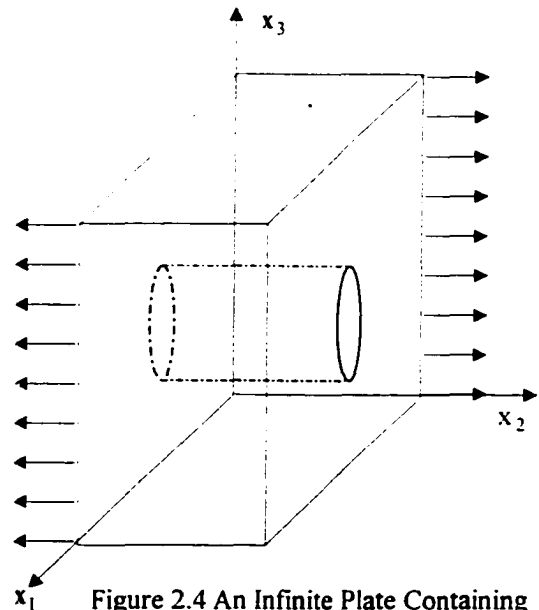


Figure 2.4 An Infinite Plate Containing a Crack of Length $2a$ Subjected to a Remote Shear Stress τ along x_3 .

the stress components are expressed by

$$\sigma_{13} = \text{Im} \phi'_{\text{III}}(z), \quad \sigma_{23} = \text{Re} \phi'_{\text{III}}(z) \quad (2.15e)$$

The following stress function is obtained by satisfying these boundary conditions.

$$\phi'_{\text{III}}(z) = \frac{\tau}{\sqrt{(1-a^2/z^2)}} \quad (2.15f)$$

From this stress function, the stress field near crack tip can be obtained by

$$\begin{aligned} \sigma_{11} &= -\tau \sqrt{\frac{a}{2r}} \sin \frac{\theta}{2} \left(2 + \cos \frac{\theta}{2} \cos \frac{3\theta}{2}\right) \\ \sigma_{22} &= \tau \sqrt{\frac{a}{2r}} \sin \frac{\theta}{2} \cos \frac{\theta}{2} \cos \frac{3\theta}{2} \\ \sigma_{12} &= \tau \sqrt{\frac{a}{2r}} \cos \frac{\theta}{2} \left(1 - \sin \frac{\theta}{2} \sin \frac{3\theta}{2}\right) \end{aligned} \quad (2.15g)$$

The displacement field is given by

$$\begin{aligned} u_1 &= \frac{\tau}{\mu} \sqrt{\frac{ar}{2}} \sin \frac{\theta}{2} \left[\frac{1}{2}(\kappa + 1) + \cos^2 \frac{\theta}{2}\right] \\ u_2 &= \frac{\tau}{\mu} \sqrt{\frac{ar}{2}} \cos \frac{\theta}{2} \left[\frac{1}{2}(1 - \kappa) - \sin^2 \frac{\theta}{2}\right] \end{aligned} \quad (2.15h)$$

By examining the stress σ_{11} in Eq. (2.11), we may write,

$$\sigma_{11(x=0)} = \sigma \sqrt{a/2r} = \sigma \frac{\sqrt{\pi a}}{\sqrt{2\pi r}} = \frac{K_I}{\sqrt{2\pi r}} \quad (2.16)$$

where $K_I = \sigma \sqrt{\pi a}$ is defined as Stress Intensity Factor for opening mode. Introducing K_I into Eq. (2.11), we can see that the local stress field around crack tip in a cracked body can be characterized in terms of a single parameter, K_I , that is related to both the nominal stress (σ) level in the body and the size of the crack (a) presented. For shear and tearing modes, the stress intensity factors are defined by K_{II} and K_{III} , respectively.

2.3.2 Fracture Strength

The theoretical fracture strength of a solid is of the order of $E/10$, but the strength of crystals and glass found in practice tend to be lower than this value by some two orders of magnitude [64]. By using a thermodynamic approach, Griffith[65] provided an energy criterion of fracture for an infinite plate with a

central crack subjected to an uniformly distributed stress. It is defined as strain energy release rate and is given by

$$G = \frac{\partial U}{\partial a} = -\frac{\sigma^2 \pi a}{E} \quad \text{for plane stress} \quad (2.17)$$

The relationship between stress intensity factor and strain energy release rate is [65]

$$G = \frac{K^2}{E} \quad (2.18)$$

2.4 ELASTIC-PLASTIC FRACTURE MECHANICS

Many engineering materials and structures often experience large deformations and display ductile behavior. Thus, for many applications, the linear elastic fracture analysis used to calculate fracture parameters such as K_{IC} is invalidated by the formation of a large-scale plastic zone and by an elastic-plastic behavior. Linear-elastic fracture mechanics therefore, is extended to elastic-plastic fracture mechanics by introducing the concepts of R_{curve}, J-integral, and crack tip opening displacement(CTOD).

In 1961, Wells [66] proposed that the fracture behavior in the vicinity of a sharp crack could be characterized by the opening of the notch faces, namely, the crack tip opening displacement (CTOD). The measurements of CTOD can be made even when there is considerable plastic flow ahead of a crack for elastic-plastic or fully plastic behavior. Several crack tip plastic models were proposed to include plastic zone size effect around crack tip and relate the CTOD to the applied stress and crack length.

2.4.1 Irwin's Plastic Zone Correction Model [67]

Considering a remotely loaded sheet in a state of plane stress, the distribution of σ_y along $y=0(\theta=0)$ can be described by the stress-field equation (Eq. 2.11) from elastic fracture mechanics and is plotted in Fig. 2.5. As r close to a , elastic stress, σ_y , approaches infinite. In practice, when applied stress reaches yield stress, σ_0 , the material undergoes plastic deformation. Thus, high level elastic stress will re-distribute around the crack tip such that no point exceeds yield stress. As a result, the stress curve must be shifted, so that equilibrium is maintained. Considering the equilibrium condition:

$$\int_0^r \frac{K}{(2\pi r)^{1/2}} dr = r_p \sigma_0 \quad (2.19)$$

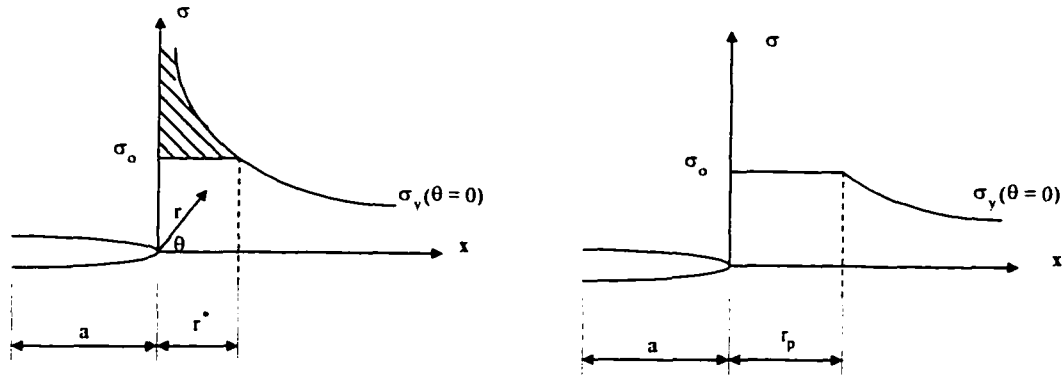


Figure 2.5 (a) Elastic Stress Distribution around Crack Tip by Using

$$\sigma_x = \frac{K_I}{(2\pi r)^{1/2}} \cos \frac{\theta}{2} \left(1 - \sin \frac{\theta}{2} \sin \frac{3\theta}{2}\right)$$

$$\sigma_y = \frac{K_I}{(2\pi r)^{1/2}} \cos \frac{\theta}{2} \left(1 + \sin \frac{\theta}{2} \sin \frac{3\theta}{2}\right)$$

(b) Irwin's Plastic Zone Model by Considering Stress redistribution around Crack Tip.

By integration, we have

$$r_p = \frac{1}{\pi} \left(\frac{K}{\sigma_o}\right)^2 \quad (2.20)$$

Assuming the plastic zone around crack tip is a circular with radius $\lambda = r_p / 2$, then

$$\lambda = \frac{1}{2\pi} \left(\frac{K}{\sigma_o}\right)^2 \quad (2.21)$$

Irwin [67] proposed that for large plastic deformation, crack length should be modified as $a_y = a + \lambda$. By introducing a_y into the crack opening equation described in [68]

$$v = \frac{2\sigma}{E} (a^2 - x^2)^{1/2} \quad (2.22)$$

crack opening displacement is given at $x=a$

$$\delta(\text{CTOD}) = \frac{4\sigma}{E} (2a\lambda)^{1/2} \quad (2.23)$$

Substituting Eq. (2.21) into Eq. (2.23), we have,

$$\delta(\text{CTOD}) = \frac{4}{\pi} \frac{K^2}{E\sigma_o} \quad (2.24)$$

2.4.2 Dugdale's Strip-Yield Model [69]

Consider a through-thickness crack in an infinite plate that is subjected to a tensile stress normal to the plane of the crack as shown in Fig. 2.6. The crack is assumed to have a length of $2(a + \rho)$, where ρ is the extent of the plastic zone that is subjected to yield-stress levels that tend to close the crack. Dugdale [69] proposed that the plastic zone size, ρ , is fixed by the requirement that the stress singularity should disappear, thus

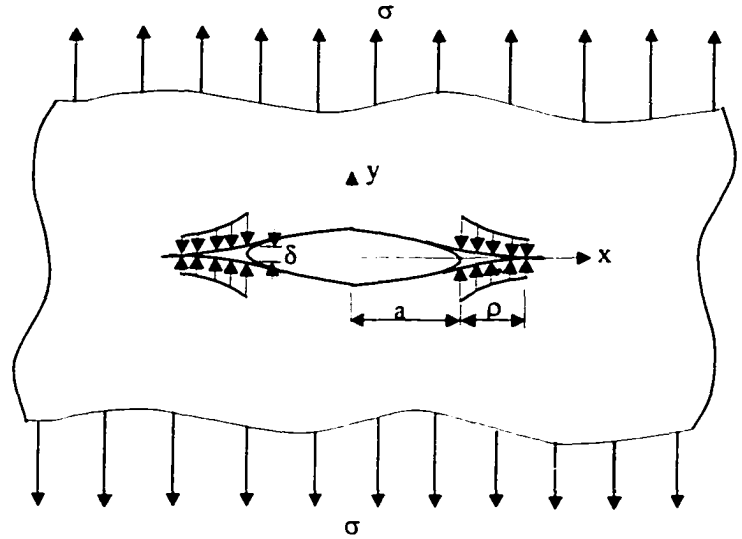


Figure 2.6 Dugdale Model for an Infinite Cracked Plate.

the superposition of stress intensity due to remotely applied stress, K_{σ} , and that due to plastic closure, K_{σ_0} , should be zero, giving,

$$K_{\sigma} + K_{\sigma_0} = 0 \quad (2.25)$$

By using physical crack length $a = (a_0 + \rho)$, we have,

$$K_{\sigma} = \sigma[\pi(a + \rho)]^{1/2} \quad (2.26)$$

By using weight function technique [68], we have

$$K_{\sigma_0} = -2\sigma_0 \left(\frac{a + \rho}{\pi}\right)^{1/2} \arccos\left(\frac{a}{a + \rho}\right) \quad (2.27)$$

Substituting Eq. (2.26) and (2.27) into Eq. (2.25), we obtain

$$\frac{a}{a + \rho} = \cos\left(\frac{\pi\sigma}{2\sigma_0}\right) \quad (2.28)$$

$$\text{If } \sigma \ll \sigma_0, \text{ then } \rho = \frac{\pi a}{8} \left(\frac{\sigma}{\sigma_0}\right)^2 = \frac{\pi}{8} \left(\frac{K}{\sigma_0}\right)^2.$$

The crack tip opening displacement is,

$$\delta(\text{CTOD}) = 8 \frac{\sigma\sigma_0}{\pi E} \ln \sec\left(\frac{\pi\sigma}{2\sigma_0}\right) \quad (2.29)$$

where σ_o — yield stress of the material

a — $\frac{1}{2}$ physical crack length

σ — nominal stress

E — modulus of elasticity of the material.

By expanding $\ln \sec\left(\frac{\pi \sigma}{2 \sigma_o}\right)$, Eq. (2.29) becomes

$$\delta(\text{CTOD}) = 8 \frac{\sigma \sigma_o}{\pi E} \left[\frac{1}{2} \left(\frac{\pi \sigma}{2 \sigma_o}\right)^2 + \frac{1}{12} \left(\frac{\pi \sigma}{2 \sigma_o}\right)^4 + \dots \right] \quad (2.30)$$

For nominal stress values less than $3/4 \sigma_o$, a reasonable approximation for $\delta(\text{CTOD})$ is

$$\delta(\text{CTOD}) = \frac{\pi \sigma^2 a}{E \sigma_o} \quad (2.31)$$

2.4.3 J-integral

Mathematical theory encounters considerable difficulties in determining concentrated stress-strain fields near notches or cracks for elastic-plastic materials. As described in the previous section and Ref [70], some simple models were proposed to solve the elastic-plastic problems of opening mode crack. However, the path-independent integral J approach provides an effective tool for some cases.

The J -integral was first identified by Rice [71]. For a two-dimensional deformation body of linear or nonlinear (elastic-plastic behavior defined by deformation theory of plasticity) elastic material with a notch and free of body force as shown in Fig. 2.7, the J -integral is defined by Rice [71] in the form

$$J = \int_{\Gamma} \left(\hat{W} dy - \mathbf{T} \cdot \frac{\partial \mathbf{u}}{\partial x} dS \right) \quad (2.32)$$

where Γ is an arbitrary contour surrounding the crack tip, the integral being evaluated in a counterclockwise manner from the lower flat notch surface and continuing along the path Γ to the upper flat surface. \hat{W} is defined as the strain-energy density i. e.

$$\hat{W} = \hat{W}(x, y) = \hat{W}(\mathbf{e}) = \int_0^{\mathbf{e}} \sigma_{ij} d\epsilon_{ij}$$

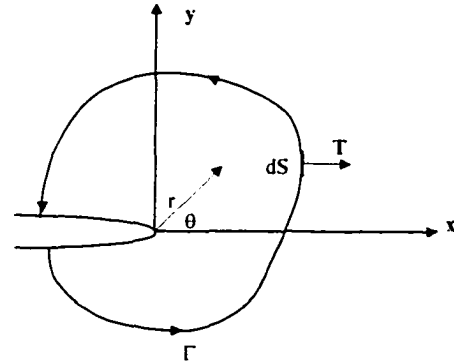


Figure 2.7 Crack Tip Coordinate System and typical Line Integral Contour.

$$J = \int_{\Gamma} \hat{W} dy - \mathbf{T} \cdot \frac{\partial \mathbf{u}}{\partial x} dS$$

\mathbf{T} is the traction vector defined according to the outward normal Γ , $T_i = \sigma_{ij}n_j$, \mathbf{u} is the displacement vector at which \mathbf{T} is applied. dS is variation of arc length along Γ .

J-integral bypasses the detailed solution of boundary-value problems that are usually very difficult to solve mathematically and characterizes the locally concentrated stress-strain field in an average sense. For linear or nonlinear elastic materials, J-integral was proven to be path independent, which makes its evaluation go sufficiently far from the crack tip region and be directly carried out.

An alternative definition was also given by Rice [72]. The alternative definition considers the variation of potential energy per unit thickness with respect to notch size. Considering two bodies of linear or nonlinear elastic material each with a notch as shown in Fig. 2.8a and 2.8b. The notched bodies differ in size, otherwise they are identical in mechanical and geometrical aspects. Assuming surface traction, T_i^o , applied on S_T and displacement u_i^o imposed on S_u . Let

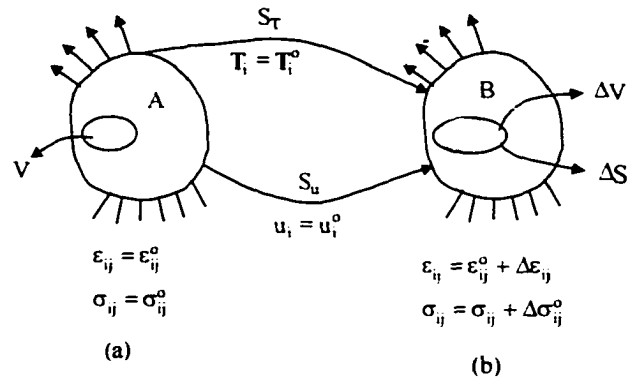


Figure 2.8 (a) and (b) Comparison of Two Notched Elastic Bodies of Identical Shape Composition, and Loading, but the Notches of The Two Bodies.

ΔS denote the newly created traction free surface and ΔV denote the corresponding volume. If σ_{ij}^o , ϵ_{ij}^o denotes the deformation state for body A, the potential energy is,

$$P^o = \int_V W(\epsilon_{mn}^o) dV - \int_{S_T} T_i^o u_i^o dS \quad (2.33)$$

For body B, the state of deformation changes to $\sigma_{ij}^o + \Delta\sigma_{ij}$, $\epsilon_{ij}^o + \Delta\epsilon_{ij}$. Defining potential energy increase as ΔP , the potential energy at the new state of deformation is

$$P^o + \Delta P = \int_{V-\Delta V} W(\epsilon_{mn}^o + \Delta\epsilon_{mn}) dV - \int_{S_T} T_i^o (u_i^o + \Delta u_i) dS \quad (2.34)$$

Considering the boundary conditions,

$\Delta T_i = 0$ on S_T , $\Delta u_i = 0$ on S_u and $T_i^o + \Delta T_i = 0$ on ΔS . we have

$$\int_{S_T} T_i^o \Delta u_i dS = \int_{V-\Delta V} (\sigma_{ij}^o + \Delta\sigma_{ij}) \Delta\epsilon_{ij} dV.$$

The potential energy decrease can be expressed as [72],

$$\begin{aligned}
 -\Delta P &= \int_{\Delta V} W(\epsilon_{mn}^o) dV + \int_{V-\Delta V} \{(\sigma_{ij}^o + \Delta\sigma_{ij})\Delta\epsilon_{ij} - [W(\epsilon_{mn}^o + \Delta\epsilon_{mn}) - W(\epsilon_{mn}^o)]\} dV \\
 &= \int_{\Delta V} W(\epsilon_{mn}^o) dV + \int_{V-\Delta V} \left\{ \int_{\epsilon_{mn}^o}^{\epsilon_{mn}^o + \Delta\epsilon_{mn}} (\sigma_{ij}^o + \Delta\sigma_{ij} - \sigma_{ij}) d\epsilon_{ij} \right\} dV
 \end{aligned} \quad (2.35)$$

Assuming the deformation satisfies stability $d\sigma_{ij}d\epsilon_{ij} \geq 0$, the strain integral of Eq. (2.35) over a straight-line path in stress space leads to

$$0 \leq \int_{\epsilon_{mn}^o}^{\epsilon_{mn}^o + \Delta\epsilon_{mn}} (\sigma_{ij}^o + \Delta\sigma_{ij} - \sigma_{ij}) d\epsilon_{ij} \leq \Delta\sigma_{ij}\Delta\epsilon_{ij} \quad (2.36)$$

By using Eq. (2.35), we have the inequalities,

$$0 \leq (-\Delta P) - \int_{\Delta V} W(\epsilon_{mn}^o) dV \leq \int_{\Delta S} \Delta T_i \Delta u_i dS \quad (2.37)$$

Suppose the notch size difference is infinitesimal, both $\Delta T_i = (\Delta\sigma_{ij})n_j$ and Δu_i are of first-order quantities. Since the integral over ΔV is first-order, the upper bound in Eq. (2.37) is second-order and tends to zero when notch size has infinitesimal change. Thus, the potential energy decrease is

$$-dP = \int_{\Delta V} W(\epsilon_{mn}^o) dV \quad (2.38)$$

Consider a two-dimensional deformation body with a flat-surfaced notch as shown in Fig. 2.9. The notch has surfaces parallel to the x_i direction and smooth arc Γ_t around the tip. Denoting the potential energy decrease per unit thickness in the x_2 direction as ΔP and notch difference as dl , the rate of decrease of potential energy per unit thickness with respect to notch size is

$$-dP/dl = \int W(\epsilon_{mn}) dx_2 \quad (2.39)$$

Considering J-integral

$$J = \int [W dx_2 - T \frac{\partial u}{\partial x_1} dS] \quad (2.40)$$

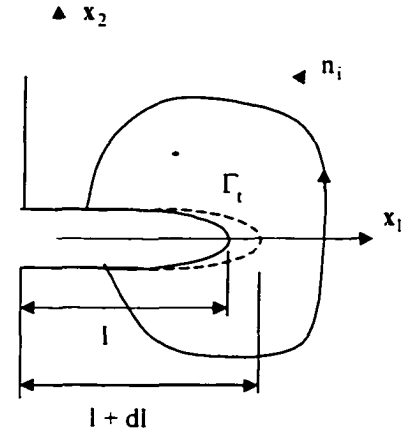


Figure 2.9 Flat Surface Notch in Two-dimensional Deformation Filed. Γ_t Denotes Curved Notch Root; Γ Denotes any Curve Surrounding the Root.

integrated along traction free notch surface Γ_t , we have

$$J = -dP/dl \quad (2.41)$$

For linear or nonlinear elastic materials, J-integral is path independent, and then Eq. (2.41) is true when it is computed along any arbitrary path around the notch.

This J-integral is defined by externally measurable variables such as load and displacement and makes direct measurement of J-integral through experiment possible.

The third method of defining J is the pure-bend-area method, which is widely used and described in ASTM Standard [73]. This standard is used to determine J_{IC} the J value at the initiation of crack growth. For bend or edge-notched specimens, the load-line displacement must be measured. The total area under the load load-line displacement curve should be measured as illustrated in Fig. 2.10. For each of several tests to different Δa , determine J as follows

$$J = \frac{A}{Bb} f\left(\frac{a_o}{W}\right) \quad (2.42)$$

where A — area under load load-point displacement record
 B — specimen thickness
 b — initial uncracked ligament, W-a
 W — specimen width
 a_o — original crack length, including fatigue crack.

For the three-point bend specimen

$$f\left(\frac{a_o}{W}\right) = 2.0$$

For the compact specimen

$$f\left(\frac{a_o}{W}\right) = 2.2$$

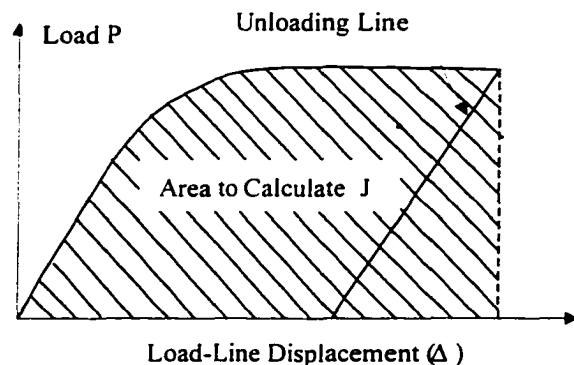


Figure 2.10 Illustration of Work to a Given Displacement.

2.4.4 R_c curve

For ductile materials, it is observed that stable crack growth accompanied by an increasing or constant load level, which indicates that material resistance to fracture must be developed in a decreasing rate with crack growth and load-bearing area reduced. This behavior is characterized by the R_c curve. The R_c curve describes the variation in material resistance to fracture, J_R , with crack length, a . It provides a record of the toughness development as a crack is driving stably under the increasing crack driving parameter.

Since the introduction of J-integral [71] parameter to describe singularity strain field around crack tip, it has become common practice to use J_R curve to characterize material resistance to fracture and crack growth behavior under monotonically increasing deformation. The multi-specimen method was first developed to determine J-integral and J_{IC} . By direct measurement on the fracture surface of a series of separate specimens, the amount of crack growth can be constructed based on these $J - \Delta a$ data. Rice et al [71] research makes it possible to use a single load-displacement curve to determine the R_c curve. An unloading compliance method was developed to measure the crack length change in a single load-displacement curve. A tentative test procedure for determining material resistance curve was proposed [74]. Based on Paris et al's work [75], stability of J-controlled crack growth was discussed by Hutchinson and Paris [68] from theoretical and analytical aspects. Formulations were presented to estimate the stability for a given specimen material and configuration. This work was extended to other specimen configurations by Ernst et al. [76] based on an alternative J-integral definition [72] and dimensional analysis of relation between load, crack length, and plastic displacement. The general formulation to calculate J, dJ, and da were derived and material tearing stability was estimated. Although the formulation was exact, these methods required a significant amount of numerical work to evaluate the load-displacement curve. A simple method to determine R_c curve was developed by Ernst et al. [77] by considering the variable separability. It was proven in [77] that load is separable in multiplication of functions of variable a/w (crack length over specimen width) and v_{pl} (plastic displacement) that is

$$F(v_{pl} / W, a / W) = g\left(\frac{a}{W}\right)H\left(\frac{v_{pl}}{W}\right) \quad (2.43)$$

and thus the load P can be expressed as

$$P = \frac{b^2}{W} F = \frac{b^2}{W} g\left(\frac{a}{W}\right)H\left(\frac{v_{pl}}{W}\right) \quad (2.44)$$

By using the third definition, J-integral can be further expressed as

$$J = \frac{\eta}{b} \int_0^v P dv \quad (2.45)$$

where

$b = W - a$. W is specimen width and a is crack length

$$\eta = \left(2 - \frac{b}{W} \frac{g'}{g}\right)$$

By introducing load P into Eq. (2.43) and considering crack growth and the load displacement curve, Ernst et al. [77] derived the following formulation to calculate J-integral

$$J_{i+1} = \left[J_i + \left(\frac{\eta}{b}\right)_i A_{i,i+1} \right] \left[1 - \left(\frac{\gamma}{b}\right)_i (a_{i+1} - a_i) \right] \quad (2.46)$$

$$\gamma = \left(\eta - 1 - \frac{b}{W} \frac{\eta'}{\eta} \right)$$

$$\eta' = d\eta / d(a / W)$$

where the subscript i (or $i + 1$) indicates functions evaluated at that step. The term $A_{i,i+1}$ refers to the area enclosed by the actual test record curve and lines of constant displacement v_i and v_{i+1} .

Standard tests for developing R _curves rely on automatic methods for measuring crack tip advance among which the elastic unloading compliance method is most frequently used. The automatic crack measuring methods require sophisticated equipment and techniques; sometimes a great deal of effort is required to achieve good results.

Lands and Herrera[78] recently proposed a method for directly determining an R _curve from a load versus displacement record. This method does not require automatic crack length measuring equipment, but is based on the principle of normalization of deformation properties of a material for which load, displacement, and crack length can be functionally related. If an appropriate functional form is assumed, the crack length can be determined directly from the corresponding load and displacement values.

If load separation parameter, S_{ij} , is a constant over the whole domain of plastic displacement, v_{pl} , then the load can be expressed in separable form of crack length, a , and plastic displacement, v_{pl} , i. e.

$$P = G(a / W)H(v_{pl} / W) \quad (2.47)$$

where W is defined as before. The normalized load, P_N , that is the load P normalized by crack length function, is a function of plastic displacement only

$$P_N = \frac{P}{G(a / W)} = H(v_{pl} / W) \quad (2.48)$$

The function $G(a/W)$ is only dependent on normalized crack length, a/W , and can be determined from the J calibration for each standard specimen geometry [79]. The total displacement v is the summation of elastic component v_{el} and plastic component v_{pl} , i. e.

$$v = v_{el} + v_{pl} \quad (2.49)$$

where

$$v_{el} = PC(a/W) \quad (2.50)$$

in which $C(a/W)$ is a compliance function. If $H(v_{pl}/W)$ is known, crack length can be determined from Eq. (2.48), (2.49), and (2.50), the values of J can be determined by using the formula in ASTM E 1152-87 and the entire R -curve can be determined.

Function of $H(v_{pl}/W)$ for a given material can be determined by assuming a proper function form with unknown constants that can be determined by calibration with experimental data. A simple power law function formed with two constants is assumed in [79]. These two constants are determined by the experimental data at initial crack length and at final crack length. The resulting R -curve agrees well with materials with limited plastic deformation. However, materials that exhibit extensive plastic deformation, do not follow a power law throughout the entire range of load vs. displacement history. In studying most test records, it was found that the deformation seemed to have a combined power law and straight line character [80] that could be best fit by an equation suggested by Orange [81]. It has the form

$$P_N = H(v_{pl}/W) = \frac{L + M(v_{pl}/W)}{N + (v_{pl}/W)} \left(\frac{v_{pl}}{W} \right) \quad (2.51)$$

where L , M , and N are the unknown constants and are to be determined by the experimental data. This function has a power law character when v_{pl} is of the order of N . For $v_{pl} \gg N$, it follows a straight line. Three calibration points have been chosen to determine the unknown constants. The first point corresponds to the point of final load displacement and crack length. The second point consists of several points chosen between the first deviation from linearity and maximum load to which the forced blunting was added. The third point is taken as a series of points at one third of the final plastic displacement used to optimize the fit of Eq. (2.51).

The normalized load-displacement curve can be obtained after L , M , and N are determined. Crack length then can be calculated from Eq. (2.48), (2.49), and (2.50) and the corresponding J value can be evaluated from formula in [73] ASTM E 1152-87 and the entire J - R curve can be established.

2-5 FATIGUE CRACK GROWTH LAWS

Fatigue is considered as a process of cumulative damage or progressive cracking under variable repeated or cyclic loads or in the presence of an aggressive environment. As a highly complex phenomenon which involves a localized progressive microstructure change and stress concentration within the material fatigue crack propagation can be characterized in three stages: crack initiation, stable crack growth, and unstable crack growth and fracture. Under cyclic elastic stress, cracks in the material will initiate from impurity, flaws and microstructure defects by cumulating dislocations of substructure and slip deformation. Further repeated load cycling will eventually cause the cracks to grow and coalesce into an open area, which is characterized by stable crack growth. Within this stage, the crack growth is relatively stable and is governed by the rate of subcritical crack propagation, which can be investigated by determining the crack growth at every cycle of load application. The detailed description of this stable stage crack growth will be given in the following section.

It has been observed that a structure component with initial crack length, $2a$, under repeated application of a stress level, σ , can experience a large number of stress cycles before fatigue failure occurs. Early investigation [82] assumed that fatigue crack growth may be directly related to the number of load repetitions and the applied stress level and can be expressed in following general form:

$$\frac{dc}{dN} = a_1 \sigma^n C^m \quad (2.52)$$

Shanley [83] proposed the following crack growth law,

$$\frac{dc}{dN} = a_1 \sigma_a^n C \quad (2.53)$$

where a_1 and n are determined empirically and σ_a is the cyclic stress level ($\sigma_{\max} - \sigma_{\min}$). It was observed that n can vary over a wide range of values.

By assuming a rigid plastic work-hardening region existing ahead of a crack tip in an infinite sheet with uniform stress acting on the boundary and perpendicular to the crack plane and the plastic zone at crack tip surrounded by elastic stress field, Head[84] developed the following fatigue model,

$$\frac{da}{dN} = \frac{C \Delta \sigma^3 a^{3/2}}{(\sigma_y - \Delta \sigma) R_p^{1/2}} \quad (2.54)$$

where a is defined as half crack length, $\Delta \sigma$ denotes the stress amplitude ($\sigma_{\max} - \sigma_{\min}$), C (constant) and σ_y (yield stress) are functions of mechanical characteristics for a given material and R_p characterizes the

size of the plastic zone around the crack tip. The value of R_p was assumed to be constant in the process of crack growth.

From dimensional analysis, Frost and Dugdale [85] suggested that the rate of crack growth should be directly proportional to the crack length and proposed the following fatigue crack growth law,

$$\frac{da}{dN} = aB(\sigma) \quad (2.55a)$$

They found that the coefficient function $B(\sigma)$ in Eq.(2.55a) determined from experimental data is proportional to the cube of the cyclic stress level. Crack growth law then can be rewritten as

$$\frac{da}{dN} = C(\sigma)^3 a \quad (2.55b)$$

Liu [86, 87] studied the same case by assuming that the material is ideal elastic-plastic with no work hardening. Using hysteresis energy absorption as a criterion for crack growth, he obtained the functional relationship for fatigue crack growth,

$$\frac{da}{dN} = C(\sigma)^2 a \quad (2.56)$$

Based on the analysis of static strength of cracked plates and using an elastic stress concentration factor K_n , McEvily and Illg [88] derived the following functional relationship to describe fatigue crack growth behavior,

$$\frac{da}{dN} = F(K_n, \sigma_{net}) \quad (2.57)$$

where $K_n = 1 + 2(a/\rho_1)^{1/2}$ for an infinite plate with an elliptical crack of length $2a$ and end radius ρ_1 . σ_{net} is defined as the net uniform stress along crack surface. By introducing the stress concentration factor K_n , which characterizes local stress intensity around crack tip, into Eq. (2.57), the crack growth law will not be limited to describe fatigue crack growth behavior for a particular configuration as was the case with the other proposed laws.

From the critical analysis of early extensive experimental observations and those proposed fatigue crack growth laws which were obtained from various materials, Paris and Erdogan [82] established a simple functional relationship relating crack growth rate da/dN with the instantaneous value of variation of stress intensity factor, ΔK ,

$$\frac{da}{dN} = A\Delta K^m \quad (2.58)$$

where A and m are fitting constants dependent on materials used in the test. This law is a direct application of linear elastic fracture mechanics to the analysis of fatigue crack growth. It is applicable to a wide range of materials, such as metal and steel, and various specimen configurations [82].

This relation, however, has been criticized by Forman [89] on the basis that it does not reflect the instability of crack growth when stress level is high and maximum stress intensity factor, K_{\max} , at crack tip reaches material toughness K_{IC} . Therefore, an empirical model was proposed to include the fatigue crack growth beyond stable stage, which has the following form,

$$\frac{da}{dN} = \frac{C\Delta K_I^n}{mK_{IC} - \Delta K_I} \quad (2.59)$$

where, n is material constant and $m = \frac{\Delta K_I}{K_{\max}}$.

Considering load ratio, R , has great influence on crack growth, Pearson [90] presented the following fatigue equation that included the load ratio effects, the critical stress intensity factor, and the instability of crack growth by

$$\frac{da}{dN} = \frac{A_1(\Delta K)^n}{(1-R)K_C - \Delta K} \quad (2.60a)$$

where, A_1 is a constant and $R = \frac{K_{\min}}{K_{\max}}$. When K_{\max} approaches K_C (critical stress intensity factor for plane stress condition), Eq. (2.60a) is modified as,

$$\frac{da}{dN} = \frac{A_2 K_C (\Delta K)^n}{(1-R)K_C - (\Delta K)^n} \quad (2.60b)$$

Hudson [91] conducted crack-propagation tests on two aluminum alloys (7075-T6 and 2024-T3) over a wide range of stress levels and stress ratio and compared the Eq. (2.58) and (2.59) to the data. Forman's equation produced an excellent fit to both the 7075-T6 and 2024-T3 data. However, Erdogan and Paris' equation also showed good correlation with the test data except at higher growth rates.

Based on fatigue crack closure experiments under constant amplitude loading on 2024-T3 aluminum alloy, Elber [92] proposed the following functional relationship for the crack growth rate,

$$\frac{da}{dN} = C\Delta K_{\text{eff}}^n \quad (2.61)$$

where ΔK_{eff} , the effective variation of stress intensity factor, is calculated from the difference between the maximum applied stress, S_{max} and the crack opening stress, S_o . Thus, crack growth should occur only during that portion of the loading cycle when the crack tip was open. The expression for the effective variation of stress intensity factor is given by,

$$\Delta K_{\text{eff}} = (S_{\text{max}} - S_o) \sqrt{\pi a} = U_o \Delta K \quad (2.62)$$

where U_o is a functional relationship which corrects the variation of elastic stress intensity factor.

Although the variation of stress intensity parameter, ΔK is widely used for correlation of fatigue crack growth rate, important limitations on the use of linear elastic fracture mechanics arise when materials are capable of large plastic deformation, such as large loads and high temperature, which induced extensive crack tip plasticity. More general criterion, which will take into account the influence of extensive plasticity on fatigue crack growth rates, has to be developed. With the advancement of elastic-plastic fracture mechanics, J-integral is considered to be a valid parameter to characterize crack growth behavior around crack tip in elastic-plastic materials. In spite of the controversy of the applicability of the J-integral in the situation that involves unloading, Dowling and Begley [93] first applied the J-integral concept to interpret their fatigue test results of elastic-plastic material under general yield conditions. The fatigue crack growth rate is expressed in the variation of J-integral instead of stress intensity factor, ΔK , i.e.

$$\frac{da}{dN} = A(\Delta J)^n \quad (2.63)$$

The applicability of the J-integral methodology to characterize fatigue crack growth behavior in the high plastic deformation range was also investigated by El. Haddad et al. [94] through fatigue tests on ASTM A516 grade 70 steel. The specimen is subjected to high levels of cyclic load. Under this loading condition, most test results exceeded the plasticity limit required to keep a specimen predominantly elastic as defined in the ASTM Standard Test for Constant Load Amplitude Fatigue Crack Growth Rates (E647-78T). Cyclic J values were determined such that plasticity and crack closure effects are accounted for. The fatigue crack growth rate is correlated by both cyclic stress intensity factor, ΔK , and cyclic J-integral value, ΔJ that may be converted by $K = \sqrt{E\Delta J}$. It was concluded that the experimental data are better represented by fatigue crack growth law expressed by ΔJ rather than that expressed by ΔK .

The conventional J-integral methodology to characterize fatigue crack growth problem is also challenged by the finding of significant acceleration of crack growth under a high level of cyclic stress with a positive mean stress. From experiments, Tanaka [95] observed that under load-controlled cycling with a tensile

mean stress, the hysteresis loop of load against displacement tended to shift horizontally and the extension deformation, or the ratchets deformation, was monotonically accumulated as a fatigue crack grows. During high stress level cycling, fatigue crack growth rates deviate from the steady state crack growth, which is defined by $\frac{da}{dN} = A\Delta K^m$. He proposed to use crack opening displacement to describe accelerated crack growth due to ratcheting.

The possibility of numerical simulation of fatigue crack growth was also investigated. The finding of the crack closure phenomenon by Elber [92] has great impact on the study of fatigue crack growth. An extensive effort was expended in an attempt to measure, characterize, and predict crack closure behavior and its effect on fatigue crack growth rates. The majority of this research has been experimental, as investigators have attempted to observe directly and quantify crack opening stresses under various loading and boundary conditions. However, the wide range of measurement techniques and measurement locations employed, have lead to a wide range of results and no clear consensus has yet emerged as to the standard experimental procedure. Another limitation of experimental approach is that critical behavior, such as displacement histories at min-section in a thick specimen, may be essentially inaccessible to any conventional measuring scheme.

An alternative approach to the study of fatigue crack closure is analytical. Analytical models of crack closure are based on a concept like the Dugdale model [69] or strip-yield model, but modification was made to leave plastically deformed material in the wake of the advancing crack. Newman [96], Budansky and Hutchinson [97], and Führung and Seeger [98, 99] studied only the crack closure behavior, while Dill and Saff [100] and Hardrath et al. [101] used the crack opening stresses from the models to predict crack growth under spectrum loading. However, these simple models generally require a number of crucial assumptions as well as simplistic versions of material models, the accuracy is not easily established.

The third approach, which involves the step-by-step elastic-plastic finite element analysis of a growing fatigue crack, is numerical. Although the cost of actually computing results is relatively high, the adaptation of a basic model to different materials, load histories, or geometry is relatively quick and cheap. Realistic constitutive models and complex crack configurations are easily accommodated. Therefore, numerical approach appears to be a promising investigation tool for the study of crack closure and its effects on fatigue crack growth rate.

The Finite element method was introduced into fatigue analysis by Miyamoto [102] to simulate crack closing, crack opening, and crack growth behavior under monotonic and cyclic loading. They investigated the changes in the stress and strain distributions and crack opening displacements upon releasing of the crack tip node, and they have observed crack closing phenomenon during unloading in a tension-to-tension cycles.

A finite element model was presented by Ohji, Ogura and Chkubo [103, 104] to study the fatigue crack closure phenomenon by taking into account crack extension and load interaction effects. This finite element model was developed so that crack extension was modeled by releasing the crack tip node at a stress level at which a reaction force of a crack tip node came up to zero for loading cycle. The amount of crack growth was determined by the length of crack tip elements. Opening and closing of the crack surfaces were detected at every loading increment and proper boundary conditions were selected for all the nodes along the crack. Crack surface opening and closing behavior were examined under both constant amplitude loading and variable amplitude loading. The effective range of the stress intensity factor, ΔK_{eff} is calculated by the equation $\Delta K_{eff} = F(a/b)\Delta\sigma_{eff}\sqrt{\pi a}$, in which a is a current crack length, $F(a/b)$ is a correction factor of the stress intensity factor for finite width that was estimated on the basis of the crack closure stress level, $\Delta\sigma_{eff}$ obtained from the analysis. It was concluded that the retardation and acceleration phenomena under variable amplitude loading are closely related with the crack closure behavior.

A comprehensive nonlinear finite element model was presented by Newman [96] and later was extended with crack growth criterion to study crack growth under monotonic and cyclic loading [105, 106]. Crack growth criterion was based on critical crack tip strain, ϵ_{yy} , whenever it equaled to or exceeded critical strain ϵ_{cr} , the crack tip node was broken and the crack advanced to the next node. The restraining force at the crack tip node was then released and redistributed. If the nodal average strain on the new crack tip was still greater than ϵ_{cr} , the crack continued to grow. If the strain was less than ϵ_{cr} , the applied load was increased until the new crack tip strain reached the critical value and the crack moved forward again. Crack growth under cyclic load was also studied.

An analytical fatigue crack closure model was developed and utilized in conjunction with a crack growth analysis program [107] to predict crack growth and fatigue life under constant amplitude and aircraft

spectrum loading. The model was based on the Dugdale model [69], but modified to leave plastically deformed material in the wake of the advancing crack tip was given by

$$\frac{da}{dN} = C_1 \Delta K_{\text{eff}}^{C_2} \frac{1 - (\Delta K_o / \Delta K_{\text{eff}})^2}{1 - (K_{\text{max}} / C_5)^2}$$

$$\Delta K_o = C_3 \left(1 - C_4 \frac{S_o}{S_{\text{max}}}\right)$$

where,

$$K_{\text{max}} = S_{\text{max}} F \sqrt{\pi a}$$

$$\Delta K_{\text{eff}} = (S_{\text{max}} - S_o) F \sqrt{\pi a}$$

and S_o denotes crack opening stress, S_{max} the maximum stress, F finite-width correction function and S_{min} the minimum stress. The constants C_1 to C_5 were determined to best-fit experimental data for constant-amplitude loading.

With regard to the difference of the crack-opening loads between plane strain and plane stress, a three-dimensional elastic-plastic finite element model was developed [108] using eight-node isoparametric, hexahedron elements. Crack-opening stress levels on the exterior and interior planes of the specimen were found to agree reasonably well with plane stress and plane strain analysis reported on the literature.

A more efficient finite element model was proposed by Nakagaki and Atluri [109]. This model incorporated special crack tip elements that takes into account stress and strain singularity near crack tip. The special hybrid elements were arranged around the crack tip with circular sector shape, which allowed crack growth in any arbitrary direction and an arbitrary amount. Crack growth criterion was proposed as,

$$\sigma_{\text{ex}} = p(S_{\text{max}} - S_o) + S_o$$

where p is a constant obtained by calibration such that the calculated S_o correlated with that observed in experimental study. The effective stress intensity factor ΔK_{eff} was defined as a function of the current crack length, a

$$\Delta K_{\text{eff}} = C_1 \sqrt{\pi(a_o + N\Delta a)} (S_{\text{max}} - S_o)$$

where C_1 is the finite element size correction factor and N is the number of load cycles. Fatigue crack growth rate was calculated by

$$\frac{da}{dN} = C(\Delta K_{\text{eff}})^n$$

where ΔK_{eff} is calculated from the finite element analysis.

Finite element model was also used to study small crack growth by Newman [110]. The 'plasticity-induced' crack closure model [107] in conjunction with crack opening stress equation [111] were used to predict fatigue life. The effective stress-intensity factor variation was calculated by

$$\Delta K_{\text{eff}} = (S_{\text{max}} - S_o) F_j \sqrt{\pi a}$$

where F_j defined as boundary correction factor. Crack opening stress equation is given by [111],

$$S_o / S_{\text{max}} = A_o + A_1 R + A_2 R^2 + A_3 R^3 \quad \text{for } R \geq 0$$

and

$$S_o / S_{\text{max}} = A_o + A_1 R \quad \text{for } -1 \leq R \leq 0$$

where $R = S_{\text{min}} / S_{\text{max}}$. When $S_o \geq S_{\text{min}}$, the coefficients were

$$\begin{aligned} A_o &= (0.825 - 0.34\alpha + 0.05\alpha^2) [\cos(\pi S_{\text{max}} / 2\sigma_o)]^{1/2} \\ A_1 &= (0.415 - 0.071\alpha) S_{\text{max}} / \sigma_o \\ A_2 &= 1 - A_o - A_1 - A_3 \\ A_3 &= 2A_o + A_1 - 1 \end{aligned}$$

The correlation between fatigue crack growth rate and effective stress intensity factor variation ΔK_{eff} can be obtained by finding an α value that will fit over wide range of crack growth rate data.

A more comprehensive review and critical study of finite element model to simulate fatigue crack closure and growth behavior was conducted by McClung and Sehilaglu [112,113]. This study was based on Lalor and Sehitoglu's previous investigation [114-116]. In regard to the accuracy and sensitivity of the finite element model, three issues were addressed in the study: mesh refinement and element type, initial defect size, stabilization behavior, and the crack tip node release scheme.

Criteria for sufficient mesh refinement was suggested based on the ratio of the element size to the forward crack tip plastic zone size,

$$R_p / a = (S_{\text{max}} / \sigma_o)^2$$

The crack advance scheme of releasing crack tip node immediately after maximum load on each cycle has recommended for general efficiency and consistent performance. Wide range influential factors, such as maximum stress, material properties, and constitutive models were examined using a two-dimensional elastic-plastic finite element model.

Considering that conventional elements are insufficient both in capturing a significant amount of forward plastic deformation of crack tip and mesh refinement to simulate actual crack growth, X. Zhang [117] incorporated 'quarter-node' singularity element in his finite element model to capture stress and strain singularity around the crack tip. Attempt to use energy release rate, G , as the crack extension criterion was made in the model, but failed by not recognizing that the mechanism for fatigue crack propagation may not be a sudden energy release but hysteric energy dissipation. The scheme of node releasing at the maximum load of a specified cycle that determined by

$$\Delta N = \frac{\Delta a}{C(\Delta K_{\text{eff}})^n}$$

was adopted in the study where Δa is the size of the crack tip element, ΔN is the number of cycles required for such an amount of crack extension. C and n are material constants obtained from the fatigue test.

CHAPTER III

REVIEW OF SHAKEDOWN THEORY

3.1 INTRODUCTION

The shakedown theory is considered a generalization of the theory of limit analysis. It was established and developed for elastic-plastic body subjected to variable repeated loads. It enriches the content of plasticity theory by taking into account failure mechanisms caused by plastic strain increments accumulating over subsequent load cycles as well as low-cycle fatigue phenomenon in the plastic analysis.

A classical limit analysis is used to determine the collapse loads and associated mechanisms of plastic collapse, this is called the static collapse. It is based on the idea that the external forces in the loading program monotonically increase proportionally each to other without recourse to a step-by-step investigation of their elastic-plastic behavior. However, when the body is subjected to several loads, each of which can vary independently between certain limits, the limit analysis may fail to give safe estimation of the collapse load although some critical combinations of loads within these prescribed bounds are considered. To the contrary, shakedown theory can provide the methodology to estimate the bounding values for complex repetitive loads.

Under random and repeated loads, the response of an elastic-plastic body is very complicated. Extensive investigation of plasticity of materials has indicated that three basic patterns can be distinguished.

- (1) Shakedown: for cyclic-independent materials, if plastic deformations stabilized within an early finite number of cycles and residual stress field, which corresponds to the plastic strains, may have developed such that the response to any further cycling is purely elastic as if the system accommodates itself to the loading program.
- (2) Alternating plasticity: if the plastic strain increments over subsequent load cycles change in sign alternatively, the summation of them is equal to zero under the loading program. As a result, the total plastic deformation is contained within the yield zone at a certain point in the system. With load cycling continuing, material in the yield zone begins cracking due to energy accumulation, which eventually leads to low cycle fatigue failure.
- (3) Incremental collapse: if the plastic strain increments are repeated in the same sign each time a critical load cycle that causes it is repeated, the total plastic strain will accumulate with each cycle that progressive deformation will develop and results in failure of the global system.

Comparing it to the step-by-step elastic-plastic analysis that is generally quite complicated, cumbersome and sometimes impractical, shakedown analysis shares the following advantages when application is concerned: (i) full description of history of loads is not necessary; (ii) essential and valuable information such as bounding value that is sufficient in engineering design is provided; (iii) direct and simple in computation method. Shakedown analysis is of great importance in the design of the elastic-plastic system of civil and mechanical engineering. Applications have been found in many areas such as nuclear reactor parts, pressure vessel and piping, offshore platform, geotechnical foundation and pavement systems.

The shakedown concept was introduced by Gruning [29] in 1926. The two fundamental theorems for the shakedown of an elastic-plastic continuum were established by Bleich-Melan [30,31,118] and Koiter [32] and are known as the static and the kinematic shakedown theorems, respectively. Since then, great progress has been made in plasticity theory. The classical shakedown theorems were also extended to include thermal loading, dynamic loading, geometrically nonlinear effects, and creep and viscous effects. A comprehensive review can be found in [37].

In this chapter, shakedown concept will be introduced by a simple example. Classical shakedown theorems will be presented with their limitations. Extensions of the classical shakedown theorems to other areas will be briefly reviewed.

3.2 NOTATION OF SHAKEDOWN

In engineering practice, the loads may act randomly, independently and repetitively, varying in magnitude, sense and direction within given limits. Therefore, the response of the elastic-plastic body is very complicated. The response of the body may be completely elastic if the load intensities remain under certain level. If load intensities are sufficiently high, progressive plastic flow may develop in the body, its instantaneous load-carrying capacity will become exhausted and the body will collapse. If the load intensities are at certain level lower than the collapse load, the plastic deformation of the body may increase with load cycling. After a sufficient number of cycling, the accumulated plastic deformation becomes excessively large and the body becomes unserviceable. If the net plastic strain increment, within one cycle, is zero and the total plastic deformation contained within the yield zone, the body may also fail by low-cycle fatigue. The body may also shakedown if the plastic deformation stabilized within early finite number of cycling and response to further load cycling is purely elastic. A very simple example to demonstrate how the elastic-plastic body responds to a repeated loading program follows.

A two-span continuous beam with a uniform cross-section is shown in Fig. 3.1. The material of the beam is characterized by plastic moment M_p and yield moment M_e . Two concentrated load W_1 and W_2 are loaded at the center of each span and vary independently within the given limits, M_o

$$0 \leq W_1 \leq W_o$$

$$0 \leq W_2 \leq W_o$$

The loading program is given as follows,

- I $W_1 = W_o, W_2 = 0;$
- II $W_1 = W_o, W_2 = W_o;$ (3.1)
- III $W_1 = W_o, W_2 = 0;$

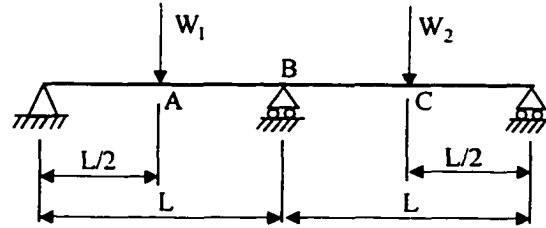


Figure 3.1 A Two-Span Beam Subjected to Cyclic Loading.

The continuous beam problem can be solved by any conventional structure analysis

method and the elastic solutions at each stage are presented in Table 3.1. From the table, it can be seen that the beam responds elastically if the following inequality is satisfied:

$$\frac{13}{64} W_o L \leq M_p$$

That is, the applied load varies within the following limits,

$$0 \leq W_o \leq 4.92 M_p / L.$$

By means of limit analysis, it is found that the beam will collapse at stage II, if the applied load W_2 is increased monotonically from zero to $W_2 = W_o = 6M_p / L$.

However, the beam behavior may be elastic even if the loads are greater than $4.92M_p / L$, provided residual moment within the beam satisfies the following conditions,

$$\begin{aligned} \frac{13}{64} W_o L + \frac{1}{2} m &\leq M_p, \\ -M_p &\leq -\frac{3}{64} W_o L + \frac{1}{2} m, \\ m &\leq M_p \\ -M_p &\leq -\frac{12}{64} W_o L + m \\ \frac{16}{64} W_o L &\leq 2M_e \\ \frac{12}{64} W_o L &\leq 2M_e \end{aligned} \quad (3.2)$$

where m is internal moment corresponding to applied load.

This is a constrained optimization problem and can be handled by any standard linear programming technique. Since only two variables are involved in this problem, it can be solved by simply rearranging these inequalities. The final results are,

$$m = \frac{1}{192} W_0 L, \quad M_p = \frac{19}{192} W_0 L$$

Then the maximum shakedown load can be determined as

$$W_0 = 5.0526 M_p / L$$

which corresponds to the value leading to the incremental collapse failure.

The last two inequalities in Eq. (3.2) define the limits for alternating plasticity. Thus, if $W_0 \leq 8M_p / L$ then the beam will be safe with regards to alternating plasticity.

Four bounding values corresponding to four different responses of the beam under the applied load are obtained from foregoing analysis. In the following, a step-by-step investigation is carried out for two intermediate load levels to demonstrate that the bounding values really set the boundaries by which the responses are different with one another under a given cyclic loading program.

The actual bending moment applied upon the beam is the sum of the elastic and the residual moments. The elastic moments at each beam section are provided in Table 3.1. The residual moments at each beam section are calculated from following formulations [84]:

$$M_2^R = -\frac{3EI}{4L}(\theta_1 + 2\theta_2 + \theta_3)$$

$$M_1^R = M_2^R = -\frac{3EI}{8L}(\theta_1 + 2\theta_2 + \theta_3)$$

where these θ_1, θ_2 and θ_3 are rotation angles at section A, B, and C, respectively and are to be determined at every loading stage in the step-by-step analysis.

Case 1. $W_0 = 5M_p / L$

At stage I, the load W_1 is applied gradually to the level W_0 while $W_2 = 0$. A plastic hinge at section A begins to develop when $W_0 = 4.92M_p / L$ and the moment M_A finally reaches the plastic moment M_p . The rotation angle at the plastic hinge and the moments at B and C are determined by the following equations:

$$\begin{aligned}
M_1^I &= M_1^E + M_1^R = \frac{13}{64} W_0 L - \frac{3 EI}{8 L} \theta_1 = M_p \\
M_2^I &= M_2^E + M_2^R = -\frac{6}{64} W_0 L - \frac{3 EI}{4 L} \theta_1 \\
M_3^I &= -\frac{3}{64} W_0 L - \frac{3 EI}{8 L} \theta_1
\end{aligned} \tag{3.3}$$

After rotation angle θ_1 is obtained from the first equation in Eq. (3.3), the moments M_2^{II} and M_3^{II} can be determined from the second and the third equations in Eq. (3.3) and are given as follows:

$$\begin{aligned}
\theta_1 &= \frac{M_0 L}{24 EI} = 0.041667 \frac{M_0 L}{EI} \\
M_1^I &= M_p \\
M_2^I &= -M_p / 2 \\
M_3^I &= -\frac{16}{64} M_p
\end{aligned}$$

At stage II, when the load W_2 is increased up to W_p while $W_1 = W_p$, section A is experienced unloading but the rotation angle θ_1^I corresponding to residual moment field $M^R(x)$ keeps no change and no additional plastic hinges develop during this process. The moments M_1^{II} , M_2^{II} and M_3^{II} are given by

$$\begin{aligned}
M_1^{II} &= M_3^{II} = \frac{10}{64} \cdot 5M_p - \frac{3EI}{8L} \frac{M_p L}{24EI} = \frac{49}{64} M_p \\
M_2^{II} &= -\frac{12}{64} \cdot 5M_p - \frac{3EI}{4} \frac{M_p L}{24EI} = -\frac{62}{64} M_p
\end{aligned}$$

At stage III, when the load W_2 is gradually removed, section A is reloaded again to its original value $M_1^{III} = M_p$. No further rotation at hinge A develops and no plastic hinges occur at other sections, the response is purely elastic. Therefore, the moments at this stage are same as stage I.

At the end of stage III, the beam is experienced one whole loading cycle with a constant residual moment field,

$$M_1^R = M_3^R = -\frac{1}{64} M_p, \quad M_2^R = -\frac{1}{32} M_p$$

which developed at first stage. The response of the beam for further loading cycle is purely elastic. The responses calculated for additional load cycles and stages are listed in Table 3.2.

Case 2. $W_o = 5.5M_p / L$

At stage I, the rotation angle θ_1^I and moments M_2^I , M_3^I are determined by Eq.(3.3)

$$\begin{aligned}\theta_1^I &= \frac{5M_p L}{16EI} \\ M_1^I &= M_p \\ M_2^I &= -\frac{3}{4}M_p \\ M_3^I &= -\frac{3}{8}M_p\end{aligned}$$

Stage II, when W_2 is loaded up to $5.5M_o / L$, a new plastic hinge develops at the section B. It rotates until $M_2 = -M_p$. Thus the rotation angle θ_2^{II} and the moments M_1^{II} , M_3^{II} are determined from the following equations:

$$\begin{aligned}M_2^{II} &= -\frac{12}{64}5.5M_o - \frac{3EI}{4L} \left(\frac{5}{16} \frac{M_o L}{EI} + 2\theta_2^{II} \right) = -M_o \\ M_1^{II} = M_3^{II} &= \frac{10}{64}5.5M_o - \frac{3EI}{8L} \left(\frac{5}{16} \frac{M_o L}{EI} + 2\theta_2^{II} \right)\end{aligned}\quad (3.4)$$

From the first equation in Eq. (3.4), θ_2^{II} can be determined, i.e.

$$\theta_2^{II} = -\frac{17}{96} \frac{M_o L}{EI} = -0.17708 \frac{M_o L}{EI}$$

Introducing θ_2^{II} into the second equation in (3.4), we obtain M_1^{II} and M_3^{II} as follows:

$$M_1^{II} = M_3^{II} = \frac{56}{64} M_o.$$

Stage III, when the load W_2 is gradually decreased from W_o to zero, section B undergoes unloading and M_1 reloads back up to M_p . After new plastic hinge θ_2^{III} develops, the rotation angle θ_1^{III} has to be determined by

$$\begin{aligned}M_1^{III} &= \frac{13}{64}5.5M_o - \frac{3EI}{8L} (\theta_1^{III} - 2 \frac{17}{96} \frac{M_o L}{EI}) = M_o \\ \theta_1^{III} &= \frac{2}{3} \frac{M_o L}{EI}\end{aligned}$$

Then the bending moments at section B and C are given by

$$M_2^{\text{III}} = -\frac{96}{128} M_o = -\frac{3}{4} M_o$$

$$M_3^{\text{III}} = -\frac{48}{128} M_o = -\frac{3}{8} M_o$$

These values are the same as in stage I, but the rotation angles have increased from θ_1^{I} and θ_2^{I} to θ_1^{III} and θ_2^{III} , respectively. In this loading case, the plastic deformations have been accumulated with load cycling. As the load cycling continues, the plastic deformations will increase cycle by cycle. Finally, this will result in the incremental collapse to occur. The calculated results for additional cycles and stages in this loading case are presented in Table 3.3.

The plastic deformation calculated at each stage during the step-by-step analysis for load case 1 and case 2 are shown in Fig. 3.2. From these plots we can see that plastic deformation develops during the first loading cycle for both case 1 and case 2. In loading case 2, plastic deformations continue to accumulate over subsequent loading cycles after they have been developed during the first cycle. When load cycling continues, excessive plastic deformations will occur until the beam fails by incremental collapse. However, in loading case 1, plastic deformations stabilized after the first loading cycle and the response to subsequent loading cycle is purely elastic, which means shakedown has occurred.

3.3 LOADING MODEL

Loads applied on an elastic-plastic body may vary randomly, independently and repetitively with time and change in magnitude, sense and direction. They can be described as functions of location and time, i.e. $T(x, t)$ and $F(x, t)$, which stand for tractions and body forces applied on the body, respectively. Exact description of the loads by functions is very complicated and difficult. However, they can be characterized by several loading patterns that vary within certain limits. Assuming an elastic-plastic body is subjected to several load-modes as shown in Fig. 3.3, where T^1 is described as wind pressure, T^2 snow pressure, T^3 mechanical load and F^1 body forces. The variations of these forces with time are assumed as in Fig. 3.4. Therefore these forces can be described as functions of location and time, i.e. $T^1(x, t)$, $T^2(x, t)$, $T^3(x, t)$ and $F^1(x, t)$. If we can use Fig. 3.3 to describe the load-modes change only with location and use Fig. 3.4 to define every load-mode magnitude change only with time, then these load functions are separable, i.e.

Table 3.1: Elastic Bending Moments at the Cross -Section in the Two-Span Beam

Loading Program	Cross Sections		
	A	B	C
$P_1 = P \quad P_2 = 0$	$13/64 \text{ PL}$	$-6/64 \text{ PL}$	$13/64 \text{ PL}$
$P_1 = P \quad P_2 = P$	$10/64 \text{ PL}$	$-12/64 \text{ PL}$	$10/64 \text{ PL}$

Table 3.2: Elastic-Plastic Bending Moments in the Two-Span Beam

Cycle Numbers	Loading Program	Moments			Rotation		Deflection
		M_A	M_B	M_C	θ_A	θ_B	D_A
1	I	M_0	$-1/2M_0$	$-16/64M_0$	$M_0L/24EI$	0	$M_0L^2/512EI$
	II	$49/64M_0$	$-62/64M_0$	$49/64M_0$	"	0	"
	I	M_0	$-1/2M_0$	$-16/64M_0$	"	0	"
2	I	M_0	$-1/2M_0$	$-16/64M_0$	"	0	"
	II	$49/64M_0$	$-62/64M_0$	$49/64M_0$	"	0	"
	I	M_0	$-1/2M_0$	$-16/64M_0$	"	0	"

Table 3.3: Elastic-Plastic Bending Moments in the Two-Span Beam (Incremental Collapse)

Cycle Numbers	Loading Program	Moments			Rotation	
		M_A	M_B	M_C	θ_A	θ_B
1	I	M_o	$-3/4M_o$	$-3/8M_o$	$5M_oL/16EI$	o
	II	$56/64M_o$	$-M_o$	$56/64M_o$	$5M_oL/16EI$	$-17M_oL/96EI$
	I	M_o	$-3/4M_o$	$-3/8M_o$	$2M_oL/3EI$	$-17M_oL/96EI$
2	I	M_o	$-3/4M_o$	$-3/8M_o$	$2M_oL/3EI$	$-17M_oL/96EI$
	II	$56/64M_o$	$-M_o$	$56/64M_o$	$2M_oL/3EI$	$-17M_oL/48EI$
	I	M_o	$-3/4M_o$	$-3/8M_o$	$49M_oL/48EI$	$-17M_oL/48EI$
3	I	M_o	$-3/4M_o$	$-3/8M_o$	$49M_oL/48EI$	$-17M_oL/48EI$
	II	$56/64M_o$	$-M_o$	$56/64M_o$	$49M_oL/48EI$	$-51M_oL/96EI$
	I	M_o	$-3/4M_o$	$-3/8M_o$	$11M_oL/8EI$	$-51M_oL/96EI$

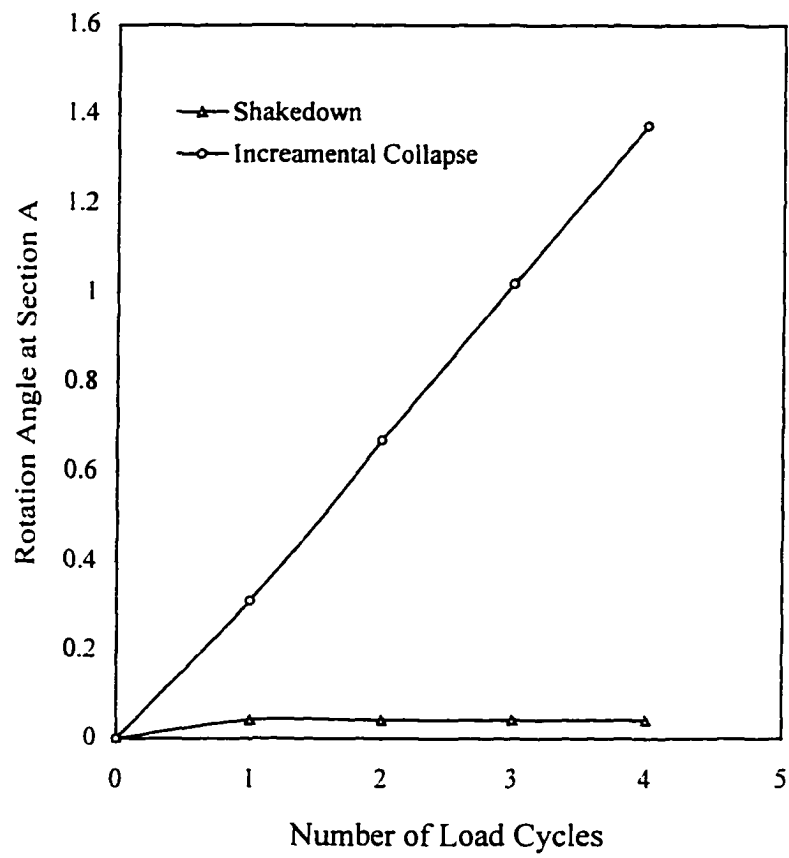


Figure 3.2 Plastic Deformation in Shakedown Analysis of Two-Span Beam.

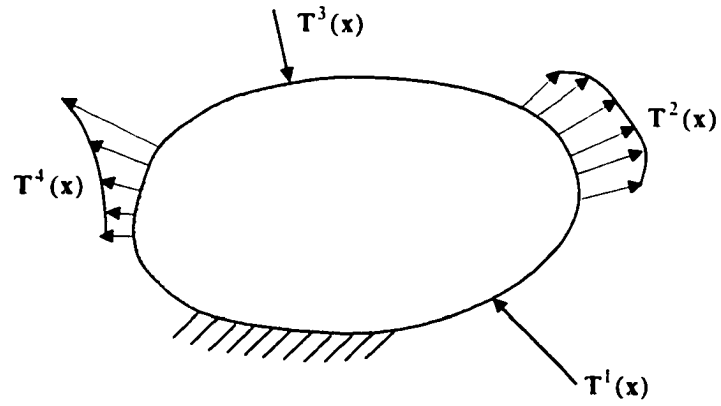


Figure 3.3 A Solid Body Subjected Arbitrary Repeated Loads.

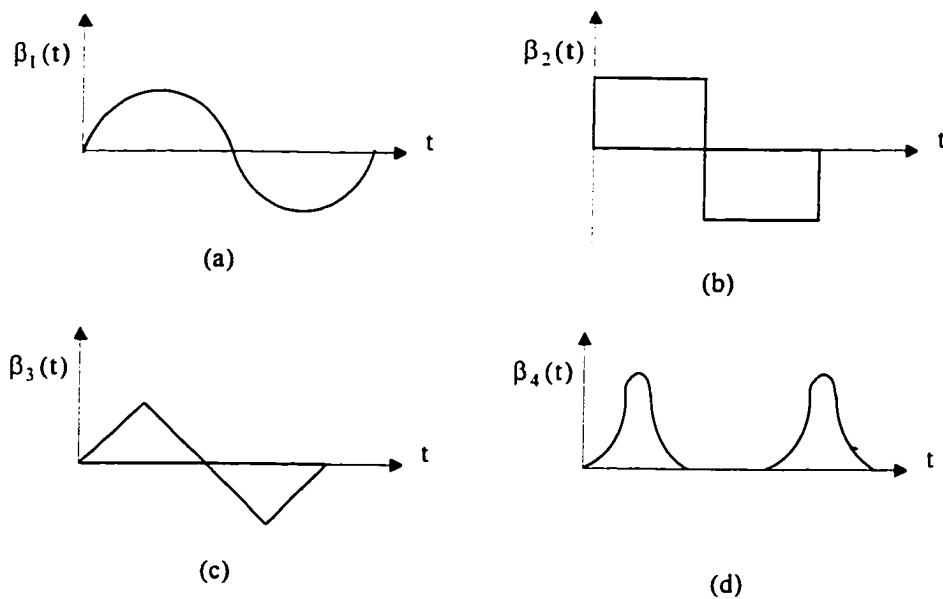


Figure 3.4 Illustration of Load Variation with Time.

they can be expressed in the following form:

$$\begin{aligned} T_i(x, t) &= \sum_s \beta_s(t) T_i^s(x) \\ F_i(x, t) &= \sum_s \beta_s(t) F_i^s(x) \end{aligned} \quad s=1, 2, \dots, r \quad (3.5)$$

where T_i^s , F_i^s are surface tractions and body forces in an s _th unit load-mode. β_s denote the load factors.

By defining a certain set, Ω , which contains the limits of load variations, the load factors, β_s , are allowed to vary within these limits. According to [119], any load factor domain, Ω , can be assumed convex and can be approximated by a finite set of linear inequalities.

$$\sum_{s=1}^r \beta_s A_{sk} \leq a_k \quad k=1, 2, \dots, m$$

Because the load domain is convex, it can be equivalently defined by its corners, $\beta_s^1, \beta_s^2, \dots, \beta_s^n$. Thus, any load factor in the domain, $\beta_s \in \Omega$, can be represented by the linear combination of the corners of the domain, Ω ,

$$\beta_s = \sum_{k=1}^n \alpha_k \beta_s^k$$

For $\alpha_k = 1$,

$$\beta_s = \sum_{k=1}^n \beta_s^k \quad (3.6)$$

Introducing En. (3.6) into En.(3.5), the loads can be expressed as

$$\begin{aligned} T_i(x, t) &= \sum_s \sum_{k=1}^n \beta_s^k T_i^s(x) = \sum_{k=1}^n \sum_s \beta_s^k T_i^s(x) \\ F_i(x, t) &= \sum_s \sum_{k=1}^n \beta_s^k F_i^s(x) = \sum_{k=1}^n \sum_s \beta_s^k F_i^s(x) \end{aligned} \quad s=1, 2, \dots, r \quad (3.7)$$

3.4 BASIC RELATIONS AND ASSUMPTIONS

The basic relations that govern the response of elastic-plastic body or structures under an applied load are based on a small deformation assumption. These relations are the same whether they are expressed in the coordinates referring to the deformed or the undeformed state. The equilibrium equations of the body under the body forces F_i and the surface tractions T_i are

$$\begin{aligned}\sigma_{ij,j} + F_i &= 0 & \text{in } V \\ \sigma_{ij}n_j &= T_i & \text{on } V_T\end{aligned}\quad (3.8)$$

where σ_{ij} is the symmetric stress tensor, V stands for the volume of the body; V_T is this part of its boundary on which the tractions are prescribed, n_j defines the outward normal to V_T . The remaining part of the surface is denoted by V_u . Geometric compatibility for the body is imposed by

$$\begin{aligned}\varepsilon_{ij} &= \frac{1}{2}(u_{i,j} + u_{j,i}) & \text{in } V \\ u_i &= u_i^0 & \text{on } V_u\end{aligned}\quad (3.9)$$

here, ε_{ij} denotes the symmetric strain tensor, u_i the displacements, u_i^0 their values on the boundary part V_u where displacements are imposed.

By means of virtual work principle, the equilibrium conditions(3.8) may be compressed into a single equation,

$$\int_V \sigma_{ij}\varepsilon_{ij}dV = \int_V F_i u_i dV + \int_{V_u} T_i u_i dS \quad (3.10)$$

which holds for any stress field σ_{ij} in equilibrium with the external loads F_i , T_i , and for admissible strain field with respect to displacement field u_i . The volume integrals are taken over the entire volume of the body and the surface integral is taken over its entire surface.

It is assumed that the actual strain ε_{ij} of an element of the body may be written as the summation of the elastic strains ε_{ij}^e , plastic strains (for contained plastic deformation) ε_{ij}^p , thermal strains ε_{ij}^0 and initial strains ε_{ij}^0 ,

$$\varepsilon_{ij} = \varepsilon_{ij}^e + \varepsilon_{ij}^p + \varepsilon_{ij}^0 + \varepsilon_{ij}^0 \quad (3.11)$$

The elastic stress-strain relationship is denoted by Hook's law,

$$\varepsilon_{ij}^e = E_{ijkl}^{-1} \sigma_{kl} \quad (3.12)$$

where E_{ijkl}^{-1} is the fourth-order tensor of elastic moduli. Considering that both σ_{ij} and ε_{ij} are symmetric tensors, E_{ijkl} is of the following symmetric properties,

$$E_{ijkl} = E_{jikl} = E_{ijlk} = E_{jilk} .$$

With the elastic energy always positive, the quadratic form,

$$E_{ijkl}\sigma_{ij}\sigma_{kl}$$

must be positive unless all stresses are zero. Thus the inverse of Eq. (3.11) is unique, that is,

$$\sigma_{ij} = E_{ijkl}\varepsilon_{kl} \quad (3.13)$$

The relation between the stresses and the plastic strains are based on Drucker's fundamental postulates, i.e.

- a) for all 'safe' states of stress $\sigma_{ij}^{(s)}$ and all 'allowable' stress $\sigma_{ij}^{(a)}$, stress σ_{ij} on the yield surface in which non-vanishing plastic strain rate $\dot{\varepsilon}_{ij}^p$ occur satisfies the following inequalities:

$$(\sigma_{ij} - \sigma_{ij}^{(s)}) > 0$$

$$(\sigma_{ij} - \sigma_{ij}^{(a)}) \geq 0$$

- b) b) if $\dot{\sigma}_{ij}$ are the stress rates corresponding to the plastic strain rate $\dot{\varepsilon}_{ij}$, then

$$\dot{\sigma}_{ij}\dot{\varepsilon}_{ij}^p \geq 0$$

- c) yield surface is convex.

For perfectly plastic materials that cannot support stresses in excess of a certain fixed yield limit, the plastic strain rates are given by the relation,

$$\dot{\varepsilon}_{ij}^p = \lambda \frac{\partial f}{\partial \sigma_{ij}} \quad (3.14)$$

where the yield function is assumed to be associated with plastic potential and is given by

$$f(\sigma_{ij}) = 0 .$$

For the regular yield surface. λ is a scalar defined by,

$$\lambda = 0 \quad \text{if } f < 0 \quad \text{and also if } f = 0 \quad \text{and } \dot{f} \equiv \frac{\partial f}{\partial \sigma_{ij}} \sigma_{ij} < 0$$

$$\lambda \geq 0 \quad \text{if } f = 0 \quad \text{and } \dot{f} = 0$$

For a workhardening material that an increase of the stresses beyond the yield limit is required for non-vanishing increment of the plastic strains, the plastic strain rates are given by the following formulations:

$$\dot{\epsilon}_{ij}^p = 0, \quad \text{if } f < 0 \quad \text{and also if } f = 0, \quad \dot{f} \equiv \frac{\partial f}{\partial \sigma_{ij}} \dot{\sigma}_{ij} \leq 0$$

$$\dot{\epsilon}_{ij}^p = h \frac{\partial f}{\partial \sigma_{ij}} \dot{f} \quad \text{if } f = 0 \quad \text{and } \dot{f} \geq 0$$

The thermal strain is determined by thermal expansion law, $\dot{\epsilon}_{ij}^{\theta} = \alpha_{ij} \dot{\theta}$ where θ indicate material temperature, α_{ij} represents the thermal expansion tensor of the material.

3.5 CLASSICAL SHAKEDOWN THEORY

3.5.1 Melan's Theorem (static shakedown theorem)

Based on those basic assumptions stated in the foregoing section and Bleich's early work on shakedown analysis in structures, Melan established a general theorem for structures and extended it to the elastic-perfect plastic continuum that is known as the static shakedown theorem. According to Koiter[32], Melan's theorem can be stated as follows:

If any time-independent distribution of residual stresses, $\bar{\rho}_{ij}$, can be found such that the sum of these residual stresses and the elastic stresses, σ_{ij}^E , is a safe state of stress

$$\sigma_{ij}^E + \bar{\rho}_{ij} = \sigma_{ij}^s$$

i.e., a state of stress inside the yield limit, at every point of the body and for all possible load combinations within the prescribed bounds, then the structure will shakedown to some time-independent distribution of residual stresses (usually depending on the actual loading program), and the response to subsequent load variations within the prescribed limits will be elastic. On the other hand, shakedown is impossible if no time-independent distribution of residual stresses can be found with the property that the sum of residual stresses and elastic stresses is an allowable state of stress at every point of the body and for all possible load combinations.

Alternatively, König [120] restated this theorem as below:

If there exists a time-independent residual stress field, $\bar{\rho}_{ij}$, and elastic stress field, $\sigma_{ij}^E(x, t)$, corresponded to the load path, β , such that

$$\begin{aligned} \bar{\rho}_{ij,j} &= 0 \quad \text{in } V, & \bar{\rho}_{ij} n_j &= 0 \quad \text{on } V_T \\ \dot{\bar{\rho}}_{ij} &= 0 \quad \text{for } t \geq 0 & \int_V E_{ijkl}^{-1} \bar{\rho}_{ij} \bar{\rho}_{kl} dV &< \infty \end{aligned} \quad (3.15)$$

$$\max_{\nu \in V} \max_{\beta, \in \Omega} f[\mu \sigma_{ij}^E(x, t) + \bar{\rho}_{ij}(x)] = 0$$

then the structure will shakedown over any load path, $\beta_s(t)$, contained within a given load domain, Ω , where μ is a real number and greater than 1.

In the application of Melan's shakedown theorem to calculate the shakedown load parameter of the engineering problem, the following question arises: does shakedown in a given loading path imply shakedown in any path contained within the same limits? With this regard, König [119] proposed the following theorems with respect to cyclic loading.

Theorem 1. If a given structure shakes down in a prescribed cyclic loading process then it shakes down also in any process for which the envelope, Σ , of elastic stress fields is contained (or coincides with) within the envelope, Σ' , relative to the given cyclic process.

Theorem 2. If a given structure shakes down in a cyclic load process which covers the whole boundary $\delta\Omega$ of a given load domain, Ω then it shakes down in any load path contained within the domain Ω .

Theorem 3. If a given structure shakes down in a cyclic loading process which contains all the corners β^i , $i=1, 2, \dots, r$ of a given load domain Ω , then it shakes down in an arbitrary loading path contained within the domain Ω .

3.5.2 Koiter's Theorem (Kinematic shakedown theorem)

The body will not shakedown, i.e. it will fail ultimately by cyclic plastic deformations, if any admissible plastic strain rate cycle $\dot{\epsilon}_{ij}^p(t)$ and any external load $F_i(t)$, $T_i(t)$ within the prescribed limits can be found for which

$$\int_0^T dt \left\{ \int_V F_i \dot{u}_i dV + \int_{S_p} T_i \dot{u}_i dS \right\} > \int_0^T dt \int_V D(\dot{\epsilon}_{ij}^p) dV \quad (3.16)$$

where $D(\dot{\epsilon}_{ij}^p)$ is the plastic energy dissipation function in the strain rate cycle $\dot{\epsilon}_{ij}^p(t)$. On the other hand, the structure will shakedown if a number $k > 1$ can be found with property that for all admissible plastic strain rate cycles $\dot{\epsilon}_{ij}^p(t)$ and all external loads $F_i(t)$, $T_i(t)$ within the prescribed limits,

$$k \int_0^T dt \left\{ \int_V F_i \dot{u}_i dV + \int_{S_p} T_i \dot{u}_i dS \right\} \leq \int_0^T dt \int_V D(\dot{\epsilon}_{ij}^p) dV \quad (3.17)$$

The upper bound of such numbers k is then obviously the factor of safety with respect to shakedown.

Alternatively, König [121] presented a general kinematic shakedown theorem, from which the perfect alternating plasticity as well as the perfect incremental collapse conditions are obtained as particular cases. It can be stated as follow:

Shakedown may be impossible if there exists a load program $\beta_s(t)$ resulting in elastic stress $\sigma_{ij}^E(x, t)$ and an independent cycle of plastic deformations $\dot{\epsilon}_{ij}^p(t)$ such that:

1°) Increments of the plastic strains over a certain time period (t_1, t_2) constitute a compatible field,

$$\Delta \bar{\epsilon}_{ij}(x) = \int_{t_1}^{t_2} \dot{\bar{\epsilon}}_{ij}(x, t) dt = \frac{1}{2}(\bar{u}_{i,j} + \bar{u}_{j,i}) \quad \bar{u}_i = 0 \quad \text{on} \quad S_u;$$

2°) The following inequality holds,

$$\int_{t_1}^{t_2} \int_V \sigma_{ij}^E(x, t) \dot{\bar{\epsilon}}_{ij}(x, t) dV dt > \int_{t_1}^{t_2} \int_V D\{\dot{\bar{\epsilon}}_{ij}(x, t)\} dV dt \quad (3.18a)$$

where $D\{\dot{\bar{\epsilon}}_{ij}\}$ denotes the dissipation associated with the plastic strain rate $\dot{\bar{\epsilon}}_{ij}$.

On the other hand, the structure will shakedown in any load path contained within the domain, Ω , for any plastic strain increments, $\Delta \bar{\epsilon}_{ij}^k(x)$, if the following inequality holds,

$$\int_{t_1}^{t_2} \int_V \sigma_{ij}^E(x, t) \dot{\bar{\epsilon}}_{ij}^k(x, t) dV dt < \int_{t_1}^{t_2} \int_V D\{\dot{\bar{\epsilon}}_{ij}^k(x, t)\} dV dt \quad (3.19a)$$

provided that,

$$\sum_{k=1}^n \Delta \bar{\epsilon}_{ij}^k(x) = \frac{1}{2}(\bar{u}_{i,j} + \bar{u}_{j,i}) \quad \bar{u}_i = 0 \quad \text{on} \quad S_u$$

By definition, shakedown will occur at any load path within the load domain, Ω . Let's consider load paths consisting of all the stress fields $\sigma_{ij}^{1E}, \sigma_{ij}^{2E}, \dots, \sigma_{ij}^{nE}$ at the corners of the domain. Denoting θ_k the respective set of instants during which elastic stress field is equal to σ_{ij}^{kE} . The Eq. (3.18a) can be rewritten in following form:

$$\int \sum_{k=1}^n \int_{\theta_k} \sigma_{ij}^{kE}(x) \dot{\bar{\epsilon}}_{ij}(x, t) dt dV > \int_{t_1}^{t_2} \int_V D\{\dot{\bar{\epsilon}}_{ij}(x, t)\} dV dt$$

Assuming strain rate, $\dot{\bar{\epsilon}}_{ij}(x, t)$, within each one of the sets θ_k can be expressed by

$$\dot{\bar{\epsilon}}_{ij}(x, t) = \Lambda(x, t) \dot{\bar{\epsilon}}_{ij}^k(x), \quad t \in \theta_k$$

and for any plastic strain history, $\varepsilon_{ij}^p(x, t)$, the following inequality holds

$$\int_{t_1}^{t_2} D(\dot{\varepsilon}_{ij}^p) dt \geq D(\varepsilon_{ij}^p(t_2) - \varepsilon_{ij}^p(t_1))$$

Then Eq. (3.18a) and (3.19a) can be rewritten as

$$\int_V \sum_{k=1}^n \sigma_{ij}^{kE}(x) \Delta \bar{\varepsilon}_{ij}^k(x) dV > \int_V \sum_{k=1}^n D\{\Delta \bar{\varepsilon}_{ij}^k(x)\} dV \quad (3.18b)$$

and

$$\int_V \sum_{k=1}^n \sigma_{ij}^{kE}(x) \Delta \bar{\varepsilon}_{ij}^k(x) dV < \int_V \sum_{k=1}^n D\{\Delta \bar{\varepsilon}_{ij}^k(x)\} dV \quad (3.19b)$$

respectively, provided that,

$$\sum_{k=1}^n \Delta \bar{\varepsilon}_{ij}^k(x) = \frac{1}{2}(\bar{u}_{i,j} + \bar{u}_{j,i}) \quad \bar{u}_i = 0 \quad \text{on } S_u.$$

Incremental Collapse Condition [121]

The incremental collapse is assumed to occur if following inequality holds,

$$\int_V \hat{\sigma}_{ij}(x) \Delta \bar{\varepsilon}_{ij}(x) dV > \int_V D(\Delta \bar{\varepsilon}_{ij}(x)) dV$$

where

$$\sum_{k=1}^n \Delta \bar{\varepsilon}_{ij}^k(x) = \frac{1}{2}(\bar{u}_{i,j} + \bar{u}_{j,i}) \quad \bar{u}_i = 0 \quad \text{on } S_u$$

On the other hand, the incremental collapse will not show up for any $\Delta \bar{\varepsilon}_{ij}(x)$ such that

$$\sum_{k=1}^n \Delta \bar{\varepsilon}_{ij}^k(x) = \frac{1}{2}(\bar{u}_{i,j} + \bar{u}_{j,i}) \quad \bar{u}_i = 0 \quad \text{on } S_u$$

the following inequality holds,

$$\int_V \hat{\sigma}_{ij}(x) \Delta \bar{\varepsilon}_{ij}(x) dV > \int_V D(\Delta \bar{\varepsilon}_{ij}(x)) dV$$

where $\hat{\sigma}_{ij}(x)$ denotes the appropriate $\sigma_{ij}^m(x)$ at the point x , which is defined by

$$\sigma_{ij}^m(x) \Delta \bar{\varepsilon}_{ij}(x) \geq \sigma_{ij}^{kE}(x) \Delta \bar{\varepsilon}_{ij}^k(x) \quad k = 1, 2, \dots, n$$

Alternating plasticity [121]

The safety condition in regard to alternating plasticity is in following form:

$$\mu \int_0^T dt \int_V \sigma_{ij}^E(x, t) \Delta \dot{\epsilon}_{ij}(x, t) dV \leq \int_0^T dt \int_V D(\Delta \dot{\epsilon}_{ij}) dV \quad .$$

provided

$$\mu > 1, \quad \int_0^T \dot{\epsilon}_{ij}(x, t) dt = 0 \quad \text{for every } x \in V$$

3.6 DEVELOPMENT IN SHAKEDOWN THEORY

Classical shakedown theory is strictly based on idealized assumptions such as elastic-perfectly plastic material which follows the associated plastic flow rule with a convex yield surface, temperature independent material property, small deformation, and quasi-static applied load. However, in practice these assumptions are not always satisfied. Therefore, the classical shakedown theorems are extended to consider the effects of relaxation of one or more of the assumptions. In this section, some developments of shakedown theory in several sub-areas are presented.

3.6.1 Thermal Loading Effect

In engineering practice, variable repeated thermal loading usually occurs accompanied with mechanical loading in structures and components, especially in civil, mechanical, and chemical engineering. Inhomogeneous temperature distribution induces thermal strain in the structure, which in many cases, is large or equal to those due to mechanical loading. Therefore, it has significant influence on plastic design of these structures. In most cases, material properties such as elastic moduli and yield stress σ_y are also dependent on temperature. Assuming elastic moduli is independent of temperature, then the classical shakedown theorems can be extended to include thermal effect [37].

Static Theorem

If there exists a factor $s > 1$ and a time independent residual stress field, ρ_{ij} , such that, for all loads and temperature variations within the prescribed limit the relation:

$$\phi[s\sigma_{ij}^E(x, \theta, t) + \rho_{ij}(x)] - K(x, \theta) \leq 0 \quad (3.20a)$$

holds, then the structure will shake down. In Eq. (3.20a), the elastic stress, σ_{ij}^E , is the summation of the stresses under mechanical loading and thermal loading, i.e. $\sigma_{ij}^E = \sigma_{ij}^e + \sigma_{ij}^T$ and holds for all temperatures.

Kinematic Theorem [37]

A structure will not shakedown (i.e. the total plastic work can tend to infinity at least for one of the possible load-temperature histories) if there exists a 'cycle' of plastic strain rates, $\dot{\epsilon}_{ij}^p(x, t)$, $t_1 \leq t \leq t_2$ and an independent 'cycle' of loads and temperature such that the following relations hold:

(a) there exists a field u satisfying the kinematic boundary condition and

$$\int_{t_1}^{t_2} \dot{\epsilon}_{ij}^p(x, t) dt = \frac{1}{2} (u_{i,j} + u_{j,i})$$

(b)
$$\int_{t_1}^{t_2} \left\{ \int_S T_i \dot{u}_i dS + \int_V \alpha_{ij} \dot{\rho}_{ij} \theta dV \right\} dt > \int_{t_1}^{t_2} \int_V D(\dot{\epsilon}_{ij}^p, \theta) dV dt$$

Here $D(\dot{\epsilon}_{ij}^p, \theta) = \sigma_{ij} \dot{\epsilon}_{ij}^p$ denotes the dissipation associated with the $\dot{\epsilon}_{ij}^p$, ρ_{ij} is the residual stress, and α_{ij} stands for the tensor of linear thermal expansion.

If the elastic modulus also changes with temperature, different residual stresses may be associated with the same plastic strain field. The static theorem has to be formulated in terms of steady plastic strains rather than in terms of residual stresses.

Static Theorem [122]

If there exists a safety factor $s > 1$ and a time-independent plastic strain field, $\bar{\epsilon}_{ij}^p$, such that, for all loads and temperature variations within a prescribed range, the following relation holds:

$$\phi[s\sigma_{ij}^E(x, \theta, t) + \rho_{ij}(x, \theta)] - K(x, \theta) \leq 0 \quad (3.20b)$$

then adaptation will occur; ρ_{ij} stands for the residual stress field associated with the constant plastic strain field, $\bar{\epsilon}_{ij}^p$, and changes with temperature due to variations of the elastic moduli, A_{ijkl} .

Kinematic Theorem [38]

Eq. (3.20b) can be rewritten in the following form:

$$\phi[s\sigma_{ij}^E(x, \theta, t) + \rho_{ij}(x, \theta)] - K(x, \theta) \leq 0 \quad (3.20c)$$

For a discretized system, an upper bound formulation can be established by means of piecewise linearization of yield function. Eq. (3.5.1b) is replaced by Y linear inequalities that can be written as follows:

$$\phi = S(\theta, t) - A(\theta)\bar{\lambda} - R(\theta) < 0 \quad (3.21)$$

where $\bar{\lambda} \geq 0$ is a Y-vector if internal variations defining the time-independent plastic strains. The projected elastic stresses, S, and the (symmetric, positive semi-definite) matrix, A, are expressed by

$$\begin{aligned} S(\theta, t) &= N^T \sigma^E(\theta, t) = N^T (B^T(\theta)\Gamma(\theta) + Z(\theta)\Gamma\theta(t)) \\ A(\theta) &= -N^T Z(\theta)N \end{aligned} \quad (3.22)$$

where $R(\theta)$ is the temperature-dependent generalized yield stress and N, Γ are constant matrices, such that $\Gamma\theta$ is the vector of generalized thermal strains and $N\bar{\lambda}$ that of time-independent plastic strains. B^T and Z are elastic operators, depending on temperature $\theta(t)$ through the elastic moduli; $B^T F$ and $Z\Gamma\theta$ give the elastic stress response to the external loads and temperature changes, respectively, and $ZN\bar{\lambda}$ provides the residual stress vector.

If shakedown occurs, Eq. (3.21) always holds for each component, hence for each component ϕ_L , evaluated at a given time t_L and instantaneous temperatures $\theta_L = \theta(t_L)$, the following inequality is complied with,

$$\phi_L = S_L(\theta_L, t_L) - \sum_k A_{Lk}(\theta_L)\bar{\lambda}_k - R_L(\theta_L) < 0 \quad L = 1, 2, \dots, Y \quad (3.23)$$

Let now vectors S^* , R^* and a matrix A^* be defined, having as L -th element or row the relevant quantities evaluated at time t_L , possibly different for each L.

$$S^* = \{S_L(\theta_L, t_L)\}; \quad R^* = \{R_L(\theta_L)\}; \quad A^* = [A_{Lk}(\theta_L)] \quad (3.24)$$

Then, if shakedown occurs, the problem,

$$S^* - A^*\bar{\lambda} - R^* < 0 \quad \bar{\lambda} \geq 0$$

admits a solution for any S^* , R^* and A^* , Eq. (3.24).

Let us consider the following related problem,

$$\mu \geq 0; \quad (A^*)^T \mu \leq \theta; \quad (S^* - R^*)^T \mu = 0 \quad (3.25)$$

an upper bound to the shakedown domain can be obtained by finding a solution to En. (3.25).

3.6.2 Dynamic Shakedown

In engineering practice, variable repeated loadings are often treated as quasi-static load, in which inertia and damping forces are ignored. This approach simplifies the calculation in design process and provides an appropriate approximation to the actual solutions when load changes slowly with respect to time. However, in most situations, variable repeated loadings may vary so rapidly that inertia and damping forces cannot be neglected. The classical shakedown theorems have to be extended to include the dynamic effect [39]. In contrast to quasi-static shakedown theory, the dynamic theory presumes that the time history of external actions is known, along with the initial conditions, and that the fictitious linear elastic stress response of the structure is calculated by any familiar of elastodynamics. In the spirit of Melan's theorem, the first dynamic adaptation theorem ensures adaptation if the yield condition is strictly fulfilled at any point and any time by the sum of a constant (in time) self-stress field and the linear elastic dynamic stress response calculated on the basis of some initial condition (not necessarily coincident with the actual ones). It can be stated as follow:

Sufficient Shakedown Condition

If a fictitious response, u_i^* , ε_{ij}^* , σ_{ij}^* and a residual stress distribution, σ_{ij}^{cd} , may be found so that,

$$\phi_r(\sigma_{ij}^* + \sigma_{ij}^{cd}) < 0 \quad r = 1, 2, \dots, n; \quad \bar{x} \in V; \quad t \in [0, t_\infty]$$

then shakedown will occur in the real response.

A necessary shakedown condition for periodic actions is given below.

If the actions are periodic and if the body in the real dynamic process shakes down, then at the least, a fictitious response must exist, which superimposed to a suitable residual stress distribution, satisfies the inequality conditions,

$$\phi_r(\sigma_{ij}^* + \sigma_{ij}^{cd}) < 0 \quad r = 1, 2, \dots, n; \quad t \in [0, t_\infty]$$

A more general formulation of the sufficient and necessary condition for shakedown follows.

Sufficient and necessary condition for shakedown is that a fictitious response and a residual stress distribution exist, which satisfy the inequality,

$$\phi_r[\sigma_{ij}^*(x, t) + \sigma_{ij}^{cd}(x)] < 0; \quad r = 1, 2, \dots, n; \quad x \in V; \quad t \in [t^*, t_\infty]$$

The second dynamic shakedown theorem basically follows Koiter's definition and is stated below (sufficient condition).

If, for all fictitious processes, an admissible plastic strain rate cycle can be found, starting from $t > t^*$ satisfying the inequality,

$$\int_{t_1}^{t_2} dt \int_V (\sigma_{ij}^* + \sigma_{ij}^{sd}) \dot{\hat{\epsilon}}_{ij}^p dV - \int_{t_1}^{t_2} dt \int_V \dot{D}(\hat{\epsilon}_{ij}^p) dV > 0$$

then the body will not shakedown.

The necessary condition for inadapation follows:

If the body will not shakedown, then for all fictitious processes and for all $t^* > 0$, some admissible plastic strain rate cycles must exist which satisfy the inequality,

$$\int_{t_1}^{t_2} dt \int_V \mu (\sigma_{ij}^* + \sigma_{ij}^{sd}) \dot{\hat{\epsilon}}_{ij}^p dV - \int_{t_1}^{t_2} dt \int_V \dot{D}(\hat{\epsilon}_{ij}^p) dV > 0; \quad \mu > 1.$$

3.6.3 Strain Hardening Effects

Melan's pioneering work in shakedown theory included both perfectly plastic and linear, unlimited kinematic hardening materials. Some particular cases in strain-hardening were also considered in [169]. Investigation has shown that the safety factor with respect to inadapation is extremely sensitive to the hardening rule adapted in the material description and exhibit obvious degeneration in some situations. Furthermore, explicit formulation of constitutive relations for complex material hardening behavior often fails to decide adequately all phases of the behavior. A three-dimensional overlay model was proposed [42,123] to simulate the elastic-plastic strain hardening behavior without using explicit constitutive relationship.

Three-dimensional Overlay Model [42,123]

A given body, V , is assumed to be composed of material points denoted by a vector $\bar{x} \in V \subset E^3$ and each material point, \bar{x} , in the body, V , is assumed to be composed of a dense spectrum of microelements numbered with scalar variable $\xi \in [0,1]$. Stresses (macrostresses) corresponding to each material point assumed to be the resultant of the microstresses of the microelements and the deformation is assumed the same for both the macroscopic material point and the microelements. These can be expressed in the following formula,

$$\begin{aligned} \sigma_{ij}(\bar{x}) &= \int_0^1 \psi_{ij}(x, \xi) d\xi \\ \eta_{ij}(\bar{x}, \xi) &= \epsilon_{ij}(\bar{x}) \quad \forall \xi \in [0,1] \end{aligned}$$

The macroscopic stress field, $\sigma_{ij}(\bar{x})$, must satisfy the static equilibrium conditions,

$$\sigma_{ij,j} + b_i = 0 \quad \text{in } V$$

and the static boundary conditions,

$$\sigma_{ij}n_j = p_i \quad \text{on } V_\sigma$$

where $\partial V = \partial V_\sigma + \partial V_u$ is the boundary of V , b_i denote body forces and p_i are surface traction on ∂V_σ .

The macroscopic strain field, ε_{ij} , is related with displacement at a material point by the kinematic relation,

$$\varepsilon_{ij} = \frac{1}{2}(u_{i,j} + u_{j,i}) \quad \text{in } V$$

with

$$u_i = u_i^0 \quad \text{on } \partial V_u$$

The microelements are assumed to be linear elastic, perfectly plastic with a convex yield function defined by $\Phi(\cdot)$ and complied with associated flow rule. The yield stresses of the microelements are denoted by $\kappa(\xi)$. For microelements, the following relations exist,

$$\begin{aligned} \eta_{ij} &= \eta_{ij}^E(\xi) + \eta_{ij}^P(\xi) \\ \eta_{ij}^E &= E_{ijkl}^{-1} \psi_{kl}(\xi) \\ \Phi(\psi_{ij}) &= k^2(\xi) \\ \dot{\eta}_{ij}^P &= \dot{\lambda}(\xi) \frac{\partial \Phi(\xi_{ij})}{\partial \psi_{ij}} \quad \dot{\lambda}(\xi) \geq 0 \\ \dot{\lambda}(\xi) \{ \Phi[\psi_{ij}(\xi)] - k^2(\xi) \} &= 0 \end{aligned}$$

where the elasticity tensor, E_{ijkl} , is positive definite and symmetric.

The function $k(\bar{x}, \xi)$ is uniquely determined for a given macroscopic σ - ε function and vice versa. In the elastic-plastic range, σ , ε , and $k(\xi)$ are related by

$$\sigma(\xi) = \int_0^\xi k(\bar{\xi}) d\bar{\xi} + (1 - \xi)k(\xi)$$

and

$$\varepsilon(\xi) = \frac{1}{E} k(\xi)$$

For given elastic and plastic microscopic strains, η_{ij}^E and η_{ij}^P , the following relations can be derived,

$$\begin{aligned}\psi_{ij}(\xi) &= E_{ijkl}[\epsilon_{kl} - \eta_{kl}^P(\xi)] \\ \sigma_{ij} &= E_{ijkl}[\epsilon_{kl} - \int_0^1 \eta_{kl}^P(\xi) d\xi] \\ \epsilon_{ij} &= E_{ijkl}^{-1} \sigma_{kl} + \int_0^1 \eta_{ij}^P(\xi) d\xi\end{aligned}$$

The plastic macrostrains, ϵ_{ij}^P , are equal to

$$\epsilon_{ij}^P = \int_0^1 \eta_{ij}^P(\xi) d\xi.$$

The difference between the microstresses, ψ_{ij} , and macrostresses, σ_{ij} , is called residual microstresses and is denoted by $\pi_{ij}(\xi)$,

$$\pi_{ij}(\xi) = E_{ijkl}[\epsilon_{kl}^P - \eta_{kl}^P(\xi)] \quad (3.26)$$

The residual microstresses satisfy the homogeneous static equilibrium conditions

$$\rho_{ij,j} = 0 \quad \text{in } V$$

and

$$\rho_{ij} n_j = 0 \quad \text{on } V_\sigma$$

By integrating the Eq. (3.26), one obtains,

$$\int_0^1 \pi_{ij}(\bar{x}, \xi) d\xi = 0 \quad \forall \bar{x} \in V$$

which shows that the resultant of $\pi_{ij}(\xi)$ does not contribute to the macrostresses.

Shakedown Theorem

For the overlay model, the following static shakedown theorem was formulated [42,123],

If there exists a time-independent residual macrostress field, $\bar{\rho}_{ij}(\bar{x})$, and a time-independent field, $\bar{\alpha}_{ij}(\bar{x})$, satisfying,

$$\Phi[m\bar{\alpha}_{ij}(\bar{x})] \leq [k(\bar{x}) - k_0(\bar{x})]^2 \quad \forall \bar{x} \in V$$

such that for all possible loads within the load domain, the condition:

$$\Phi\{m[\sigma_{ij}^E(\bar{x}, t) + \bar{\rho}_{ij}(\bar{x}) - \bar{\alpha}_{ij}(\bar{x})]\} \leq k_0^2(\bar{x})$$

is fulfilled $\forall \bar{x} \in V$ and $\forall t > 0$, where $m > 1$ is a safety factor against inadaption, then the total plastic energy dissipation within an arbitrary load path contained within the same load domain is bounded.

The backstresses, $\bar{\alpha}_{ij}(\bar{x})$, were introduced to describe the translation of the initial yield surface in the stress space. This theorem indicates that the necessary shakedown conditions for a kinematic hardening material are sufficient ones for the proposed overlay model.

This formulation is in a general form. For special case, which $\bar{\alpha}_{ij}(\bar{x}) = 0$, it reduces to Melan's theorem for an elastic-perfectly plastic material [31]. For $k(x) \rightarrow \infty$, we obtain the static shakedown formulation derived by Melan for linear, unlimited kinematic hardening material.

CHAPTER IV

A NUMERICAL APPROACH TO FATIGUE

4.1 INTRODUCTION

Fatigue has long been recognized as a common failure mechanism and distress mode that occurs in engineering structures and components under variable repeated loads. Extensive investigations of fatigue crack growth behavior for metals, various high yield strength steels and alloys, and other materials have indicated that three distinct stages exist in fatigue crack growth process, which are crack initiation, stable crack propagation, and unstable crack propagation and fracture. For small-scale yield zone around the crack tip, where linear elastic fracture mechanics is applicable, Paris' law [82] that relates crack growth rate, da/dN , with variation of stress intensity factor, ΔK , gives a considerably accurate description of fatigue crack growth behavior within a stable stage of crack growth. Various modifications to Paris' law have been proposed to include the influence of different factors on fatigue crack growth behavior and many fatigue equations (crack growth law) for different materials are reported [124]. Fracture parameters such as maximum stress intensity factor, K_{max} , and toughness, K_C , are incorporated into the fatigue equation to describe fatigue crack growth from stable stage to unstable stage and fracture. When material is capable of large-scale plastic deformation around crack tip, elastic-plastic fracture mechanics is utilized to study crack growth behavior. Cyclic J-integral (ΔJ) instead of the variation of stress intensity factor is used in fatigue equation to describe fatigue behavior [93].

Theoretical, analytical, and experimental investigations have provided detailed description of crack growth mechanisms both in microscopic and macroscopic aspects. Both the fracture mechanisms of plastic blunting and dimple formation have been recognized. Under variable repeated loads, fatigue crack growth is characterized by plastic blunting at moderate stress intensities and by dimple formation at high stress intensities that is considered to be controlled by maximum stress intensity factor. Analytical formulations for fatigue crack growth derived both for plastic blunting and dimple formation mechanisms are presented in [125,126]. Fracture parameters such as K_C and K_{max} are incorporated into these formulations by considering the boundary conditions of crack growth. For the transition region from plastic blunting to dimple formation, Schwable[127] used the linear combination of the formulations for plastic blunting and dimple formation to describe crack growth behavior. For elastic-plastic materials, Musuva et al. [128] directly superpose the crack growth rate by plastic blunting and crack growth by dimple formation that is characterized by the R_curve to describe the fatigue crack growth behavior from stable stage to unstable stage using J-integral.

Recent experimental results have shown that under load-controlled cyclic loading with a tensile mean stress, the hysteresis loop against displacement tended to shift horizontally and the extensional deformation, or the ratcheting deformation, was monotonically accumulated as a fatigue crack grew and that the initial stage of acceleration is not caused by the change of crack growth mode, and that the static mode fracture mechanism is operating in the rapid acceleration stage [95]. Based on these observations, Tanaka et al [95] presented an upper bound crack growth rate equation by using the power law function of crack tip opening displacement (CTOD) to describe fatigue crack growth behavior under high cyclic stresses.

The discovery of crack closure phenomenon by Elber [92] made it possible to simulate fatigue crack growth by calculating crack opening (or closing) stress using finite element method. Early numerical investigations mainly focus on studying of crack tip opening displacement, computing crack opening(or closing) stresses, and analyzing over loading and under loading influence on crack growth behavior under monotonic and/or cyclic loading. Three major crack growth criteria are employed in these numerical investigations. These are releasing crack tip node at maximum load with stabilization [104,105,106], releasing crack tip node at minimum load [129,103], and releasing crack tip node immediately after maximum load [116,117]. The amount of crack growth is determined by the element size arranged along crack growth line. However, both the strategy of crack growth element by element and the releasing crack tip node scheme make the simulation of crack growth in finite element model typically arbitrary.

A few efforts were also made in an attempt to establish a fatigue equation and predict fatigue life numerically [130,131,132]. In 1977, Newman Jr. [105] incorporated a critical strain criterion in his nonlinear finite element program to simulate fatigue crack growth and intended to establish functional a relationship between fatigue crack growth rate and the variation of stress intensity factor. His investigation results show that both finite element mesh size arranged along the crack growth line and preset critical strain value, ϵ_{cr} , have considerable influence on the applied stress level and hence on fatigue crack growth rate. Later, a critical crack opening stress criterion was proposed by Nakagaki et al. [109] to simulate crack growth, in which the critical stress level was defined as $\sigma_{ex} = p(\sigma_{max} - \sigma_{op})$, where p is determined by calibration such that the calculated σ_{op} correlated with experimental results. Such defined critical stress is found to be dependent on material properties and to some extent on the analysis procedure itself. X. Zhang et al [133,117] proposed a modification to the technique of releasing crack tip node at the maximum load of a cycle. In this technique, crack growth is simulated by releasing the crack tip node at the maximum load of a cycle and advancing the crack tip one element length in front. The number of cycles required for this amount of growth was determined by a modified Paris' law [133]. This strategy is rather realistic, but material constants, C and n , in

modified Paris' law have to be determined by the fatigue test in advance. These numerical approaches are either dependent on finite element mesh size arranged along the crack growth line or dependent on fatigue test to obtain fitting constants in fatigue crack growth law. Therefore, the crack growth criterion, the amount of crack growth during each cycle, and unstable crack growth and final fracture become the fundamental issues in simulating fatigue crack growth behavior and predicting fatigue life by using numerical methods.

By using parameters of fracture mechanics to characterize the two crack growth mechanisms in simulating fatigue crack growth and predicting fatigue life, a numerical approach is proposed in this study. The proposed crack growth criterion is a practical and fundamental approach, taking into account material resistance to fracture and singularity of stress-strain field around crack tip in simulation of fatigue crack growth without using empirical or experimental constants. Crack propagation is simulated by shifting the R -curve along the crack growth direction. Unstable fatigue crack growth and related critical crack length for a given cyclic loading level is determined by fitting numerically obtained crack increments and its corresponding cyclic J -integral values. Fatigue life then can be predicted by integrating the fatigue equation. This proposed numerical approach is based on the following assumptions:

- R -curve is assumed to represent material resistance to crack growth under monotonic loading.
- Fatigue crack growth is the combined contribution of component by dimple formation and component by plastic blunting in different percentages at different crack growth stages.
- Crack growth only occurs during the load rising portion of each cycle.
- Crack closing, residual stress, and dynamic acceleration effects are not included in this study. Opening crack mode (Mode I) is used throughout this study.

4.2 MATERIAL RESISTANCE CURVE R -curve

The existence of a relationship between the J -integral and the amount of stable crack growth under monotonic load, i.e. material resistance to crack growth curve (R -curve) has been recognized and utilized in studies by Rice [134], Paris et al. [75], Hutchison et al. [135], and Shih et al. [136]. J -integral concept that directly related to the locally concentrated strain field was first identified by Rice [71] for two dimensional linear

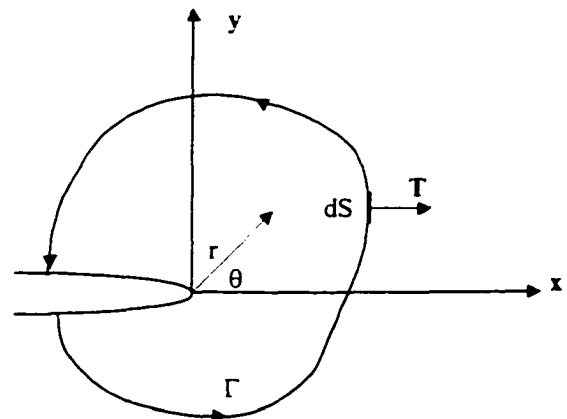


Figure 4.1 Crack Tip Coordinate System and typical Line Integral Contour.

elastic and elastic-plastic (deformation theory of plasticity or nonlinear elastic) materials and is given in the following form,

$$J = \int_{\Gamma} (\hat{W} dy - \mathbf{T} \frac{\partial \mathbf{u}}{\partial x} dS) \quad (4.1)$$

where, \hat{W} denotes the strain energy density that can be calculated by $\hat{W}(\epsilon_{ij}) = \int_0^{\epsilon_{ij}} \sigma_{ij} d\epsilon_{ij}$. \mathbf{T} defines the traction vector along arbitrary line integral path Γ , $\mathbf{T} = \sigma_{ij} n_j$, \mathbf{u} is a vector of displacement field at any point within Γ and dS is a line element along the integral path, Γ as shown in Fig. 4.1.

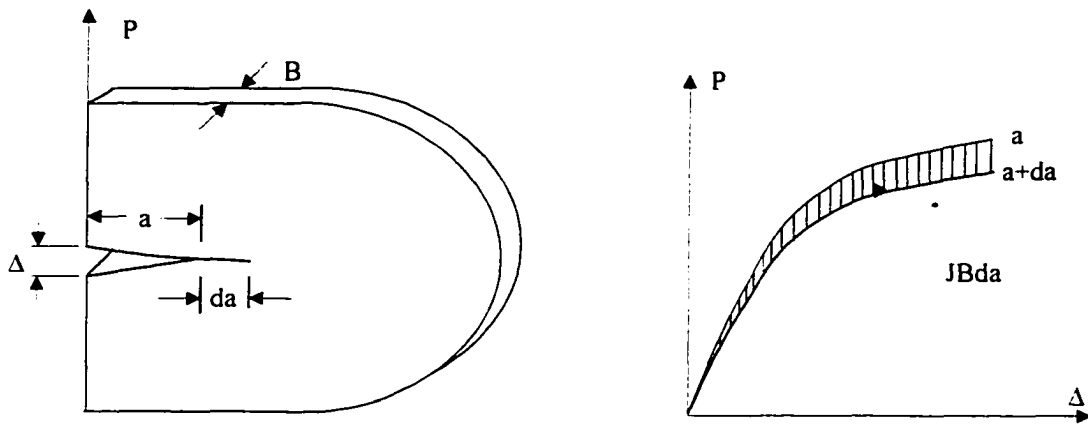


Figure 4.2 An Alternative Interpretation of J-integral.

An alternative expression of J-integral in terms of energy variation that is directly related to exteriorly measurable quantities, such as load and displacement, was also proposed by Rice [72] for two dimensional elastic (linear or nonlinear) materials,

$$J = - \frac{\partial (U/B)}{\partial a} \quad (4.2a)$$

where U/B is the potential energy per unit thickness, B , and is defined by

$$U/B = \iint_A \hat{W} dx dy - \int \mathbf{T} \cdot \mathbf{u} dS$$

where A is the area of the considered two dimensional problem as shown in Fig. 4.2 and Γ , \hat{W} , \mathbf{u} , \mathbf{T} are defined as before.

For elastic-plastic, considering the area under load-displacement curve, $P-\Delta$ (where P is load per unit thickness and Δ is the load point displacement) Eq. (4.2a) is further explicitly expressed in load, P , and load point displacement, Δ , by Ernst et al [77] as follows:

$$J = \int_b^P \frac{\partial \Delta}{\partial a} dP = - \int_b^{\Delta} \frac{\partial P}{\partial a} d\Delta \quad (4.2b)$$

For convenience, Ernst expressed the load point displacement, Δ , as the summation of linear elastic part, Δ_{el} , and plastic part, Δ_{pl} , and presented J-integral of Eq. (4.2b) in the following form,

$$J = G(P, a) - \int_b^{\Delta_{pl}} \left(\frac{\partial P}{\partial a} \right)_{\Delta_{pl}} d\Delta_{pl} \quad (4.2c)$$

where, $G(P, a)$ is the energy release rate defined in linear elastic fracture mechanics [65],

$$J_{el} = \int_b^P \left(\frac{\partial \Delta_{el}}{\partial a} \right) dP = G(P, a) \quad (4.2d)$$

and

$$\int_b^P \left(\frac{\partial \Delta_{pl}}{\partial a} \right)_P dP = - \int_b^{\Delta_{pl}} \left(\frac{\partial P}{\partial a} \right)_{\Delta_{pl}} d\Delta_{pl} \quad (4.2e)$$

Based on this alternative J-integral definition, material resistance to fracture curve, R_{curve} , can be developed from load-displacement curves by calculating J-integral value and corresponding crack increment, da , from the following equations derived by Ernst et al [76] for general specimen configuration of elastic-plastic material,

$$J = G + \bar{J}_{pl}|_{b=b_0} + \int_{a_0}^a \frac{1}{b} [-\bar{J}_{pl} + \frac{3b^2}{W^2} \int_b^{\Delta_{pl}} \frac{\partial F_I}{\partial (\frac{a}{W})} d\Delta_{pl} - \frac{b^3}{W^3} \int_b^{\Delta_{pl}} \frac{\partial F_I}{\partial (\frac{a}{W})^2} d\Delta_{pl}] da \quad (4.3a)$$

and

$$da = \frac{\frac{b^2}{W^2} \frac{\partial F_I}{\partial (\frac{\Delta_{pl}}{W})} d\Delta_{pl} - dP}{2 \frac{b}{W} F_I - \frac{b^2}{W^2} \frac{\partial F_I}{\partial (\frac{a}{W})}} \quad (4.3b)$$

$$\text{where } \bar{J}_{pl} = \frac{2b}{W} \int_0^{\Delta_{pl}} F_1 d\Delta_{pl} - \frac{b^2}{W^2} \int_0^{\Delta_{pl}} \frac{\partial F_1}{\partial \left(\frac{a}{W}\right)} d\Delta_{pl}$$

$$\frac{PW}{b^2} = F_1 \left(\frac{\Delta_{pl}}{W}, \frac{a}{W} \right)$$

P - load per unit thickness

a - crack length, a_0 initial crack length

W - specimen width as shown in Fig. 4.7

b - remaining ligament at the cracked section

b_0 - initial remaining ligament

Δ_{pl} - plastic displacement along applied load line.

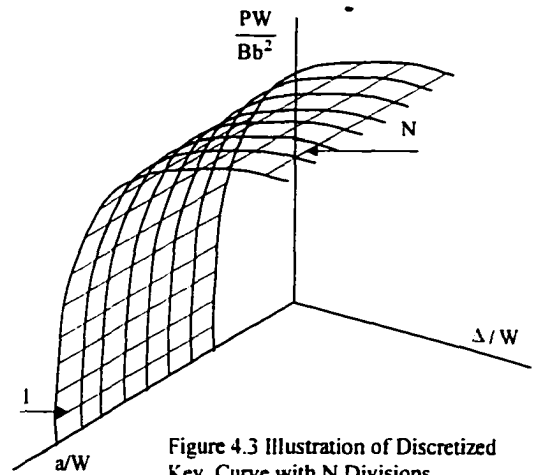


Figure 4.3 Illustration of Discretized Key Curve with N Divisions.

Function $F_1 \left(\frac{\Delta_{pl}}{W}, \frac{a}{W} \right)$ (also called key curve) in Eq. (4.3) can be constructed for a given specimen geometry [156]. R_{curve}, then can be directly obtained from load displacement curves by using F₁ function to calculate J and the amount of crack extension. A discretized formulation of Eq. (4.3) is given in [137] and is rewritten in the following for convenience,

$$\delta J_n = \left[\frac{2b}{W} F_{1n} - \frac{b^2}{W^2} \frac{\partial F_1^*}{\partial \left(\frac{a}{W}\right)_n} \right] \delta \Delta_n + \left[-\frac{2}{W} \sum_{i=1}^n F_{1i} \delta \Delta_i + \frac{4b}{W^2} \sum_{i=1}^n \frac{\partial F_1^*}{\partial \left(\frac{a}{W}\right)_i} \delta \Delta_i \right] \delta a_n \quad (4.4a)$$

and

$$\delta a_n = \frac{\frac{b^2}{W^2} \frac{\partial F_1^*}{\partial \left(\frac{\Delta}{W}\right)_n} \delta \Delta_n - \delta P_n}{\frac{2b}{W} F_{1n} - \frac{b^2}{W^2} \frac{\partial F_1^*}{\partial \left(\frac{a}{W}\right)_n}} \quad (4.4b)$$

where n is the current number of divisions of discretized load-displacement curve. The term of F_1 is directly evaluated from load displacement curve of a given specimen. F_1^* is evaluated from F_1 calibration curve defined by $F_1 \left(\frac{\Delta_{pl}}{W}, \frac{a}{W} \right) = \frac{PW}{b^2}$. N is the total number of the divisions of load displacement curve as shown in Fig. 4.3.

The total J and Δa are

$$J = \sum_{i=1}^N \delta J_i \quad (4.5a)$$

$$\Delta a = \sum_{i=1}^N \delta a_i \quad (4.5b)$$

The last point (N+1) of the N divisions is determined by finding the displacement point corresponding to the maximum load of the specimen with the shortest crack. At this point a crack begins to initiate or is occurring. A program is developed in the current study to implement these equations. R_curve then can be evaluated based on load-displacement curves.

4.3 CRACK DRIVING FORCE J_curve

$J_integral$, as defined by Rice [72], is an average measurement of intensity of the locally concentrated strain field around notch or crack under given loads. Several techniques to evaluate the J -integral theoretically [138,139], numerically [102], and experimentally [140] have been reported. Therefore, J_curve , the variation of $J_integral$ value with crack length under a given load level, can be developed. From Eq. (4.2), it is observed that the functional relationship between load and displacement includes the crack length as the third variable. For function F_1 at two different crack length, a_i and a_j , it has been proven that [141] if the separable parameter,

$$S_{ij} = \frac{F_1\left(\frac{a_i}{W}, \frac{\Delta_{pl}}{W}\right)}{F_1\left(\frac{a_j}{W}, \frac{\Delta_{pl}}{W}\right)}$$

is a constant over the whole domain of plastic displacement, Δ_{pl} , the load, P , can be expressed by two separable variables that are crack length, a , and Δ_{pl} . It is assumed by Ernst et al [77] that the load, P , can be expressed in the following form,

$$P = \frac{b^2}{W} F_1\left(\frac{a}{W}, \frac{\Delta_{pl}}{W}\right) = \frac{b^2}{W} \Psi\left(\frac{a}{W}\right) \Phi\left(\frac{\Delta_{pl}}{W}\right) \quad (4.6)$$

then, two different J -integral formulations are derived in the current study from Eq. (4.6) and given in the following. For a given plastic displacement, Δ_{pl} , the function $\Phi\left(\frac{\Delta_{pl}}{W}\right)$ can be evaluated and may be

expressed as

$$\Phi\left(\frac{\Delta_{pl}}{W}\right) = \alpha(\Delta_{pl})^\beta \quad (4.7)$$

Introducing Eq. (4.7) into Eq. (4.6), we have

$$P = \alpha \cdot (\Delta_{pl})^\beta \cdot \Psi\left(\frac{a}{W}\right) \quad (4.8)$$

where α and β are constants, $\Psi\left(\frac{a}{W}\right)$ is a function of crack length only. Introducing Eq. (4.8) into Eq. (4.2c), the J-integral can be evaluated by

$$\begin{aligned} J(a, \Delta_{pl}) &= G(P, a) - \int_0^{\Delta_{pl}} \left(\frac{\partial P}{\partial a}\right)_{\Delta_{pl}} d\Delta_{pl} \\ &= G(P, a) - \bar{\alpha} g\left(\frac{a}{W}\right) (\Delta_{pl})^{1+\beta} \end{aligned} \quad (4.9a)$$

where $\bar{\alpha} = \frac{\alpha}{(1+\beta)W}$ and $g\left(\frac{a}{W}\right) = \Phi'\left(\frac{a}{W}\right)$.

Following the same argument, for a given load level P , we may express the plastic displacement according to Eq. (4.6) as following

$$\Delta_{pl} = \lambda P^\eta H\left(\frac{a}{W}\right) \quad (4.10)$$

Introducing Eq. (4.10) into Eq. (4.2c), we obtain the J-integral formulation for a constant load P

$$\begin{aligned} J(a, P) &= G(P, a) + \int_0^P \left(\frac{\partial \Delta_{pl}}{\partial a}\right)_P dP \\ &= G(P, a) + \bar{\lambda} h\left(\frac{a}{W}\right) P^{1+\eta} \end{aligned} \quad (4.9b)$$

in which λ , η and $\bar{\lambda} = \frac{\lambda}{(1+\eta)W}$ are constants. $h\left(\frac{a}{W}\right) = H'\left(\frac{a}{W}\right)$ is a function of crack length. Once the

function $\Phi = \left(\frac{\Delta_{pl}}{W}\right)$ and $\Psi\left(\frac{a}{W}\right)$ in Eq. (4.6) have been obtained, Eq. (4.9) can be used to determine J -curves under a constant load or under a constant displacement.

4.4 CRACK GROWTH UNDER MONOTONIC LOAD

The amount of crack growth under monotonic load can be determined in the process of evaluating R_curve developed from load displacement curves as described in foregoing section. However, to simulate fatigue crack growth under cyclic load, a numerical approach is proposed in this study to determine the amount of crack growth by using J_curve and R_curve .

Under a constant load, the crack driving force in terms of J-integral that varies with crack length can be evaluated by Eq. (4.9). For a given elastic-plastic material and two dimensional geometric configuration, the functional relationship of J versus crack length, a, which is termed as J_curve may be, for simplicity, represented by

$$J(a, P) = \lambda P^{1+\eta} f(a) \quad (4.11a)$$

where $f(a)$ is a function of crack length only.

On the other hand, material resistance to crack growth curve, R_curve that is determined by Eq. (4.3) may be expressed as power function of crack extension,

$$J_R(a_0, a) = C(a - a_0)^m \quad (4.11b)$$

where C and m are fitting constants and dependent on material analyzed. The crack driving force, J can be used in conjunction with R_curve to determine the amount of crack growth. Considering a diagram in which a typical R_curve and a J_curve both plotted in the same coordinate system as shown in Fig. 4.4, differentiation of crack length can be obtained by differentiating R_curve with respect to crack length a,

$$da = [J'_R(a_0, a)]^{-1} dJ(a, P) \quad (4.12)$$

Assuming the load is continuously increased from 0 to P and crack extended from a_0 to a, then crack incremental can be evaluated by,

$$\Delta a = \int_{a_0}^a da = \int_{a_0(a_0)}^{a(a)} [J'_R(a_0, a)]^{-1} dJ(a, P) \quad (4.13)$$

By introducing $dJ(a, P) = \frac{\partial J}{\partial P} dP + \frac{\partial J}{\partial a} da$ and $J'(a_0, a) = Cm(a - a_0)^{m-1}$ into the above equation and considering R_curve and J_curve intercepted at crack length, a, then the amount of crack growth under

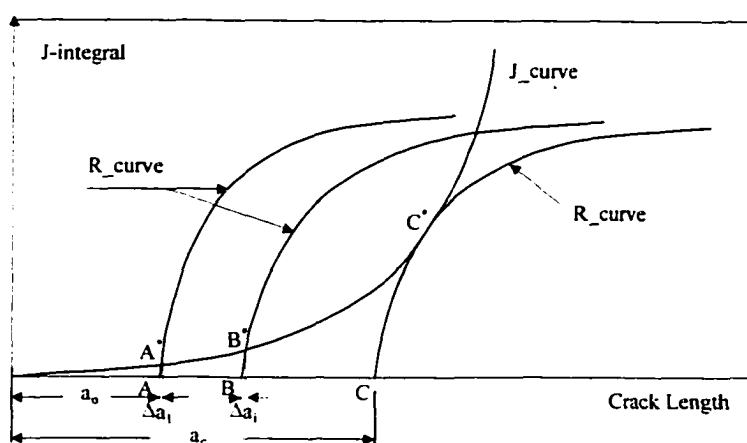


Figure 4.4 Illustration of Crack Increments Calculation and Shifting R_curve .

monotonic load can be calculated by integrating Eq. (4.12) from a_0 to a and is given by the following equation,

$$\Delta a = \int_{a_0}^a \lambda [Cm(a-a_0)^{m-1}]^{-1} [(1+\eta)P^\eta f(a) \overline{N}(a, a_0) + P^{1+\eta} f(a)] da \quad (4.14)$$

where $\overline{N}(a, a_0) = \frac{N'(a, a_0)}{(1+\eta)P^\eta}$ and $N'(a, a_0) = \frac{C(a, a_0)^m}{\lambda f(a)}$. The J -integral value corresponding to the crack growth, Δa , can be evaluated by introducing Δa into Eq. (4.11b).

4.5 SIMULATION OF CRACK PROPAGATION

Under assumption that stable crack growth satisfies J -controlled conditions, the requirements for crack growth within stable range can be defined, from elastic-plastic fracture mechanics point of view, by

$$J(a, P) \geq J_R(a - a_0)$$

From Fig. 4.4, it can be seen that under a specific load level P , crack will grow from a_0 to $a = a_0 + \Delta a_1$ and crack tip will move along crack growth direction from point A to point A'. At point A', where crack length is $a = a_0 + \Delta a_1$, J -curve intercepts with R -curve i.e. $J(a, P) = J_R(a_0, a)$. Further crack growth beyond this point is impossible. Because for any crack length, $a_i > a_0 + \Delta a_1$, the calculated $J(a_i, P)$ is less than $J_R(a_0, a_i)$. Additional energy has to be provided externally to the system to continue the crack propagation process. Increasing the applied load level from P to P_1 results in J -integral value increasing from $J(a, P)$ to $J(a, P_1)$ such that $J(a_1, P_1) > J_R(a_0, a_1)$, which will leads to stable crack growth under monotonic load. In the case of cyclic loading, the applied load cycles between maximum load level P_{max} and minimum load level P_{min} , which provides additional energy (hysteretic energy dissipation) for fatigue crack growth. To simulate the crack propagation process under cyclic load numerically, R -curve is shifted along with crack tip advancement. Therefore, at initial crack length a_0 , R -curve originated from point A, and can be expressed as,

$$J_R(a, a_0) = C(a - a_0)^m$$

After crack grows the amount of Δa , crack tip advances to $a = a_0 + \Delta a$ and R -curve will originate from point B and can be represented by the equation,

$$J_R(a, a_0 + \Delta a) = C[a - (a_0 + \Delta a)]^m$$

From Fig. 4.4, it can be seen that with the R -curve shifting, J -integral value, $J(a, P)$ at crack tip, a , becomes larger than $J_R(a, a_o + \Delta a)$ value around crack tip, then crack begins to propagate again. By introducing $J_R(a, a_o + \Delta a)$ into Eq. (4.14), another crack incremental Δa_i will be computed. Thus, by shifting R -curve along crack growth direction with crack tip advancement, crack will propagate incremental by incremental until unstable growth occurs.

Based on the assumption, the crack extension that is calculated by Eq. (4.14) during the process of R -curve shifting is equal to fatigue crack growth rate, i. e.

$$\frac{da}{dN} = \Delta a$$

Therefore, the functional relationship between fatigue crack growth rate and the variation of J -integral, ΔJ can be established by fitting the computed data pairs, Δa and ΔJ and is given by,

$$\frac{da}{dN} = f(\Delta J, A, B) \quad (4.15)$$

where A and B are fitting constants dependent on material analyzed.

4.6 MODIFIED FATIGUE CRACK GROWTH RATE

The fatigue crack growth rate presented in the foregoing section is established by simply fitting a series of data pairs of crack incremental, Δa_i and the variation of J -integral value, $\Delta J(a_i, P)$, which are computed by using R -curve shifting technique. As it is known that both R -curve and J -curve are developed under monotonic load, the computed crack incremental Δa_i from these two curves still characterizes monotonic crack growth properties. To take account of cyclic load effect into fatigue crack growth rate, modification of crack increments, Δa_i is made by examining the crack tip deformation under both monotonic loading and cyclic loading.

4.6.1 Plastic Zone Size

From crack tip deformation mechanism analysis, where small scale yield zone around crack tip is assumed, Rice [142] has derived the following formulations to evaluate plastic zone size around crack tip and crack opening displacement for elastic perfect plastic material with Tresca-Mises yield criterion. The formulations he derived for plastic zone size for mode I under monotonic load is given by,

$$\omega = \frac{\pi K_I^2}{8 \sigma_o^2} \quad (4.16a)$$

and crack opening displacement by

$$u_o = \frac{(\kappa + 1) K_I^2}{16G\sigma_o} \quad (4.16b)$$

Under cyclic load, he gives the following formulation to evaluate plastic zone size,

$$\Delta\omega = \frac{\pi(\Delta K_I)^2}{32\sigma_o^2} \quad (4.17a)$$

and the displacement by

$$\Delta u_o = \frac{(\kappa + 1)(\Delta K_I)^2}{32G\sigma_o} \quad (4.17b)$$

where

σ_o denotes material yield stress,

K_I stress intensity factor for mode I ,

$\Delta K_I = K_{\max} - K_{\min}$, variation of stress intensity factor under cyclic load (quasi-static)

$\kappa = 3-4\nu$ for plane strain and $\kappa = 3-\nu / 1+\nu$ for general plane stress,

G is shear modulus.

Comparison between the displacement under monotonic load and displacement under cyclic load gives

$$\Delta u_o = \frac{1}{2} \left(\frac{\Delta K_I}{K_I} \right)^2 u_o \quad (4.18)$$

4.6.2 Fatigue Crack Growth Rate

As suggested in Ref [125], the plastic deformations at the crack tip are responsible for crack growth (for mode I , plane strain condition). At the blunting crack tip caused by shear deformations, two displacements can be distinguished: the crack opening displacement δ_y and the crack advance displacement δ_x . The crack growth rate is calculated based on the consideration that the amount of crack growth, Δa , for plane strain condition during each load cycle is equal to the crack advance displacement calculated for the load rising portion of each cycle.

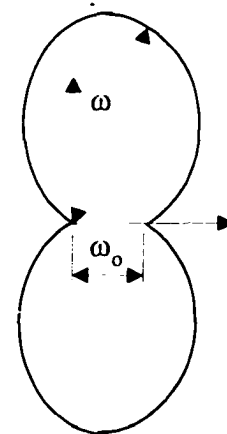


Figure 4.5 Plastic Zone Size Notation.

Under monotonic loading, the crack tip opening displacement δ_{ty} has been derived in Ref [125] for elastic-perfectly plastic material under plane strain condition and is rewritten in the following

$$\delta_{ty} = u_o = \frac{4(1-\nu)}{\pi} \gamma_o \omega \quad (4.19a)$$

and the crack advance displacement can be calculated by

$$\delta_{tx} = \frac{\omega_o}{\omega} \delta_{ty} = \frac{\omega_o}{\omega} u_o \quad (4.19b)$$

where ω denotes the maximum extent of the plastic zone and ω_o denotes the extent of the plastic zone on the uncracked ligament as shown in Fig. 4.5.

The crack advance displacement for crack opening mode I under cyclic load is also given by [125],

$$\Delta \delta_{tx} = \frac{\omega_o}{\omega} \Delta \delta_{ty} = \frac{\omega_o}{\omega} \Delta u_o \quad (4.20)$$

Then crack growth rate is defined by

$$\frac{da}{dN} \equiv \Delta \delta_{tx} = \frac{\omega_o}{\omega} \Delta u_o \quad (4.21)$$

By introducing $\Delta u_o = \frac{1}{2} \left(\frac{\Delta K_I}{K_I} \right)^2 u_o$ and Eq. (4.19b) into Eq. (4.21) then,

$$\frac{da}{dN} \equiv \Delta \delta_{tx} = \frac{1}{2} \left(\frac{\Delta K_I}{K_I} \right)^2 \delta_{tx} \quad (4.22a)$$

Here, for small-scale yielding and plane strain condition, crack growth is dominated by plastic blunting and is roughly approximated by $\Delta a = \delta_{tx}$. If the variation of stress intensity factor under cyclic load and stress intensity factor under monotonic load are identical, then Eq. (4.22a) can be rewritten as

$$\frac{da}{dN} = \frac{1}{2} \Delta a \quad (4.22b)$$

which gives the relationship between the fatigue crack growth rate under cyclic load and the crack growth under monotonic load.

This procedure may be extended to plane stress condition by assuming that,

$$\Delta a = \delta_{tx} = \alpha \delta_{ty} = \alpha u_o \quad (4.23a)$$

and

$$\Delta\delta_{\text{tx}} = \alpha \cdot \Delta u_o \quad (4.23b)$$

where α is a scalar factor. By introducing Eq. (4.18) and Eq. (4.23) into Eq. (4.21), we have

$$\frac{da}{dN} \equiv \Delta\delta_{\text{tx}} = \frac{1}{2} \left(\frac{\Delta K_I}{K_I} \right)^2 \Delta a \quad (4.24a)$$

If it is assumed that ΔK_I and K_I is identical, then crack growth rate is given by

$$\frac{da}{dN} \equiv \Delta\delta_{\text{tx}} = \frac{1}{2} \Delta a \quad (4.24b)$$

Crack extension and the variation of J -integral value under a specific load level can be calculated by Eq. (4.3). Fatigue crack growth rate then can be calculated through Eq. (4.22b) or Eq. (4.24). Functional relationship between $\frac{da}{dN}$ and cyclic J -integral, ΔJ , can be established by using least square fitting technique,

$$\frac{da}{dN} = f(\Delta J, A, B) \quad (4.25)$$

where A and B are fitting constants and dependent on material analyzed.

4.7 UNSTABLE CRACK GROWTH

As described in foregoing sections, fatigue crack propagation under cyclic load may be simulated by using crack driving force, J _curve, in conjunction with material resistance to crack growth, R _curve, that is shifted along crack growth line. As crack grows increment by increment, R _curve is shifted along advancing crack tip. A tangent point can always be found between the shifted R _curve and a J _curve at a specific cyclic load level. After this tangent point is reached, J _curve value is always greater than R _curve value, which means crack growth will become unstable and the material will fail by fracture. For a considered problem under a given applied load level, J _curve is a function of current crack length, a , only. R _curve is a function of the crack increment, $(a - a_0)$ only. The instability of crack growth is defined by

$$\left(\frac{\partial J}{\partial a} \right)_p \geq \frac{dJ_R}{da} \quad (4.26)$$

Functional relationship for J _curve and R _curve can be established by the method described in foregoing section. $\left(\frac{\partial J}{\partial a} \right)_p$ and $\frac{dJ_R}{da}$ can be evaluated by differentiating J _curve and R _curve, respectively. The critical crack length where unstable growth begins can be determined by

$$\left(\frac{\partial J}{\partial a}\right)_p = \frac{dJ_R}{da} \quad (4.27)$$

4.8 FATIGUE LIFE

The traditional approach to predict fatigue life of engineering structures or components under cyclic load by means of S-N data, cannot separate out crack initiation and propagation stages and cannot be applied to determine the structural life-expectancy with a crack-like defect of a known size. By using fracture mechanics parameter ΔK to characterize crack growth behavior, fatigue crack growth rate, such as Paris' law, can be established for a given material from fatigue test. Therefore, the number of cycles required for a crack to extend from a initial crack length to a given crack length can be obtained by integrating fatigue crack growth rate equation. However, to predict fatigue life, the final crack length has to be determined in advance and the total fatigue life should also include the contribution of unstable crack growth and fracture, where Paris' law is invalid. On the other hand, the configuration correction factor in the formulae to calculate the variation of stress intensity factor ΔK , is only available for very simple and limited specimen geometry. Therefore, the application of the method is very limited.

The proposed engineering approach can resolve these difficulties encountered in predicting fatigue life by using traditional S-N curve or Paris law. In the proposed approach, fatigue crack growth rate equation can be established and the critical crack length can be determined by using shifted R _curve and J _curve. The number of load cycles for every crack increment within the range from initial crack length to critical crack length can be evaluated by integrating fatigue crack growth rate equation with respect to crack length, this is,

$$\Delta N_i = \int_{a_i}^{a_{i+1}} dN = \int_{a_i}^{a_{i+1}} \frac{da}{f(J(a), A, B)} \quad (4.28)$$

Then, the fatigue life is the summation of all these number of load cycles, ΔN_i , from a_0 to critical crack length, a_{cr} ,

$$N_f = \sum_{i=1}^m \Delta N_i \quad (4.29)$$

where m is numbers of crack increment from a_0 to a_{cr} .

4.9 J-CONTROLLED CRACK GROWTH

A proposed numerical approach has been presented in the previous sections, which is based on the fundamental concept of elastic-plastic fracture mechanics. This approach is assuming that J-integral is a valid parameter to characterize locally concentrated stress-strain field around crack tip and control the small crack growth. However, the applicability of J-integral to characterize the near crack tip field for growing crack is subjected several restrictions. To ground the proposed numerical algorithm on a solid basis and to obtain a reliable result, the restrictions will be reviewed in this section and have to be satisfied in the applications.

It is evident that J-integral or stress intensity factor, K_I , uniquely measures the intensity of the stress-strain fields surrounding the immediate vicinity of the crack tip under small-scale yield condition [135]. Therefore, J-integral can be used to characterize material resistance to crack growth by means of J resistance curve under condition that the amount of crack growth is small compared to all other relevant geometric dimensions,

$$\Delta a \ll R$$

where R is some fraction of the plastic zone size. However, under large-scale yield condition and in the presence of significant amount of crack extension, the condition for

J-integral characterizing the near crack tip field becomes more involved. Hutchinson et al. [135], Rice [134] and Shih et al. [136] have shown that under certain conditions, there exists a small region around crack tip where crack growth is controlled by J-integral. The work by Hutchinson et al. [135], Rice [134], and Shih et al [136] will be briefly reviewed below.

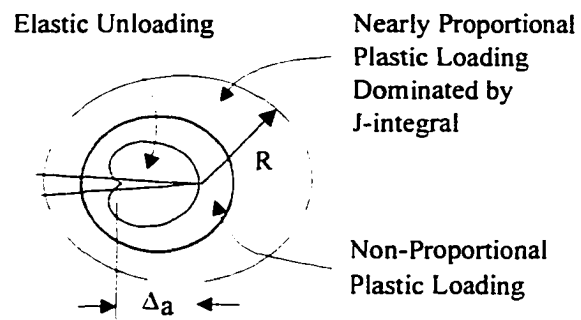


Figure 4.6 Denotation of Terms in Condition of J-controlled Crack Growth.

Three different regions around crack tip, as shown in Fig. 4.6, can be identified in the case of stationary crack:

- 1) Fracture process zone which consists of elastic unloading and non-proportional plastic loading.
- 2) A nearly proportional loading zone exists around the fracture process zone, which is known as the Hutchinson-Rice-Rosengren (HRR) [143] field and can be characterized by J-integral. Within this zone, the stresses and strains can be given by

$$\begin{aligned}\sigma_{ij} &= \sigma_o \left(\frac{EJ}{\sigma_o^2 I_n r} \right)^{1/(n+1)} \tilde{\sigma}_{ij}(\theta, n) \\ \varepsilon_{ij} &= \frac{\sigma_o}{E} \left(\frac{EJ}{\sigma_o^2 I_n r} \right)^{n/(n+1)} \tilde{\varepsilon}_{ij}(\theta, n)\end{aligned}\quad (4.30)$$

where

J is J-integral defined by Rice [71]

σ_o is initial yield stress

E denotes elastic modulus

r is radial distance from crack tip

$\tilde{\sigma}_{ij}, \tilde{\varepsilon}_{ij}$ are known dimensionless functions of the circumferential position θ and the hardening exponent n

I_n a constant which is a function only of n [135,144].

- 3) Elastic-plastic field that encompasses HRR field, in which stresses and strains can be described by flow theory of plasticity.

In crack growth situations, the near-tip field is far more complex than in the stationary case. Based on a J_2 flow theory of plasticity for an ideally plastic material, Rice [134] showed that the incremental strains in the immediate vicinity of the crack tip are functions of an increase of the crack opening displacement, $d\delta$ and the increment of the crack extension, da .

$$d\varepsilon_{ij} = \frac{d\delta}{r} f_{ij}(\theta) + \frac{\sigma_o}{E} \frac{da}{r} \ln \frac{R(\theta)}{r} g_{ij}(\theta) \quad (4.31)$$

Eq. (4.31) can be rewritten as the rate of change of the strain field with crack growth,

$$\frac{d\varepsilon_{ij}}{da} = \frac{1}{r} \frac{d\delta}{da} f_{ij}(\theta) + \frac{\sigma_o}{E} \frac{1}{r} \ln \frac{R(\theta)}{r} g_{ij}(\theta) \quad (4.32)$$

where, $R(\theta)$ is a measure of the distance to the elastic-plastic boundary, g_{ij} is a dimensionless function of order unity and $f_{ij} = \alpha \tilde{\varepsilon}_{ij}(\theta) / I_n$, α is a scalar factor. The first term represents a proportional part of strain field, while the second term represents a non-proportional part caused by the advance of the stress field. If

$$\frac{d\delta}{da} \gg \frac{\sigma_o}{E} \ln \left(\frac{R(\theta)}{r} \right) \quad (4.33)$$

is satisfied, the strains at the crack tip are uniquely characterized by the crack tip opening angle, $d\delta / da$.

From J_2 deformation theory of plasticity, Hutchinson and Paris[138] derived the strain increments for hardening material as follows:

$$d\varepsilon_{ij} = k_n J^{n/(n+1)} r^{-(n/(n+1))} \left\{ \frac{n}{n+1} \frac{dJ}{J} \tilde{\varepsilon}_{ij} + \frac{da}{r} \tilde{\beta}_{ij} \right\} \quad (4.34)$$

For an ideally plastic material, this expression reduces to [30]

$$d\varepsilon_{ij} = \frac{1}{\alpha \sigma_0} \frac{dJ}{r} f_{ij}(\theta) + \frac{1}{\alpha \sigma_0} J \frac{da}{r^2} \tilde{\beta}_{ij}(\theta) \quad (4.35)$$

where $\tilde{\beta}_{ij}(\theta)$ is a dimensionless quantity of order unity. Eq. (4.35) can be rewritten in terms of the rate of change of strain with respect to crack extension,

$$\frac{d\varepsilon_{ij}}{da} = \left(\frac{1}{\alpha \sigma_0} \right) \frac{1}{r} \frac{dJ}{da} f_{ij}(\theta) + \left(\frac{1}{\alpha \sigma_0} \right) \frac{J}{r^2} \tilde{\beta}_{ij}(\theta) \quad (4.36)$$

If the condition,

$$\frac{dJ}{da} \gg \frac{J}{r} \quad (4.37)$$

is satisfied, the near crack tip field is uniquely characterized by J -integral.

Although Eq. (4.32) and Eq. (4.35) are derived from two different plastic theories, they bear a similar structure. Their first term represents proportional increments in the strain fields due to the increase in size or strength of the HRR singularity, while the second terms represent the non-proportional strain increments due to the advance of the HRR field with the extension crack. Therefore, when the fracture process zone is enclosed in the region dominated by $d\delta / da$ or dJ/da , Eq. (4.32) and Eq. (4.35) provide the basis for a δ -based or a J -based resistance approach for stable crack growth.

If a material-based length quantity D is defined as

$$\frac{1}{D} = \frac{dJ}{da} \frac{1}{J}$$

and $r < R$, then Eq. (4.37) can be restated as

$$D \ll r < R \quad (4.38)$$

For fully yield condition, R will be some fraction of the relevant uncracked ligament, b . By defining a non-dimensional parameter

$$\omega = \frac{b \, dJ}{J \, da} \quad (4.39)$$

the condition for J-controlled stable crack growth can be restated as

$$\omega \gg 1.$$

In addition, the uncracked ligament of the test specimen must also satisfy

$$\rho \equiv \frac{b}{J_R / \sigma_y} \gg 1 \quad (4.40)$$

4.10 EXAMPLES

By means of the proposed numerical algorithm, fatigue analysis was carried out for several examples with different materials. The numerical results are compared with available experimental data. They show very strong correlations.

4.10.1 EXAMPLE 1

As discussed in foregoing sections, crack driving force curve, J -curve, can be used in conjunction with the material resistance curve, R -curve, to predict fatigue life numerically. In this example, the proposed numerical procedure will be examined by analyzing fatigue behavior of a compact specimen of A533B steel at 93°C (200°F). Comprehensive investigations of fracture behavior of these specimens have been carried out by Shih et al [136,143] and Andrews et al [145]. A brief description of their investigations will be given here and some of the experimental results will be employed in the analysis to predict fatigue life.

The specimen geometry was complied with the standard compact specimen (ASTM E399-74). Modifications were made to permit measurement of the load line deflection and the opening displacement near the crack tip as shown in Fig. 4.7. The uniaxial stress-strain curve for this specimen and its characterization by the Ramberg-Osgood law are given in Fig. 4.8. Elastic modulus E , poisson ratio ν , and initial yield stress σ_0 are taken to be $207 \times 10^3 \text{ MPa}$ ($30 \times 10^6 \text{ psi}$), 0.3 and 414 MPa ($60 \times 10^3 \text{ psi}$), respectively. The least squares curve fitting method gives $\alpha=1.12$ and $n=9.7$ in the fitting equation.

The elastic-plastic estimation of J -integral value for the compact specimen has been obtained by Kumar et al [146] and is re-presented here as

$$J = f_1(a_c) \frac{P^2}{E'} + \alpha \sigma_0 \epsilon_0 c h_1(a/W, n) [P/P_0]^{n-1} \quad (4.41)$$

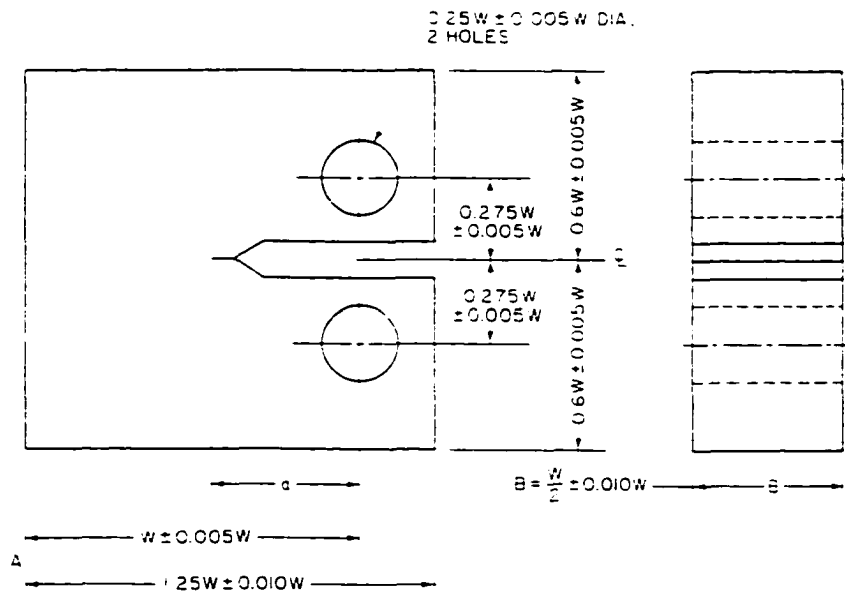


Figure 4.7: Geometry of ASTM Standard Compact Tension Specimen.

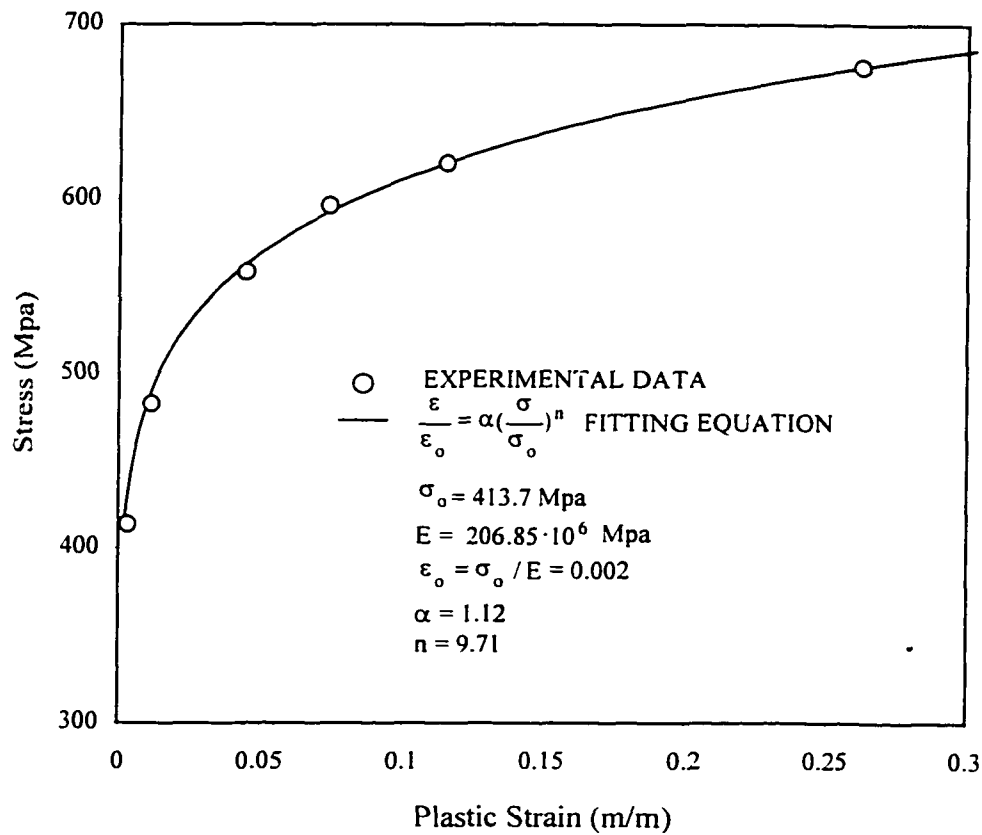


Figure 4.8: Stress-Strain Curve for A533B Steel at 200° F and Its Representation by the Ramberg-Osgood Law.

where

α is a scalar factor, ϵ_0 is initial plastic strain

P is the applied load per unit thickness,

a is the crack length, W specimen width $c = W - a$ is the uncracked ligament as shown in Fig. 4.7 .

$E' = E$, for plane stress, $E' = E / (1 - \nu^2)$ for plane strain.

$a_e = a + \phi r_y$ denotes effective crack length, in which $r_y = \frac{1}{\beta\pi} \left[\frac{n-1}{n+1} \right] \left(\frac{K_I}{\sigma_0} \right)^2$ is plastic zone size

and $\phi = \frac{1}{1 + \left(\frac{P}{P_0}\right)^2}$. For plane strain condition, $\beta=2$.

The function $f_1(a_c)$ is determined by

$$f_1(a/W) = \left[0.2960\left(\frac{a}{W}\right) - 1.855\left(\frac{a}{W}\right)^2 + 6.557\left(\frac{a}{W}\right)^3 - 10.7\left(\frac{a}{W}\right)^4 + 6.389\left(\frac{a}{W}\right)^5 \right]$$

The function h_1 can be obtained from Table A.1. P_0 is the limit load per unit thickness and is given by

$$P_0 = 1.455\eta c\sigma_0$$

$$\eta = \left[(2a/c)^2 + 2(2a/c) + 2 \right]^{1/2} - [2a/c + 1]$$

For some specific load levels, J -integral within a given crack length range are calculated by substituting the value of h_1 in Eq. (4.41) and presented in Table A.2 and plotted in Fig. 4.9.

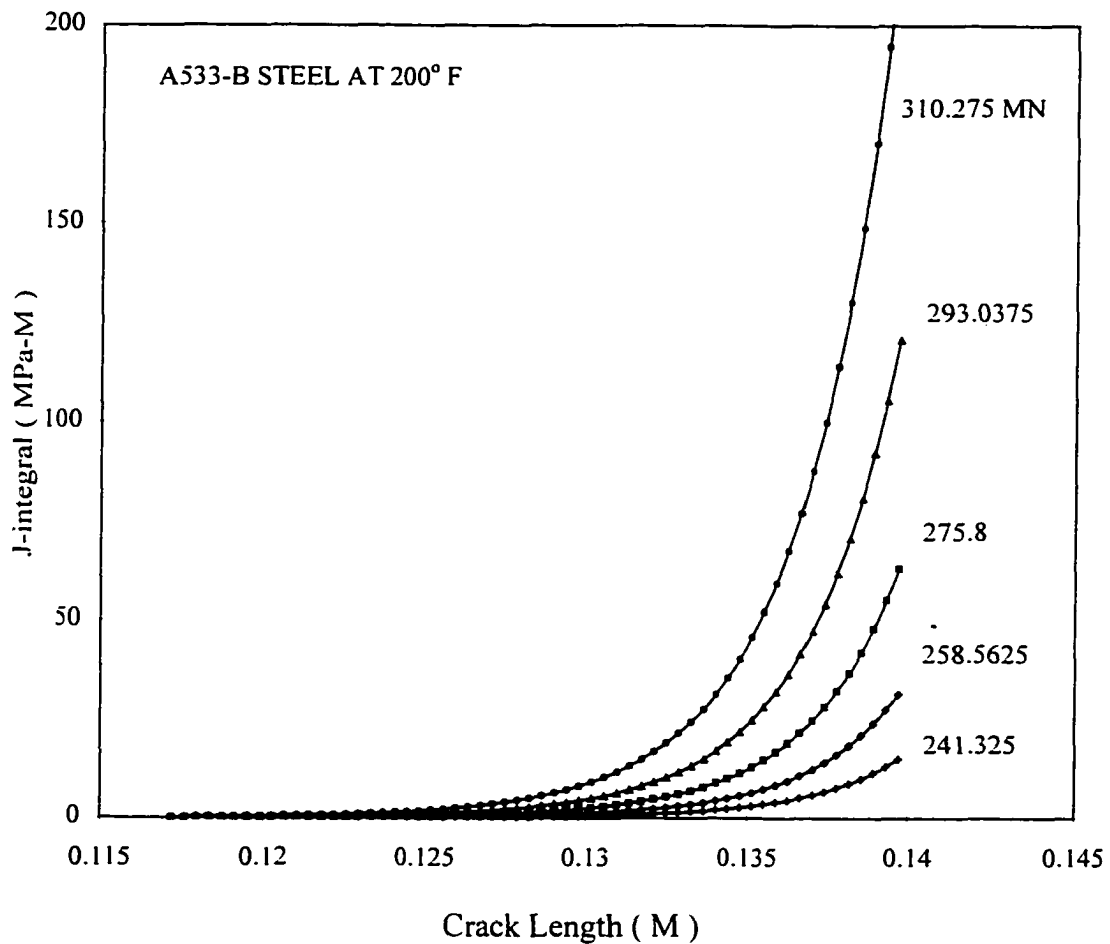


Figure 4.9: J-integral versus Crack Length Curves with Load as the Parameter for Plane Strain Compact Specimen of A533-B Steel.

By fitting the test data of crack growth resistance provided in Shih's [136] experiments using nonlinear fitting technique, functional relationship for the R_curve can be established. For some specific crack lengths, J-integral value can be calculated from this R-curve and are given in Table A.3 and plotted in Fig. 4.10

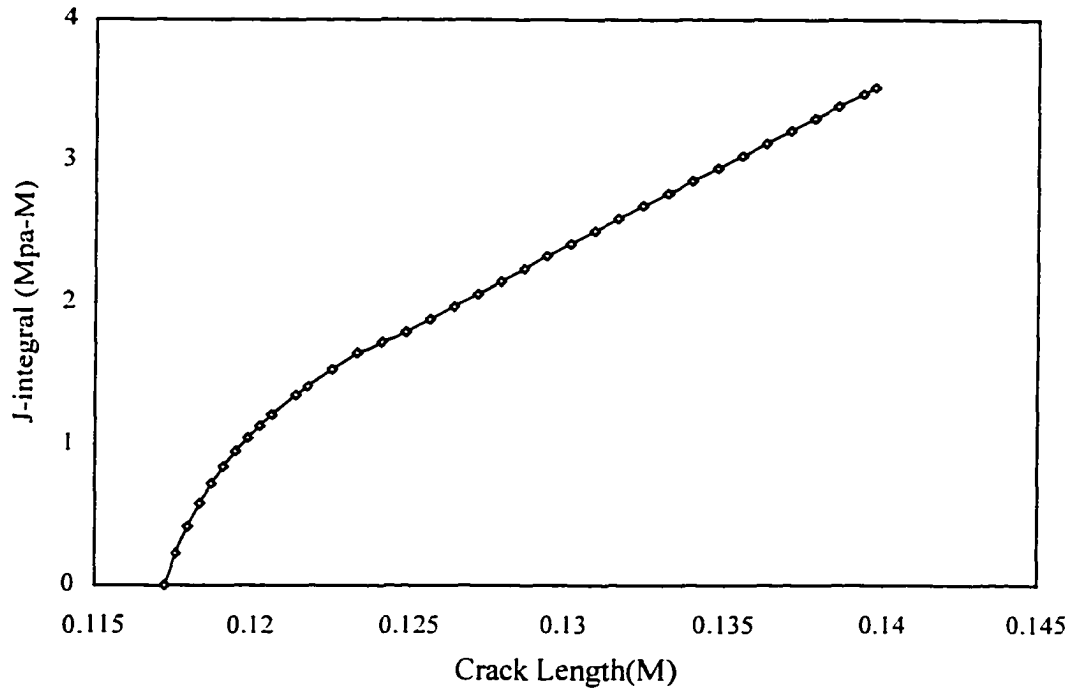


Figure 4.10: R_curve for Compact Specimen of A533B Steel at 200° F.

Both the R_curve and J_curve are taken as input of a fatigue analysis program (FLAP_1.0) developed based on the proposed numerical procedure. Fatigue analysis was carried out. From the fatigue analysis results, crack increments that directly calculated from shifted R_curves and J_curves are extracted and presented in Table A.4. By considering the difference of crack tip deformation between monotonic and cyclic loadings, these crack increments in Table A.4 are modified according to the foregoing section to include the cyclic loading effects and are shown in Table A.5. Table A.6 provides cyclic increments of J-integral corresponding to the crack increments listed in Table A.4 and Table A.5. These cyclic increments of J-integral value are computed by assuming that it is two times of the J-integral value, δJ , that is directly calculated from shifted R_curves and J_curves, i.e.

$$\Delta J = 2\delta J = J$$

where J is J-integral value under monotonic load.

By fitting the data pairs Δa in Table A.5 and ΔJ in Table A.6, we obtain fatigue crack growth rate equation

$$\frac{da}{dN} = 2.4 \cdot 10^{-5} (\Delta J)^{1.1}$$

The fatigue crack growth rate curve, together with the fitting data given in Table A.5 and Table A.6 are plotted in Fig. 4.11.

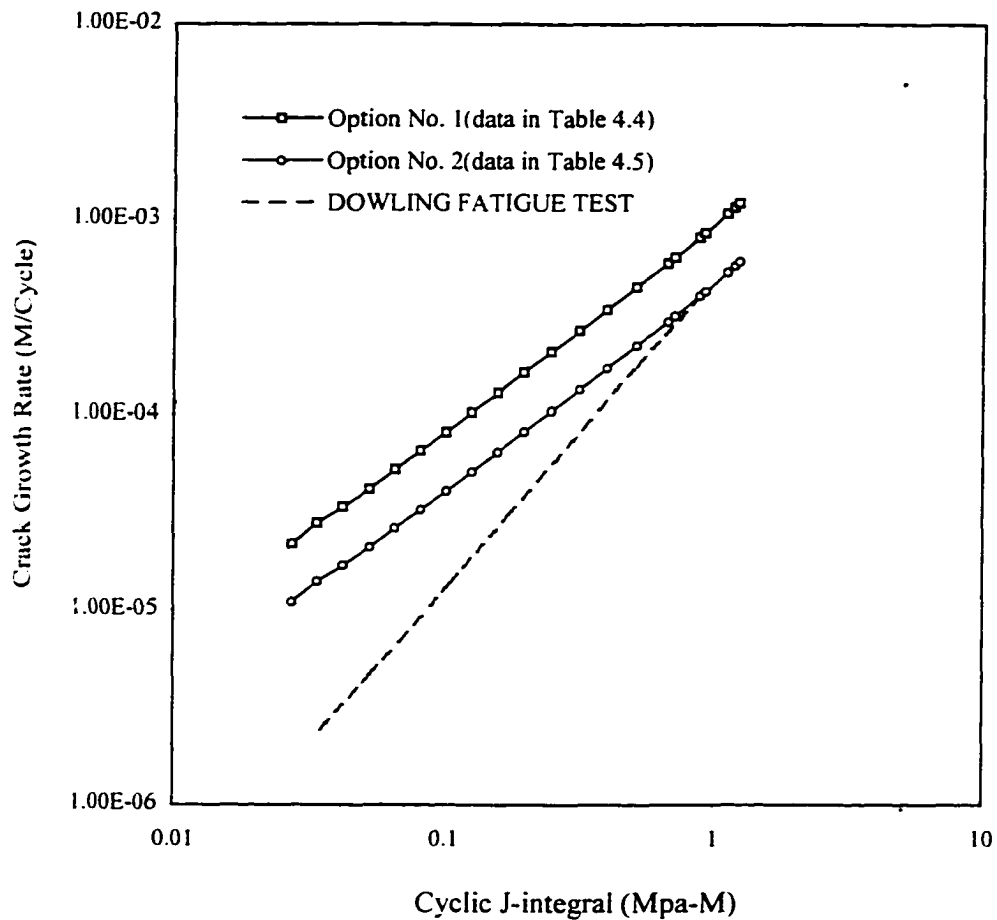


Figure 4.11: Fatigue Crack Growth Rate as a Function of Cyclic J-integral for A533B Steel at 200°F (Current Study) and 97°F (Dowling Fatigue Test).

No fatigue test data were available for these specimens of steel A533B at 200°F. However, for comparison, Dowling's [93] fatigue test results on the same material at different temperatures, $\sigma_y = 70.0\text{ksi}$ and $T=97^\circ\text{F}$, is also presented in Fig. 4.11. By comparing the numerical prediction of fatigue crack growth rate with experimental results, we can see that the proposed numerical procedure gives reasonable prediction of fatigue crack growth rate.

Fatigue life at a given load level can also be calculated within the program(FLAP_1.0) by integrating the fatigue equation incremental by incremental from initial crack length, c_0 to critical crack length c_{cr} . At every load level, fatigue lives are calculated and presented in Table A.6 and plotted in Fig. 4.12.

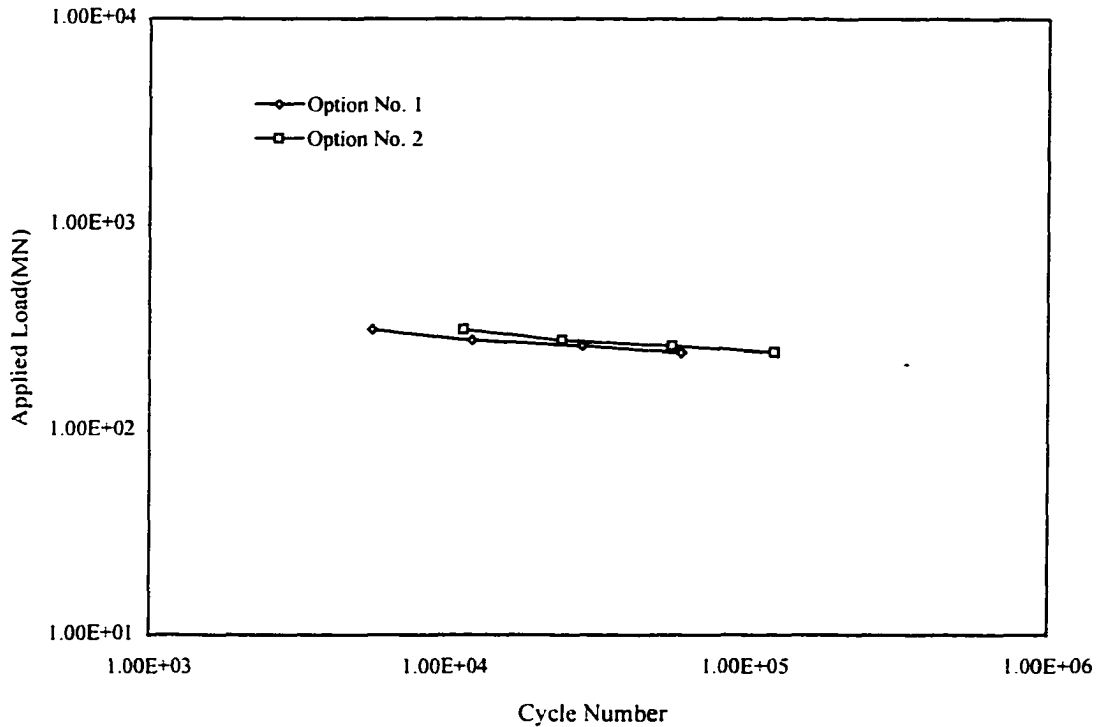


Figure 4.12: Numerical Prediction of Fatigue Life at Different Load Levels for Compact Specimen of A533B Steel at 200°F.

The J-controlled requirements for using J-integral in stable crack growth have been verified in [136, 145] for R_{curve} obtained from plane-strain compact tension specimen of A533-B steel. With regards to use R_{curve} and J_{curve} to simulate fatigue crack propagation, J-controlled requirements also have to be satisfied so that J-integral is valid parameter to characterize near-tip stress-strain field. In this example, the

J-controlled requirements are verified by introducing every crack increment and its corresponding J-integral into Eq. (4.39) and Eq. (4.40). The crack increment and its corresponding J-integral value can be found in Table A.4 and Table A.6, respectively. The onset J-integral, J_{IC} , and flow stress, σ_y , are given in [145]. The computation results show that

$$\omega_{\min} = 128 \gg 1$$

$$\omega_{\max} = 180 \gg 1$$

and

$$\rho_{\min} = 61 \gg 1$$

$$\rho_{\max} = 3053 \gg 1$$

which satisfy the J-controlled requirements. Comparing the results with recommended lower bound value

200 in [147], we can see that the $\rho = \frac{b}{J_R / \sigma_y}$ at some points is not satisfied.

4.10.2 EXAMPLE 2

In this example, fatigue behavior of a four point prismatic bending beam is examined using the proposed numerical approach. The beam is made of soil-cement material. Its elastic properties are given by elastic modulus $E=1.724 \times 10^3$ MPa (2.5×10^5 psi), and poisson ratio $\nu=0.15$. Its plastic properties are described by Mohr-Coulomb model with cohesion $C=2.586$ MPa (375.0 psi), and internal friction angle $\phi=42^\circ$. The difference in this example from

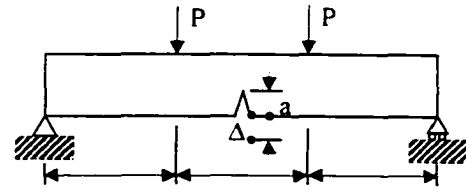


Figure 4.13: (a) Four-Point Beam Used In Fatigue Analysis.

example 1 is that there are no sufficient experimental data to establish J resistance curve for the material. Second there is no available standard test procedure to conduct the J resistance curve test. Therefore, numerical approach described in section 4.2 has to be used to establish R_curve used in fatigue analysis. The beam is 0.0762 M(3.0 inches) high, 0.0762 M(3.0 inches) thick and 0.4572 M(18.0 inches) long. The major and minor span are 0.4572 M(18.0 inches) and 0.1524 M(6.0 inches), respectively, as shown in Fig. 4.13. Considering the symmetry of geometry and applied load, only half of the beam is modeled in numerical analysis using finite element method. Eight-node isoparametric element is used throughout the half beam. Quarter point singularity element is arranged around crack tip. The finite element mesh is shown in Fig. 4.13. For a given crack length, a load displacement curve is traced and J-integral value is computed at each displacement increment by using ABAQUS [148], a general finite element analysis

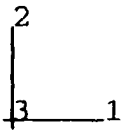
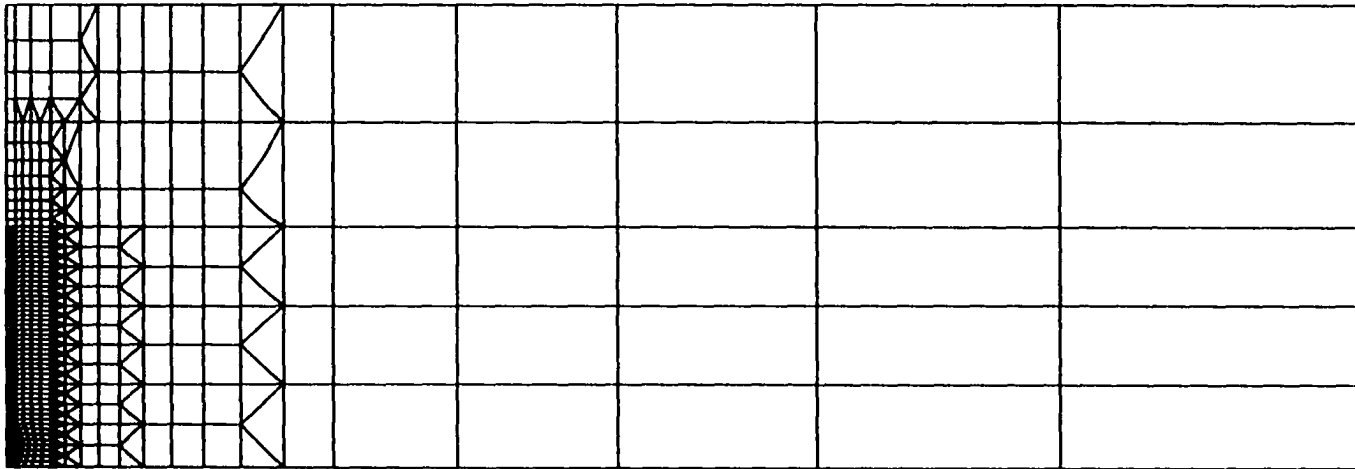


Figure 4.13(b): Finite Element Mesh for Half of the Four-point Beam.

program. A typical load displacement curve computed from ABAQUS is shown in Fig. 4.14. For different crack lengths, a group of load displacement curves and J-integral vs. displacement curves are established. These two groups of curves are taken as input of the fatigue analysis program (FLAP_1.0) which is based on the proposed numerical procedure. From these two groups of curves, R_curve and J_curve are evaluated by the program. Figure 4.15 shows a typical R_curve of the considered material. Based on these R_curves and J_curves, the increments of crack growth, Δa , and increments of J-integral, ΔJ , are computed within the range from initial crack length to critical crack length. These values are presented in Table A.8-A.10. According to the assumptions, fatigue crack growth rate can be obtained by fitting these computed data pairs Δa in Table A.8 and Table A.9 and ΔJ in Table A.10. The fitting curve, together with computed data, is plotted in Fig. 4.16. At each given load level, fatigue lives can be computed by integrating the fatigue crack growth rate equation incremental by incremental from initial crack length, c_0 , to critical crack length c_{cr} . For different load levels, fatigue lives are evaluated. At a given load level, initial flexural stress can be calculated for the beam. These initial flexural stresses at different load levels and corresponding fatigue lives constitute an S-N curve, as shown in Fig. 4.17.

A Flexural fatigue test has been conducted on the same material by Pretorius [149]. The test was conducted under load control condition. Strains on the top and bottom surface of the beam are monitored. From the measured strains, initial flexural stress, and initial radius of curvature ratio can be computed. By means of linear least fitting technique, three fatigue life equations in three independent variables i.e. initial flexural strain, initial flexural stress and initial radius of curvature were obtained. These equations and fatigue test data are given in Table A.11 and plotted in Fig. 4.18, respectively. The fatigue life at specific stress level is recalculated from the initial stress fatigue equation listed in Table A.11 and together with numerical predicted fatigue life are plotted in Fig. 4.17. By comparing these two curves, we can conclude that the predicted fatigue life using the proposed numerical procedure is agree very well with Pretorius[149] experimental results.

The applicability of fracture mechanics to soil-cement material has been investigated experimentally by a few investigators [150, 151]. Fracture parameters, such as stress intensity factor, K, energy release rate factor, G, J-integral, and R_curve were obtained for several different soil-cement materials. The experimental results shown that there is a tendency of relating stress intensity factor to the crack propagation rate[150]. Fatigue crack growth law was also developed in [151].

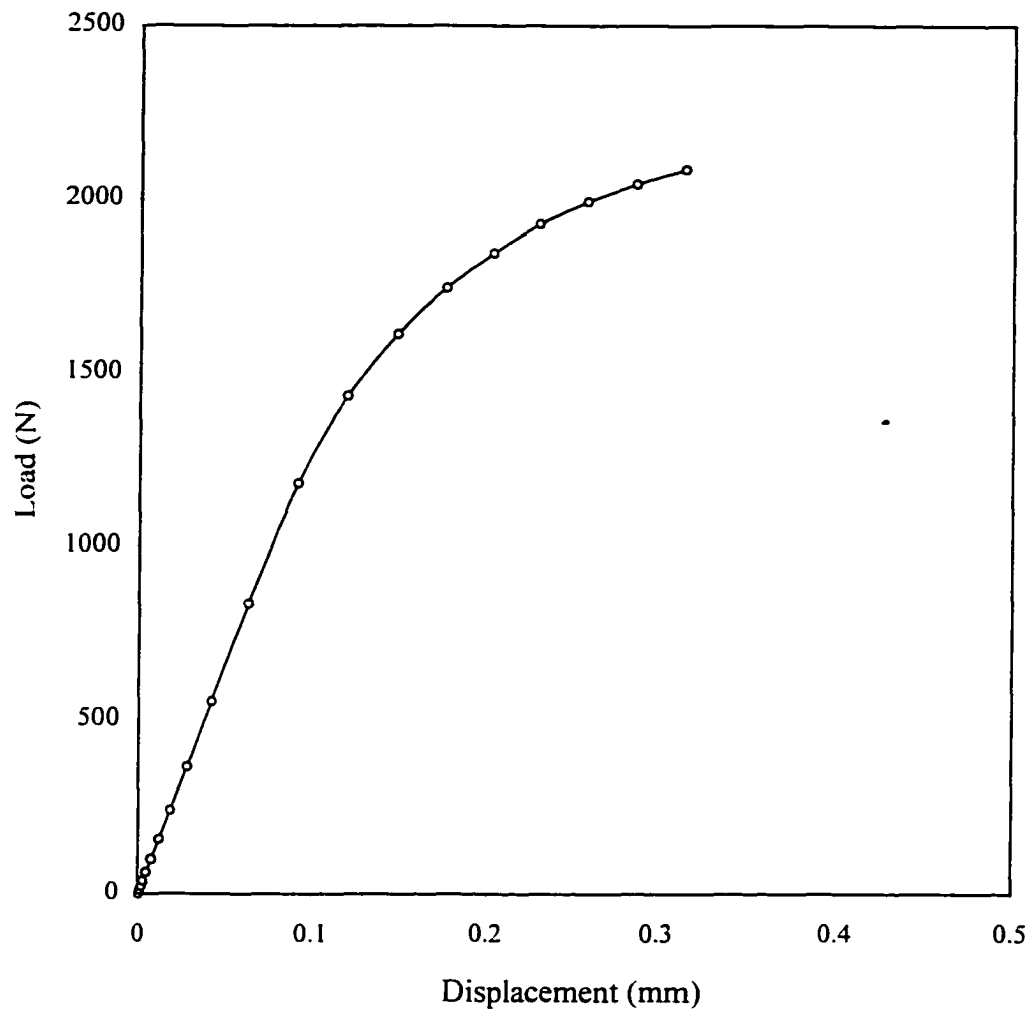


Figure 4.14: Load as a Function of Load-line Displacement for Beaming Beam of Soil-Cement Material with Cohesion $C = 2.586$ Mpa. and Internal Friction Angle $\phi = 42^\circ$.

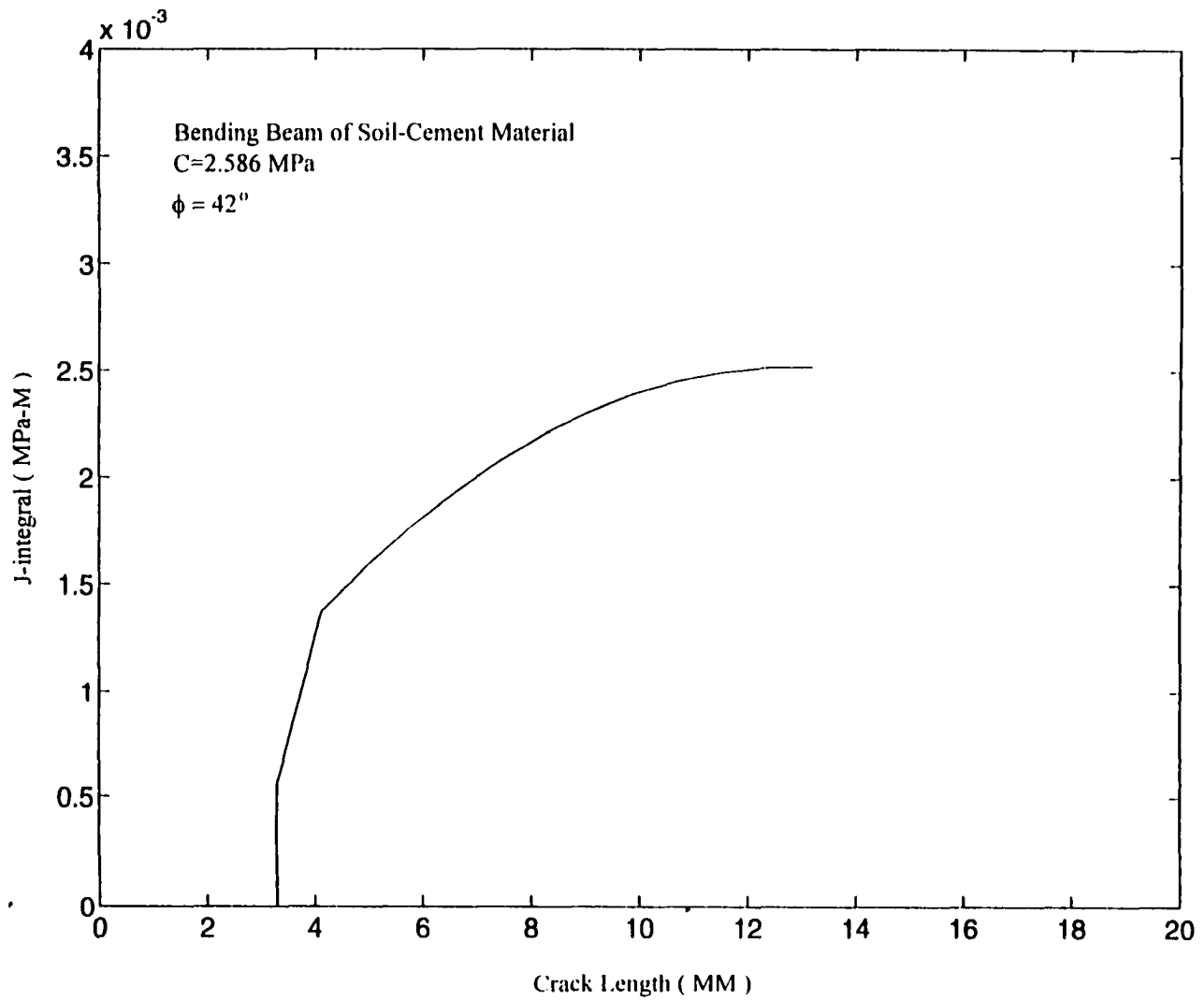


Figure 4.15: J-Resistance Curve for Bending Beam of Soil-Cement Material.

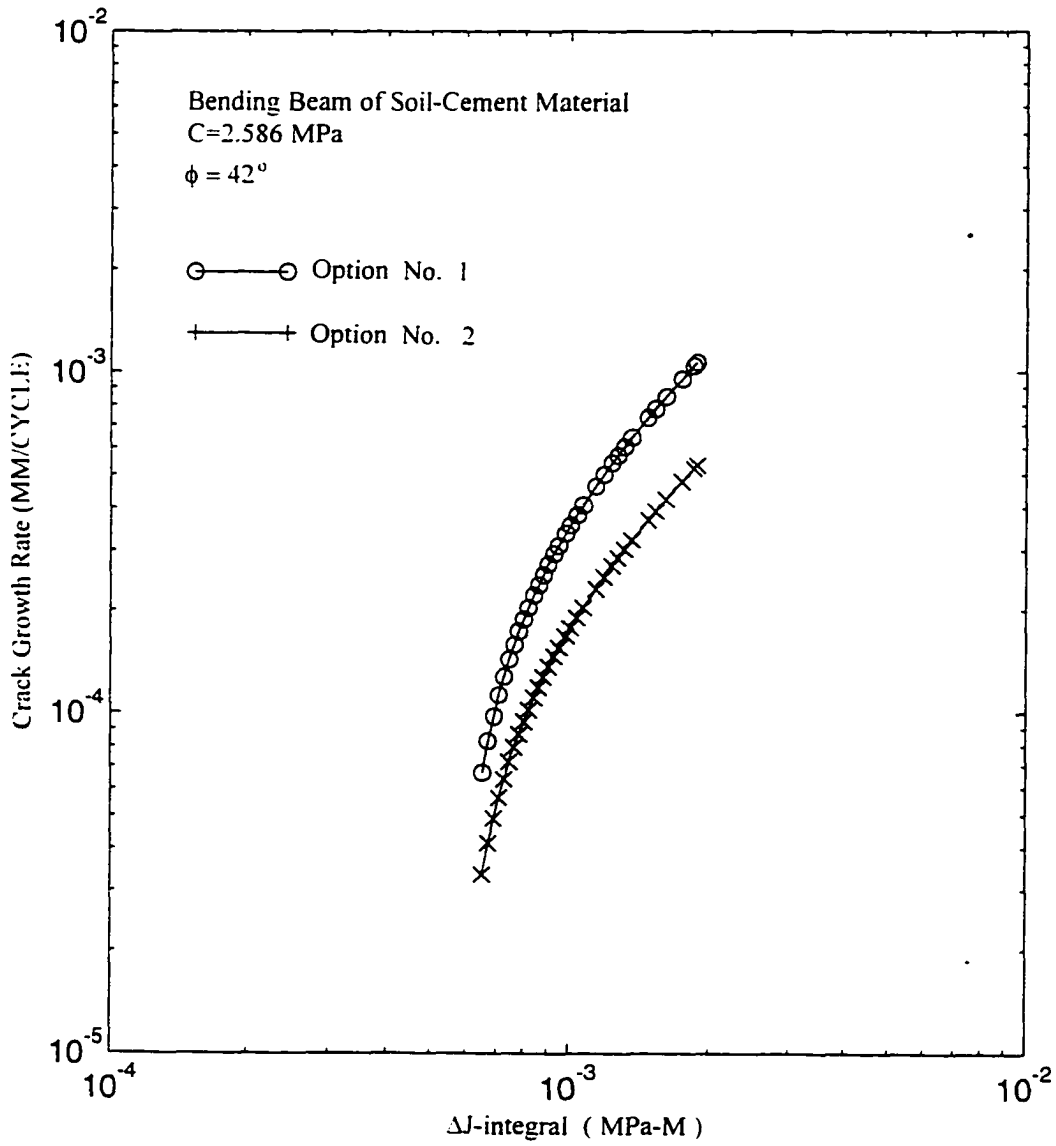


Figure 4.16: Fatigue Crack Growth Rate Changes with Cyclic J-integral for Bending Beam of Soil-Cement Material.

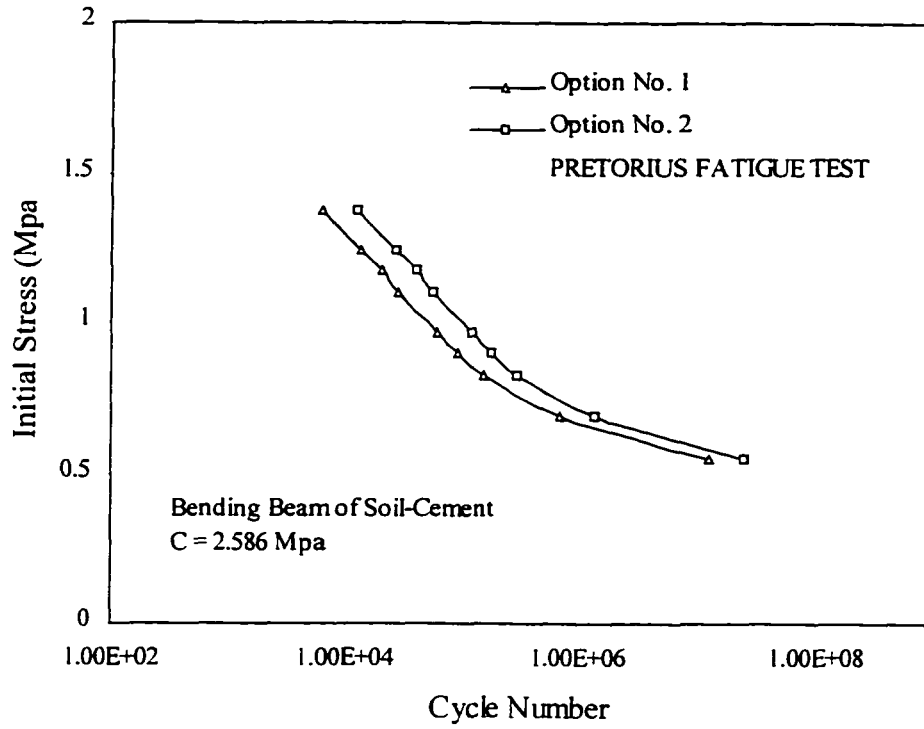


Figure 4.17: Fatigue Life Changes with Internal Flexural Stress For Bending Beam($\varphi = 42^\circ$).

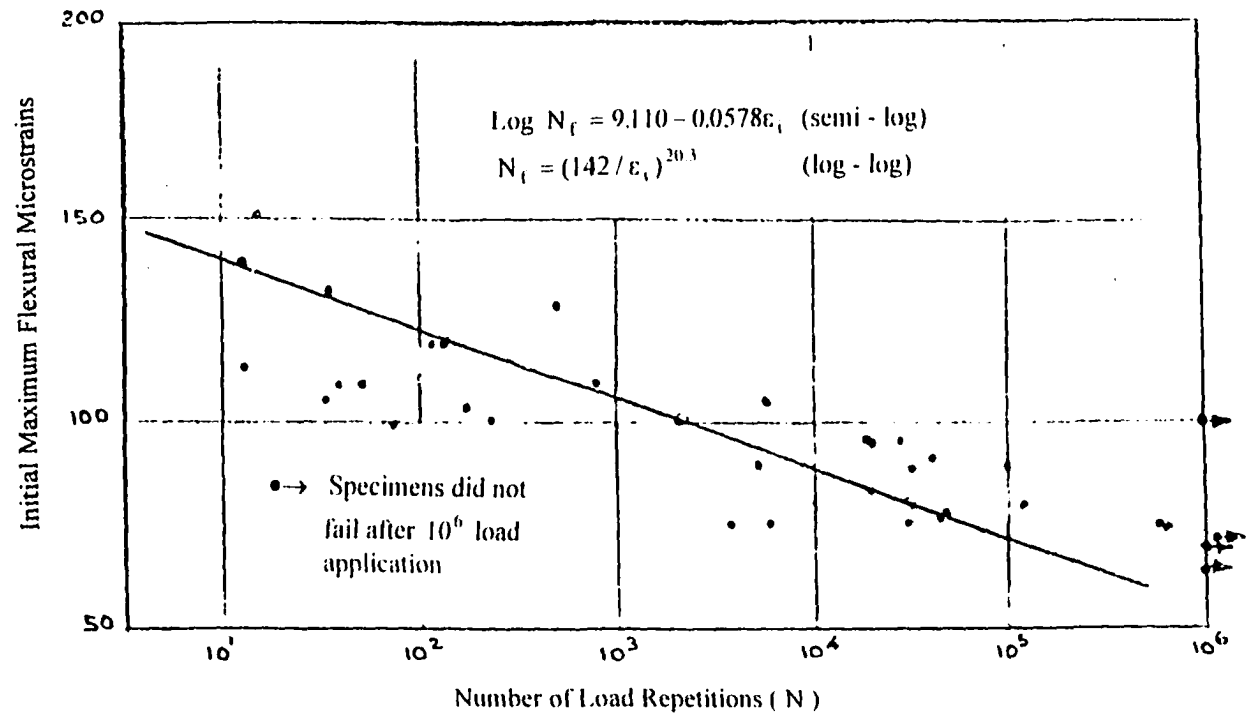


Figure 4.18: Fatigue of Flexural Specimens of Soil-Cement Material with Cohesion $C=2.586$ Mpa and Internal Friction Angle $\phi = 42^\circ$.

Soil-cement material generally is regarded as linear elastic. When microcracking developed around the crack tip, it may have also behaved nonlinearly. Although the process zone surrounding the crack tip is primarily due to microcracking that is confined to a relatively small process zone, the macrocracks still follow certain fracture modes as shown in test specimen.

If the crack tip process zone is small in relation to the crack length and other specimen dimensions, stress intensity factor, K or J -integral, can be used to characterize near-tip stress or strain field. As long as the dimensions of the test specimen satisfy the requirements specified in ASTM standard test procedures, enough constraint should occur in the vicinity of the crack tip, which ensures the crack tip process zone within small size. In this case, the ratio of specimen width and thickness $W/B=2.0$, is within ASTM standard requirement and, it is sufficient to provide the necessary constraint. When ASTM standard requirements are satisfied, the radius of the plane-strain plastic zone size should not exceed $r_y=B/50$. On the other hand, plastic zone size can be evaluated by [142]

$$\omega = \frac{\pi K_I^2}{8\sigma_o^2} \quad (4.45)$$

and the crack opening displacement by

$$u_o = \frac{(\kappa + 1) K_I^2}{16G\sigma_o} \quad (4.46)$$

By introducing Eq. (4.46) into Eq. (4.45), the plastic zone size can be calculated by

$$\omega = \frac{\pi E}{(1 - \nu^2)\sigma_o} u_o \quad (4.47)$$

Assuming $E \approx 500\sigma_o$, then Eq. (4.47) can be rewritten as

$$\omega = \frac{500\pi}{1 - \nu^2} u_o \approx 1600u_o \quad (4.48)$$

Therefore, the plastic zone size will fall within the following range

$$1600u_o \leq \omega \leq \frac{B}{50}$$

In this example, the thickness of the beam is $B=76.2(\text{mm})$ and r_y is approximately equals to $1.52(\text{mm})$. The maximum and minimum crack increment and corresponding J -integral can be found in Table A.10 and Table A.11 and are

$$(\Delta a)_{\max} = 0.001069 \quad (\text{mm}); \quad (\Delta J)_{\max} = 0.001874 \quad (\text{MPa})$$

and

$$(\Delta a)_{\min} = 0.000067 \quad (\text{mm}); \quad (\Delta J)_{\max} = 0.000652 \quad (\text{MPa})$$

According to [71, 152], crack opening displacement can be determined by

$$\delta = \frac{J_R}{\alpha \sigma_o} \quad (4.49)$$

where α is a constant and set to 1 here.

By assuming the tensile strength is dominant yield stress in the crack growth process, the plastic zone size can be evaluated as follows,

$$\omega_{\max} = 0.651 < B/50 = 1.52 \quad \text{for maximum crack increment}$$

$$\omega_{\min} = 0.2266 < B/50 = 1.52 \quad \text{for minimum crack increment}$$

Comparing the plastic zone size with crack increments, we obtained

$$\frac{(\Delta a)_{\max}}{\omega_{\max}} = 0.0016 \ll 1 \quad \text{and} \quad \frac{(\Delta a)_{\min}}{\omega_{\min}} = 0.0003 \ll 1$$

Therefore, the requirement for J-controlled crack growth is satisfied.

4.10.3 EXAMPLE 3

The fatigue behavior of the beam in example 2 is re-examined here using asphalt cement materials. Like soil-cement material, asphalt cement material is also treated as Mohr-Coulomb type $C-\phi$ material. Viscous effect is not considered in this analysis. Detailed description of the material properties is given in Table A.12.

The procedure to obtain load displacement curves, J-integral versus displacement curves, R -curves and J -curves is same as that described in example 2 and will not be repeated in this example. The numerical results of increments of crack growth and increments of J-integral obtained from the program (FLAP_1.0) are given in Table A.13-A.15 and Table A.16-A.18, respectively for the material at 10°F and at 68°F . Fatigue tests on the same materials have been carried out by Salam [24]. The fatigue test data were presented by means of S-N curves. In constructing these S-N curves, the nominal stresses are determined by simply assuming a beam whose depth is reduced by the size of the notch. A log-log plot of nominal stress versus fatigue life is shown in Fig. 4.19 for different notch sizes. The S-N curve with notch size $a/h = 0.4$, and the numerically predicted fatigue life curve are plotted in Fig. 4.20 for the material at 10°F

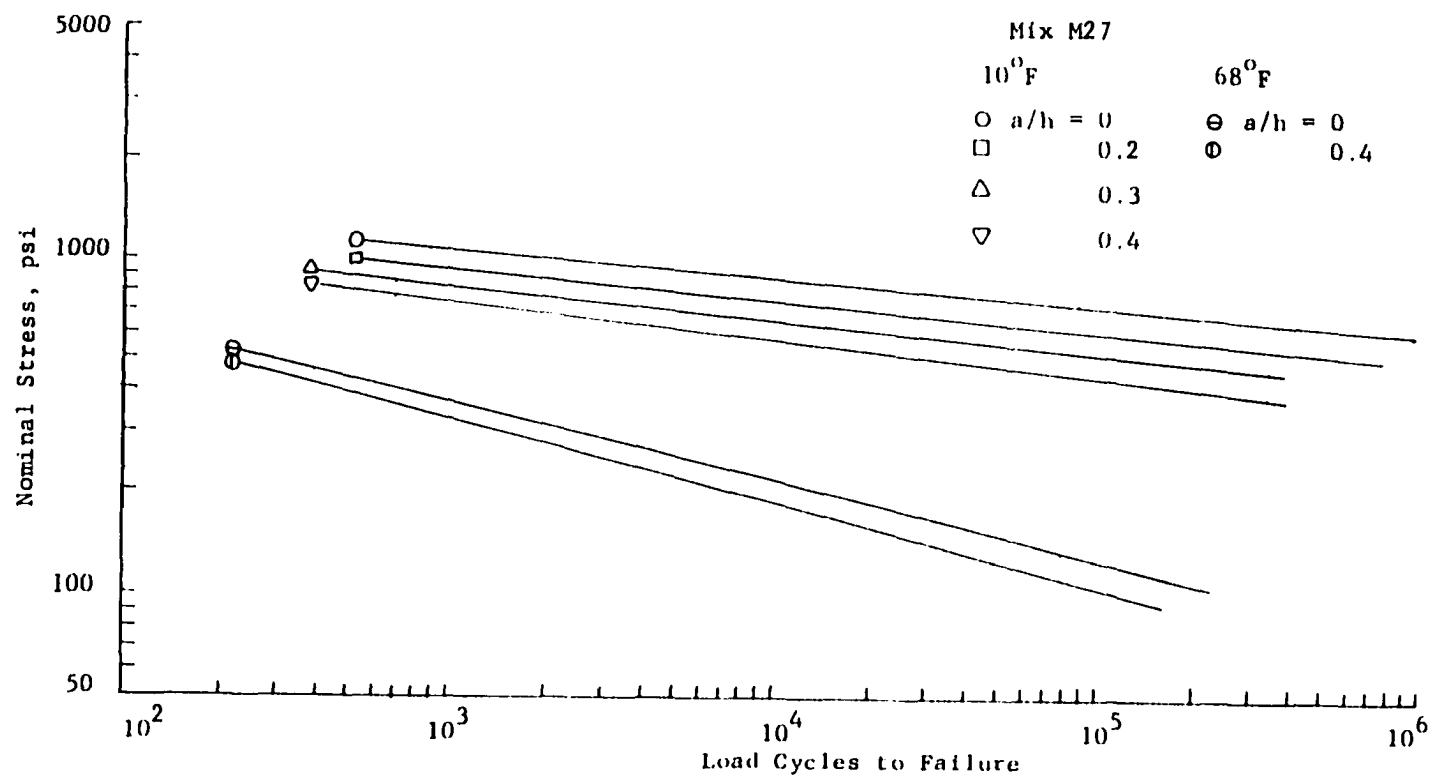


Figure 4.19: Normal Stress as a Function of Fatigue Life for Bending Beam of Asphalt-Cement Material at 10⁰ F and 68⁰ F.

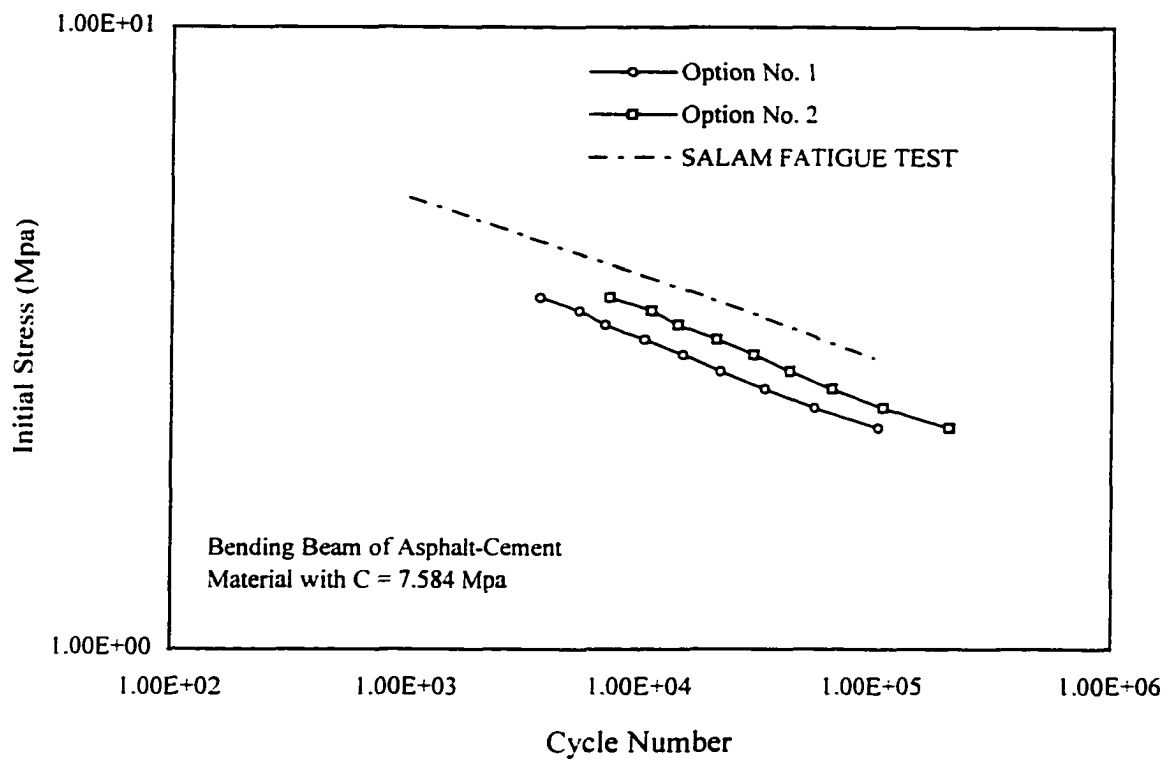


Figure 4.20: Numerical Predicted Fatigue Life Variations with Initial Flexural Stress(S-N Curve) for Beading Beam of Asphalt Cement Material at 10° F ($\phi = 48^{\circ}$).

and Fig. 4.21 for the material at 68° F. Once again, the proposed numerical procedure gives a very good prediction of fatigue life in comparison with experimental results.

Extensive experimental investigation and theoretical models [25] have related fracture mechanics parameters (K, J) to the fatigue crack growth in asphalt cement materials. Asphalt cement material is generally considered visco-elastic or visco-plastic. However, at lower temperatures, as the material studied in this example, the material behavior is dominated by elasticity. In this case, small crack tip process zone assumption still holds in the analysis of stable crack growth. Therefore, the same procedure described in example 2 can also be used here to verify J-controlled crack growth conditions.

For the material at 10° F, from Table(4.13) and (4.14), we find

$$\begin{aligned}(\Delta a)_{\max} &= 0.00182 \quad (\text{mm}) \\ (\Delta J)_{\max} &= 0.008529 \quad (\text{MPa} - \text{mm})\end{aligned}$$

and

$$\begin{aligned}(\Delta a)_{\min} &= 0.00201 \quad (\text{mm}) \\ (\Delta J)_{\min} &= 0.003613 \quad (\text{MPa} - \text{mm})\end{aligned}$$

The plastic zone size can be calculated and is given by

$$\begin{aligned}\omega_{\max} &= 1.12 < B/50 = 1.52 \quad \text{for maximum crack increment} \\ \omega_{\min} &= 0.0264 < B/50 = 1.52 \quad \text{for minimum crack increment}\end{aligned}$$

Comparing the crack increments with plastic zone size, we have

$$\begin{aligned}\frac{(\Delta a)_{\max}}{\omega_{\max}} &= 0.0016 \ll 1 \\ \frac{(\Delta a)_{\min}}{\omega_{\min}} &= 0.000423 \ll 1\end{aligned}$$

J-controlled stable crack growth condition is satisfied at 10° F.

At 68° F, from Table A.16 and Table A.18, we found

$$\begin{aligned}(\Delta a)_{\max} &= 0.002016 \quad (\text{mm}) \\ (\Delta J)_{\max} &= 0.007676 \quad (\text{MPa} - \text{mm})\end{aligned}$$

and

$$\begin{aligned}(\Delta a)_{\min} &= 0.000145 \quad (\text{mm}) \\ (\Delta J)_{\min} &= 0.001294 \quad (\text{MPa} - \text{mm})\end{aligned}$$

From these values, we obtain

$$\omega_{\max} = 1.008 < B / 50 = 1.52 \quad \text{for maximum crack increment}$$

$$\omega_{\min} = 0.429 < B / 50 = 1.52 \quad \text{for minimum crack increment}$$

and

$$\frac{(\Delta a)_{\max}}{\omega_{\max}} = 0.002 \ll 1$$

$$\frac{(\Delta a)_{\min}}{\omega_{\min}} = 0.00034 \ll 1$$

J-controlled stable crack growth requirement is also satisfied at 68° F .

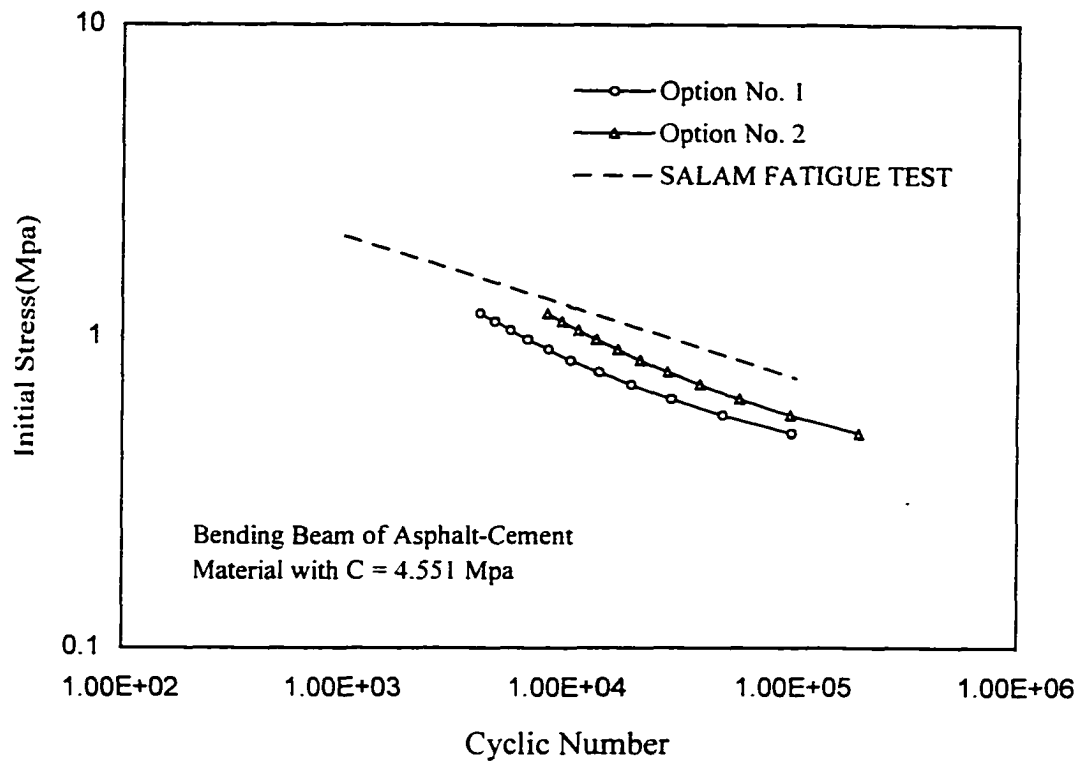


Figure 4.21: Numerical Predicted Fatigue Life Variations with Initial Flexural Stress(S-N Curve) for Beading Beam of Asphalt Cement Material at 68° F($\phi = 17^\circ$).

SUMMARY

A numerical approach to fatigue analysis is proposed in this chapter. This approach is based on the fundamental concept of elastic-plastic fracture mechanics. It utilizes crack driving parameter, J-integral curve, in conjunction with material resistance to fracture curve, R_curve, to determine the amount of crack growth. Crack propagation is simulated by shifting R_curve along crack growth direction after each crack extension. Critical crack growth length is determined by finding the tangent point between shifted R_curve and J_curve. The crack increment determined by J_curve and R_curve is modified by considering the difference between plastic zone size under cyclic loading and monotonic loading. Thus, cyclic loading effects can be taken into account. From these modified crack increments and their corresponding cyclic J-integral, the functional relationship of fatigue crack growth rate can be developed by using curve-fitting technique. Fatigue life is then calculated by integrating crack growth rate function from initial crack length to critical crack length. S-N curve that is used in fatigue design can also be established.

There are several advantages when compared to other numerical approaches.

1. The amount of crack growth during each load cycle does not depend on the element size arranged along crack growth direction.
2. Fatigue crack growth rate can be established directly by fitting those numerically obtained crack increments and cyclic J-integrals.
3. Fatigue life prediction does not depend on parameters that have to be obtained from fatigue tests.
4. Unstable crack growth can be determined and critical crack length can be calculated.

Three fatigue problems with different material properties are analyzed by using the proposed numerical algorithm. For steel material, the fatigue analysis directly use J_curve constructed from analytical formulation of J-integral and R_curve obtained from experiment to determine crack increments. For other two problems where analytical J-integral formulation and experimental R_curve are not available, a numerical procedure is introduced to establish these curves. These numerical results are compared with available experimental results, which show very good agreement and consistence as indicated in these examples.

This numerical algorithm works very well with simple loading problems such as bending beam specimen and compact specimen. For complex loading, the procedure to establish J_curve and R_curve has to be modified to satisfy different boundary conditions. Each fatigue analysis requires as many as 10–20 specimens with different initial crack lengths to obtained load displacement curves. Majority part of the computation time is spent on this step. Further investigation of elastic-plastic analysis algorithm to increase convergence speed and

reduce computing time is recommended. Mesh size around the crack region should be identical among all these specimens with different crack lengths.

CHAPTER V

NUMERICAL ALGORITHM FOR STATIC SHAKEDOWN ANALYSIS

5.1 INTRODUCTION

The response of an elastic-plastic system under randomly repeated loading programs may be very complicated. Extensive investigations have indicated that three basic response patterns can be distinguished:

Shakedown: If plastic deformations stabilized within early finite number of cycles, residual stress field, corresponding to the plastic strains, may develop such that the response to any further cycling is in a purely elastic manner, as if the system accommodates itself to the loading program.

Alternating plasticity: If the plastic strain increment changes alternatively in sign in every cycle under repeated loading, they tend to cancel each other out. As a result, the total deformation is contained within the yield zone at a certain point in the system. With load cycle continuing, material in the yield zone begins to cracking, which eventually leads to low cycle fatigue failure.

Incremental collapse: If the plastic strain incremental in each load cycle is of the same sign, the total plastic strain will accumulate with each cycle so that progressive deformation will develop and result in failure of the global system.

Shakedown theory has great importance in the design of an elastic-plastic system in civil and mechanical engineering. The shakedown concept was introduced by Grüning [29] in 1926. The two fundamental theorems for the shakedown of an elastic-perfectly plastic continuum were developed by Melan [31,118] based on Bleich's work [30], and Koiter [32]. They are known as the static and the kinematic shakedown theorems, respectively. The classical shakedown theorems are also extended to include thermo-loading, dynamic loading, geometrically nonlinear effects, and creep and viscous effects. A comprehensive review can be found in [37]. Applications of the shakedown theorems have been found in many areas such as nuclear reactor parts, pressure vessel and piping, offshore platforms, geotechnical foundation, and layered pavement systems.

Analytical evaluation of shakedown load is complicated and can be performed only for discrete or simple continuous systems [153,154,47]. A matrix theory, based on finite element discretization and which, in principle, permits the evaluation of the shakedown load for a general continuum, was proposed by Maier

[47,155]. The first numerical calculation of the shakedown load of continuum was conducted by Belytschko [48]. He formulated the static shakedown theorem as a nonlinear mathematical programming problem and implemented it by means of an equilibrated finite element model. He applied the method to find shakedown load of a square plate with a circular hole subjected to a biaxial repeated loading program under plane stress condition. Corradi et al. [49] studied the same problem by means of a dual linear programming approach, which reduces the number of constraints in Maier's approach to Melan's theorem and bypasses the computation difficulty in nonlinear programming. Their approach is mainly based on expressing the yield condition by means of the coordinates of the vertices of the yield polyhedron and is implemented by using a compatible finite element model. Hung et al. [50] presented a finite element nonlinear programming formulation for the shakedown analysis, based on the static theorem and the 'yield criterion of the mean.' This approach reduces the number of discrete nonlinear yield constraints in Belytschko's formulation by averaging the yield function over each element. For a fine mesh, the error in this procedure becomes very small as it was successfully used in limit analysis by Hung [156]. A finite element program based on the kinematic formulation and linearization of Von Mises yield criterion was developed by Aboustit et al. [53] in their investigation of limit load of a uniformly loaded strip footing underlined by a shallow stratum of undrained clay. A plane strain shakedown analysis of a footing, underlined by dry soil and subjected to variable repeated loading was also carried out in their study. The same algorithm then was extended to include dynamic effects on shakedown load by Halder et al. [157] and Mohr-Coulomb type yield surface was linearized and used in the analysis. The shakedown load of a fluid-saturated foundation soil was calculated for different cases. The analysis results show that dynamic loading and gravity loading have significant influence on the shakedown load. A finite element program based on compatible finite element formulation coupled with nonlinear mathematical programming was developed by Raad et al. [56] for the shakedown analysis of a layered pavement system. In their approach, Mohr-Coulomb yield condition as inequality constraint was directly included in mathematical programming and the equilibrium and boundary conditions are accounted for as nodal forces in a weak sense. The nonlinear programming problem is solved by means of the Hooke and Jeeves [59] pattern search algorithm. Shakedown load was calculated for a layered pavement system with different thicknesses and material properties. The same program was used by Boubibane et al. [158] in shakedown analysis of pavement system with consideration for the anisotropic property of the materials.

The major difference among various computational methods in shakedown analysis is the way to handle the inequality constraint, i.e. yield condition. The linear programming approach proposed by Maier [47] using piecewisely linearized yield function (linear inequality constraints) to approximate nonlinear inequality constraints can be implemented by means of standard and fairly reliable linear programming

routines. The large number of linear inequality constraints required to approximate the nonlinear inequality constraint was reduced by Corradi et al. [49] using a dual linear programming approach. However, the yield condition can only be approximately satisfied at every checkpoint in this approach. On the other hand, in the nonlinear programming approach that directly uses yield function as constraint in the optimization process, the yield condition can be exactly satisfied at every checkpoint and only a single constraint is imposed at every checkpoint. But nonlinear optimization techniques are often difficult to implement. In Belytschko's approach [48], the constructed pseudo-objective function does not include equality constraints for residual stresses. The equilibrium condition of residual stresses is assumed to be satisfied by using proper stress function. In Raad's approach [56], the equality constraints for residual stresses are included in pseudo-objective function, but inequality constraints for yield conditions are excluded. The yield condition is separately computed and satisfied at every check point during Hooke and Jeeves [59] pattern search process. By doing so, it implicitly uses the penalty function method [159], but with penalty factor for the inequality constraints being equal to zero. In principle, all conditions and constraints of the problem are satisfied in this algorithm. However, because no stress state information within or on the yield surface is included in pseudo-objective function, the search direction in the optimization process may not be adjusted according to yield state.

In this study, a modified nonlinear programming algorithm is proposed based on Belytschko's [48] approach and Raad's [56] approach. The proposed numerical algorithm is based on compatible finite element method coupled with nonlinear programming technique. The pseudo-objective function includes both the inequality and equality constraints with each term normalized by corresponding yield stress and reference load, respectively, which makes them scalars and consistent with the original objective function, a load parameter. The penalty factors for these two terms are set to unit. Multidirectional search algorithm [160,161] is adopted in this approach as an optimizer to promote the efficiency in the optimization process. A finite element program is developed based on the proposed approach. Shakedown analyses were conducted for several examples using this approach and compared with available theoretical and numerical results. The comparisons show very good agreement.

5.2 STATIC SHAKEDOWN THEOREM

Considering a three dimensional elastic-perfectly plastic body, B , occupying the volume, V , and bounded by the surface, S . Any particle within the body is defined by Cartesian coordinates $\mathbf{x}=[x_1, x_2, x_3]$ and its displacement referred to the coordinate is defined by $\mathbf{u}=[u_1, u_2, u_3]$. Body force is denoted by X_i in V .

Surface traction p_i is applied on S_F and surface displacement u^o is prescribed on S_u . Here, $S = S_F + S_u$. The deformation of the body is assumed quasi-static under external load application.

The static shakedown theorem can be stated as follows. If there exists a time-independent residual stress field, $\bar{\rho}_{ij}$ and elastic stress field, $\sigma_{ij}^E(\mathbf{x}, t)$ corresponding to the load path β_s such that

$$\begin{aligned} \bar{\rho}_{ij,j} &= 0 \quad \text{in } V, \quad \bar{\rho}_{ij}n_j = 0 \quad \text{on } S_F \\ \dot{\bar{\rho}}_{ij} &= 0 \quad \text{for } t \geq 0 \quad \int_V E_{ijkl}^{-1} \bar{\rho}_{ij} \bar{\rho}_{kl} dV < \infty \\ \max_{\mathbf{x} \in V} \max_{\beta_s \in \Omega} f[\mu \sigma_{ij}^E(\mathbf{x}, t) + \bar{\rho}_{ij}(\mathbf{x})] &= 0 \end{aligned} \quad (5.1)$$

then the structure will shakedown over any load path $\beta_s(t)$ contained within a given load domain Ω , where $\bar{\rho}_{ij,j}$ denotes partial differentiation of residual stress components, $\bar{\rho}_{ij}$ with respect to the coordinates x_j , $\dot{\bar{\rho}}_{ij}$ is residual stress rate. E_{ijkl}^{-1} is the fourth-order tensor of elastic moduli, n_j is the unit outward normal vector to the surface S , and μ is a real number and greater than 1.

This fundamental static shakedown theorem provides a lower-bound bounding value for considered elastic-plastic continuum under prescribed random load within domain Ω . To evaluate the lower bound load parameter corresponding to a time-independent residual stress field, $\bar{\rho}_{ij}$, which satisfies the equilibrium equation, boundary condition and yield condition, the static shakedown theorem may be transformed into the following nonlinear mathematical programming problem:

$$\begin{aligned} \text{Max: } & \mu \\ \text{s. t. } & f[\mu \sigma_{ij}^E(\mathbf{x}, t) + \bar{\rho}_{ij}(\mathbf{x})] \leq 0 \quad \forall \mathbf{x} \in V \\ & \bar{\rho}_{ij,j}(\mathbf{x}) = 0 \quad \forall \mathbf{x} \in V \\ & \bar{\rho}_{ij}n_j = 0 \quad \forall \mathbf{x} \in S_F \end{aligned} \quad (5.2a)$$

here μ is defined as load parameter.

By application of the virtual work equation, $\int_V \sigma_{ij} \epsilon_{ij} dV = \int_V X_i u_i dV + \int_{S_F} p_i u_i dS$, the two equality constraints in Eq. (5.2a) can be compressed into a single weak form equation,

$$\int_V \bar{\rho}_{ij} \varepsilon_{ij} dV = 0 \quad (5.3)$$

where

$$\varepsilon_{ij} = \frac{1}{2}(u_{i,j} + u_{j,i}) \quad \text{with } u_i = 0 \text{ on } S_u$$

is an arbitrary virtual kinematically admissible strain field and σ_{ij} is stresses in equilibrium with the external load, X_i, p_i . The mathematical programming problem Eq. (5.2a) then can be rewritten as

$$\text{Max: } \mu \quad (5.2b)$$

$$\text{s. t. } f[\mu \sigma_{ij}^E(\mathbf{x}, t) + \bar{\rho}_{ij}(\mathbf{x})] \leq 0 \quad \forall \mathbf{x} \in V \quad (5.2c)$$

$$\int_V \bar{\rho}_{ij} \varepsilon_{ij} dV = 0 \quad \forall \mathbf{x} \in V \quad (5.2d)$$

5.3 FINITE ELEMENT FORMULATIONS

The continuum problem is usually discretized into a finite number of elements connected by nodes. The field variables can be evaluated by any standard numerical procedures. The determination of the shakedown load reduces to an optimization problem by coupling of the finite element method with suitable mathematical programming technique. For discretized systems, the elastic stresses $\sigma_{ij}^E(\mathbf{x}, t)$ at every integral point can be determined by finite element method as follows

$$[K]u = P^0 \quad (5.4a)$$

$$\sigma = DBu^e \quad (5.4b)$$

where $[K]$ - a $n \times n$ system stiffness matrix, n is the number of degree of freedom of the system.

u - $n \times 1$ system nodal displacement vector.

u^e - $3 \times NK \times 1$ nodal displacement vector of an element. NK is the number of nodes of N_{th} element.

P^0 - $n \times 1$ reference load vector.

σ - 6×1 stress vector at an integral point.

B - $6 \times 3 \times NK$ strain matrix.

D - 6×6 elastic modulus matrix.

The equilibrium equation of Eq. (5.2d) for the residual stresses can be transformed into nodal forces by integrating over every element within V . The displacement field $u_i(\mathbf{x})$ in an element is approximated by means of nodal displacements $(u_i^e)^k$ of the element and shape functions $N_k(\mathbf{x})$,

$$u_i(\mathbf{x}) = \sum_{k=1}^{NK} (u_i^e)^k N_k(\mathbf{x}) \quad (5.5)$$

where k denotes the k _th node of an element. The virtual strain field is calculated by

$$\varepsilon(\mathbf{x}, t) = \mathbf{B}(\mathbf{x})\mathbf{u}^e \quad (5.6)$$

The integral of Eq. (5.2d) is calculated over every element in V . For an element number l , the integral is numerically calculated by using Gauss-quadrature,

$$\mathbf{R}_l = \int_{V_e} \rho_{ij} \varepsilon_{ij} dV = \int_{V_e} \rho_{ij} \mathbf{B}(\mathbf{x}) \mathbf{u}^e dV = (\mathbf{u}^e)^T \sum_{i=1}^{NG} \mathbf{B}^T(\mathbf{x}^i) \boldsymbol{\rho}_i \omega_i \quad (5.7)$$

where $\mathbf{R}_l = [X_l^1, Y_l^1, Z_l^1, \dots, X_l^{NG}, Y_l^{NG}, Z_l^{NG}]^T$ a $NG \times 1$ force vector of element l . NG is the numbers of Gauss-integral point.

$\boldsymbol{\rho}_i = [\rho_{11}^i, \rho_{22}^i, \rho_{33}^i, \rho_{12}^i, \rho_{13}^i, \rho_{23}^i]^T$ a 6×1 residual stress vector at the i _th Gaussian point.

V_e is the element volume.

ω_i the weighting factor for the i _th Gaussian point.

The nodal forces at each element can be assembled into resultant nodal forces at each node, i , of the system

$$X_i = \sum_{k=1}^{NE} X_i^k \quad Y_i = \sum_{k=1}^{NE} Y_i^k \quad Z_i = \sum_{k=1}^{NE} Z_i^k \quad (5.8)$$

where NE is number of element around node i . X_i^k, Y_i^k, Z_i^k are nodal forces along x, y and z direction in system coordinate calculated from Eq.(5.4).

Now the mathematical programming problem for discretized system with NP nodes and M checkpoints can be formulated as follows,

Max: μ

$$\text{s. t. } f[\mu \sigma_{ij}^E(\mathbf{x}^k, t) + \bar{\rho}_{ij}(\mathbf{x}^k)] \leq 0 \quad k=1, \dots, M$$

$$X_i = \sum_{k=1}^{NE} X_i^k = 0 \quad Y_i = \sum_{k=1}^{NE} Y_i^k = 0 \quad Z_i = \sum_{k=1}^{NE} Z_i^k = 0 \quad i=1, \dots, NP \quad (5.9)$$

These formulations can be applied to axisymmetric and two-dimensional shakedown problems by reducing the index from 3 to 2 without losing generality.

5.4 MULTIDIMENSIONAL SEARCH ALGORITHM

The constrained optimization problem can be transformed into a sequential unconstrained minimization problem by constructing a pseudo-objective function by using penalty function method [159] i. e.,

$$T(\mu, \sigma_{ij}^*, \bar{\rho}_{ij}) = -\mu - \sigma_0^k / f(\sigma_{ij}^*, \bar{\rho}_{ij}) + \sum_i^{NP} [(X_i^2 + Y_i^2 + Z_i^2) / (P^0)^2] \quad (5.10)$$

where $f(\sigma_{ij}^*, \bar{\rho}_{ij}) = f(\sigma_{ij}^0 + \sigma_{ij}^s + \mu \sigma_{ij}^E + \bar{\rho}_{ij})$

- yield function. For pressure-dependent materials, Mohr-Coulomb yield function,

$$f = \sigma_1(1 + \sin \phi) - \sigma_3(1 - \sin \phi) - 2C \cos \phi = 0, \text{ may be used.}$$

For pressure-independent materials von Mises yield function may be used,

$$f = [(\sigma_x - \sigma_y)^2 + (\sigma_y - \sigma_z)^2 + (\sigma_z - \sigma_x)^2 + 6(\tau_{xy}^2 + \tau_{yz}^2 + \tau_{zx}^2)] / 6 = \tau_0^2 \quad \tau_0 = \sigma_0 / \sqrt{3}$$

σ_{ij}^0 - stresses in equilibrium with body force f^0 .

σ_{ij}^s - stresses in equilibrium with statically applied force f^s .

σ_{ij}^E - elastic stresses corresponding to the reference force P^0 .

σ_0^k - a yield stress for a given material, k is an integer its value dependent on yield function used in the analysis for Mohr-Coulomb yield function $k=1$ and for Von Mises yield function $k=2$.

Now the optimization problem becomes,

$$\text{Min } T(\mu, \sigma_{ij}^*, \bar{\rho}_{ij}) \quad (5.11)$$

It can be solved by any suitable unconstrained optimization algorithm.

The nonlinear optimization approach has been utilized in searching the shakedown load by several investigators, among which a sequential unconstrained minimization technique[48] and Hooke and Jeeves pattern search algorithm[59] are employed, respectively. However, these algorithms are either very difficult in computation aspect or rather time-consuming in search the optimum, especially in solving actual engineering problems. To enhance the efficiency in searching shakedown load using nonlinear optimization algorithm, the multidirectional search algorithm proposed in [160] is adopted in the current study. This algorithm will briefly reviewed in the following section. Detailed description and convergence analysis can be found in [161].

For a discretized system of the engineering problem, the determination of the shakedown load using a nonlinear optimization technique involves a large number of variables and is very time-consuming. For

instance, considering the two dimensional problem with EN elements, each element has four nodes. If we use 2×2 Gauss-quadrature to calculate stresses within an element, the total optimization variables will be $12*EN$. In the three-dimensional case, the number of variables is $48*EN$. In practical engineering problems, hundreds of elements are usually used in the finite element model. Therefore, the choice of an optimization algorithm is crucial both in using computation resources and in promoting the accuracy of the numerical results. The multidirectional search algorithm was presented by Toczon[161] and is rewritten below.

Given an initial simplex S_0 with vertices $\langle v_0^0, v_1^0, \dots, v_n^0 \rangle$, choose $\mu, \theta \in \mathbb{Q}$ such that

```

/* expansion factor */
 $\mu \in (1, +\infty)$ , and
/* contraction factor */
 $\theta \in (0, 1)$ .
for  $i=0, \dots, n$                                      /*** initialization loop ***/
    calculate  $f(v_i^k)$ 
end
 $k \leftarrow 0$ 
while (stopping criterion is not satisfied) do         /*** outer while loop ***/
    /* find a new best vertex */
     $j \leftarrow \arg \min_i \{ f(v_i^k) : i=0, \dots, n \}$ 
    swap  $v_j^k$  and  $v_0^k$ 
    repeat                                             /** inner repeat loop **/
        Check the stopping criterion.
        /* rotation step */
        for  $i=1, \dots, n$ 
             $r_i^k \leftarrow v_0^k - (v_i^k - v_0^k)$ 
            calculate  $f(r_i^k)$ 
        end
        replaced = ( $\min \{ f(v_i^k) : i=0, \dots, n \} < f(v_0^k)$ )
        if replaced then
            /* expansion step */
            for  $i=1, \dots, n$ 

```



```

     $e_i^k \leftarrow v_0^k - \mu(v_i^k - v_0^k)$ 
    calculate  $f(e_i^k)$ 
  end
  if (min {  $f(e_i^k) : i=0, \dots, n$  } < min {  $f(r_i^k) : i=0, \dots, n$  }) then
    /* accept expansion */
     $v_i^k \leftarrow e_i^k$  for  $i=1, \dots, n$ 
  else
    /* accept rotation */
     $v_i^k \leftarrow r_i^k$  for  $i=1, \dots, n$ 
  endif
else
  /* contraction */
  for  $i=1, \dots, n$ 
     $c_i^k \leftarrow v_0^k - \theta(v_i^k - v_0^k)$ 
    calculate  $f(c_i^k)$ 
  end
  replaced = (min {  $f(c_i^k) : i=0, \dots, n$  } <  $f(v_i^k)$ )
  /* accept contraction */
   $v_i^k \leftarrow c_i^k$  for  $i=1, \dots, n$ 
endif
until replaced /* end repeat loop */
k ← k+1
end /***** end while loop *****/

```

5.5 IMPLEMENTATION OF THE NUMERICAL ALGORITHM

The multidirectional search algorithm provides a method to search for best vertex that leads to minimum object function. This algorithm as a optimizer is incorporated into a finite element program to determine the shakedown load in the current study. The program is developed based on the following procedure:

A . Determining initial simplex S_0 with vertices $\langle v_0^0, v_1^0, \dots, v_n^0 \rangle$,

The initial simplex S_0 should contain a vertex close to the solution. To form the initial simplex S_0 , the following steps are followed.

Find minimum load factor among those related to each integral point for a reference load P^0 using yield function i. e.,

$$\begin{aligned} f_k[\mu\sigma_{ij}^E(x_k, t)] &= 0 \\ \mu_0 &\leftarrow \min\{\mu_k : k = 1, N\} \\ k_0 &\leftarrow \arg \min_i\{\mu_i : i = 1, N\} \end{aligned} \quad (5.12)$$

k_0 is the first point to yield under load $\mu_0 P^0$. Then the elastic stress field is shifted to this point that is on the yield surface. The initial residual stress field is constructed such that its superposition with the elastic stress field will make the yield function to be the minimum value at point k_0 , while keep the stress state at other points within yield surface. Using the initial residual stress superposed with one small disturbance at only one component direction of stress forms each vertex. The initial simplex is then constructed by all these vertices i. e. $\langle v_0^0, v_1^0, \dots, v_n^0 \rangle$.

B. Search for the desired minimum object function related to μ_0

The multidirectional search algorithm is used in this step to find a direction along which the minimum objective function corresponding to μ_0 is expected. The search is then shifted to this new direction. The search will be continued until the objective function satisfies a given convergence criterion. There are three possible trial steps in the algorithm. They are rotation, expansion, and contraction. Each step is defined as following

Rotation step $r \leftarrow v_0 - (v - v_0) \quad i=1, \dots, n$

Expansion step $r \leftarrow v_0 - \mu(v - v_0) \quad \mu \in (1, +\infty) \quad (5.13)$

Contraction step $r \leftarrow v_0 + \theta(v - v_0) \quad \theta \in (0, 1)$.

The choice of μ and θ is usually dependent on the requirement of convergence speed. In this algorithm, the rotation step is always computed to test for the next best vertex. If a new best vertex has been identified, an expansion step along the same direction is computed. If the expansion step is successful, i.e. the objective function is smaller than that computed from rotation step, the simplex is updated. Otherwise, the simplex is

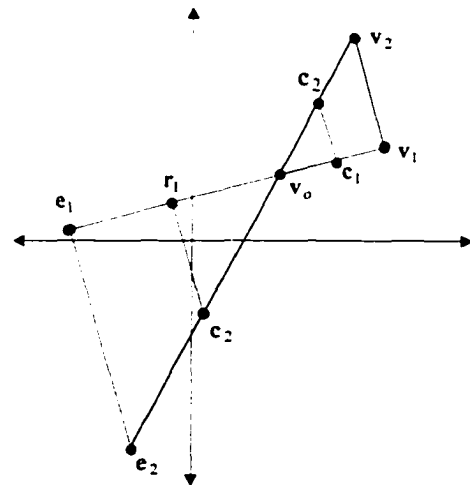


Figure 5.1: The Three Possible Steps Given the Simplex S with Vertices $\langle v_0, v_1, v_2 \rangle$.

updated at rotation step. If the rotation step is not successful, the contraction step is computed and automatically accepted. The three steps can be visualized as in Fig. 5.1.

The convergence criterion for this search algorithm is defined as

$$|T(\mu, \sigma_{ij}^*, \bar{\rho}_{ij})| < \varepsilon' \quad (5.14a)$$

where ε' is a small positive real number. From the analysis of pseudo-objective function of Eq. (5.10), we can see that the minimum value of the second term cannot be less than 1 and the third term will approach zero after a certain number of iterations. Still, within each load step, μ is a constant value during the search iteration. Therefore, the convergence criterion of Eq. (5.10) can be alternatively rewritten in the following form

$$|T(\mu, \sigma_{ij}^*, \bar{\rho}_{ij}) + \mu| < \varepsilon'' \quad (5.14b)$$

where $\varepsilon'' = 1 + \varepsilon_0$, ε_0 is a small positive real number and has to be predefined for a given problem.

For a layered pavement system, sand is usually used as subgrade material, which has a high internal friction angle (ϕ) with zero cohesion (C). In this case, the yield strength of the material

$$f_t = \frac{2C \cos \phi}{1 + \sin \phi} \quad \text{or} \quad f_c = \frac{2C \cos \phi}{1 - \sin \phi}$$

goes to zero. The pseudo-objective function reduces to the following form:

$$T(\mu, \sigma_{ij}^*, \bar{\rho}_{ij}) = -\mu + \sum_1^{NP} [X_1^2 + Y_1^2 + Z_1^2] / (P^0)^2 \quad (5.14c)$$

which is identical with the one used in Raad's optimization algorithm[56].

If the equilibrated finite element model is used in the analysis and assumed that equilibrium condition is satisfied throughout the iteration step, the third term in Eq. (5.10) is equal to zero. Then, the pseudo-objective function is reduced to

$$T(\mu, \sigma_{ij}^*, \bar{\rho}_{ij}) = -\mu - \sigma_o^k / f(\sigma_{ij}^*, \bar{\rho}_{ij}) \quad (5.14d)$$

which is identical with the one used in Belytschko's formulation[48].

Therefore, Eq. (5.10) represents a general form of pseudo-objective function used in optimization algorithm in lower bound shakedown analysis.

In case Eq. (5.14b) is difficult to be satisfied, an alternative convergence condition is used

$$|T(\mu_k, \sigma_{ij}^k, \bar{\rho}_{ij}^k) - T(\mu_{k-1}, \sigma_{ij}^k, \bar{\rho}_{ij}^{k-1})| \leq \varepsilon' \quad (5.15)$$

C. Update load factor based on current $\bar{\rho}_{ij}$

Based on the updated simplex S_0 obtained from the last step, the vertex (i.e. the residual stress vector in this case) along which objective function reaches minimum value can be extracted. From this residual stress field, the shakedown load factor can be updated by solving the yield function for μ_k at each integral point, i. e.

$$f_k [\mu_k \sigma_{ij}^E(x_k, t), \bar{\rho}_{ij}(x_k)] = 0 \quad k=1, \dots, N$$

The new load factor can be obtained by

$$\mu_n \leftarrow \min \{\mu_k : k = 1, \dots, N\}$$

If the new load factor, μ_n , is greater than the previous one, μ_{n-1} , the simplex is then updated. The updated simplex is also checked to satisfy the requirement that the residual stress field itself has to satisfy the yield condition at reference load $P^0 = 0$. i. e.

$$f_k [\bar{\rho}_{ij}(x_k)] = 0 \quad k=1, \dots, N$$

In case this condition is not satisfied, a modification is made to this simplex. Once the yield condition is satisfied at every point, a new initial simplex is formed based on this modified simplex. Another round of multidirectional search will begin. A new best vertex will be search based on the updated shakedown load factor μ_n . Step B and C will be repeated until the condition

$$|\mu_{i+1} - \mu_i| \leq \varepsilon$$

is satisfied, where ε is a predefined positive real number, in this case it takes 0.0001.

D. Check $\bar{\rho}_{ij}(x)$ to satisfy $f(\bar{\rho}_{ij}(x)) \leq 0$

The final residual stress field obtained from the previous step is checked at each integral point by means of yield function. If the yield function condition is satisfied at every point, the μ_{i+1} is taken as the shakedown load factor. Otherwise, the residual stress field is modified such that,

$$f_k [\bar{\rho}_{ij}(x_k)] \leq 0 \quad k=1, \dots, N$$

is satisfied.

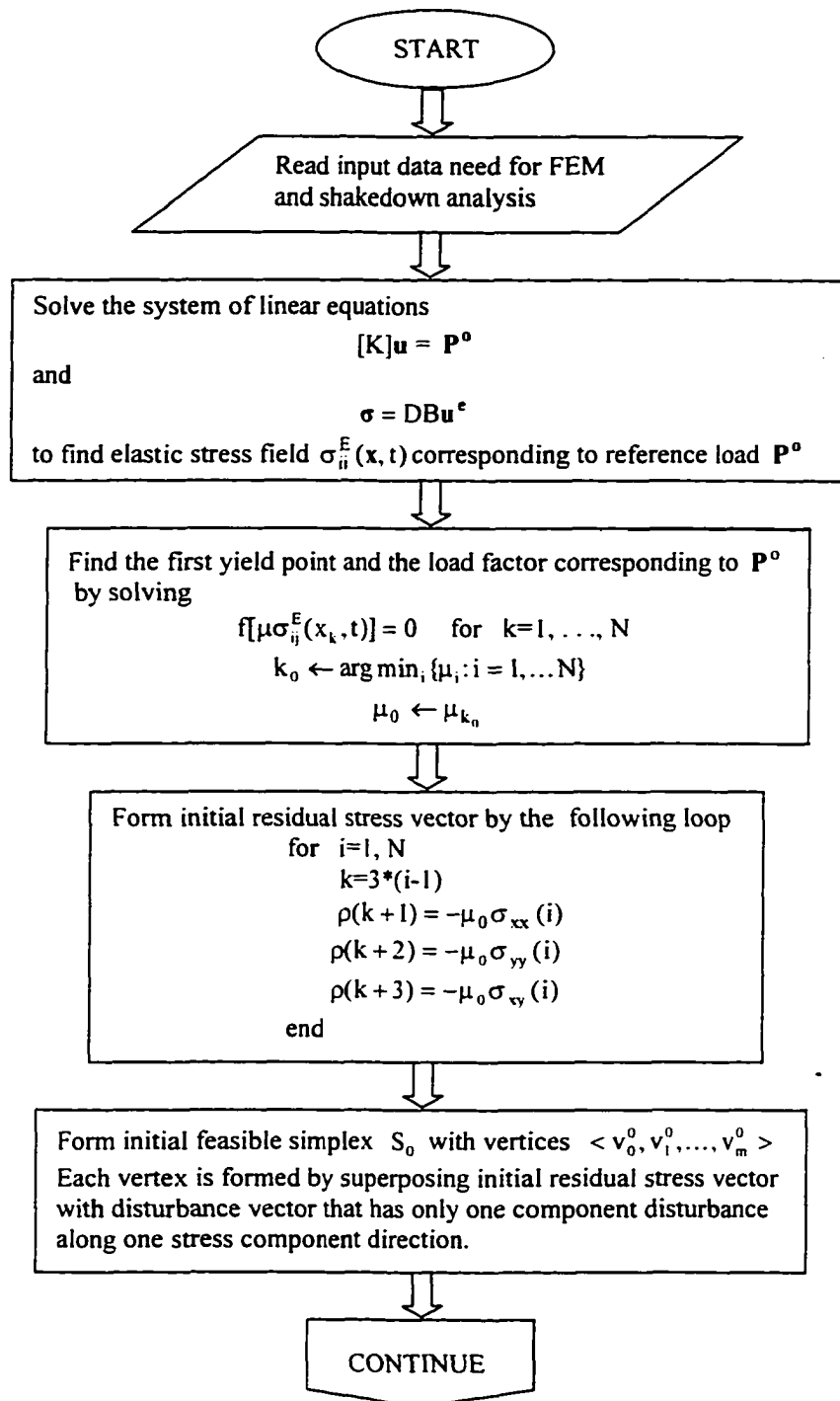
If the condition is satisfied, the shakedown load factor is calculated by solving

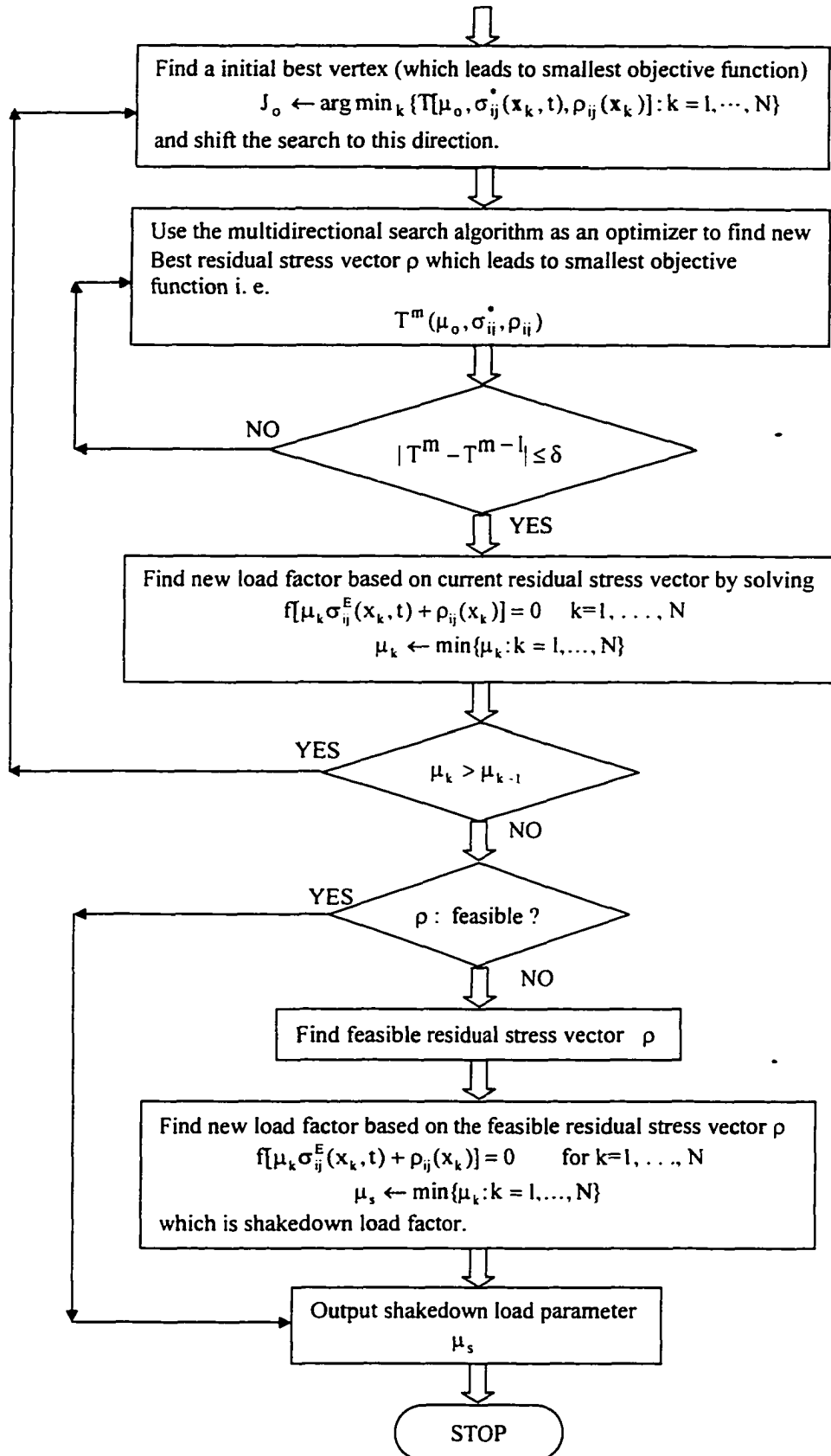
$$f_k [\mu_k \sigma_{ij}^E(x_k, t), \lambda \bar{\rho}_{ij}(x_k)] \leq 0$$

for μ_k and

$$\mu_{shkdn} \leftarrow \min \{\mu_k : i = 1, \dots, N\}$$

If the condition is not satisfied by the modified step, last step load factor, μ_i , will be taken as the shakedown load factor. The flow chart of the algorithm follows.





5.6 EXAMPLES

Based on the algorithm presented in foregoing sections, a finite element program coupled with a multidirectional search technique is developed for shakedown analysis of engineering problems. Several classical problems are considered in this section. The numerical results of shakedown analysis using the proposed algorithm are compared with available theoretical and numerical solutions. The comparisons show that current numerical results agree very well with other results. These results are also compared with upper bound results, which show considerable consistency.

5.6.1 EXAMPLE 1

The problem considered in this example is a fixed end beam with a roller supporter at the other end. The loaded beam is shown in Fig. 5.2. Its dimension and material properties have been described in Chapter Six. Four different finite element meshes as shown in Fig. 5.3 to 5.6 are used in the lower bound shakedown analysis. Same as in upper bound

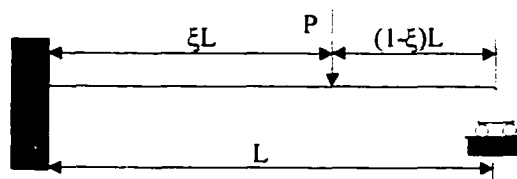


Figure 5.2: A Beam with One Fixed End and One Roller Supported End.

situation, the lower bound shakedown loads were calculated at three different locations along the beam (i. e. $L/3$, $L/2$, $2L/3$). The results are presented in Table 5.1. From these numerical results, we can see the influence of finite element mesh sizes and element side-size ratios on the shakedown load value. Fig. 5.7 shows the shakedown loads variations with the finite element number used in the mesh. This curve shows that coarse mesh gives a higher load value than the finer mesh does. As the mesh become finer, shakedown load is convergent to a constant value.

The theoretical formulations to calculate the shakedown load for the beam have been presented by König [120] and rewritten in Chapter Six. Using these formulations the shakedown loads are calculated at locations $L/3$, $L/2$, and $2L/3$ and given in Table 5.1 along with upper bound load values obtained in Chapter Six. The collapse load calculated from König's formulation [120] and computed by using step by step finite element analysis are also listed in Table 5.1.

Mesh size influence on both the upper bound (from Chapter Six) and lower bound shakedown load are given in Fig. 5.8 for load applied at $L/2$ along with the theoretical results. From this figure, we can see that shakedown load approaches constant value as the finite element mesh becomes finer. However, the numerical results of upper bound shakedown load is lower than theoretical value when element numbers of the mesh are larger than 36. These results may be caused by the following two factors. One is that the

SHAKEDOWN ANALYSIS (LOWER BOUND):

Load Applied at: L/3 L/2 2L/3
 Elastic Limit : 5.428 5.338 5.141
 Shakedown Load: 6.404 6.168 6.249

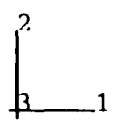
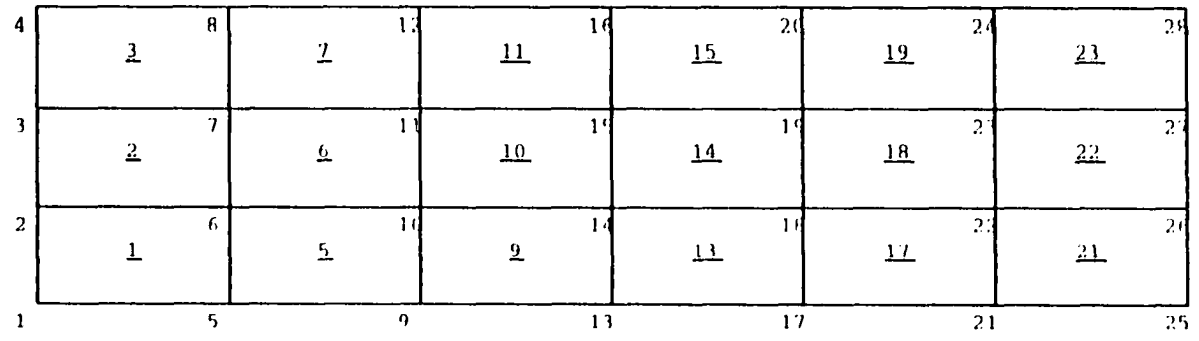


Figure 5.3: Finite Element Mesh for Fixed End Beam with 18 Elements and 20 Nodes.

SHAKEDOWN ANALYSIS (LOWER BOUND):

Load Applied at: 1/3 1/2 2L/3
 Elastic Limit : 4.372 4.368 4.181
 Shakedown Load: 6.140 5.399 5.310

4	8	11	14	18	21	24	27	30	33	36	39	42	45	48	51
	<u>3</u>	<u>7</u>	<u>11</u>	<u>15</u>	<u>19</u>	<u>23</u>	<u>27</u>	<u>31</u>	<u>35</u>	<u>39</u>	<u>43</u>	<u>47</u>			
3	7	11	14	18	21	24	27	30	33	36	39	42	45	48	51
	<u>2</u>	<u>6</u>	<u>10</u>	<u>14</u>	<u>18</u>	<u>22</u>	<u>26</u>	<u>30</u>	<u>34</u>	<u>38</u>	<u>42</u>	<u>46</u>			
2	6	10	14	18	21	24	27	30	33	36	39	42	45	48	51
	<u>1</u>	<u>5</u>	<u>9</u>	<u>13</u>	<u>17</u>	<u>21</u>	<u>25</u>	<u>29</u>	<u>33</u>	<u>37</u>	<u>41</u>	<u>45</u>			
1	5	9	13	17	21	25	29	33	37	41	45	49			

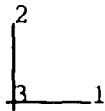


Figure 5.4: Finite Element Mesh for Fixed End Beam with 16 Elements and 52 Nodes.

SHAKEDOWN ANALYSIS (LOWER BOUND):

Load Applied at: 1/3 1/2 2L/3
 Elastic Limit : 3.897 3.955 4.233
 Shakedown Load: 5.615 5.351 5.088

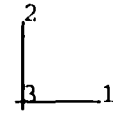
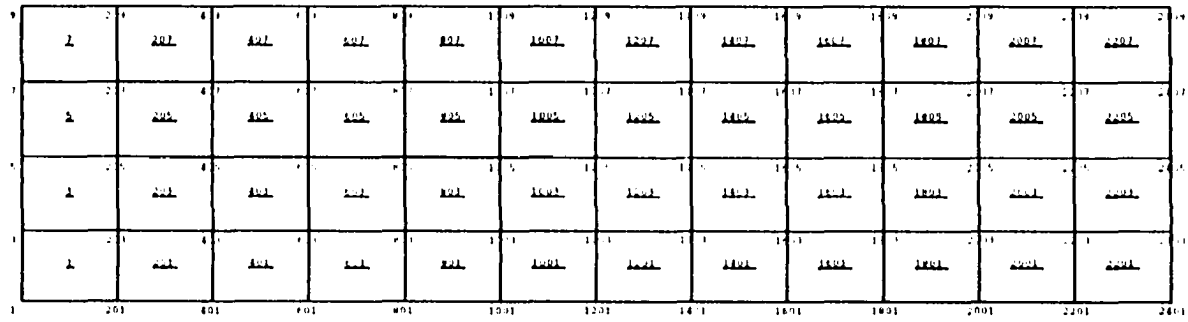


Figure 5.5: Finite Element Mesh for Fixed End Beam with 48 Elements and 65 Nodes

SHAKEDOWN ANALYSIS (LOWER BOUND) :

Load Applied at: 1/3 1/2 2L/3
 Elastic Limit : 3.383 3.469 3.340
 Shakedown Load: 5.522 4.933 4.796

9	1	207	407	607	807	1007	1207	1407	1607	1807	2007	2207	2407	2607	2807	3007
7	2	205	405	605	805	1005	1205	1405	1605	1805	2005	2205	2405	2605	2805	3005
5	1	201	401	601	801	1001	1201	1401	1601	1801	2001	2201	2401	2601	2801	3001
3	1	201	401	601	801	1001	1201	1401	1601	1801	2001	2201	2401	2601	2801	3001



Figure 5.6: Finite Element Mesh for Fixed End Beam with 64 Elements and 85 Nodes.

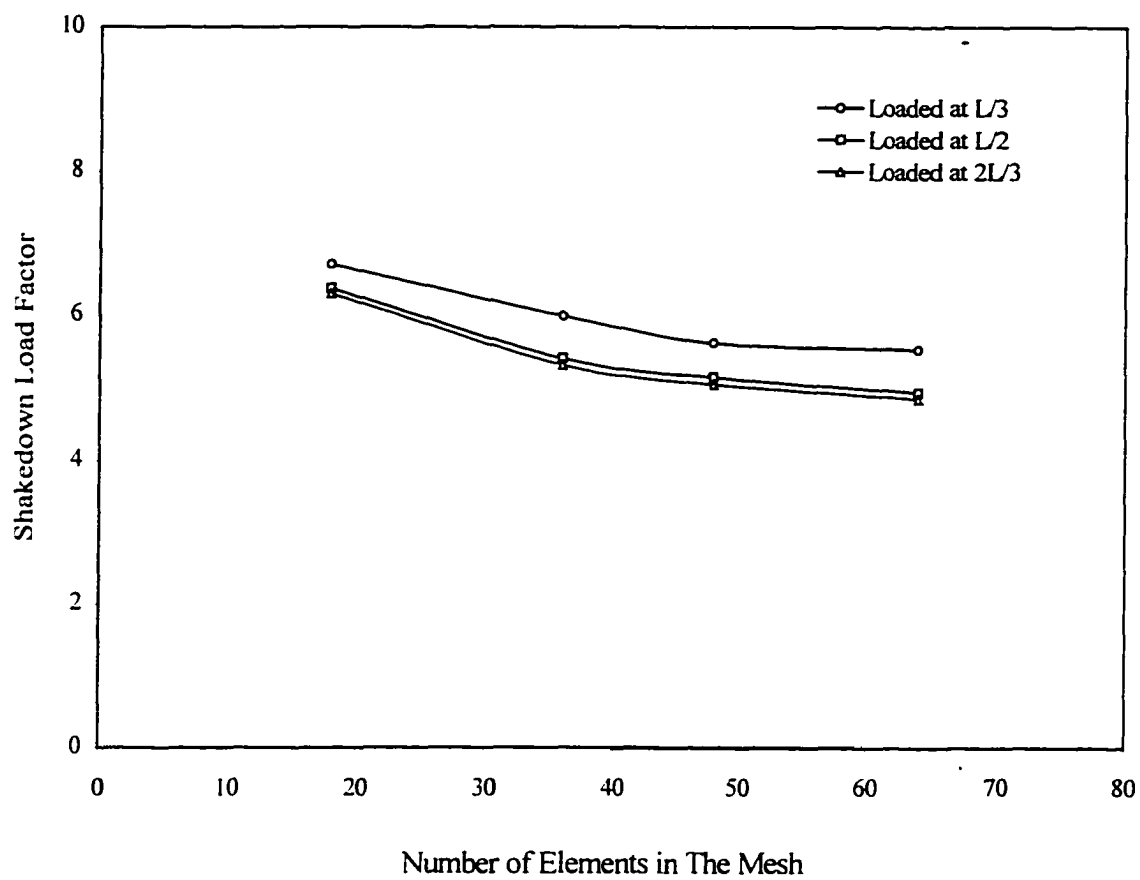


Figure 5.7 Finite Element Mesh Influence on Lower Bound Shakedown Load.

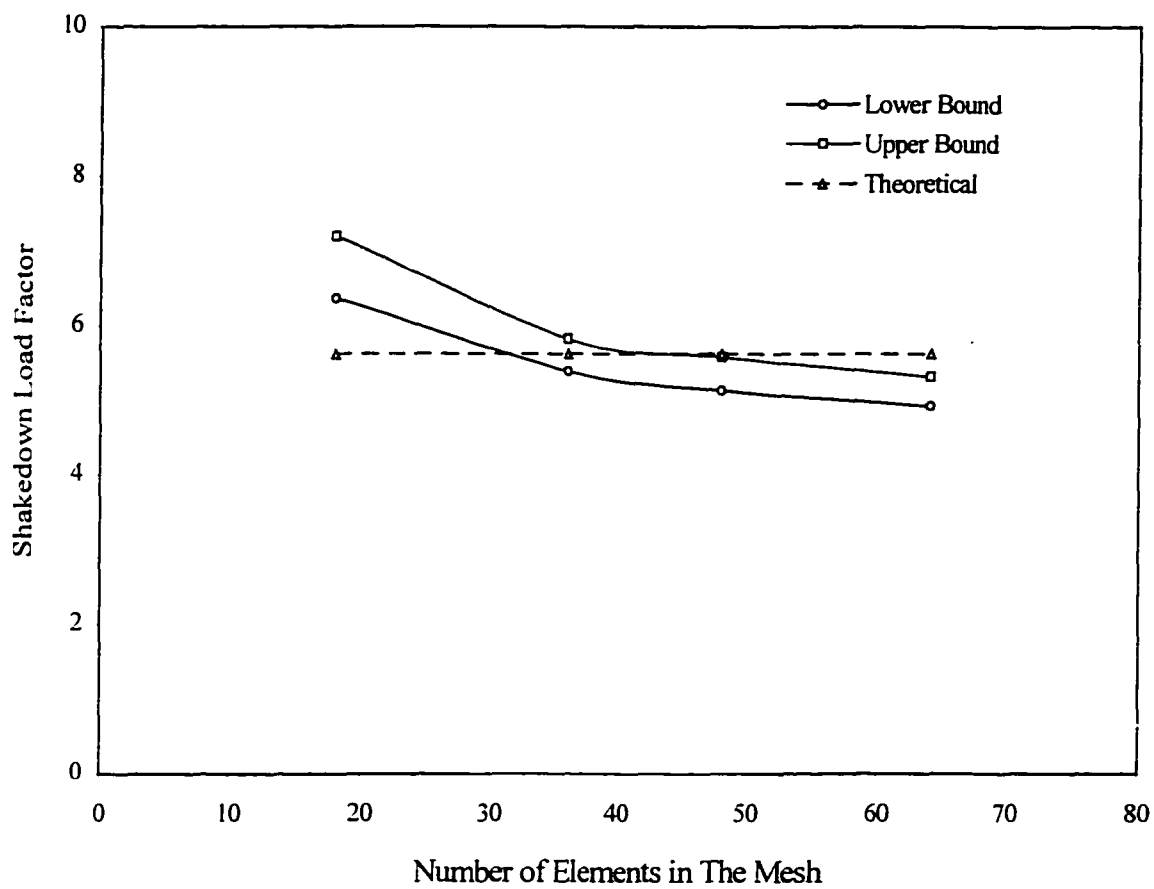


Figure 5.8: Finite Element Mesh Influence on Shakedown Load for Load Applied at $L/2$.

TABLE 5.1: SHAKEDOWN ANALYSIS FOR FIXED END BEAM

ELEMENT No.	LOAD APPLIED AT								
	L / 3			L / 2			2L / 3		
	Elastic Limit	Upper Bound	Lower Bound	Elastic Limit	Upper Bound	Lower Bound	Elastic Limit	Upper Bound	Lower Bound
	λ_{EL}	λ_{SH}	λ_{SH}	λ_{EL}	λ_{SH}	λ_{SH}	λ_{EL}	λ_{SH}	λ_{SH}
18	5.428	7.676	6.404	5.338	7.204	6.368	5.141	7.183	6.249
36	4.372	7.063	6.14	4.368	5.724	5.399	4.181	5.615	5.31
48	3.897	5.898	5.615	3.955	5.586	5.351	4.233	5.423	5.088
64	3.383	5.642	5.522	3.469	5.076	4.933	3.34	4.987	4.796
Theoretical									
Shakedown	3.375	6.75		3.333	5.625		3.62	5.625	
Collapse		7.031			5.625			5.625	
Step By Step Finite Element Analysis									
Collapse		7.129			6.145			6.039	

* Shakedown load is equal to load factor*P [here P = 100 lb.(444 N)]

performance of four-point isoparametric plane stress element is not very good in beam bending analysis. The second one may be the element locking effects.

5.6.2 EXAMPLE 2

The lower bound shakedown load of a thin square plate with a central circular hole subjected to biaxial loading at its edges is examined in this example by using the proposed numerical approach. The lower bound shakedown load for this classical problem has been computed by Belytschko [48] who used the equilibrated finite element method coupled with nonlinear programming technique. The upper bound load was given by Carradi et al. [49] by means of compatible finite element method in conjunction with linear programming technique. The upper bound solutions for the problem have been presented in Chapter Six by using proposed numerical algorithms for the upper bound shakedown analysis. For the same cases discussed in Chapter Six, the lower bound shakedown loads are calculated in this example.

Considering that loading and geometry are symmetric in both X and Y axial, only one quarter of the plate is used in the analysis. The plate is divided into 40 rectangular elements with 54 nodes as shown in Fig. 5.9. The numerical results of the lower bound shakedown load are illustrated in Fig. 5.10. Comparing this result with theoretical value of $0.47\sigma_0$ [155], it is 7% lower.

The mesh influence on the lower bound load value is also investigated in this example. Accordingly, a new different mesh is designed and shown in Fig. 5.11. For different mesh ratios, the lower bound shakedown loads are calculated and illustrated in Fig. 5.11. The variation of lower bound shakedown load factors with the mesh ratio as plotted in Fig. 5.12. From this plot, we can see that as the meshes become finer, the lower bound load is convergent to a constant value. The load factor varies with the finite element meshes both for lower bound and upper bound are plotted in Fig. 5.13 along with the analytical result.

5.6.3 EXAMPLE 3

Shakedown analyses of layered pavement systems for different cases were conducted by Raad et al [56]. In this example, shakedown behavior of two-layered pavement system is reexamined using the proposed numerical algorithm. The finite element model and the material properties used in the shakedown analysis are shown in Fig. 5.14 and Table 5.2, respectively. Two situations were studied in this example. In the first situation, the surface layer with 9-in. thickness overlies on a stiff subgrade. Two kind of materials were used for the surface layer (case 3A and 4A). The shakedown loads were calculated at different temperatures, which are represented by different elastic modulus as shown in Table 5.2. The numerical results are presented in Fig 5.15. From these results, we can see that the increase of elastic modulus does

not raises the shakedown load values, which indicates that the majority part of the traffic load is carried by surface layer. However, the results show that the shakedown load increases with the increase of tensile strength of the material, as shown in Fig. 5.15 (case 3A and 4A). In the second situation, the surface layer overlies on two different sub-grade materials (case 1B and 2B) and changes in thickness. The numerical results show that the shakedown loads increase with the increase of the thickness of the surface layer. The rate of the shakedown load increases with the thickness of surface layer is lower for soft sub-grade than that for stiff sub-grade as shown in Fig. 5.16. The numerical results in [56] are also shown in Fig. 5.15 and Fig. 5.16 as a comparison. From these figures, we can see that the results are rather consistent.

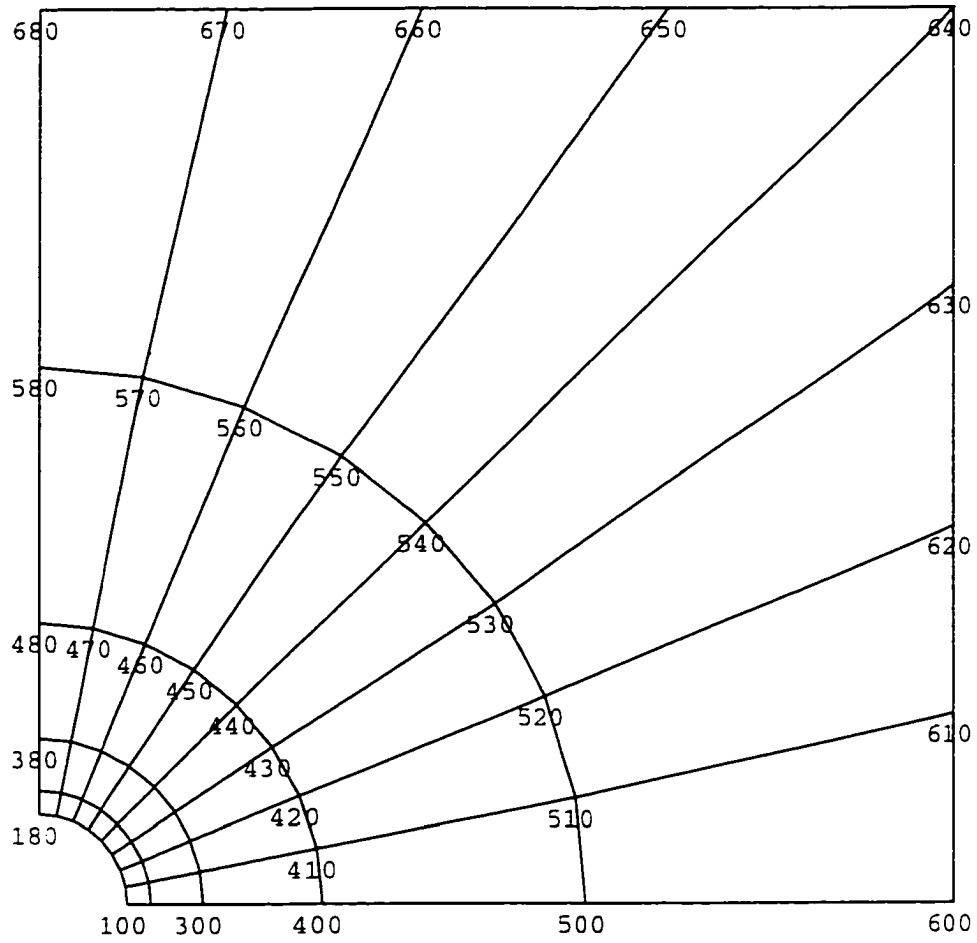


Figure 5.9: A Finite Element Mesh for a Thin Biaxial Tension Square Plate with a Central Hole(Only One Quarter is Shown).

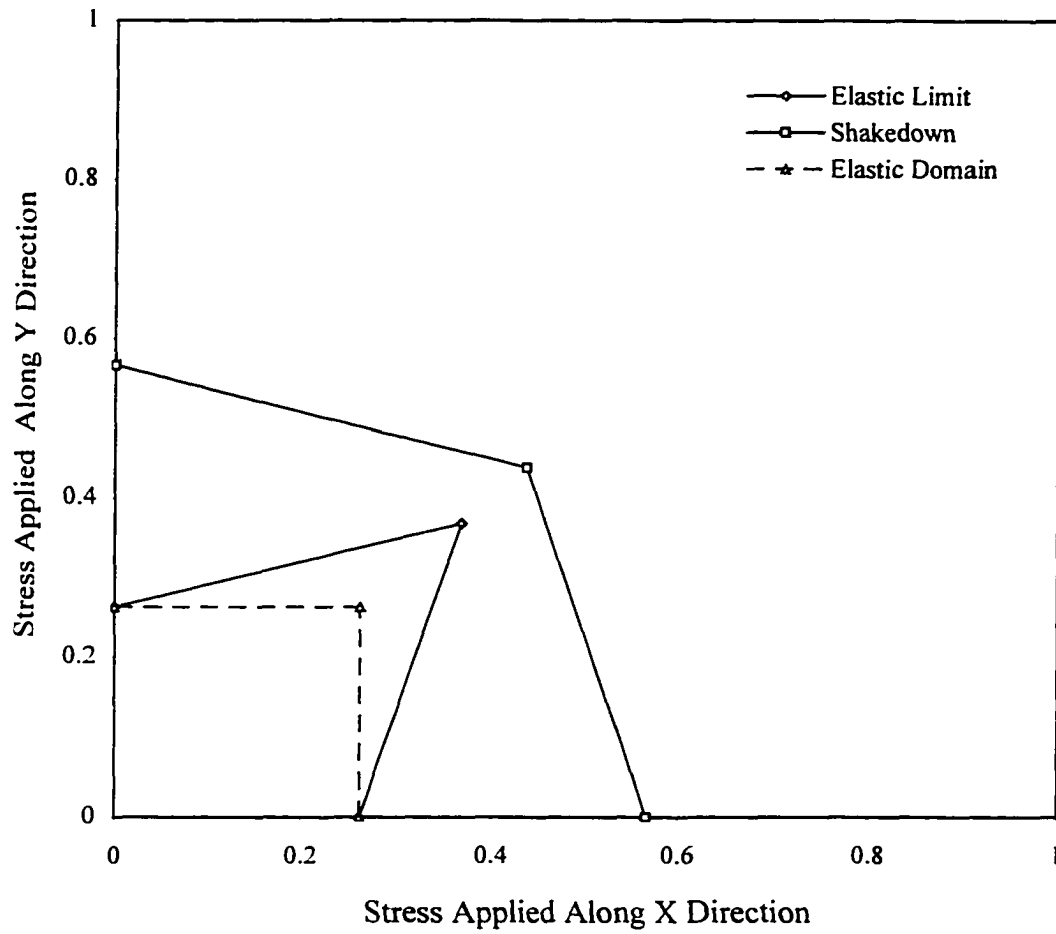


Figure 5.10: Lower Bound Shakedown Analysis Results of Thin Plate with Central Hole.
 (**The Value in the Plot is the Ratio of σ/σ_0).

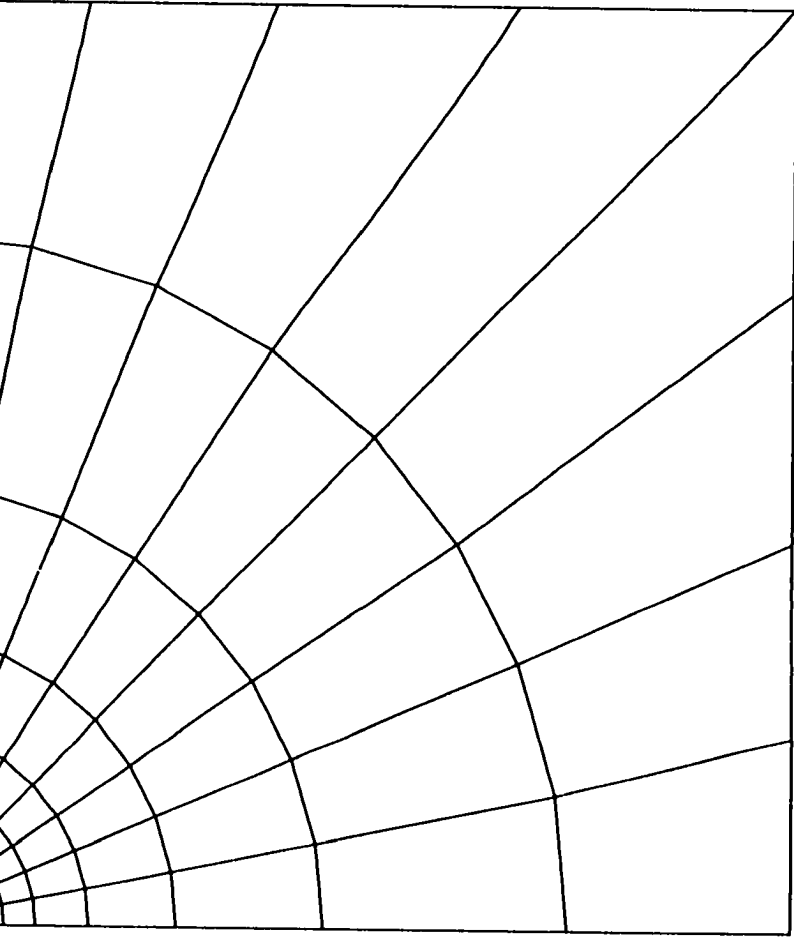
SHAKEDOWN ANALYSIS (LOWER) :

<u>Bias</u>	<u>Limit Load</u>	<u>Shakedown</u>
0.55	0.36	0.444
0.60	0.37	0.454
0.65	0.38	0.481
0.70	0.39	0.534
0.80	0.42	0.618

Figure 5.11:

Finite Element Mesh and Numerical Results of Mesh Influence Analysis
Bias = l_0 / l_1 . Shakedown Load in the Table is σ / σ_0 . σ_0 is initial yield stress.





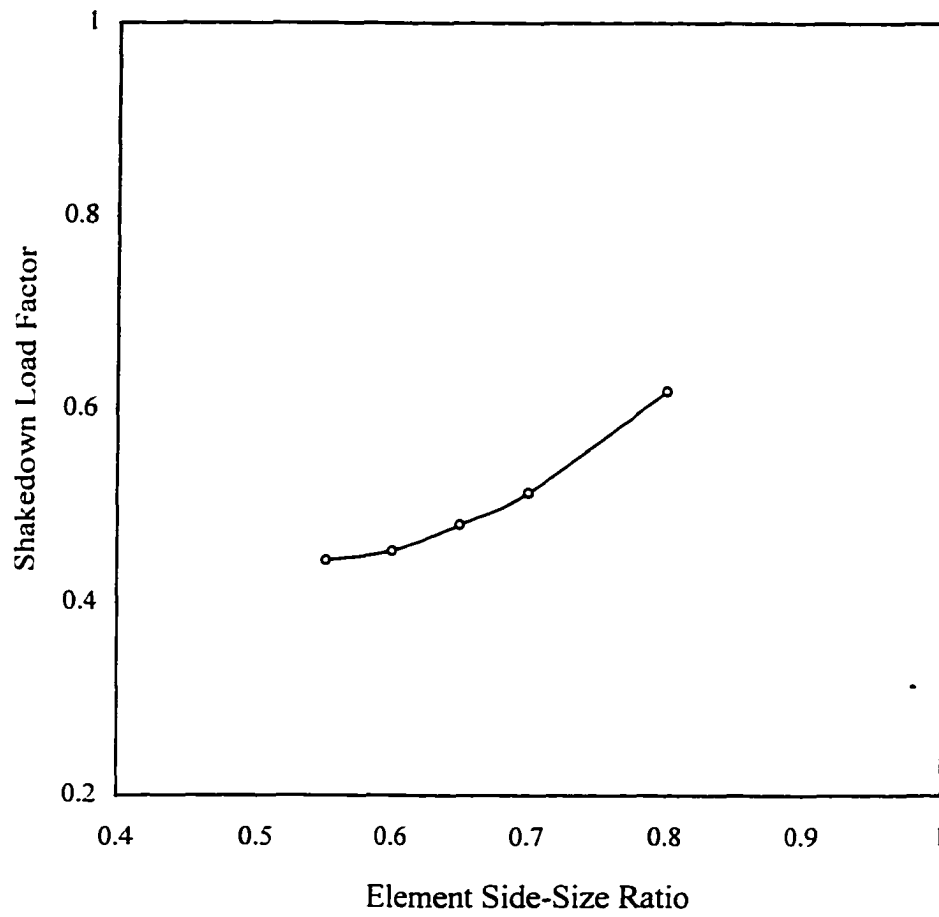


Figure 5.12: Finite Element Mesh Size Influence on Lower Shakedown Load for a Thin Plate with Circular Central Hole and is Subjected Biaxial Tension Stress.

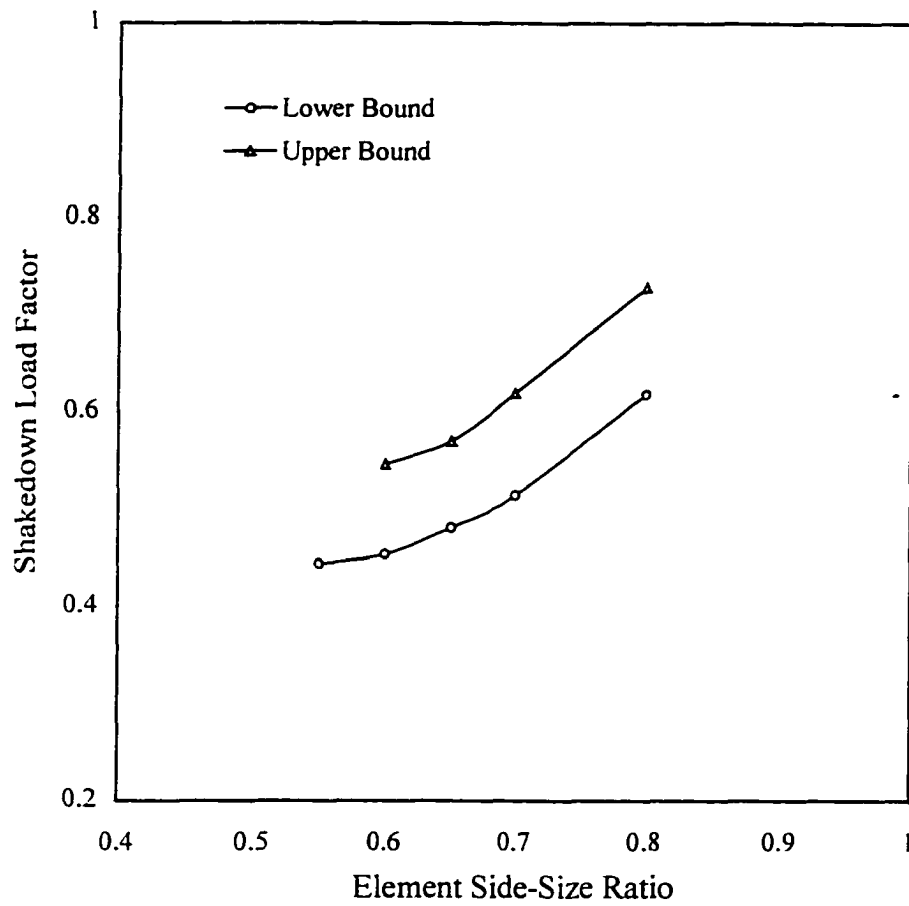


Figure 5.13: Finite Element Mesh Size Influence on Shakedown Load for a Thin Plate with Circular Central Hole and is Subjected to Biaxial Tension Stress.

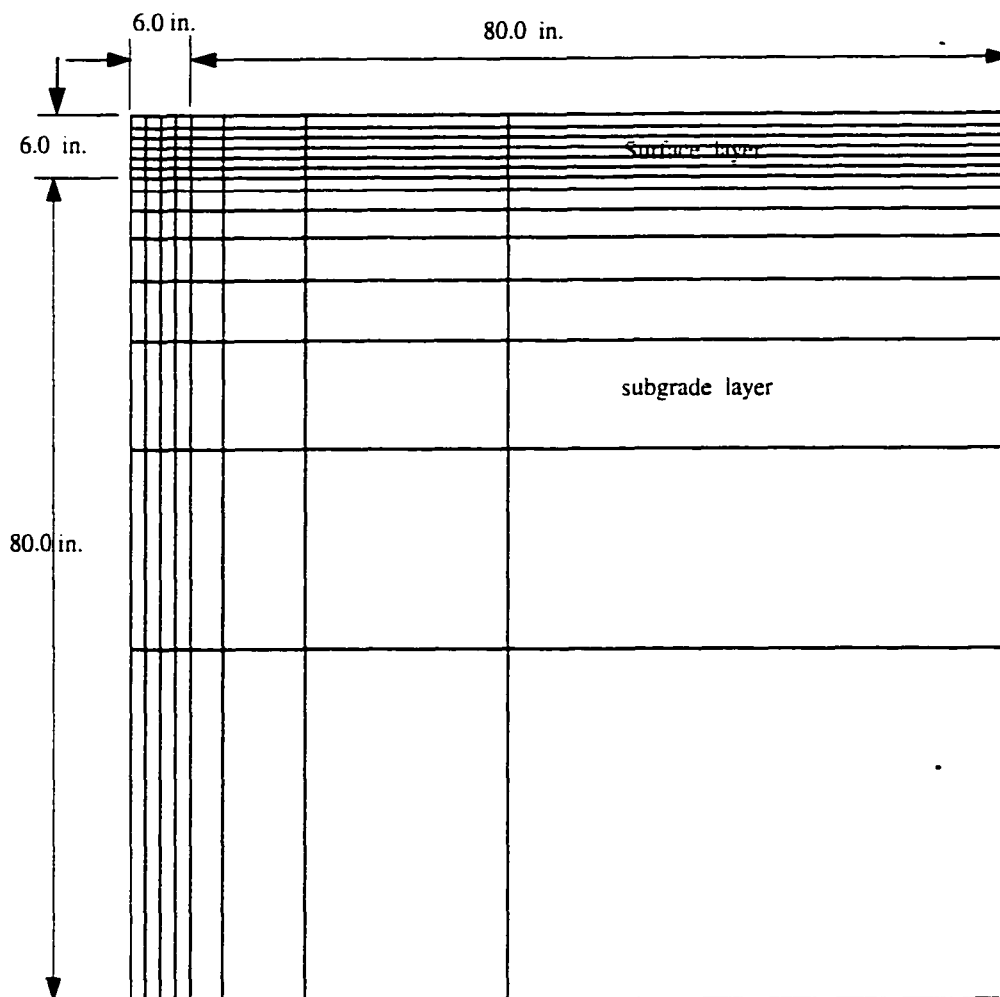


Figure 5.14: Finite Element Mesh for Two-Layer Pavement System in Shakedown Analysis (1 in. = 25.4 mm).

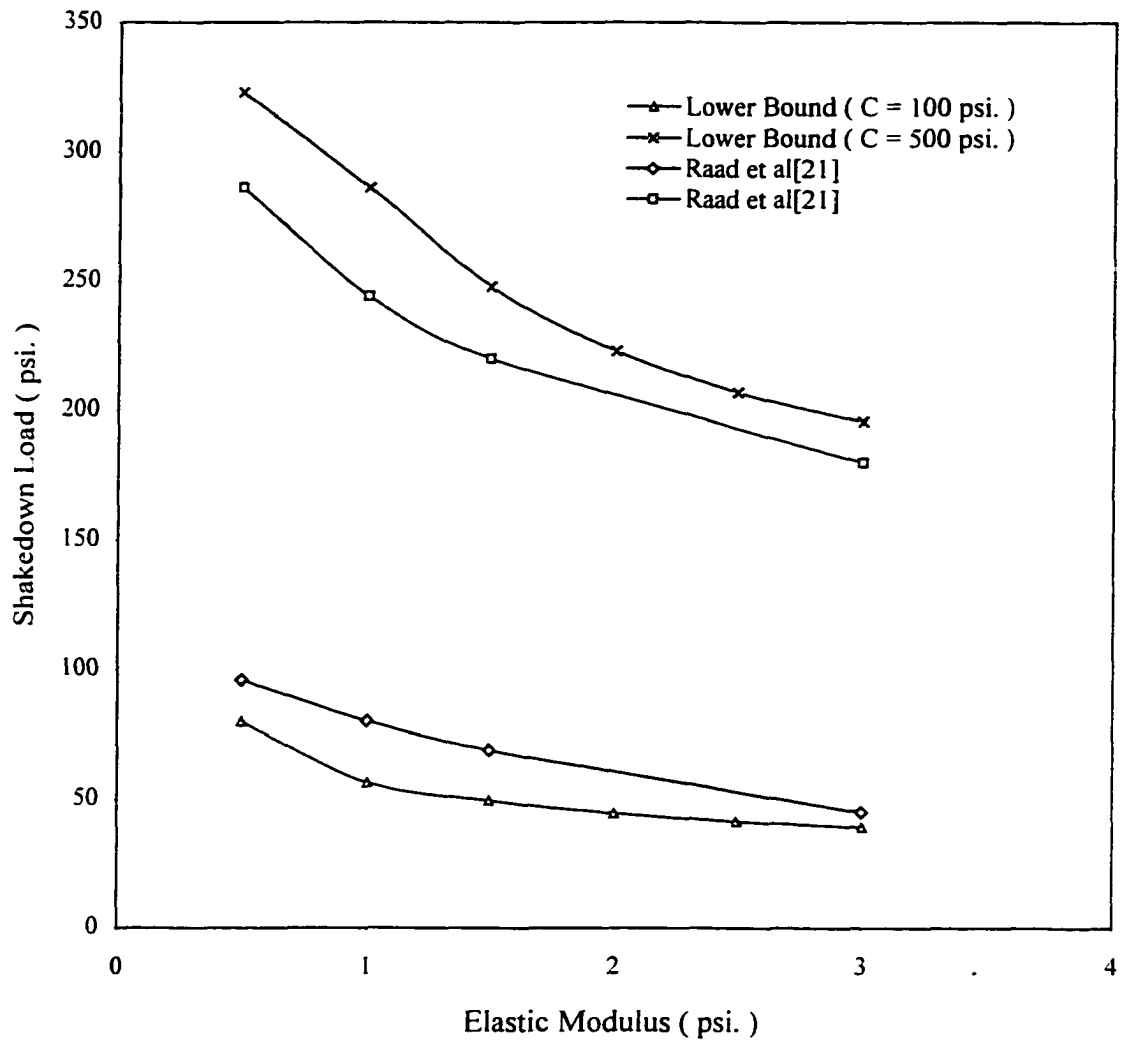


Figure 5.15: Variations of Shakedown Load with Elastic Modulus of Surface Layer with Different Cohesion (1 psi. = 6.895 kPa)

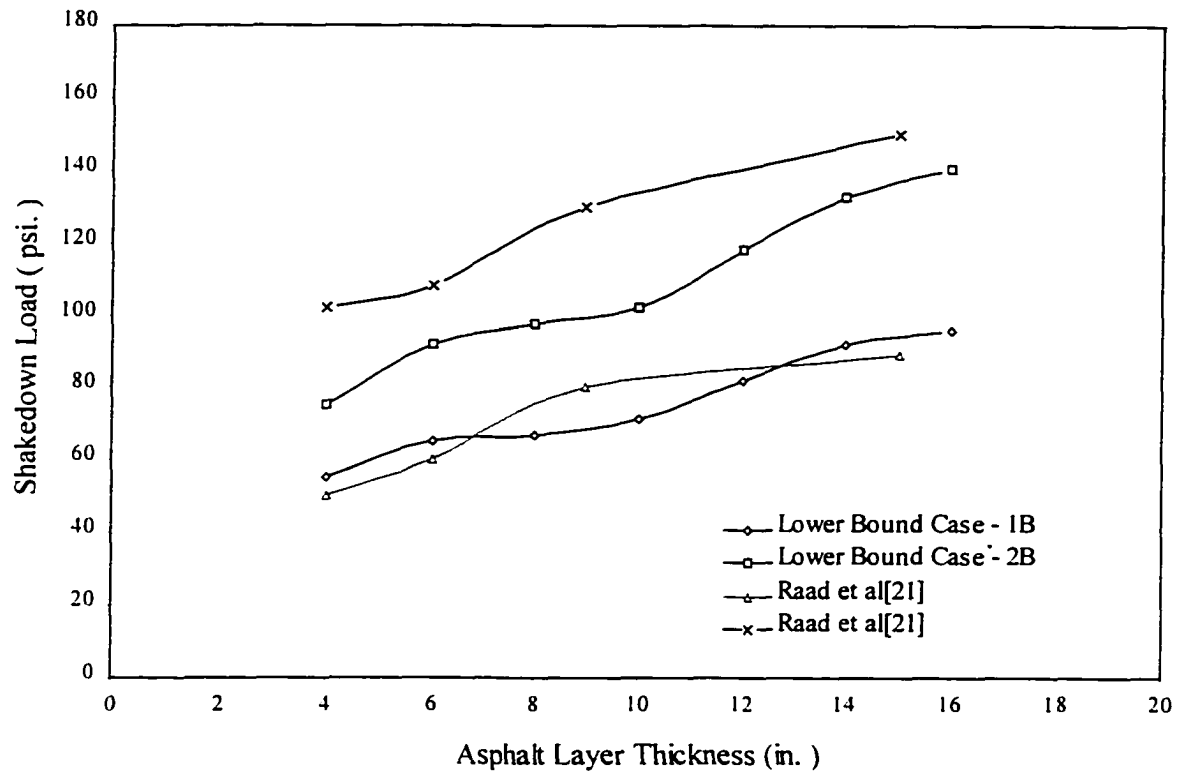


Figure 5.16: The Variations of Shakedown Load with Surface Layer Thickness for Stiff Subgrade(1 in. = 25.4 mm; 1 psi. =6.895 kPa).

Table 5.2: MATERIAL PROPERTIES USED IN TWO-LAYERED PAVEMENT SYSTEM SHAKEDOWN ANALYSIS

	Surface Layer					Subgrade Layer			
	E_1	H_1	v_1	C_1	ϕ_1	E_2	v_2	C_2	ϕ_2
	psi.	in.	-	psi.	degree	psi.	-	psi.	degree
Case 3A	$0.5 \cdot 10^6$								
	$1.0 \cdot 10^6$	9	0.25	100	35°	20000	0.47	20	0°
	$1.5 \cdot 10^6$								
	$3.0 \cdot 10^6$								
Case 4A	$0.5 \cdot 10^6$								
	$1.0 \cdot 10^6$	9	0.25	500	35°	20000	0.47	20	0°
	$1.5 \cdot 10^6$								
	$3.0 \cdot 10^6$								
Case 1B		4							
	$1.5 \cdot 10^6$	6	0.25	200	35°	3000	0.47	3	0°
		9							
		15							
Case 2B		4							
	$1.5 \cdot 10^6$	6	0.25	200	35°	20000	0.47	20	0°
		9							
		15							

** 1 in. = 25.4 mm 1 psi. = 6.895 kPa.

5.7 SUMMARY

The static shakedown theorem is reviewed in this chapter. A numerical algorithm based on the finite element method coupled with a nonlinear programming technique is proposed to evaluate approximate the lower bound shakedown load. The proposed algorithm is different from others in the following two aspects:

1. Both the inequality and equality constraints are included in the pseudo-objective function under consideration that the residual stress field is optimized with respect to both conditions. These two terms are normalized with yield stress and reference load, respectively, so that the three terms in the pseudo-objective function are consistent with the original objective function, a scalar. The penalty factors for these two terms are set to unit, so that no iteration is carried out with respect to different penalty factors.
2. A multidirectional search algorithm is used in the optimization process to improve the convergence speed. As with other search algorithms, the majority part of computation time is spent on search optimum direction and minimizing the objective function. When a problem becomes large and involves many variables, convergence is rather slow and the algorithm becomes impractical. A multidirectional search algorithm searches the optimum direction in n directions simultaneously, which saves a large amount of computation time. On the other hand, the adoption of a multidirectional search algorithm makes it possible to use more integral points to describe the stress state of an element rather than only one integral point.

Three examples that include beam, thin plate, and two-layered pavement systems are studied by using the proposed numerical algorithm and compared with available analytical and numerical results. The influence of finite element mesh size on shakedown loads is also investigated for beam and plate. The numerical results show that coarse mesh size usually gives higher shakedown load values than finer mesh sizes. However, as the mesh become finer, the shakedown load approaches a constant value.

Current studies reveal some problems that may be subjected to further investigations.

1. The numerical analysis of the shakedown load has shown that the optimization search basically goes around several critical integral points. Most of the body remains at its initial state during the search. Therefore, deduction of search variables and limiting the search within sub-region will greatly cut off the computation time in the optimization search process.
2. A unit penalty factor is used in the pseudo-objective function in the current study and the numerical results show quite reasonable consistency with available analytical and numerical results. However,

the penalty factor generally has great influence on the convergence speed and the accuracy of the optimization variable. Therefore, further study which looks into how different penalty factors influence the shakedown load may be necessary.

3. The numerical results have shown that finite element mesh sizes and element side-size ratios have certain influences on shakedown load values. To ground the comparison of different numerical algorithms and the accuracy of the analysis results on a common condition, it is suggested that a reasonable and identical finite element mesh size, mesh size ratio and element type be used for each algorithm.
4. Considering the upper and lower bound character of the approximate influence coefficients obtained in equilibrium and displacement finite element models, equilibrium finite element model always provides conservative estimate of shakedown load while displacement finite element model gives higher shakedown load value. Therefore, an equilibrium finite element model may be more preferable to use in lower bound shakedown analysis.

CHAPTER VI

AN ALGORITHM OF KINEMATIC SHAKEDOWN ANALYSIS

6.1 INTRODUCTION

The kinematic shakedown theory, as a complementary to the static shakedown theory [31], was established by Koiter [162] in 1960, which can be considered as a generalization of kinematic method of limit analysis. The difference between these two theories is that in limit analysis one only considers the critical kinematically admissible velocity field at the instantaneous moment of collapse; in shakedown analysis one has to deal with restricted but unspecified plastic deformation paths over any arbitrary time interval in a long term process. During the implementation of kinematic shakedown theorem, difficulties arise in constructing the kinematically admissible plastic deformation path and the integration along the path. Researches have been carried out to eliminate the time variable from the formulation of the kinematic method in shakedown theory. An incremental collapse mode approach has been employed by Gokhfeld [163, 164] to reduce the time integrals in Koiter's kinematic shakedown theorem and evaluate upper bound load factor. Subsequently, Sawczuk [165], Gokhfeld and Cherniavski [163], König [119] and Nguyen and Merrelle [in 166], among others, used the same approach to evaluate the safety factor in practical cases. In this approach, a special mode of incremental collapse is assumed, i.e. the principal plastic deformation orientation is constant. This assumption may not guarantee that the best evaluation in this class equals the precise value of the safety factor. A modification to this approach is made by Pham and Stumpf [167] to consider more general plastic strain rate fields; therefore, a better upper bound load factor is assumed to be obtained. Polizzoto et al [45] approach the problem by replacing the integration over the time interval by integration over the set of basic loads, and formulate a kinematic method similar to that of limit analysis. An alternative approach is to deduce a kinematical method from the static one by means of mathematical programming method. For discretized elastic-plastic systems with piecewise linearized yield surface, Corradi et al. [49] formulate the kinematic formulation in the framework of the dual linear programming approach, in which the integration along any path is not required. A convex analysis approach is used by Kamenjarzh and Weichert [168] and Kamenjarzh and Merzljakov [169] to establish a kinematic method for the safety factor evaluation when the yield surface is not necessarily piecewise linear. In this approach, they transform the static extremum problem into a standard form of the convex analysis, and derive a dual problem by the usual procedure of convex analysis. The derived dual problem is a kinematic one, which is defined on a set of kinematically admissible velocity fields. This approach results in an upper bound safety factor without integration along any plastic deformation path. An explicit formula for the upper bound is

derived by Kamenjarzh [170] for the shakedown problem with a polyhedron set of variable loads. Conditions are established under which the infimum of upper bounds over a set of regular velocity fields equals the safety factor.

Although these proposed approaches have succeeded in eliminating the time variable in the kinematic shakedown theorem established by Koiter [162], construction of kinematically admissible plastic paths is still not well resolved in numerical implementation, especially when optimization method is used in searching the safety load factor. In the current study, Kamenjarzh's explicit formula for the upper bound is employed in the numerical implementation. A algorithm that utilize eigen-mode to construct the admissible plastic deformation path is proposed to calculate the safety load factor. A multidirectional search algorithm [160] is adopted here to solve the nonlinear mathematical programming problem.

6.2 FORMULATION OF KINEMATIC THEOREM

The loads applied on a elastic-plastic body may vary independently in sense, direction and intensity, but can be characterized by a finite number of loading types that their variation range can be defined by a load domain Ω in the r -dimensional space of the parameters β_s , $s=1,2, \dots, r$. Then the surface traction applied on the body, $T_i(x, t)$ and body forces $F_i(x, t)$ can be expressed by their load parameters,

$$\begin{aligned} T_i(x, t) &= \sum_{s=1}^r \beta_s(t) T_i^s(x), \quad x \in S_T \\ F_i(x, t) &= \sum_{s=1}^r \beta_s(t) F_i^s(x), \quad x \in V \end{aligned} \quad (6.1)$$

Here, T_i^s, F_i^s are surface traction and body forces in an s -th unit load mode, V stands for body volume and S_T is that part of its surface on which the stress boundary conditions are prescribed, the remaining part of that is denoted by S_u . It is assumed that the domain Ω is convex, $\beta_s^1, \beta_s^2, \dots, \beta_s^n$ are the corners of the domain and $\sigma_{ij}^{1E}, \sigma_{ij}^{2E}, \dots, \sigma_{ij}^{nE}$ are the unique respective elastic stress field. Also it is assumed that there is a real number $\mu > 1$, that $\mu\beta_s(t) \in \Omega$.

Based on Koiter's [162] and König's [121] upper bound formulations, the kinematic shakedown theorem can be stated as the following:

The body will not shakedown if there exists a load program $\beta_s(t)$ resulting in elastic stress $\sigma_{ij}^E(x, t)$ and an independent cycle of plastic deformations $\bar{\epsilon}_{ij}(x, t)$ such that:

1°) increments of the plastic strains over a certain time period (t_1, t_2) constitute a compatible field,

$$\Delta \bar{\epsilon}_{ij}(x) = \int_{t_1}^{t_2} \dot{\bar{\epsilon}}_{ij}(x, t) dt = \frac{1}{2}(\bar{u}_{i,j} + \bar{u}_{j,i}) \quad \bar{u}_i = 0 \quad \text{on } S_u;$$

2°) the following inequality holds,

$$\int_{t_1}^{t_2} \int_V \sigma_{ij}^E(x, t) \dot{\bar{\epsilon}}_{ij}(x, t) dV dt > \int_{t_1}^{t_2} \int_V D\{\dot{\bar{\epsilon}}_{ij}(x, t)\} dV dt \quad (6.2a)$$

where $D\{\dot{\bar{\epsilon}}_{ij}\} = \sigma_{ij} \dot{\bar{\epsilon}}_{ij}^k$ denotes the rate of internal energy dissipation associated with the plastic strain rate $\dot{\bar{\epsilon}}_{ij}^k$, in which the stresses σ_{ij} satisfy the yield condition $f(\sigma_{ij}) = F(\sigma_{ij}) - k^2 = 0$. $F(\sigma_{ij})$ is a scalar function of stresses and k is a material constant for perfectly plastic material. \bar{u} is defined as displacement field.

On the other hand, the structure will shakedown in any load path contained within the domain Ω , for any plastic strain increments $\Delta \bar{\epsilon}_{ij}^k(x)$, if a number $\mu > 1$ can be found that the following inequality holds,

$$\mu \int_{t_1}^{t_2} \int_V \sigma_{ij}^E(x, t) \dot{\bar{\epsilon}}_{ij}(x, t) dV dt < \int_{t_1}^{t_2} \int_V D\{\dot{\bar{\epsilon}}_{ij}(x, t)\} dV dt \quad (6.3a)$$

It has been proved that [119] if a given structure shakes down in a cyclic loading process which contains all the corners β^i , $i=1, 2, \dots, n$, of a given load domain Ω , then it shakes down in an arbitrary loading path contained within the domain. Therefore, considering an arbitrary load path's consisting of all the stress fields at the corners of the domain Ω , $\sigma_{ij}^{1E}, \sigma_{ij}^{2E}, \dots, \sigma_{ij}^{nE}$, and p_k representing the set of instants corresponding to elastic stress field σ_{ij}^{kE} , then the inadaptation condition Eq. (6.2a) reduced to the following form:

$$\int_V \sum_{k=1}^n \int_{p_k} \sigma_{ij}^{kE}(x) \dot{\bar{\epsilon}}_{ij}(x, t) dt dV > \int_{t_1}^{t_2} \int_V D\{\dot{\bar{\epsilon}}_{ij}(x, t)\} dV dt \quad (6.2b)$$

Assuming that the strain rate $\dot{\bar{\epsilon}}_{ij}(x, t)$ keeps constant orientation within each one of the sets p_k , it can be expressed as

$$\dot{\bar{\epsilon}}_{ij}^k(x, t) = \Lambda(x, t) \dot{\bar{\epsilon}}_{ij}^k(x) \quad t \in p_k \quad (6.4)$$

where $\Lambda(x, t)$ is a scalar function and $\dot{\Lambda}(x, t) \geq 0$, $\Lambda(x, 0) = 0$, $\Lambda(x, T) = 1$.

The increment of the plastic strains corresponding to instant p_k is given by

$$\Delta \bar{\varepsilon}_{ij}^k(x) = \int_{p_k} \Lambda(x, t) \dot{\bar{\varepsilon}}_{ij}^k(x) dt$$

It can also be shown that for any plastic strain history $\varepsilon_{ij}^p(x, t)$, the following inequality holds [121]

$$\int_{t_1}^{t_2} D(\dot{\bar{\varepsilon}}_{ij}^p) dt \geq D(\varepsilon_{ij}^p(t_2) - \varepsilon_{ij}^p(t_1)) = D(\Delta \varepsilon_{ij}^p) \quad (6.5)$$

By using Eq. (6.4) and Eq. (6.5), the inadapation condition (6.2a) can be further written in the following form

$$\int_V \sum_{k=1}^n \sigma_{ij}^{kE}(x) \Delta \bar{\varepsilon}_{ij}^k(x) dV > \int_V \sum_{k=1}^n D(\Delta \bar{\varepsilon}_{ij}^k(x)) dV \quad (6.2c)$$

Following the same argument, the shakedown condition Eq. (3) becomes

$$\mu \int_V \sum_{k=1}^n \sigma_{ij}^{kE}(x) \Delta \bar{\varepsilon}_{ij}^k(x) dV < \int_V \sum_{k=1}^n D(\Delta \bar{\varepsilon}_{ij}^k(x)) dV \quad (6.3b)$$

provided that,

$$\sum_{k=1}^n \Delta \bar{\varepsilon}_{ij}^k(x) = \frac{1}{2}(\bar{u}_{i,j} + \bar{u}_{j,i}) \quad \bar{u}_i = 0 \quad \text{on } S_u$$

In this formulation, as indicated in Eq. (6.4), a constant orientation of plastic strain rate $\dot{\bar{\varepsilon}}_{ij}^k(x, t)$ is assumed. In a practical situation, for a given system, it is difficult to say that the system will fail by a specific mechanism. This consideration limits the practical value of the incremental collapse mode approach. Alternatively, by means of convex analysis, Kamenjarzh and Weichert [168] formulate the kinematic shakedown theorem into a standard form of the convex optimization problem and is briefly reviewed below.

First, the static shakedown theorem is transformed into the standard convex optimization problem using Minkowski function, i.e.

$$\frac{1}{s_\Delta} = \inf \{F(p) : p \in \Sigma\} \quad (6.6a)$$

Here, Σ is a subspace in S that denotes a space of stress fields; F is defined as a convex function. The dual extremum problem of static extremum problem is the kinematic extremum problem of the shakedown theory and is given by

$$\frac{1}{s_\Delta} \geq \sup \{-G(e) : e \in \text{DefV}\} \quad (6.6b)$$

where, $G(e)$ is Fenchel transformation defines the polar function of the function F with respect to the chosen bilinear form $G(e) = \sup\{\langle \sigma, e \rangle - F(\sigma) : \sigma \in S\}$
 e kinematically admissible strain rate fields
 V is a space of virtual velocity fields
 Def is the strain rate operator
 E is a space of kinematically admissible strain rate fields e .

For a polyhedron set of variable loads, the explicit kinematic extremum problem is given in the following form

$$s = \inf\left\{ \frac{D(e_1) + \dots + D(e_m)}{\langle e_1, \tau_1 \rangle + \dots + \langle e_m, \tau_m \rangle} : e_1, \dots, e_m \in E \quad \begin{array}{l} e_1 + \dots + e_m \in (\text{Def}V)_{(m)}, \\ \langle e_1, \tau_1 \rangle + \dots + \langle e_m, \tau_m \rangle >> 0 \end{array} \right\} \quad (6.6c)$$

where e_k denotes kinematically admissible strain rate fields, and is the summation of elastic strain rate

$$e^e \text{ and plastic strain rate } e^p \text{ i.e. } e_k = e_k^e + e_k^p,$$

τ_k is the elastic stress field corresponding to the load $l_k = \text{conv}(l_1, \dots, l_n)$,

$$\langle e_k, \tau_k \rangle = \int_V e_k \tau_k dV$$

$$D(e) = \sup\{\langle e, s \rangle : s \in C\}, \quad e \in E$$

C defines the set of admissible stress fields

s is a stress field.

A detailed derivation of Eq. (6.6c) was presented by Kamenjarzh[170]. Now, the consideration is given to construct an arbitrary kinematically admissible cycle of plastic rate and the upper bound formulation for Mohr-Coulomb type materials. For other materials, the same procedure may be followed.

6.3 PLASTIC DISSIPATION AND VIRTUAL WORK

In the application of shakedown analysis to pressure dependent materials such as soil and concrete, the mechanical behaviors are usually characterized by Mohr-Coulomb failure criterion. The Mohr-Coulomb yield function can be expressed in the following form

$$f(\sigma) = \sigma_1(1 + \sin \phi) - \sigma_3(1 - \sin \phi) - 2C \cos \phi = 0 \quad (6.7)$$

where σ_1 and σ_3 are principal stresses, C is the material cohesion and ϕ the angle of internal friction. Geometrically, Eq. (6.7) represents an irregular hexagonal pyramid in principal stress space as shown in

Fig. 6.1. Considering stress discontinuity at the corners of the yield surface, three cases have to be examined in deriving plastic energy dissipation for a three-dimensional problem.

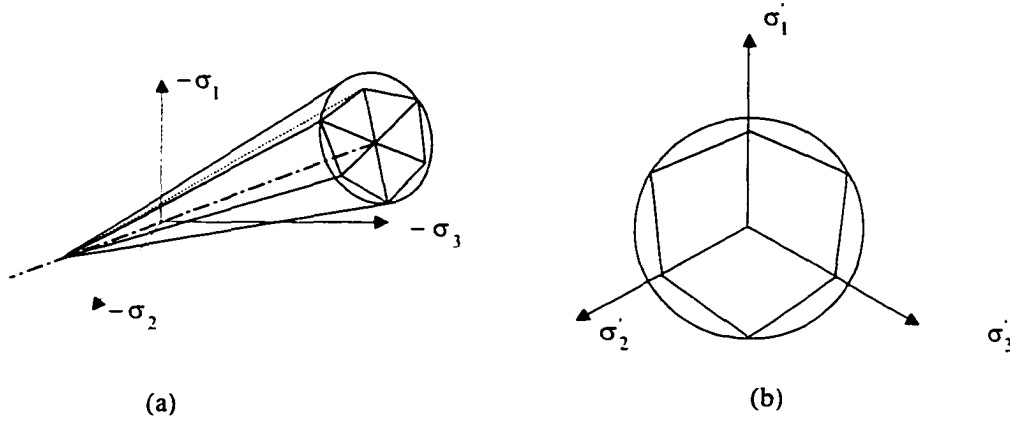


Figure 6.1 Drucker-Prager and Mohr-Coulomb Criteria.
(a) in Principal Stress Space; (b) in the Deviatoric Plane.

Case 1. The yield stress point is at the plane surface of the pyramid where $\sigma_1 > \sigma_2 > \sigma_3$ holds. By assuming plastic deformation follows associated flow rule, the plastic strain can be expressed in following form for a given loading path, p_k

$$\dot{\epsilon}_{ij}^k = \dot{\lambda} \frac{\partial f}{\partial \sigma_{ij}} \quad (6.8)$$

Introducing the yield function Eq. (6.7) into Eq. (6.8), we obtain plastic strain increments,

$$\dot{\epsilon}_1^k = m\dot{\lambda}; \quad \dot{\epsilon}_2^k = 0; \quad \dot{\epsilon}_3^k = -\dot{\lambda} \quad \dot{\lambda} \geq 0 \quad (6.9)$$

where m is obtained by considering the ratio of principal plastic strains ,

$$\frac{\dot{\epsilon}_1^k}{\dot{\epsilon}_3^k} = \frac{\partial f / \partial \sigma_1}{\partial f / \partial \sigma_3} = -\frac{1 + \sin \phi}{1 - \sin \phi}$$

which leads to the following relationship between the plastic strain components,

$$\dot{\epsilon}_1^k = -\dot{\epsilon}_3^k \frac{1 + \sin \phi}{1 - \sin \phi} = -m\dot{\epsilon}_3^k$$

The rate of plastic energy dissipation corresponds to a given loading path, p_k within the loading domain Ω can be calculated by

$$\dot{d} = \sigma_1 \dot{\epsilon}_1^k + \sigma_2 \dot{\epsilon}_2^k + \sigma_3 \dot{\epsilon}_3^k \quad (6.10)$$

Introducing Eq. (6.9) into Eq. (6.10), the rate of energy dissipation for a given plastic deformation path, can be obtained by

$$\dot{d} = (m\sigma_1 - \sigma_3)\dot{\lambda} \quad (6.11)$$

Case 2. The yield stress is at the edges of the pyramid, where $\sigma_1 > \sigma_2 = \sigma_3$. Because two plane surfaces intercept at the edge, the stresses at the edge satisfy the two yield functions

$$m\sigma_1 - \sigma_3 = f'_c \quad (6.12a)$$

and

$$m\sigma_1 - \sigma_2 = f'_c \quad (6.12b)$$

By using flow rule, plastic strain increments that are normal to the two yield surfaces defined by Eq. (6.12) are given by

$$\begin{aligned} (\dot{\bar{\epsilon}}_1^k)^1 &= m\dot{\lambda}_1; & (\dot{\bar{\epsilon}}_2^k)^1 &= 0; & (\dot{\bar{\epsilon}}_3^k)^1 &= -\dot{\lambda}_1 & \text{normal to surface1} \\ (\dot{\bar{\epsilon}}_1^k)^2 &= m\dot{\lambda}_2; & (\dot{\bar{\epsilon}}_2^k)^2 &= -\dot{\lambda}_2 & (\dot{\bar{\epsilon}}_3^k)^2 &= 0 & \text{normal to surface2.} \end{aligned} \quad (6.13)$$

The plastic strain increments at edge are the summation of the two sets of plastic strain increments, i.e.

$$\begin{aligned} \dot{\bar{\epsilon}}_1^k &= (\dot{\bar{\epsilon}}_1^k)^1 + (\dot{\bar{\epsilon}}_1^k)^2 = m(\dot{\lambda}_1 + \dot{\lambda}_2); \\ \dot{\bar{\epsilon}}_2^k &= (\dot{\bar{\epsilon}}_2^k)^1 + (\dot{\bar{\epsilon}}_2^k)^2 = -\dot{\lambda}_2; \\ \dot{\bar{\epsilon}}_3^k &= (\dot{\bar{\epsilon}}_3^k)^1 + (\dot{\bar{\epsilon}}_3^k)^2 = -\dot{\lambda}_1. \end{aligned} \quad (6.14)$$

The rate of energy dissipation then can be calculated by

$$\dot{d} = \sigma_1 \dot{\bar{\epsilon}}_1^k + \sigma_2 \dot{\bar{\epsilon}}_2^k + \sigma_3 \dot{\bar{\epsilon}}_3^k = (m\sigma_1 - \sigma_3)(\dot{\lambda}_1 + \dot{\lambda}_2) = f'_c \dot{\bar{\lambda}} \quad (6.15)$$

where $f'_c = (m\sigma_1 - \sigma_3)$ and $\dot{\bar{\lambda}} = (\dot{\lambda}_1 + \dot{\lambda}_2)$.

Case 3. The yield stress point is at apex of the pyramid, where $\sigma_1 = \sigma_2 = \sigma_3$. There are six planes surfaces intercepting at the apex of the pyramid, the stresses at the apex of the pyramid satisfy the following yield functions

$$\begin{aligned} m\sigma_1 - \sigma_3 &= \sigma_1(m-1)f'_c \\ m\sigma_2 - \sigma_3 &= \sigma_2(m-1)f'_c \\ m\sigma_3 - \sigma_1 &= \sigma_3(m-1)f'_c \end{aligned} \quad (6.16)$$

Three sets of plastic strain increments that are normal to plane surfaces of the pyramid can be obtained

$$\begin{aligned}
(\dot{\bar{\epsilon}}_1^k)^1 &= (m-1)\dot{\lambda}_1; & (\dot{\bar{\epsilon}}_2^k)^1 &= 0; & (\dot{\bar{\epsilon}}_3^k)^1 &= 0; \\
(\dot{\bar{\epsilon}}_1^k)^2 &= 0; & (\dot{\bar{\epsilon}}_2^k)^2 &= (m-1)\dot{\lambda}_2; & (\dot{\bar{\epsilon}}_3^k)^2 &= 0; \\
(\dot{\bar{\epsilon}}_1^k)^3 &= 0; & (\dot{\bar{\epsilon}}_2^k)^3 &= 0; & (\dot{\bar{\epsilon}}_3^k)^3 &= (m-1)\dot{\lambda}_3
\end{aligned} \tag{6.17}$$

Then, the plastic strain increments at the apex is the summation of the three sets of plastic strain increments

$$\begin{aligned}
\dot{\bar{\epsilon}}_1^k &= (\dot{\bar{\epsilon}}_1^k)^1 + (\dot{\bar{\epsilon}}_1^k)^2 + (\dot{\bar{\epsilon}}_1^k)^3 = (m-1)\dot{\lambda}_1 \\
\dot{\bar{\epsilon}}_2^k &= (\dot{\bar{\epsilon}}_2^k)^1 + (\dot{\bar{\epsilon}}_2^k)^2 + (\dot{\bar{\epsilon}}_2^k)^3 = (m-1)\dot{\lambda}_2 \\
\dot{\bar{\epsilon}}_3^k &= (\dot{\bar{\epsilon}}_3^k)^1 + (\dot{\bar{\epsilon}}_3^k)^2 + (\dot{\bar{\epsilon}}_3^k)^3 = (m-1)\dot{\lambda}_3
\end{aligned} \tag{6.18}$$

The energy dissipation then can be calculated by

$$\dot{d}^k = \sigma_1 \dot{\bar{\epsilon}}_1^k + \sigma_2 \dot{\bar{\epsilon}}_2^k + \sigma_3 \dot{\bar{\epsilon}}_3^k = \sigma_1 (m-1)\dot{\lambda}_1 + \sigma_2 (m-1)\dot{\lambda}_2 + \sigma_3 (m-1)\dot{\lambda}_3 = f'_c \dot{\lambda} \tag{6.19}$$

The plastic energy dissipation within an element is the integration of each point over the element, i.e.

$$\dot{D}^k = \int_V \dot{d}^k dV = \int_V (\sigma_1 \dot{\bar{\epsilon}}_1^k + \sigma_2 \dot{\bar{\epsilon}}_2^k + \sigma_3 \dot{\bar{\epsilon}}_3^k) dV \tag{6.20a}$$

$$\dot{D}^k = \int_V f'_c \dot{\lambda} dV = \int_V (m\sigma_1 - \sigma_3) \dot{\lambda} dV = \int_V \frac{2C \cos \phi}{1 - \sin \phi} \dot{\lambda} dV \tag{6.20b}$$

where σ_1 and σ_3 satisfy yield function Eq. (6.7).

For the axisymmetric problem, three principal stresses can be obtained from quasi-static analysis; therefore, the formulation to calculate the rate of energy dissipation is the same as in the three-dimensional case.

For the two-dimensional problem, the plastic energy dissipation is always confined within a plane and independent of the third direction. The formulations to calculate energy dissipation in plane stress or in plane strain problem are the same. Therefore, only the plane strain problem is considered in the derivation of formulation of energy dissipation.

For the plane strain problem, Mohr-Coulomb yield function is given by Eq. (6.7). From flow rule, the plastic increments for a given plastic load path, p_k can be calculated by

$$\dot{\bar{\epsilon}}_1^k = m\dot{\lambda}; \quad \dot{\bar{\epsilon}}_2^k = 0; \quad \dot{\bar{\epsilon}}_3^k = -\dot{\lambda} \quad \dot{\lambda} \geq 0. \tag{6.21}$$

The energy dissipation then can be calculated by

$$\dot{d}^k = \sigma_1 \dot{\bar{\epsilon}}_1^k + \sigma_2 \dot{\bar{\epsilon}}_2^k + \sigma_3 \dot{\bar{\epsilon}}_3^k = (m\sigma_1 - \sigma_3) \dot{\lambda} = f'_c \dot{\lambda} \quad (6.22a)$$

The plastic energy dissipation rate within an element can be obtained by integrating of Eq. (6.22a) over the element domain.

$$\dot{D}^k = \int_V f'_c \dot{\lambda} dV = \int_V (m\sigma_1 - \sigma_3) \dot{\lambda} dV = \int_V \frac{2C \cos \phi}{1 - \sin \phi} \dot{\lambda} dV \quad (6.22b)$$

The virtual work rate within an element done by a given load path under any kinematic admissible plastic strain rate $\dot{\bar{\epsilon}}_{ij}^k(x)$ is calculated by

$$\dot{W}^k = \int_V \sigma_{ij}^{kE} \dot{\bar{\epsilon}}_{ij}^k dV$$

By denoting the bilinear form as,

$$\langle e^k, \sigma^{kE} \rangle = \int_V e^k \cdot \sigma^{kE} dV = \int_V \sigma_{ij}^{kE} \dot{\bar{\epsilon}}_{ij}^k dV$$

Then, we have,

$$\langle e^k, \sigma^{kE} \rangle = \int_V e^k \cdot \sigma^{kE} dV = \int_V (\sigma_1^{kE} \dot{\bar{\epsilon}}_1^k + \sigma_2^{kE} \dot{\bar{\epsilon}}_2^k + \sigma_3^{kE} \dot{\bar{\epsilon}}_3^k) dV$$

For the plane strain problem, by considering the relationship of strain components, we have,

$$\langle e^k, \sigma^{kE} \rangle = \int_V \frac{(\sigma_1^{kE} - \sigma_3^{kE}) + (\sigma_1^{kE} + \sigma_3^{kE}) \sin \phi}{1 - \sin \phi} \dot{\lambda} dV \quad .$$

The total plastic energy dissipation rate of considered body for any arbitrary load paths are given by

$$D = \int_V \sum_{k=1}^n D^k \{\dot{\bar{\epsilon}}_{ij}^k(x)\} dV = \sum_{l=1}^M \sum_{k=1}^n D^k \{\dot{\bar{\epsilon}}_{ij}^k(x)\} \quad (6.23)$$

and the total virtual work rate is,

$$W = \int_V \sum_{k=1}^n \sigma_{ij}^{kE}(x) \dot{\bar{\epsilon}}_{ij}^k(x) dV = \sum_{l=1}^M \sum_{k=1}^n \sigma_{ij}^{kE}(x) \dot{\bar{\epsilon}}_{ij}^k(x) \quad (6.24)$$

where n is the number of corners of the loading domain and M is the number of discretized elements of the considered body.

The upper bound load parameter then can be determined by the following formulation,

$$\mu \leq \frac{D}{W} \equiv \frac{\int_V \sum_{k=1}^n D\{\dot{\bar{\epsilon}}_{ij}^k(x)\} dV}{\int_V \sum_{k=1}^n \sigma_{ij}^{kE}(x) \dot{\bar{\epsilon}}_{ij}^k(x) dV} = \frac{\sum_{j=1}^M \sum_{k=1}^n D^k \{\dot{\bar{\epsilon}}_{ij}^k\}}{\sum_{j=1}^M \sum_{k=1}^n \sigma_{ij}^{kE} \dot{\bar{\epsilon}}_{ij}^k} \quad (6.25)$$

For any loading paths, Eq. (6.25) will compute an upper bound load factor. The infimum of these will give us the safe upper bound load factor that can be determined by standard the convex optimization technique.

6.4 DETERMINATION OF ADMISSIBLE PLASTIC STRAIN FIELD

In the implementation of kinematic shakedown theorem, difficulties arise in constructing the kinematically admissible plastic deformation paths and integrating along the paths. Although several approaches to kinematic shakedown theorem have been proposed, in which the time variable is eliminated in the formulations so that mathematical difficulty is reduced to the same order as that of a kinematic limit problem, the numerical implementation is rather involved and practical application is limited. With this regards, all possible admissible plastic deformation paths have to be constructed in the process of optimization, in which each will give us a upper bound shakedown load factor. The safe upper bound load factor is extremum that has to be found among all these load factors by a mathematical programming technique. By using the properties of eigen-mode that characterize every possible deformation mode of loaded body, a numerical procedure is proposed in this section to construct all possible admissible plastic paths and to find the safe load factor by using multidirectional search optimization algorithm.

From Lagrange's Equation [171],

$$\frac{d}{dt} \left(\frac{\partial T}{\partial \dot{q}_j} \right) - \frac{\partial T}{\partial q_j} + \frac{\partial U}{\partial q_j} = Q_{Aj} \quad (6.26)$$

the equations of motion in generalized coordinates q can be obtained for a elastic system as follows,

$$[m_{kl}] \{\ddot{q}\} + [k_{kl}] \{q\} = \{Q\}_A \quad (6.27a)$$

where

$$T = \frac{1}{2} \sum_k \sum_l m_{kl} \dot{q}_k \dot{q}_l, \text{ the kinematic energy of the system}$$

$$U = \frac{1}{2} \sum_k \sum_l k_{kl} q_k q_l, \text{ the strain energy}$$

$$m_{kl} = \sum_j m_j \frac{\partial u_j}{\partial q_k} \frac{\partial u_j}{\partial q_l}, \text{ generalized mass}$$

$[k_{kl}]$ - the generalized stiffness matrix

Q_A - the generalized applied forces.

u - displacement in geometric coordinate.

The natural frequencies and modes of the system can be determined by solving the eigen-value problem of the homogeneous algebraic equation corresponding to Eq. (6.27a), i.e.

$$[m_{kl}]\{\ddot{q}\} + [k_{kl}]\{q\} = 0 \quad (6.27b)$$

Assuming the displacement in generalized coordinate is given by $q = \hat{q} \sin(\omega t + \alpha)$. By introducing q into Eq. (6.27b), we then have,

$$([K] - \omega^2 M)\{\hat{q}\} = 0 \quad (6.27c)$$

where $[K]$ is defined as a system stiffness matrix and M is a system mass matrix.

A nontrivial solution to Eq.(6.27c) exists only when its determinant vanishes, that is,

$$|[K] - \omega^2 M| = 0 \quad (6.27d)$$

The Eq. (6.27d) is called a characteristic equation of the system. Expansion of the determinant will give an algebraic equation of the N -th degree in frequency parameter ω^2 for a system having N degrees of freedom. The N roots of this equation ($\omega_1, \omega_2, \dots, \omega_n$) represent the frequencies of the N modes of deformation that are possible in the system. The frequency vector is denoted by

$$\omega = [\omega_1, \omega_2, \dots, \omega_n]^T \quad (6.28)$$

When the natural frequencies of the system have been determined from Eq. (6.27a), the eigen-vector, i.e. the deformation modes then can be obtained by solving the homogeneous equation (6.27d) corresponding to every eigen-value. The following matrix can denote the natural mode vector

$$\Phi = \{\phi_1, \phi_2, \dots, \phi_n\} = \begin{bmatrix} \phi_{11} & \phi_{12} & \dots & \phi_{1N} \\ \phi_{21} & \phi_{22} & \dots & \phi_{2N} \\ \vdots & \vdots & \dots & \vdots \\ \phi_{N1} & \phi_{N2} & \dots & \phi_{NN} \end{bmatrix} \quad (6.29)$$

By means of orthogonality relationships of the natural mode given by the following equations:

$$\phi_m^T M \phi_n = 0; \quad \phi_m^T K \phi_n = 0 \quad m \neq n$$

the generalized mass, generalized stiffness and generalized force can be obtained by the following equations:

$$M_n = \phi_n^T M \phi_n; \quad K_n = \phi_n^T K \phi_n; \quad P_n(t) = \phi_n^T P(t) \quad (6.30)$$

Because the eigen-vectors corresponding to N different eigen-values are linear independent, they constitute a basis of a linear space \wp (displacement vector space). Thus, each vector in \wp can be expressed as a linear combination of these basis vectors, that is,

$$q = \phi_1 \eta_1 + \phi_2 \eta_2 + \dots + \phi_n \eta_n = \sum_{k=1}^n \phi_k \eta_k = \Phi \bar{\eta} \quad (6.31)$$

with $\bar{\eta} = [\eta_1, \eta_2, \dots, \eta_n] \in \mathcal{R}^n$ a normal coordinates in \mathcal{R}^n space. For a given displacement vector q , the normal coordinate vector $\bar{\eta}$ is uniquely determined due to the linear independence of the basis vector Φ . To evaluate any arbitrary normal coordinate η_k , Eq. (6.31) is multiplied by the product of the transpose of the corresponding normal vector and the mass matrix, $\phi_k^T m$, i.e.,

$$\phi_k^T m q = \phi_k^T m \Phi \bar{\eta} \quad (6.32)$$

Expanding the right-hand side of Eq. (6.32) gives

$$\phi_k^T m \Phi q = \phi_k^T m \phi_1 q_1 + \phi_k^T m \phi_2 q_2 + \dots + \phi_k^T m \phi_k q_k + \dots + \phi_k^T m \phi_n q_n \quad (6.33)$$

By means of the orthogonality property of eigen-vector with respect to mass, all terms in Eq. (6.33) vanish except that corresponding to ϕ_k . By introducing this one term on the right side of Eq. (6.32) gives

$$\phi_k^T m q = \phi_k^T m \phi_k \eta_k$$

from which,

$$\eta_k = \frac{\phi_k^T m q}{\phi_k^T m \phi_k} \quad (6.34)$$

By using generalized mass, Eq. (6.34) can be rewritten as

$$\eta_k = \frac{\phi_k^T m \dot{q}}{m_k} \quad (6.35)$$

That the differentiation of Eq. (6.35) with respect to time gives the velocity field,

$$\dot{q} = \sum_{k=1}^n \phi_k \dot{\eta}_k = \Phi \dot{\eta} \quad (6.36a)$$

with the normal coordinate is given by

$$\dot{\eta}_k = \frac{\phi_k^T m \dot{q}}{m_k} \quad (6.36b)$$

Eq. (6.36a) indicates that any admissible velocity field at the loading corner can be constructed by means of linear combination of eigen-vector Φ , i.e.

$$\dot{q}_s^k = \sum_{l=1}^N \phi_l \dot{\eta}_s^l \quad s=1,2,\dots,n$$

k is a any instance of velocity filed at loading corner and N is the degree of freedom of the system.

Then the admissible plastic strain rate at loading corner is given by,

$$\Delta \dot{\epsilon}_{ij}^k = \frac{1}{2} (\dot{q}_{i,j}^k + \dot{q}_{j,i}^k)$$

where the velocity field \dot{q}_j^k satisfies the boundary conditions.

6.5 IMPLEMENTATION

Once the arbitrary admissible plastic strain path is constructed, the external work rate and internal plastic energy dissipation rate for the discretized system can be calculated by using Eq.(6.20) and Eq. (6.24). The upper bound load parameter is determined by Eq. (6.25). The safe upper bound shakedown load is determined by finding the infimum of the upper bounds using a nonlinear mathematical programming technique. There are two steps involved in the upper bound shakedown analysis. First, a numerical method has to be employed to find the stress-strain field at reference state (P_o) and velocity basis to construct admissible strain rate. Second, a nonlinear mathematical programming technique has to be utilized to find the extremum of upper bounds. In this step, multidirectional search is used as an optimizer.

A finite element method coupled with multidirectional search algorithm is employed in this study to conduct the upper bound shakedown analysis. The algorithm used in the program is illustrated in the following

ALGORITHM

1^o) For discretized system using FEM to find eigen-vectors corresponding to N degree of freedom system.

$$M\ddot{v} + Kv = 0$$

and elastic stress field at loading corners of the domain Ω , $\sigma_{ij}^{1E}, \sigma_{ij}^{2E}, \dots, \sigma_{ij}^{nE}$,

$$Ku_L = P_L^0 \quad L=1,2,\dots,N$$

$$\sigma = DBu^e$$

2^o) Constructing velocity field at each loading corner by using the linear combination of eigen-vectors.

$$\dot{v}^k = \sum_L \phi_L \dot{\eta}_L^k$$

and admissible plastic strain path at each corner,

$$\Delta \bar{\epsilon}_{ij}^k = B\dot{v}^e \quad k=1,2,\dots,n$$

3^o) Find initial search direction by giving each velocity vector at loading corner a disturbance, which will lead to smallest objective function and shift the search in this direction.

4^o) Beginning from the initial search direction, multidirectional search is used as a optimizer to find new search direction which will lead to smallest objective function.

5^o) Check if the convergence criterion has been satisfied, i.e.

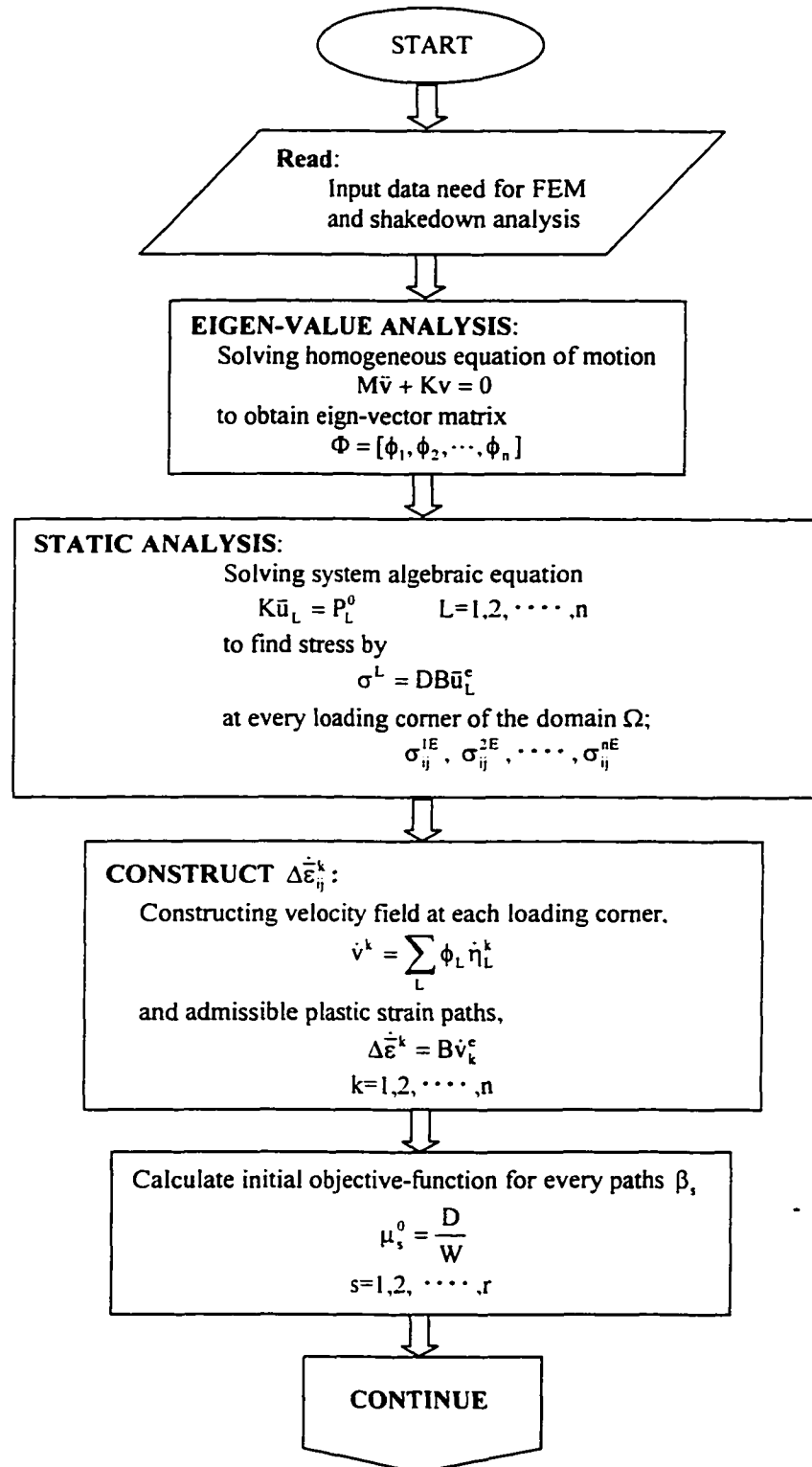
$$|\mu_{k-1} - \mu_k| < \delta$$

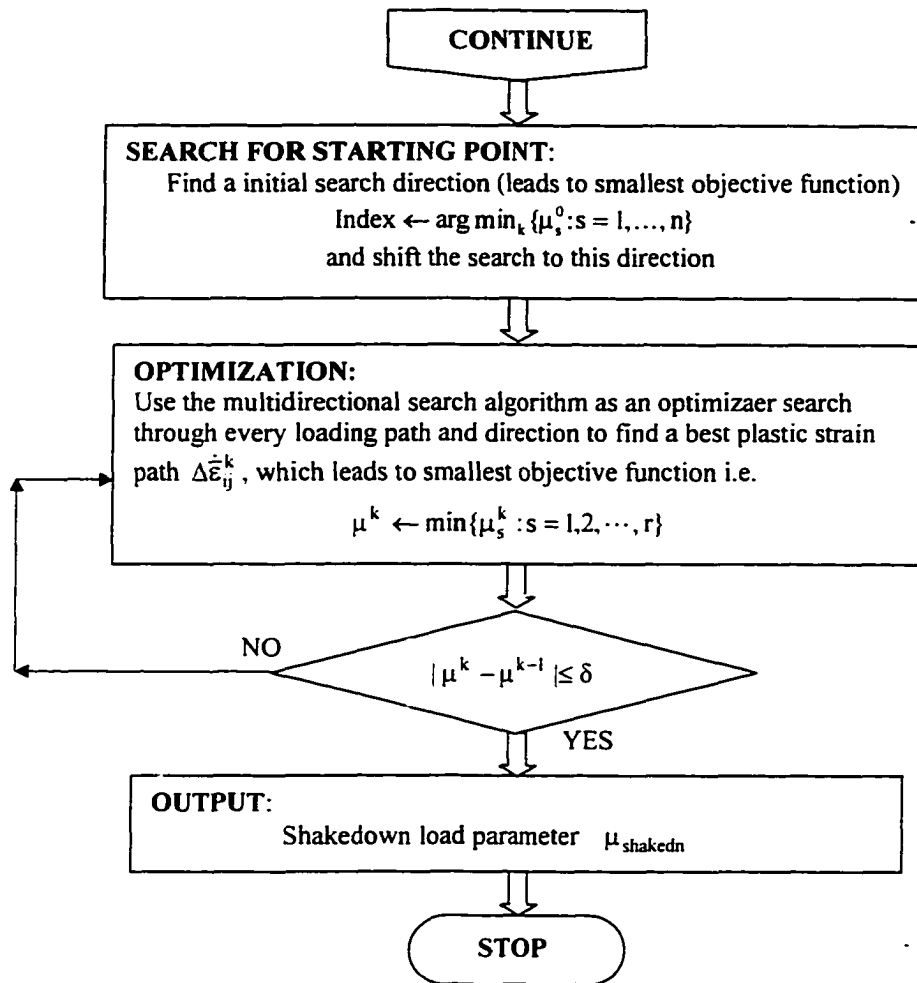
If it is satisfied then go to step 6^o)

else go to step 4^o)

6^o) Output Load parameter μ .

A flow chart can be found in the following page.





6.6 EXAMPLES

A program has been developed based on the proposed algorithm. The upper bound shakedown analysis is conducted for several example problems. These numerical results are compared with available numerical and analytical results.

6.6.1 EXAMPLE I

The proposed numerical approach is used in the upper bound shakedown analysis of a beam with one fixed end and the other end is simply supported by a roller as shown in Fig. 6.2. The cross section of the beam is rectangular with thickness $B=25.4$ mm(1.0 in.), height $H=76.2$ mm(3.0 in.), and span $L=304.8$ mm(12.0 in.). The material is assumed elastic-perfectly plastic and obeys the Von Mises

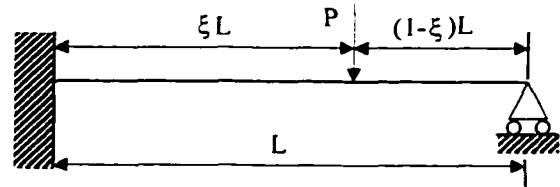


Figure 6.2: A Beam with One Fixed End and One Roller Supported End.

yield criterion. The elastic properties are given by elastic modulus $E = 241 \cdot 10^3$ Mpa.($3.5 \cdot 10^7$ psi.) and Poisson ratio $\nu = 0.15$. The plastic behavior is characterized by yield stress $\sigma_o = 3.5$ Mpa. (500.0 psi).

Four different finite element meshes, as shown in Fig. 6.3 to Fig. 6.6 are used in the analysis. The shakedown loads were calculated at three different locations(i. e $L/3$, $L/2$, and $2L/3$) and the results are presented in Table 6.1. The numerical results show the mesh size influence on the shakedown load. The course mesh gives higher load value than the finer mesh. Fig. 6.7 shows the shakedown load variation with finite element number used in the mesh. As the mesh become finer, the shakedown load is convergent to a constant value.

The theoretical formulations to calculate the shakedown load for the same beam are presented by König [120] and are rewritten below

$$P = \frac{M_o}{\beta L} \frac{2}{\xi(2-3\xi+\xi^2)} \quad \text{for } \xi \leq 0.5858$$

$$P = \frac{M_o}{\beta L} \frac{2}{\xi(3-4\xi+\xi^2)} \quad \text{for } \xi \geq 0.5858$$

where M_o is full plastic moment of the cross-section of the beam, $\beta = M_o / M_e$ shape factor and M_e is yield moment.

SHAKEDOWN ANALYSIS (UPPER BOUND) :

Load Applied at: $L/3$ $L/2$ $2L/3$
 Shakedown Load: 7.676 7.204 7.183

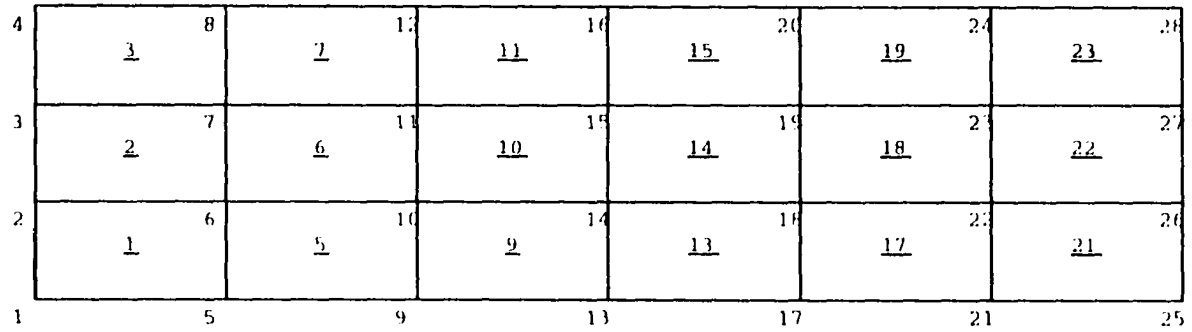


Figure 6.3: Finite Element Mesh for Fixed End Beam with 18 Elements and 20 Nodes.

SHAKEDOWN ANALYSIS (UPPER BOUND) :

Load Applied at: L/3 L/2 2L/3
 Shakedown Load: 7.063 5.724 5.615

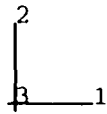
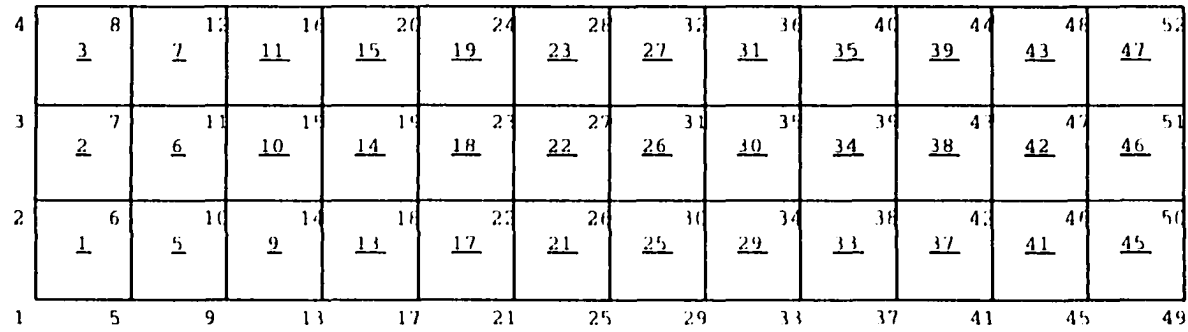


Figure 6.4: Finite Element Mesh for Fixed End Beam with 36 Elements and 52 Nodes.

SHAKEDOWN ANALYSIS(UPPER BOUND):

Load Applied at: 1/3 1/2 21/3
 Shakedown Load: 5.898 5.586 5.423

9	207	407	607	807	1007	1207	1407	1607	1807	2007	2207	2407
7	205	405	605	805	1005	1205	1405	1605	1805	2005	2205	2405
5	203	403	603	803	1003	1203	1403	1603	1803	2003	2203	2403
3	201	401	601	801	1001	1201	1401	1601	1801	2001	2201	2401

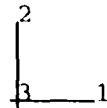


Figure 6.5: Finite Element Mesh for Fixed End Beam with 48 Elements and 65 Nodes.

SHAKEDOWN ANALYSIS (UPPER BOUND):

Load Applied at: L/3 L/2 2L/3
 Shakedown Load: 5.642 5.076 4.987

2	207	407	607	807	1007	1207	1407	1607	1807	2007	2207	2407	2607	2807	3007	3207
2	205	405	605	805	1005	1205	1405	1605	1805	2005	2205	2405	2605	2805	3005	3205
1	204	404	604	804	1004	1204	1404	1604	1804	2004	2204	2404	2604	2804	3004	3204
1	201	401	601	801	1001	1201	1401	1601	1801	2001	2201	2401	2601	2801	3001	3201

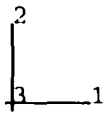


Figure 6.6: Finite Element Mesh for Fixed End Beam with 64 Elements and 85 Nodes.

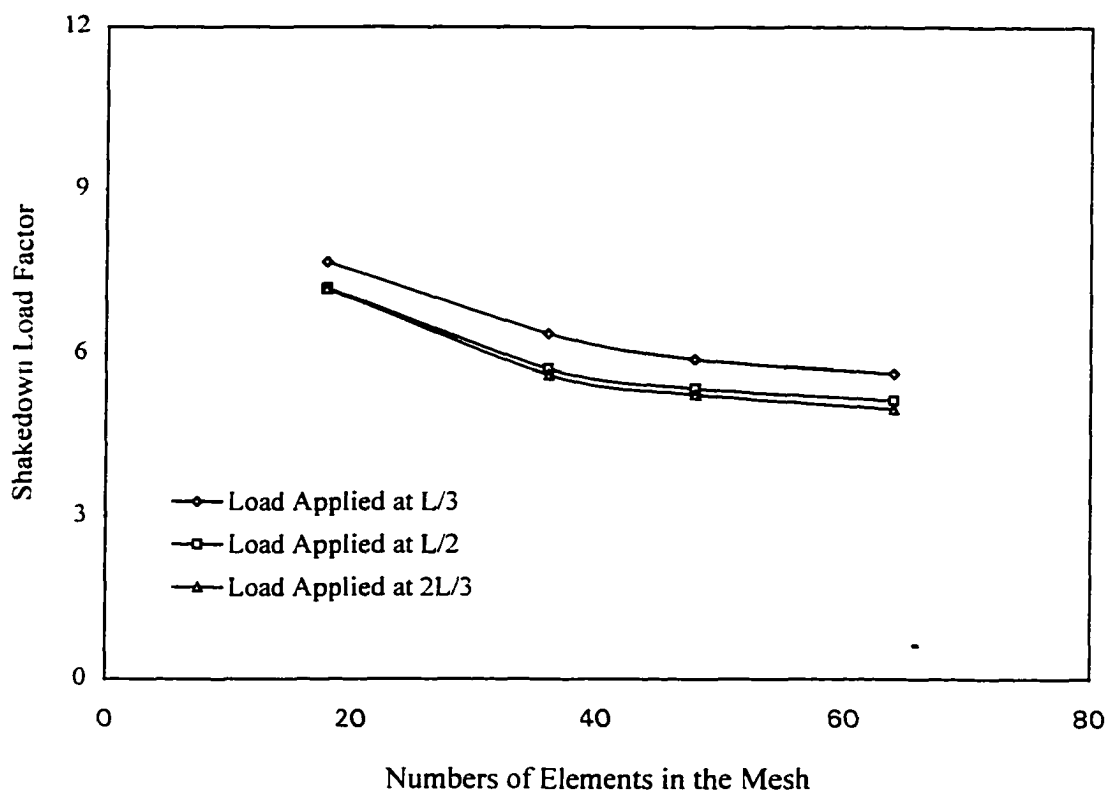


Figure 6.7 Finite Element Mesh Influence on Shakedown Load(Upper Bound).

Table 6.1: SHAKEDOWN ANALYSIS FOR FIXED END BEAM(UPPER BOUND)

ELEMENT No.	LOAD APPLIED AT					
	L / 3		L / 2		2L / 3	
	λ_{EL}	λ_{SH}	λ_{EL}	λ_{SH}	λ_{EL}	λ_{SH}
18	5.428	7.676	5.338	7.204	5.141	7.183
36	4.372	7.063	4.368	5.724	4.181	5.615
48	3.897	5.898	3.955	5.586	4.233	5.423
64	3.383	5.642	3.469	5.076	3.34	4.987
Theoretical						
Shakedown	3.375	6.75	3.333	5.625	3.62	5.625
Collapse		7.031		5.625		5.625
Step By Step Finite Element Analysis						
Collapse		7.129		6.145		6.039

* Shakedown load is equal to load factor*P [here P = 100 lb.(444 N)]

The shakedown load at $L/3$, $L/2$, and $2L/3$ are calculated using these formulation and listed in Table 6.1. From these values in the table, we can see the difference between the theoretical results and the numerical results. The difference basically caused by numerical approximation on the one hand and on the other hand theoretical formulation is derived from plastic analysis of structural mechanics, while the numerical method treat the beam as a two-dimensional continuum problem. The formulae to calculate elastic limit and collapse load are also presented by König [120] for the beam and given as below.

Elastic limit load

$$P = \frac{M_o}{\beta L} \frac{4}{\xi(2-3\xi+\xi^2)} \quad \text{for } \xi \leq 2(1-1/\sqrt{\beta})$$

$$P = \frac{M_o}{\beta L} \frac{2-\xi}{\xi(1-\xi)} \quad \text{for } \xi \geq 2(1-1/\sqrt{\beta})$$

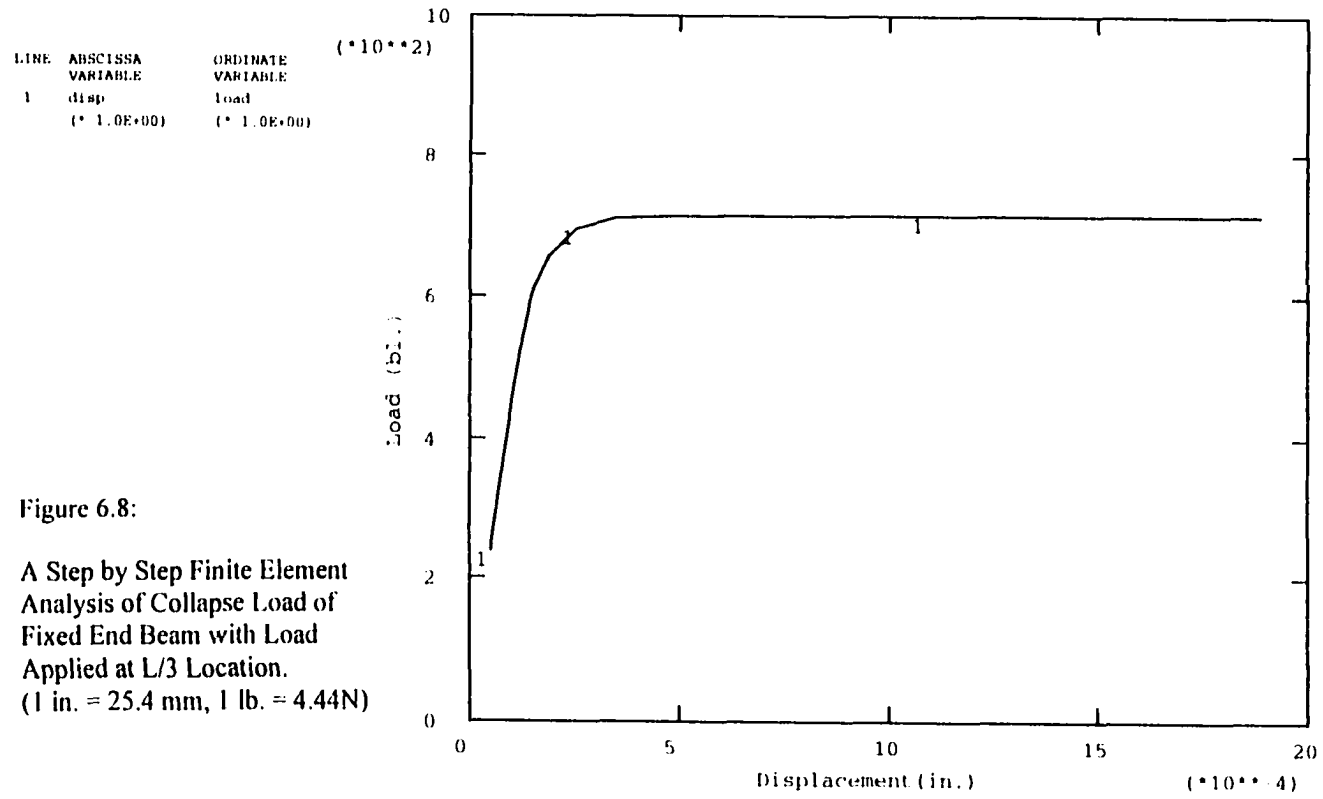
Collapse load

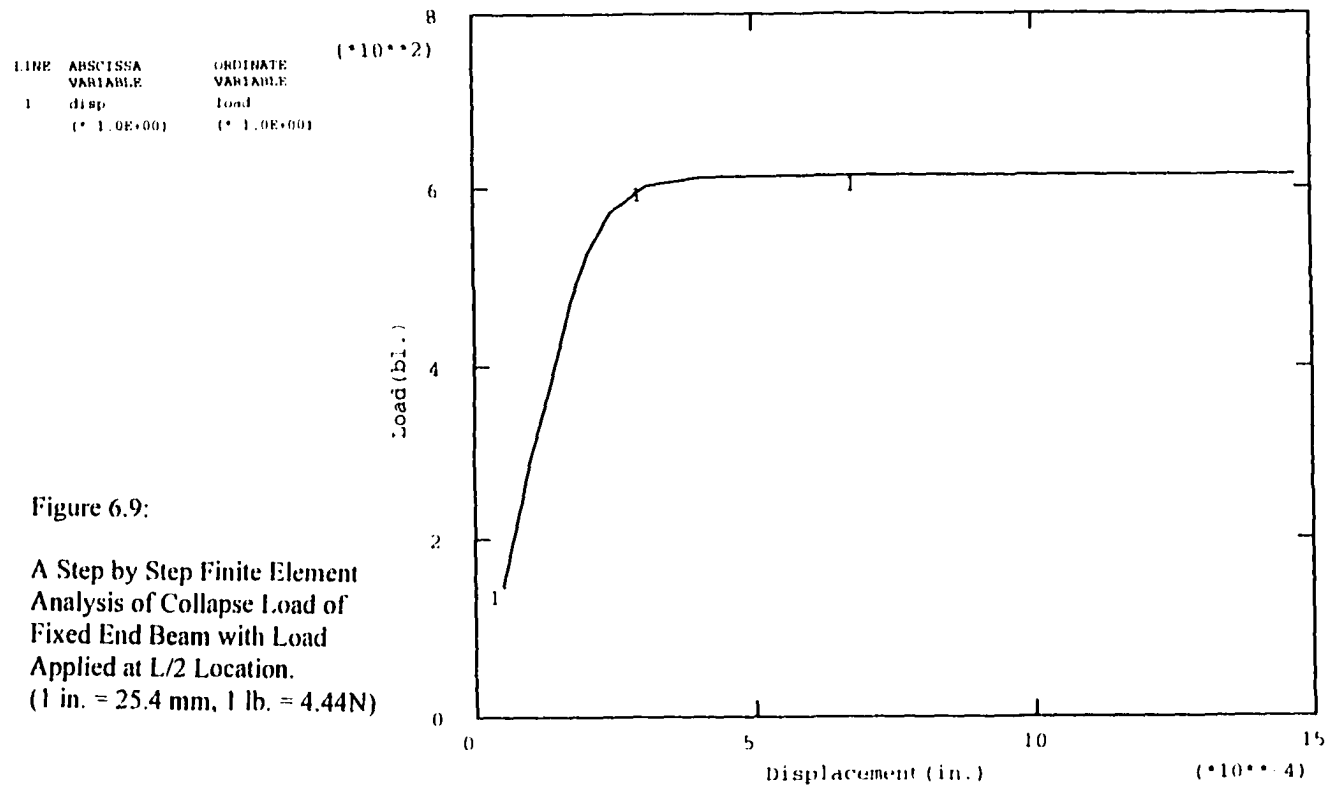
$$P = \frac{M_o}{L} \frac{2-\xi}{\xi(1-\xi)}$$

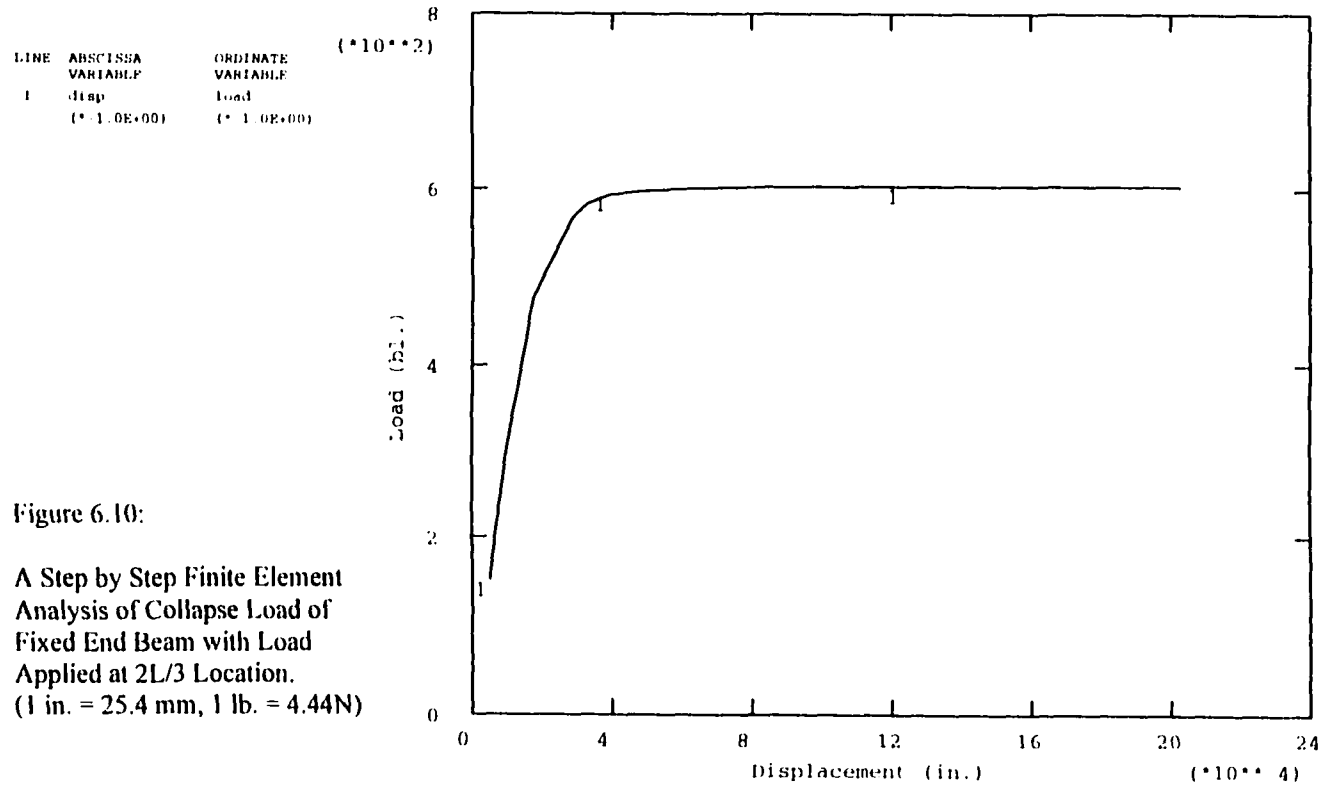
The elastic limit load and collapse load is calculated according these formulations and presented in Table 6.1. The collapse load is also calculated using step by step finite element analysis for the mesh with 64 elements. The results are shown in Fig. 6.8 to Fig. 6.10 for load applied at $L/3$, $L/2$, and $2L/3$, respectively.

6.6.2 EXAMPLE 2

A thin square plate with a central circular hole subjected to biaxial loading at its edges as shown in Fig. 6.11 is examined by the proposed numerical approach. The lower bound shakedown load for the classical plane stress problem has been calculated by Belytschko [48]. He use equilibrated finite element method coupled with nonlinear programming technique to search for the shakedown load factor. His numerical results are relisted in Table 6.2. Based on Maier's approach[47,153], Carradi and Zavelani [49] use compatible finite element method in conjunction with linear programming technique to obtain both lower and upper bound shakedown load factors that are also listed in Table 6.2. Fig. 6.12 and Fig. 6.13 illustrate Belytschko and Carradi's shakedown analysis results, respectively. In the current study, the plate is divided into 40 rectangular elements with 54 nodes as shown in Fig. 6.14. The numerical results of the shakedown analysis are illustrated in Fig. 6.15. Comparing all these numerical results with theoretical results of $0.47 \sigma_o$ [48], Belytschko's value is 9% lower than the analytical value, while that of Carradi 's is 7% higher, and the current results gives 5% higher. The mesh influence on shakedown load is also investigated in this study. For the comparison of mesh size influence, a different mesh is generated and shown in Fig 6.16. These are 6 rings of element around the circular hole. The ring expands from the hole to the edge. The elements within a ring are identical. The element sizes within adjacent rings have a constant







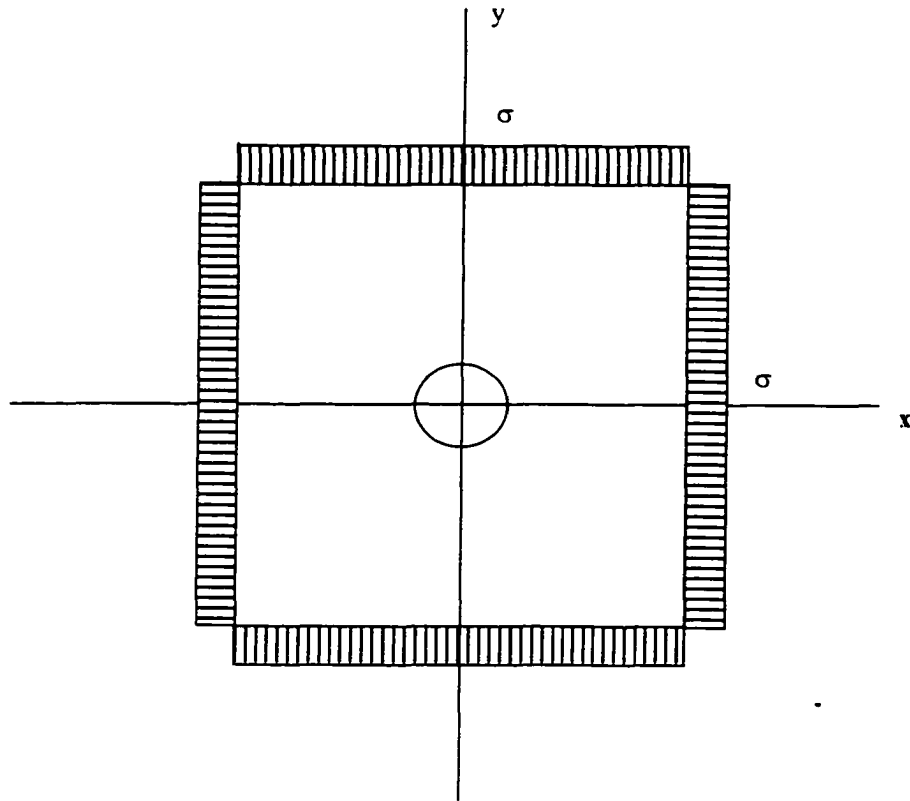


Figure 6.11 A Thin Plane Stress Plate with a Circular Hole and Subjected to Biaxial Tension Stress σ .

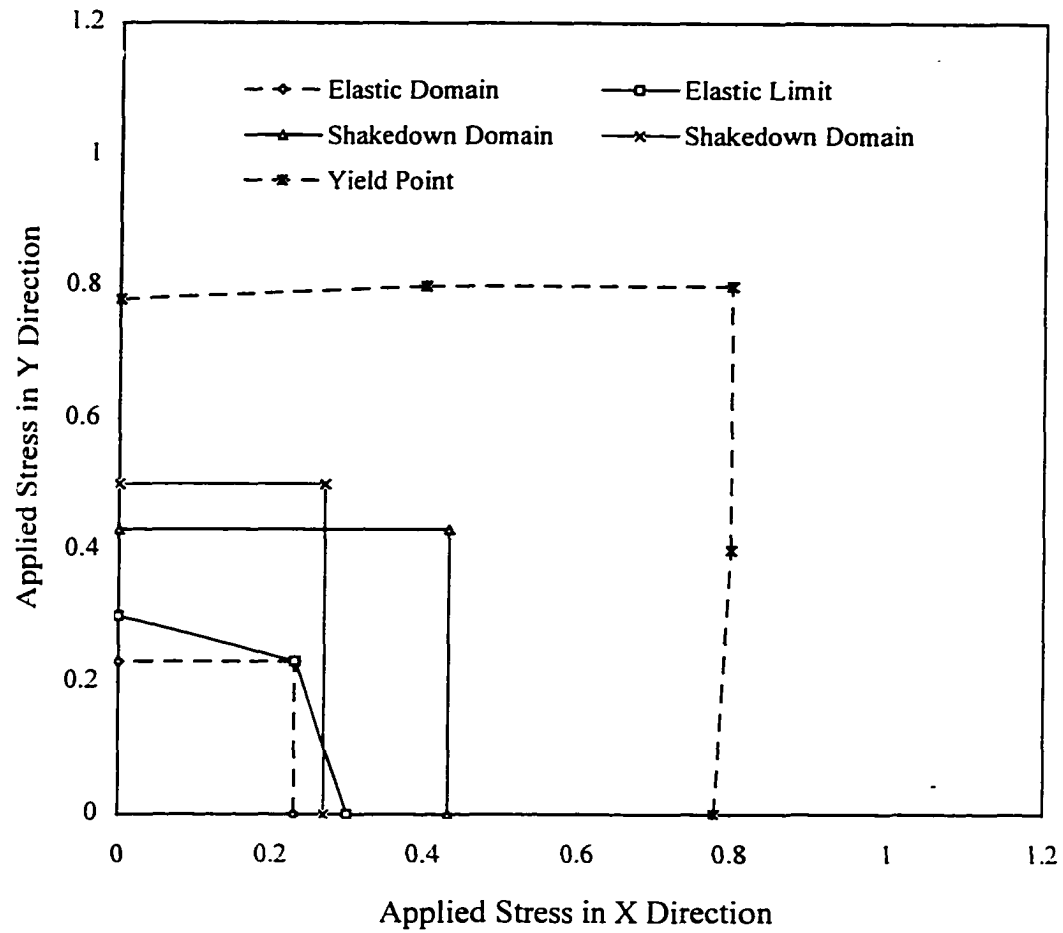


Figure 6.12: Elastic, Shakedown and Limit Load Domains for a Thin Plate with a Circular Hole Subjected to Biaxial Tension Stress Along Its Edges(Adopted from T. Belytschko[10]).

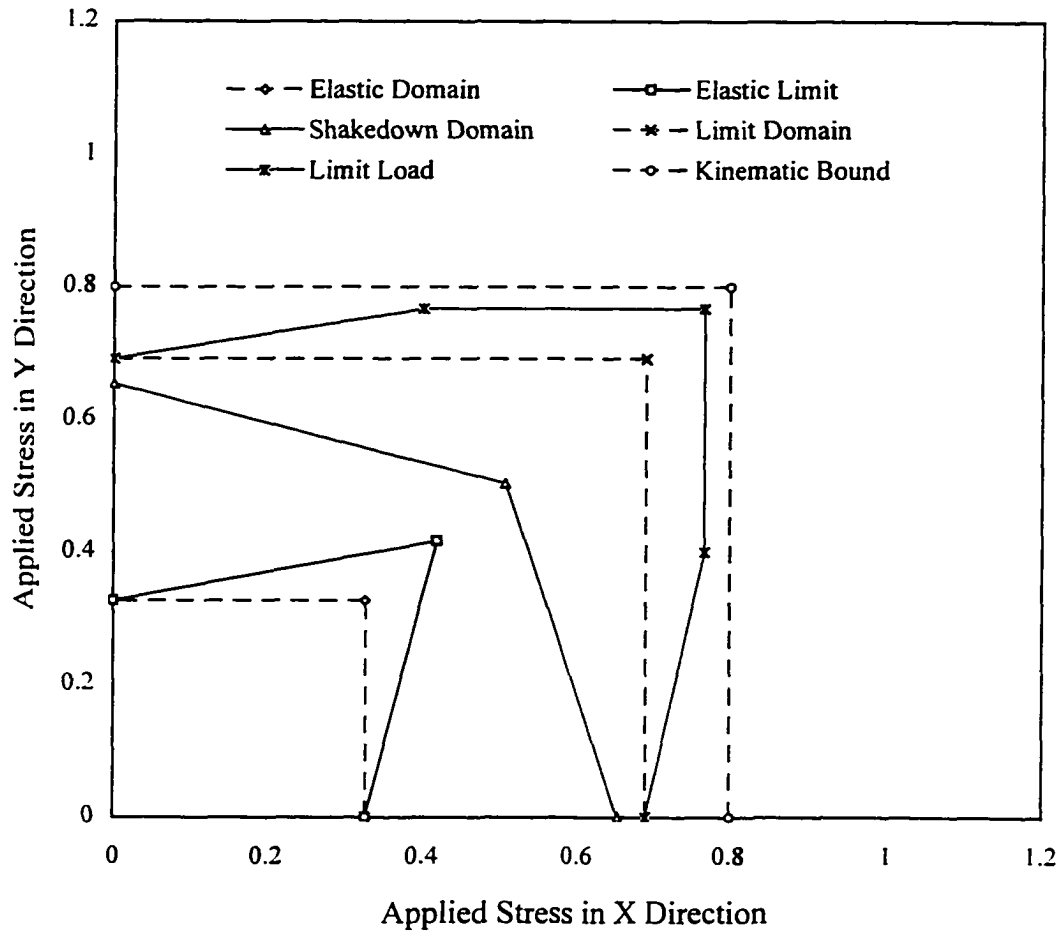


Figure 6.13: Elastic, Shakedown and Limit Load Domains for a Thin Plate with a Circular Hole Subjected to Biaxial Tension Stress Along Its Edges(Adopted from L. Corradi[25]).

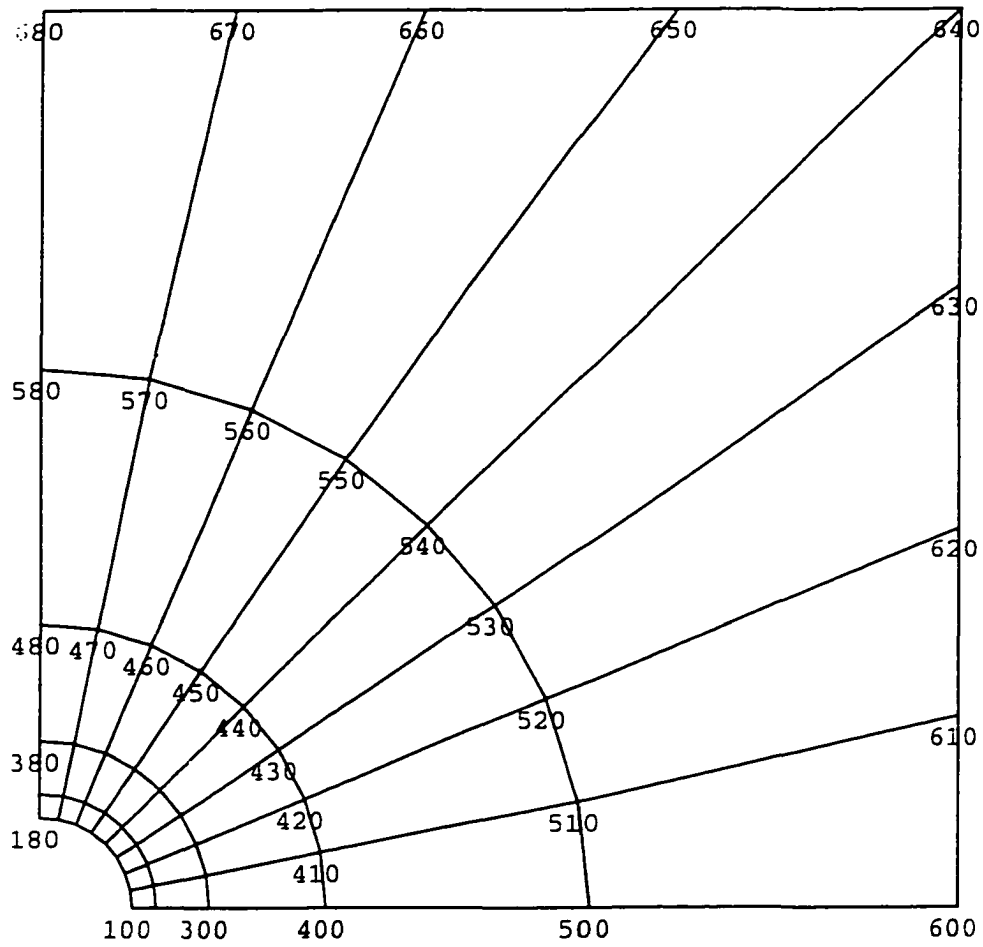


Figure 6.14: A Finite Element Mesh for a Thin Biaxial Tension Square Plate with a Central Hole(Only One Quarter is Shown).

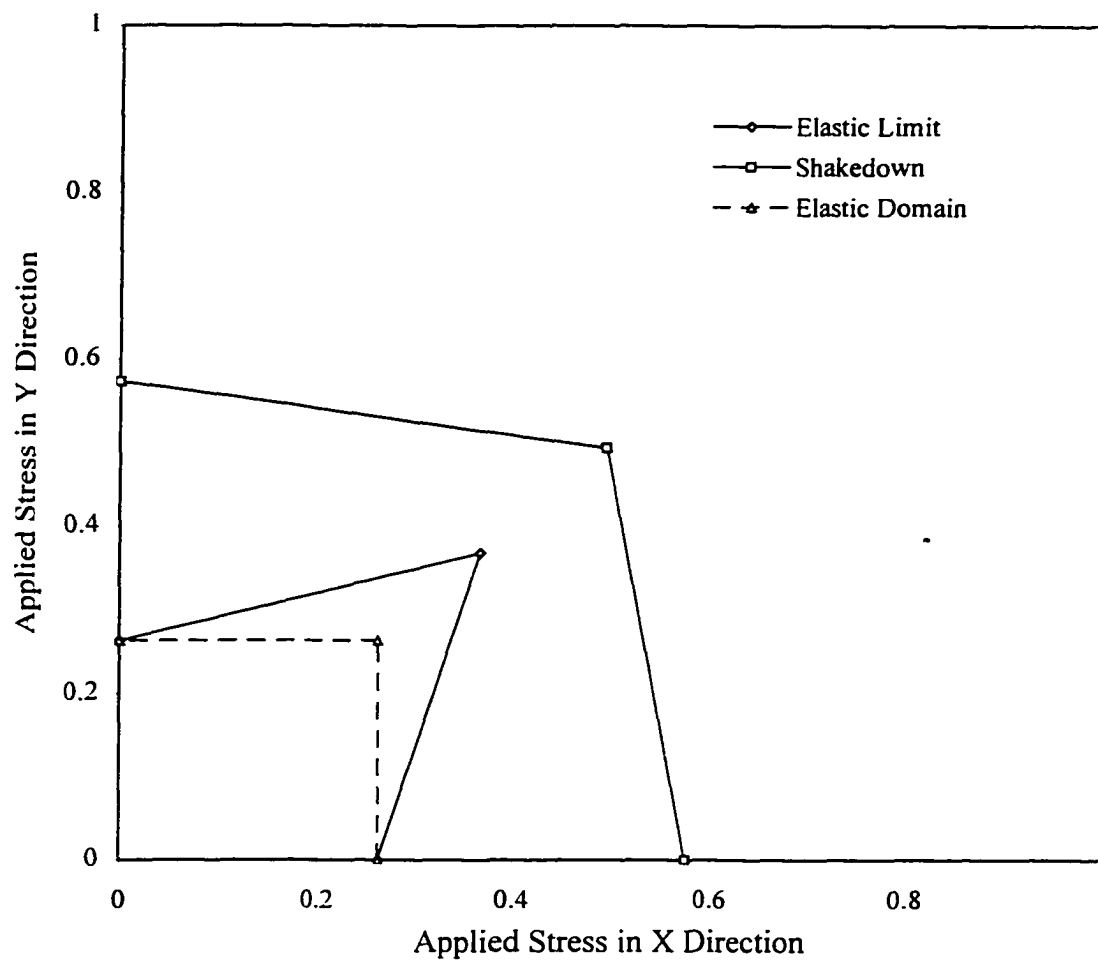


Figure 6.15: Shakedown Analysis Results of Thin Plate with Central Hole.

**The Value in the Plot is the Ratio of σ/σ_0 .

SHAKEDOWN ANALYSIS (UPPER) :

Bias	Shakedown Load
0.60	0.5662
0.65	0.5696
0.70	0.6190
0.80	0.7280

Figure 6.16:

Finite Element Mesh and Numerical Results of Mesh Influence Analysis
 Bias = I_0 / I_1 . Shakedown Load in the Table is σ / σ_0 . σ_0 is initial yield stress.

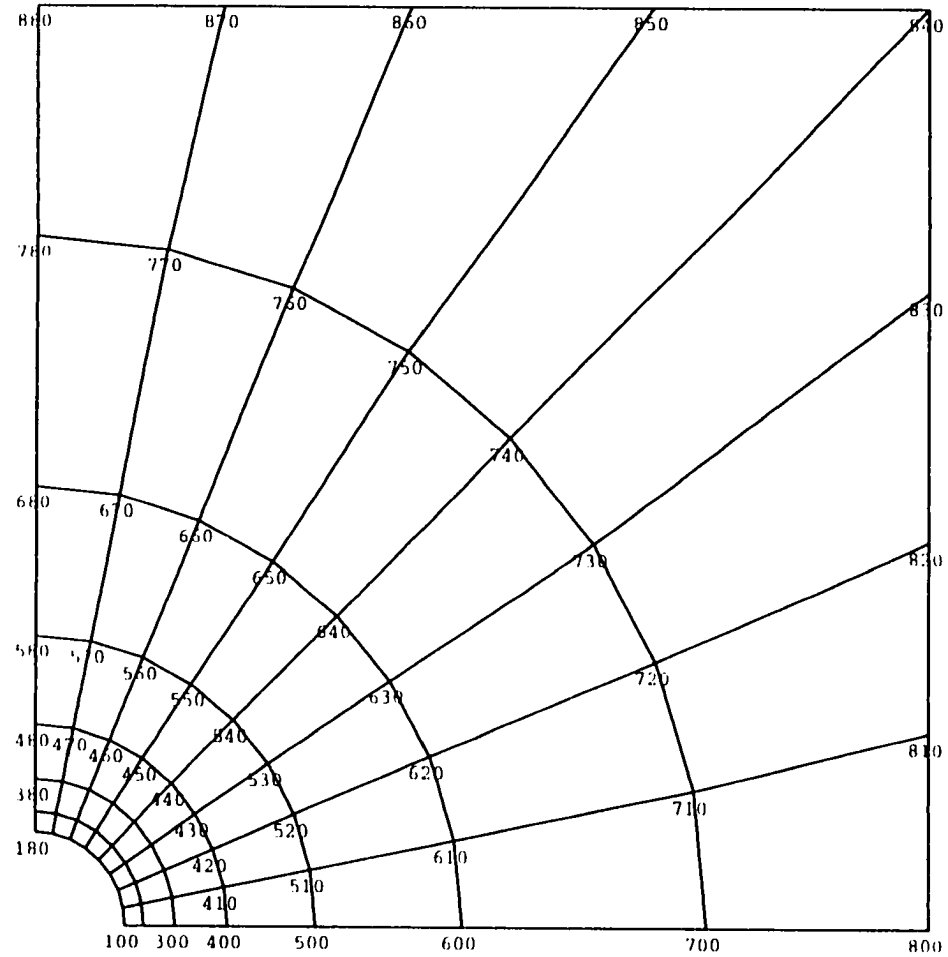


Table 6.2: Shakedown Analysis for a Thin Plate with a Circular Hole

Loading Program	Elastic Limit			Shakedown Load Factor		
	Current	Belytschko	Corradi	Current Upper	Belytschko Lower	Corradi Upper
$T_1 = 0 \quad T_2 = \sigma$	0.263	0.3	0.327	0.574	0.501	0.654
$T_1 = \sigma \quad T_2 = \sigma$	0.368	0.231	0.417	0.494	0.431	0.504

**The Values in the Table is the Ratio of Applied Stress/Yield Stress.

side-size ratio. By adjusting this ratio, the meshes around the hole become finer or course accordingly. For different mesh ratios, the shakedown loads are calculated and listed in Fig. 6.16. The variation of the shakedown load factors with the mesh ratio is shown in Fig. 6.17. It can be seen that as the meshes become finer, shakedown load converges to a constant value.

6.6.3 EXAMPLE 3

In this example, the shakedown analysis is applied to geotechnical material. The problem considered is a shallow stratum of undrained clay under a uniform strip load. The mechanical behavior of the material is considered as elastic-perfectly plastic. The elastic properties are described by elastic modulus $E = 3.5 \cdot 10^7$ psi. and Poisson ratio $\nu = 0.15$. The plastic behavior obeys the Mohr-Coulomb failure criterion with associated flow rule. The boundary conditions are assumed the same as those used by Höeg [172] and Chen [173]. The base of the stratum is rigid and perfectly rough, while vertical boundary is assumed to be rigid and perfectly smooth. A uniform mesh with 120 nodes and 98 rectangular elements that is same as that used by Chen [173] in his limit analysis is employed again in the shakedown analysis. The dimension of this stratum and its finite element model are shown in Fig. 6.18.

Upper bound shakedown load is calculated by using the loading program shown in Fig. 6.19 and the result is given in Table 6.3. The limit analysis of the plane strain problem has been conducted by Chen [173], among others, using Von Mises yield criterion. These results are also provided in Table 6.3. From Table 6.3, it can be seen that the upper bound shakedown load is slightly lower than value obtained from limit analysis. The collapse load is also calculated in this study by tracing the load displacement curve. The result is shown in Fig. 6.20 and the limit load is 104 psi. Therefore, Mohr-Coulomb criterion gives higher limit load value than Von Mises criterion.

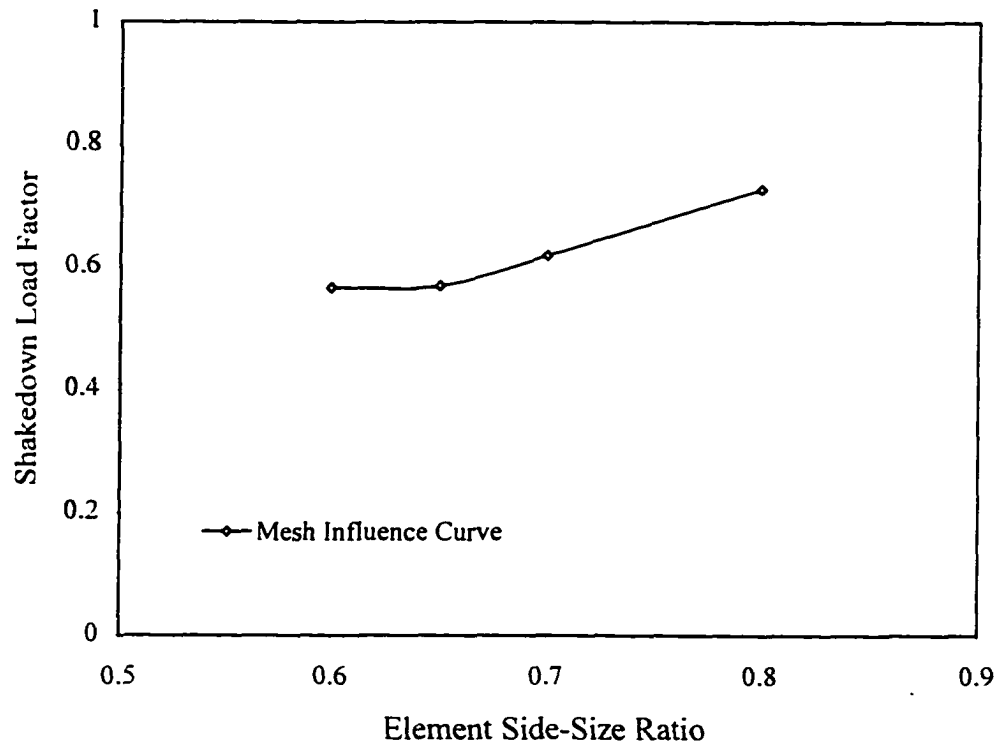


Figure 6.17 Finite Element Mesh Size Influence on Shakedown Load Factor for Thin Plate with Circular Central Hole and Subjected to Biaxial Tension Stress.

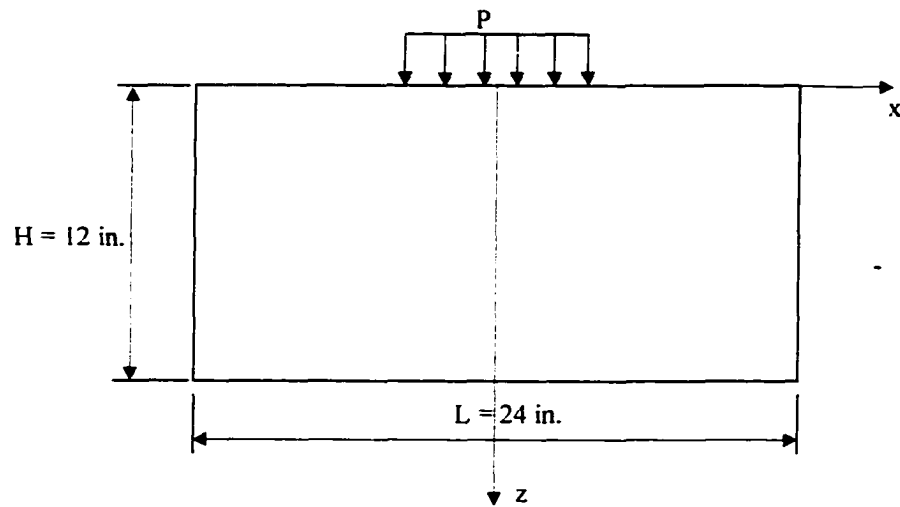


Figure 6.18(a): A Stratum Supported by Rigid Sublayer Subjected to Uniformly Distributed Strip Load(1 in. = 25.4 mm. 1 psi. = 6.895 kPa.).

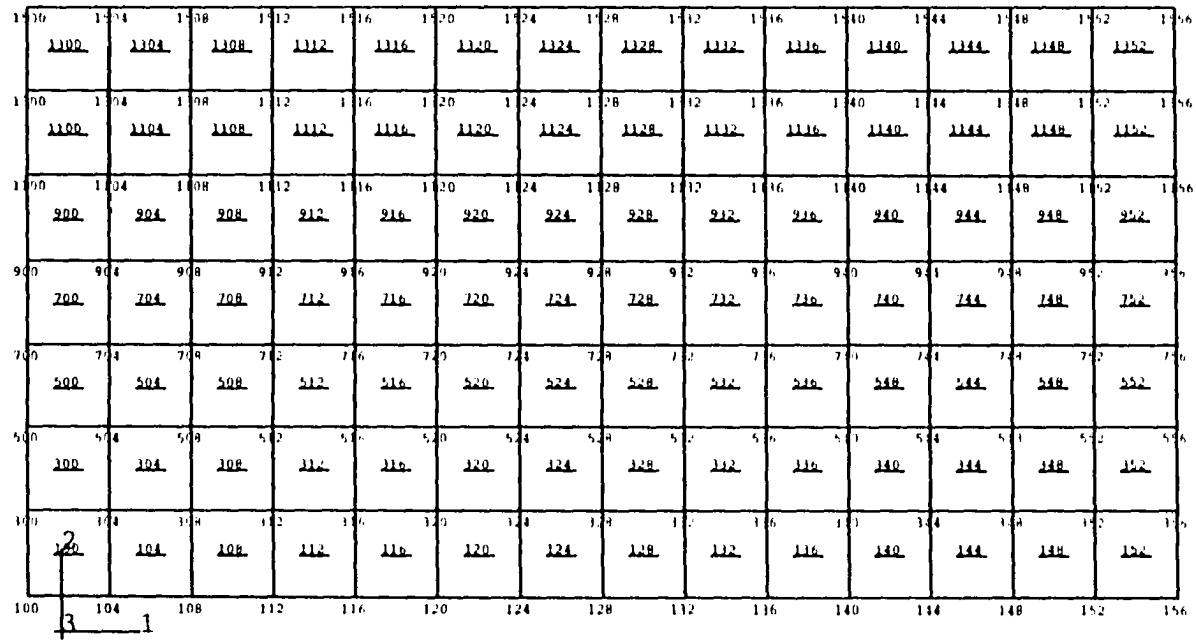


Figure 6.18(b): Finite Element Mesh for Half of the Stratum.

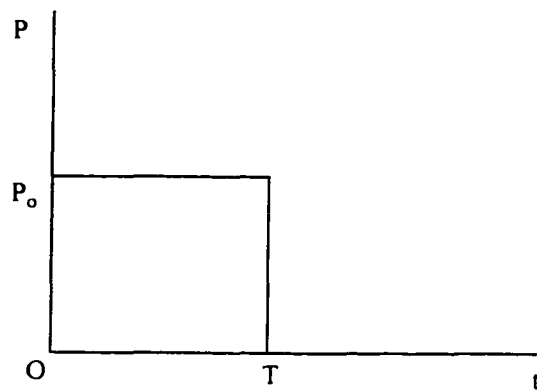
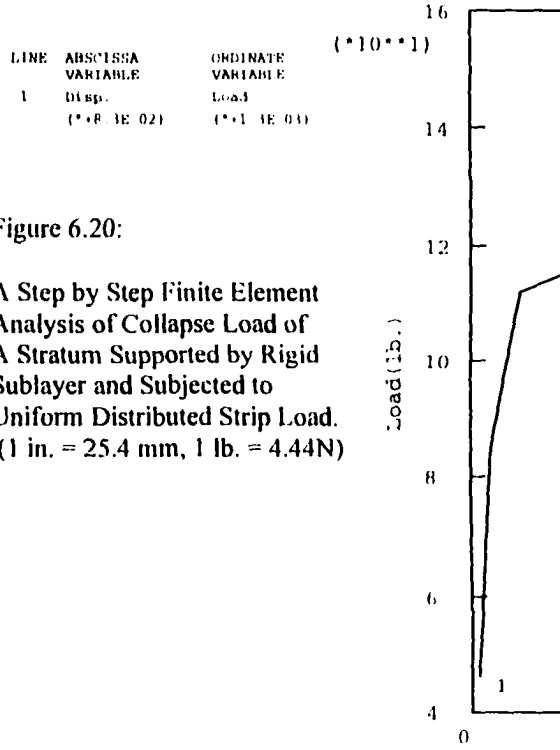


Figure 6.19 Loading Program Used in Upper Bound Shakedown Analysis of a Stratum Supported by Rigid Sublayer.



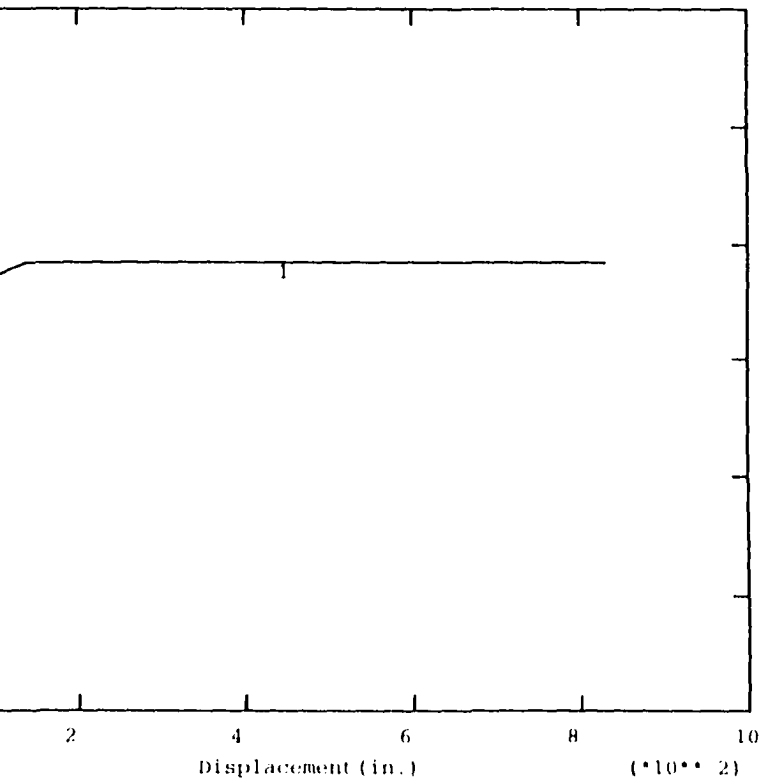


Table 6.3 Collapse Loads for the Stratum

Reference	Analysis Method	Material Model	Collapse Load (psi.)
Höeg	Elastic-Plastic Analysis – F. D. M.	Trasca	90
Chen	Elastic-Plastic Analysis – F. E. M.	Von Mises	92
Valliappan[174]	Elastic-Plastic Analysis – F. E. M.	Von Mises	78
Aboustit[53]	Limit Analysis – F. E. M.	Von Mises	85
Current Study	Elastic-Plastic Analysis – F. E. M.	Mohr-Coulomb	106
Current Study	Shakedown Analysis – Upper Bound	Mohr-Coulomb	80

* F. D. M. For Finite Difference Method.

** F. E. M. For Finite Element Method.

6.6.4 EXAMPLE 4

The approximate lower bound shakedown loads for two-layered pavement system have been calculated in chapter V. In this example, the upper bound shakedown loads will be examined for the same problem by using the proposed numerical algorithm. The finite element mesh and the material used in the analysis can be found in Fig.5.16 and Table 5.2, respectively. The numerical results for different elastic modulus of asphalt layer are shown in Fig. 6.21. From these curves, we can see that the increases of elastic modulus of asphalt layer do not give rise to the shakedown load of the system, which is the same as in lower bound situation. Figure 6.22 shows the differences between lower bound and upper bound results. These curves show that at higher elastic modulus, lower bound and upper bound shakedown load are very close. The variations of upper bound shakedown loads with the thickness of asphalt layer are illustrated in Fig. 6.23 for two different sub-grade materials. These results indicated that shakedown load increases with both the asphalt layer thickness and strength of sub-grade materials. Figure 6.24 and 6.25 show the differences between lower bound loads and upper bound shakedown loads. These results are also compared with the results in[56], which show they are rather consistent.

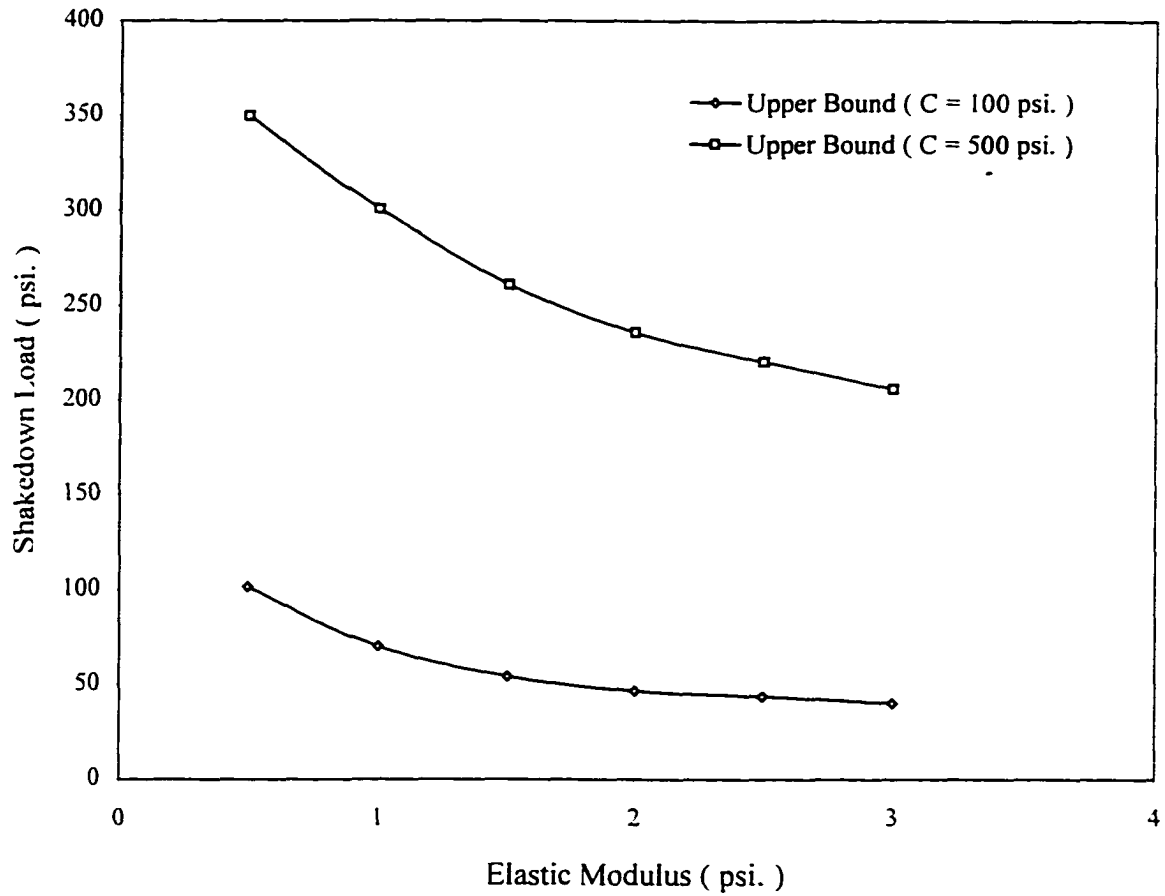


Figure 6.21: The Variations of Shakedown Load with with Elastic Moduli of Surface Loayer with Different Cohensions.(1 psi = 6.895 kPa)

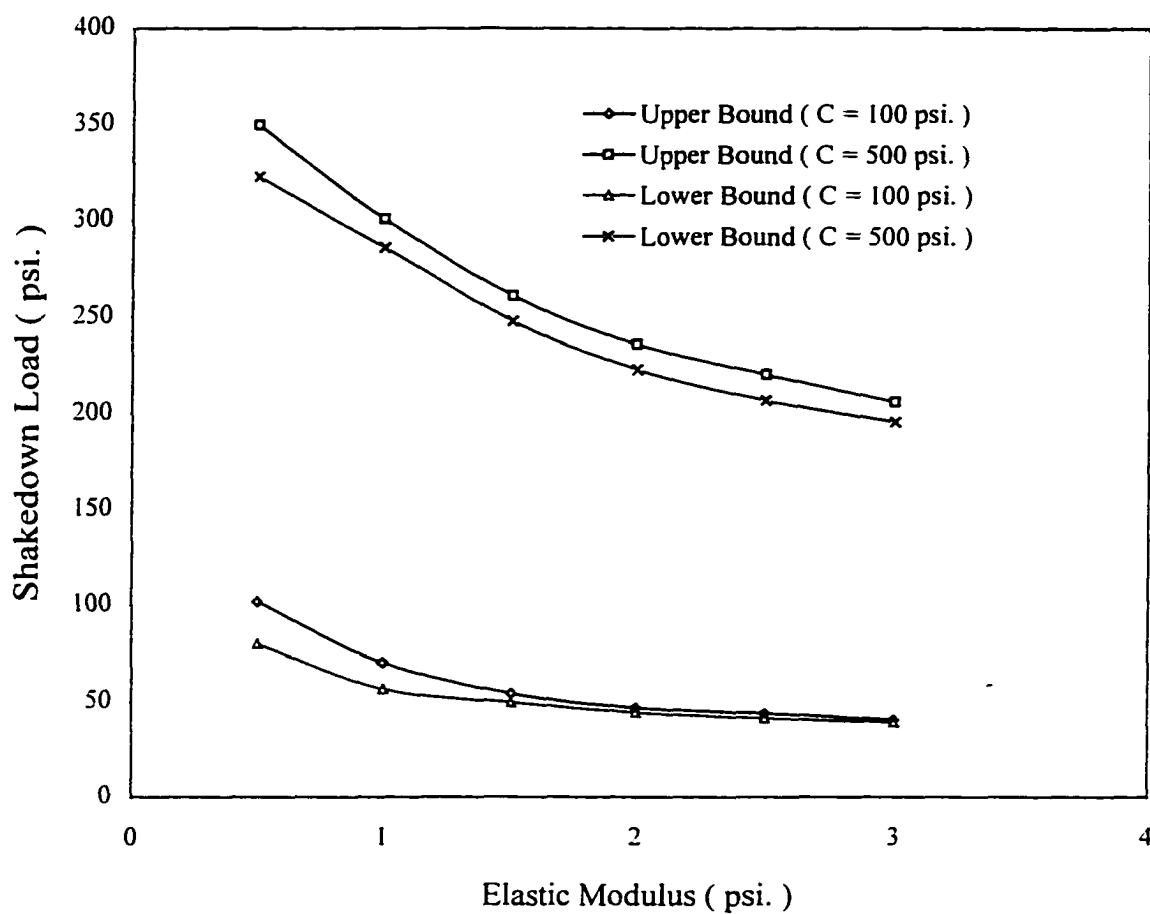


Figure 6.22: The Variations of Shakedown Load with Elastic Moduli of Surface Loayer with Different Cohesion(1 psi = 6.895 kPa).

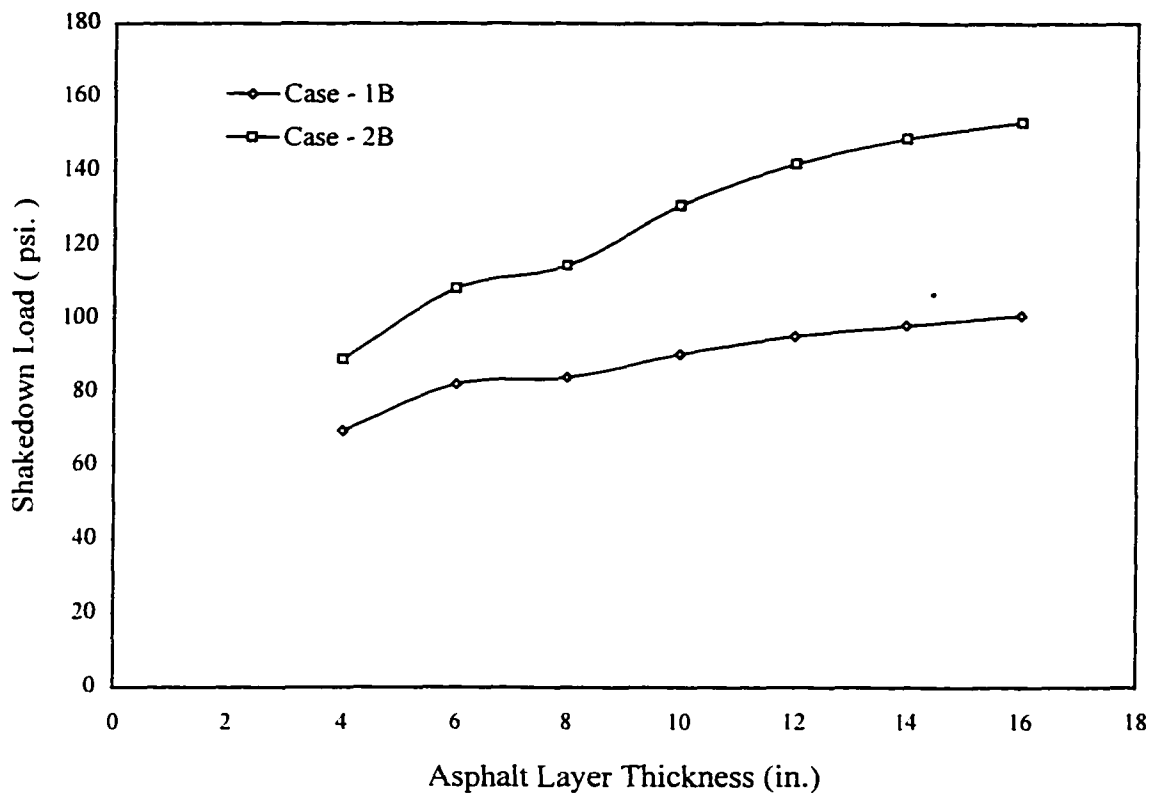


Figure 6.23: The Variations of Shakedown Load with Surface Layer Thickness for Stiff Subgrade(Upper Bound).

** 1 psi. = 6.895 kPa; 1 in. = 25.4 mm.

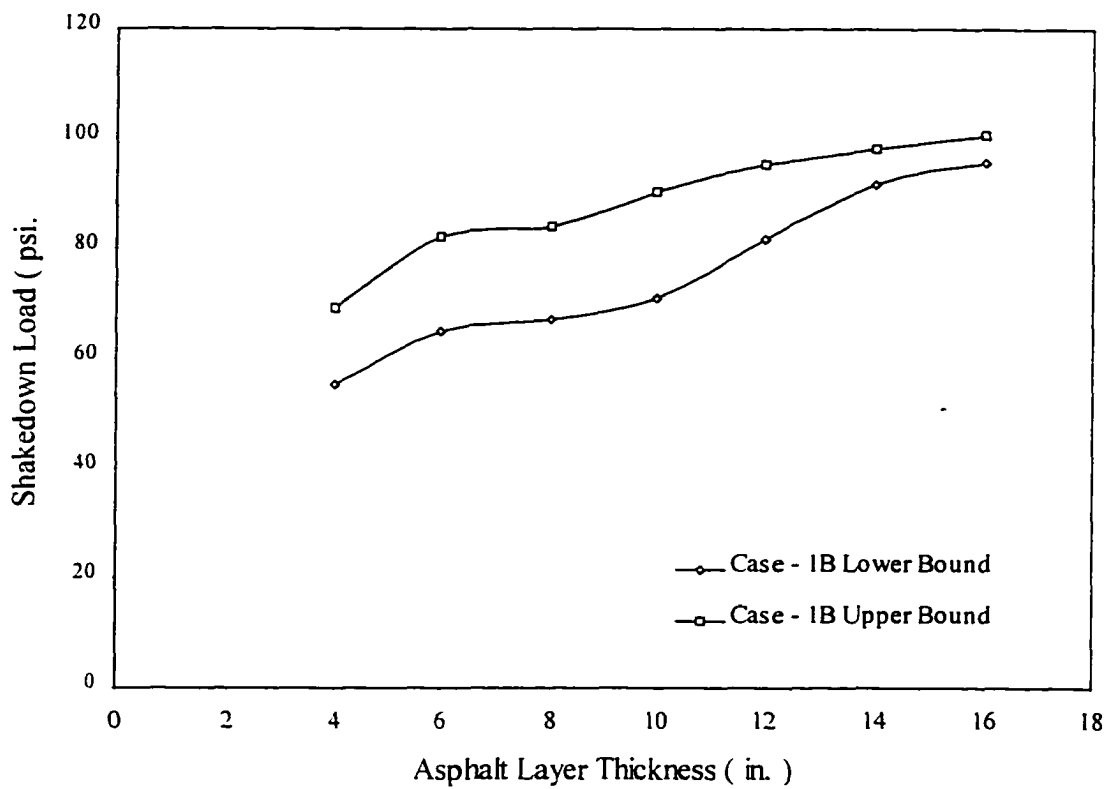


Figure 6.24: The Variations of Shakedown Load with Surface Layer Thickness for Soft Subgrade(Upper & Lower Bound).

** 1 in. = 25.4 mm; 1 psi. = 6.895 kPa.

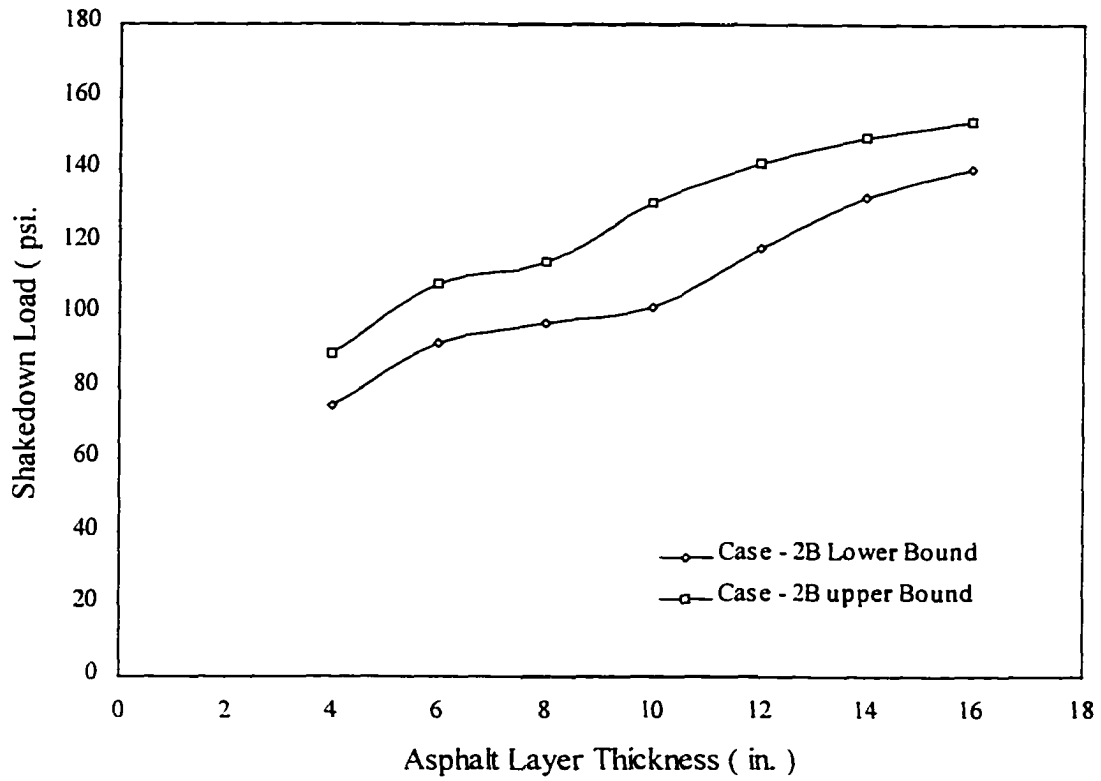


Figure 6.25 The Variations of Shakedown Load with Surface Layer Thickness for Stiff Subgrade(Upper and Lower Bound).

** 1 in. = 25.4 mm; 1 psi. = 6.895 kPa.

SUMMARY

The kinematic shakedown theory is briefly reviewed in this chapter. An algorithm that utilize the eigen-mode to construct an arbitrary admissible plastic deformation path is proposed to calculate the safety load factor by using Mamanjarzh's convex analysis approach to the upper bound shakedown problem. This proposed numerical algorithm has two distinctive aspects from other approaches.

1. The convex approach proposed by Kamenjarzh does not require the yield surface be piecewise linearized.
2. The orientation of an admissible plastic deformation path constructed by using eigen-mode does not fix in a constant direction.

To save computation resource in the search for the optimum direction and to minimize the objective function, a multidirectional search algorithm is employed in the optimization process.

Several classical problems are re-examined by using the proposed numerical algorithm. The numerical results show very good consistency with the available analytical and numerical results. The influence of a finite element size and element side-size ratio is also investigated in this study. The results for the number of problems have indicated that as the mesh size becomes small and finer, the upper bound shakedown load approaches a constant value.

Comparisons between the upper bound and lower bound shakedown loads are also made among these problems. The results show that upper bound values are higher than lower bound values for all of the problems and they are very close at some portions of these problems. It may conclude that the true shakedown load may lie between these upper and lower values.

The algorithm that uses eigen-mode to construct an admissible plastic deformation path works very well with small and medium size problems. The computations converge very quickly to their approximate bounding values. However, when the size of the problem becomes large and has a large number of finite elements and nodes, the space for storing every eigen-mode and the loop for searching optimum direction are also increased. Therefore, convergence speed becomes very slow.

As suggested by Prof. Lee [175], a sensitivity analysis of upper bound values to different mass matrices was conducted for the problem with same stiffness matrix. The results show that upper bound shakedown loads are dependent on mass matrix. Considering that different approaches in forming mass matrix will influence shakedown load values of same stiffness matrix, it is recommended by Prof. Lee [175] that the

eigen-mode of stiffness matrix be used in the upper bound shakedown analysis to construct arbitrary admissible plastic deformation path. With regards to this, further investigation is needed.

CHAPTER VII

APPLICATIONS

7.1 INTRODUCTION

In the previous chapters, numerical algorithms have been proposed for fatigue analysis, lower bound shakedown analysis, and upper bound shakedown analysis, respectively. Examples were presented in some chapters and the numerical results were compared with available analytical, experimental, and numerical results. In this chapter, these proposed numerical algorithms are applied to the analysis of actual engineering problems.

7.2 TWO-LAYERED PAVEMENT SYSTEM

A two-layered pavement system as shown in Fig. 7.1 is analyzed in this section. The surface layer is made of asphalt concrete material with elastic modulus $E = 3.0 \cdot 10^6$ psi.(20700 Mpa), Poisson ratio $\nu = 0.35$, cohesion $C = 1100$ psi. (7.6 Mpa) and internal friction angle $\phi = 48^\circ$ at temperature $T = 10^\circ$ F. The subgrade layer is made of conventional sand material with $E = 7800$ psi.(54 Mpa), $\nu = 0.45$, $C = 12$ psi.(0.08 Mpa), and $\phi = 0^\circ$. Fatigue and shakedown behavior were investigated for the system, respectively. Combined effects of fatigue and shakedown mechanism will be discussed according to the numerical results of fatigue and shakedown analysis.

7.2.1 Fatigue Analysis

Fatigue Analysis was conducted for the two-layered pavement system by using the proposed numerical algorithm. Considering fatigue failure mostly occurs in the surface layer, the asphalt concrete layer is treated as elastic-plastic material obeys Drucker-Prager yield criterion and the subgrade layer is assumed to behave elastically like half elastic space. Every layer is divided into numbers of four-node elements. The finite element mesh for the system is shown in Fig. 7.2. Following the numerical procedure that has been discussed in chapter IV, fatigue analysis was carried out. Elastic-plastic behavior was analyzed by using ABAQUS[148] to obtain load versus displacement and J-integral versus displacement curves for different initial crack lengths. These data are then taken as input data of program FLAP_1.0 to perform fatigue analysis for the whole pavement system. About 20 different load levels were considered in the fatigue analysis. The numerical results of fatigue crack growth rate for the system are presented in Fig. 7.3. From this figure, we can see that for every load level, fatigue behavior of the system is uniquely represented by

the curve of fatigue crack growth rate under given boundary conditions. For each load level, fatigue life was calculated and plotted in Fig. 7.4.

7.2.2 Shakedown analysis

For the same system, shakedown analysis was also conducted to calculate approximate lower bound and upper bound load values. In shakedown analysis, both the surface layer and subgrade layer were treated as elastic-plastic materials that obey Mohr-Coulomb yield criterion. The finite element mesh of the system for shakedown analysis is shown in Fig. 7.5. The existence of crack in the surface layer introduces singularity stress fields around the crack tip where the shakedown theory is not applicable. To approximately calculate the shakedown load, two steps were taken. First, the sharp crack is replaced by a notch with finite radius at its root as shown in Fig. 7.5b. The shakedown analysis was conducted for different notch sizes and the results were presented in Fig. 7.6. The numerical results provide us rather low shakedown load values. The reason for these is obvious. The elastic solution at the root of the notch under reference load gives very high stress values compared with other regions as shown in Fig. 7.7. In actual situation, the material will experience elastic-plastic deformation, the high stress level around notch root will redistribute whenever it excess yield stress of the material and plastic zone will form around the root of the notch. To be consistent with the actual situation, the second step was taken. The elements that have rather high stress values around notch root were taken out from the shakedown analysis so that higher shakedown load values were obtained. The results were also shown in Fig. 7.6. The upper bound shakedown loads were also calculated for different notch sizes same as lower bound cases and presented in Fig. 7.6 too.

7.2.3 Fatigue and Shakedown

In fatigue analysis, critical crack lengths with respect to each load level can be calculated, and the curve of the load level which vary with crack lengths was developed as shown in Fig. 7.8. Comparing the results of shakedown analysis as shown in Fig. 7.6, the shakedown analysis gives much lower values than fatigue analysis. Two reasons were considered to cause the differences.

- a. Different crack shape. Sharp crack was used in fatigue analysis, while notch was used in shakedown analysis.
- b. Different finite element mesh. Finer finite element mesh was used in fatigue analysis than that used in the shakedown analysis as shown in Fig. 7.2 and Fig. 7.5.

Shakedown behavior of a cracked body has been investigated experimentally, analytically, and numerically by Huang and Stein [176-178]. As indicated in their studies, the threshold for crack propagation in cyclic load condition is due to the shakedown of the cracked body. Therefore, the fatigue threshold of cracked body can be predicted by using the shakedown theory. As most fatigue tests have

shown that the load level at fatigue threshold is lower than the load level when fatigue failure occurs, the current results of fatigue and shakedown analysis are consistent with Huang and Stein's [176] results.

7.3 SHAKEDOWN OF THREE-LAYERED PAVEMENT

Shakedown behavior of a three-layered pavement system, as shown in Fig. 7.9, is analyzed in this section. Lower and upper bound shakedown loads were calculated for different thickness of the surface layer. The influence of material properties such as cohesion and internal friction angle on shakedown load was investigated. The numerical results were compared among plane strain, axisymmetric, and three-dimensional conditions. The surface layer of the pavement system is made of asphalt concrete with cohesion $C = 1100$ psi.(7.6 Mpa) and the internal friction angle $\phi = 35^\circ$. The base material is made of gravel with $C = 5$ psi.(0.0345 Mpa) and $\phi = 40^\circ$. Silty material is used for subgrade where $C = 6$ psi. (0.414 Mpa) and $\phi = 0^\circ$. The dimension of the pavement system and the material properties are given in Fig. 7.9 and Table 7.1, respectively.

7.3.1 Results

The actual pavement system can be treated as a plane strain problem (by considering that the traffic load applies along longitude direction and deformation is uniformly distributed in the same direction), axisymmetric (under consideration that the tire load acts on a circular area), and three-dimensional problem. Under a plane strain condition, shakedown loads (both the lower and upper bound values) were calculated for different thickness of the surface layer as described in Table 7.2. The calculated results are illustrated in Fig. 7.10. These results indicate that shakedown loads increase with the thickness of surface layer. For a given thickness of the surface layer, lower shakedown loads were calculated for different cohesion and internal friction angles of base layer under plane strain and axisymmetric conditions. The computed results show that internal friction angle does not have significant influence on shakedown load values, which can be see from Fig. 7.11 - 7.15. Figure 7.11 shows the lower bound shakedown loads at different cohesion $C = 0, 0.0345, \text{ and } 0.069$ Mpa. It indicates that large C value gives higher shakedown load values. This figure also shows that the shakedown load of plane strain condition gives lower value than axisymmetric condition for $C = 0.0345$ Mpa. Under plane strain, axisymmetric, and three-dimensional conditions, upper bound shakedown loads were also calculated for different base materials and are presented in Fig. 7.12. The comparison shows that the results between axisymmetric and three-dimensional conditions are very close at $C = 0.0345$ Mpa, but the results for plane strain condition are very low when compared with the results for axisymmetric and three-dimensional conditions. Fig. 7.13 to 7.15 show the difference between lower bound and upper bound shakedown loads for different cohesion values.

7.4 SUMMARY

Fatigue behavior of full-depth pavement of asphalt concrete was analyzed using the proposed numerical algorithm. Fatigue crack growth rate was obtained for the system and fatigue life was predicted. The numerical results show consistency with the fatigue test of asphalt concrete beam[24]. The shakedown analysis was also carried out for the same pavement system. To avoid numerical difficulty, the sharp crack was replaced by a notch with a finite radius at its root. Several different notch sizes were used to calculate the lower bound and upper bound shakedown loads. The variation of shakedown load with notch size was compared with the variation of fatigue failure load with crack length. The result show that the shakedown load is lower than the fatigue failure load. Two reasons may cause the differences: (a) different crack shapes; and (b) different finite element meshes. However, considering that the fatigue threshold is due to the shakedown of the cracked body [60-62], the proposed numerical analysis provides a reasonable result.

A shakedown analysis was also conducted for a full-depth three-layered pavement system. The numerical analysis results show that:

1. The shakedown load increases with the increase of the thickness of the surface layer.
2. The cohesion parameter of the surface layer has significant influence on shakedown load values.
3. The internal friction angle value of the surface layer does not have significant influence on shakedown load values.
4. The shakedown load values have larger difference between plane strain condition and axisymmetric condition the difference between three-dimensional condition and axisymmetric condition.
5. The analysis of finite element size influence on shakedown load does not conduct for these cases discussed in this section. However, it is recommended and necessary to use optimum finite element mesh size to obtain accurate results.
6. Upper bound shakedown analysis requires large amount of CPU time both in extract eigen-value and optimization process. Further investigation is necessary to reduce the dimension of optimization variables and cut short CPU time.

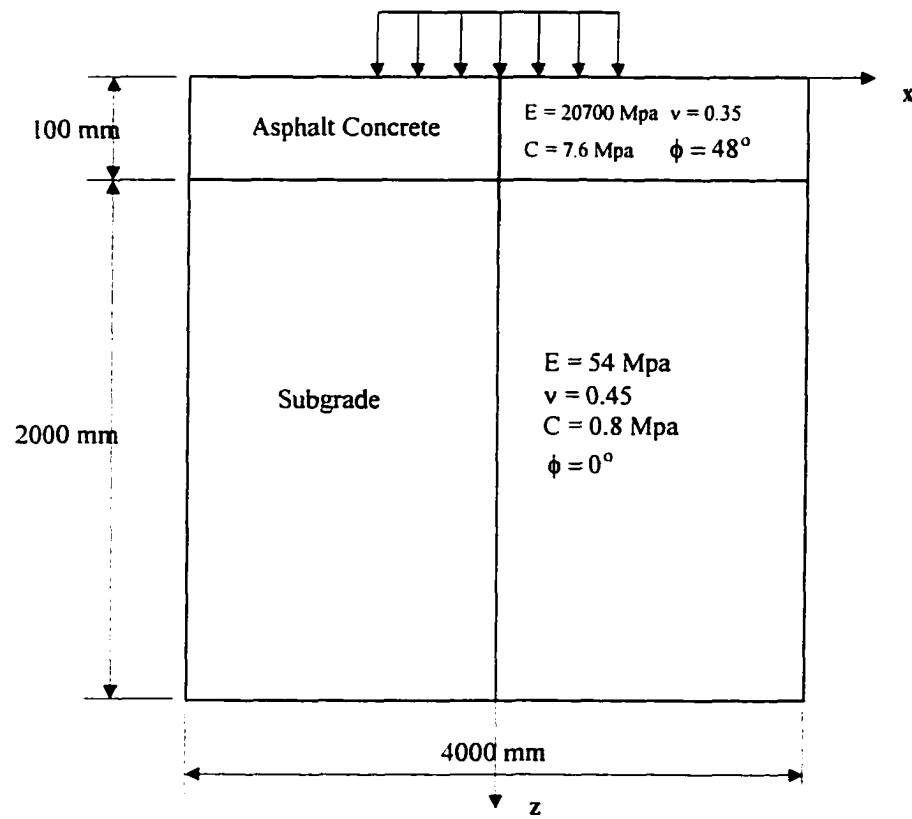


Figure 7.1 Dimension of Two-Layered Pavement System.

Crack Tip Mesh Shown in (b) ->

Figure 7.2a: Finite Element Mesh of Two Layered Pavement System in Fatigue Analysis.

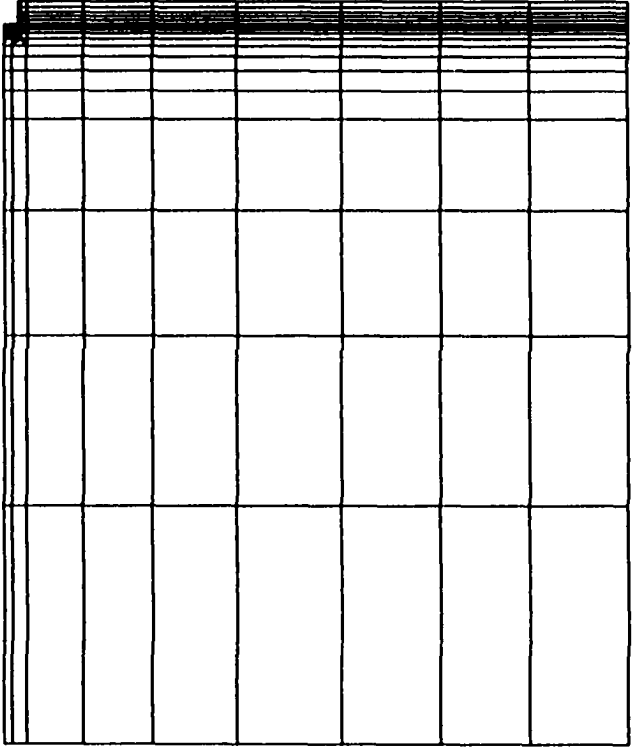
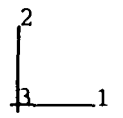
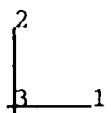
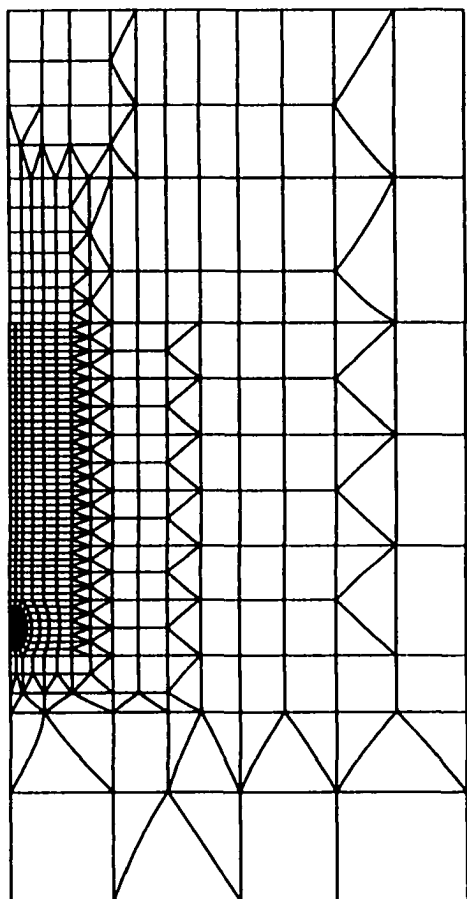


Figure 7.2b: Crack Tip Finite Element Mesh of Two-layered Pavement System in Fatigue Analysis.



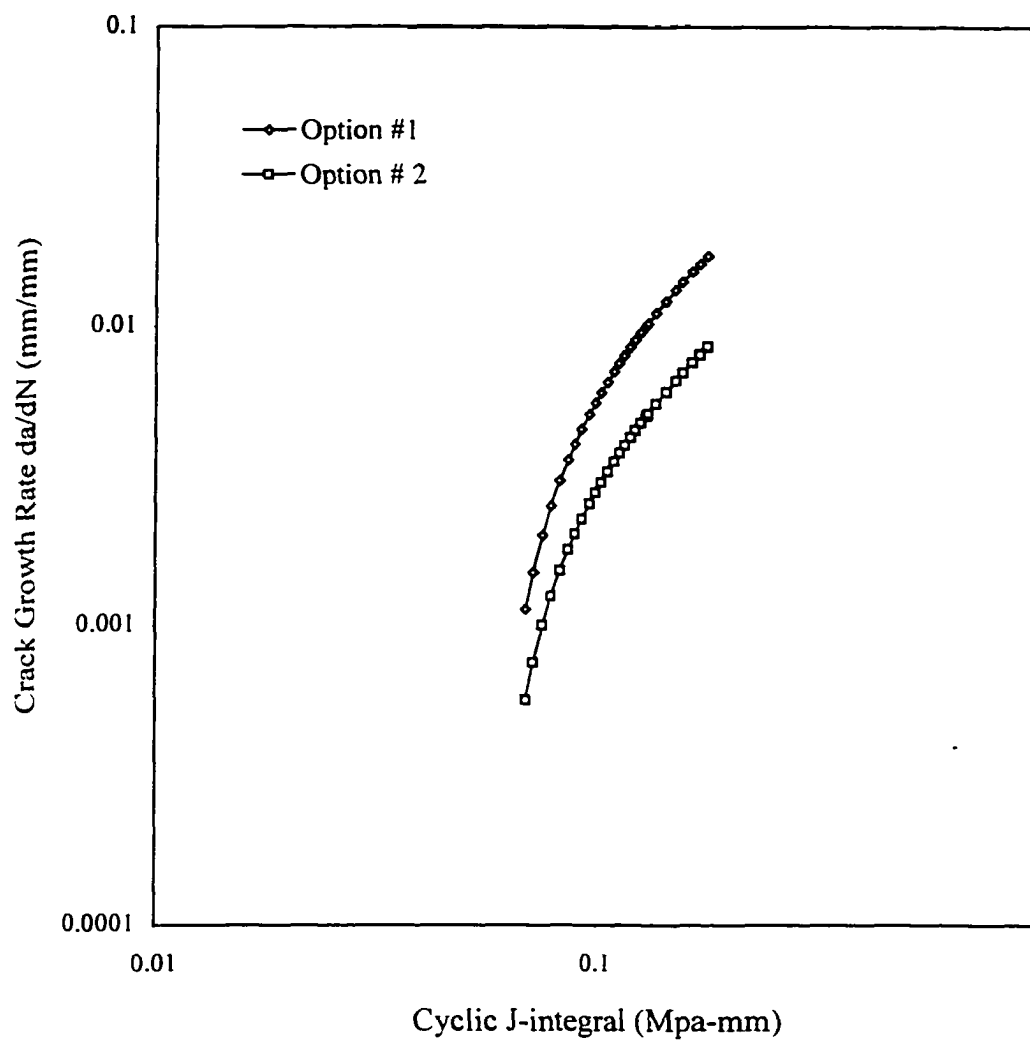


Figure 7.3 Fatigue Crack Growth Rate for Two-Layered Pavement System.
(1) without Modification of da/dN . (2) with Modification of da/dN by Considering Crack Tip Deformation.

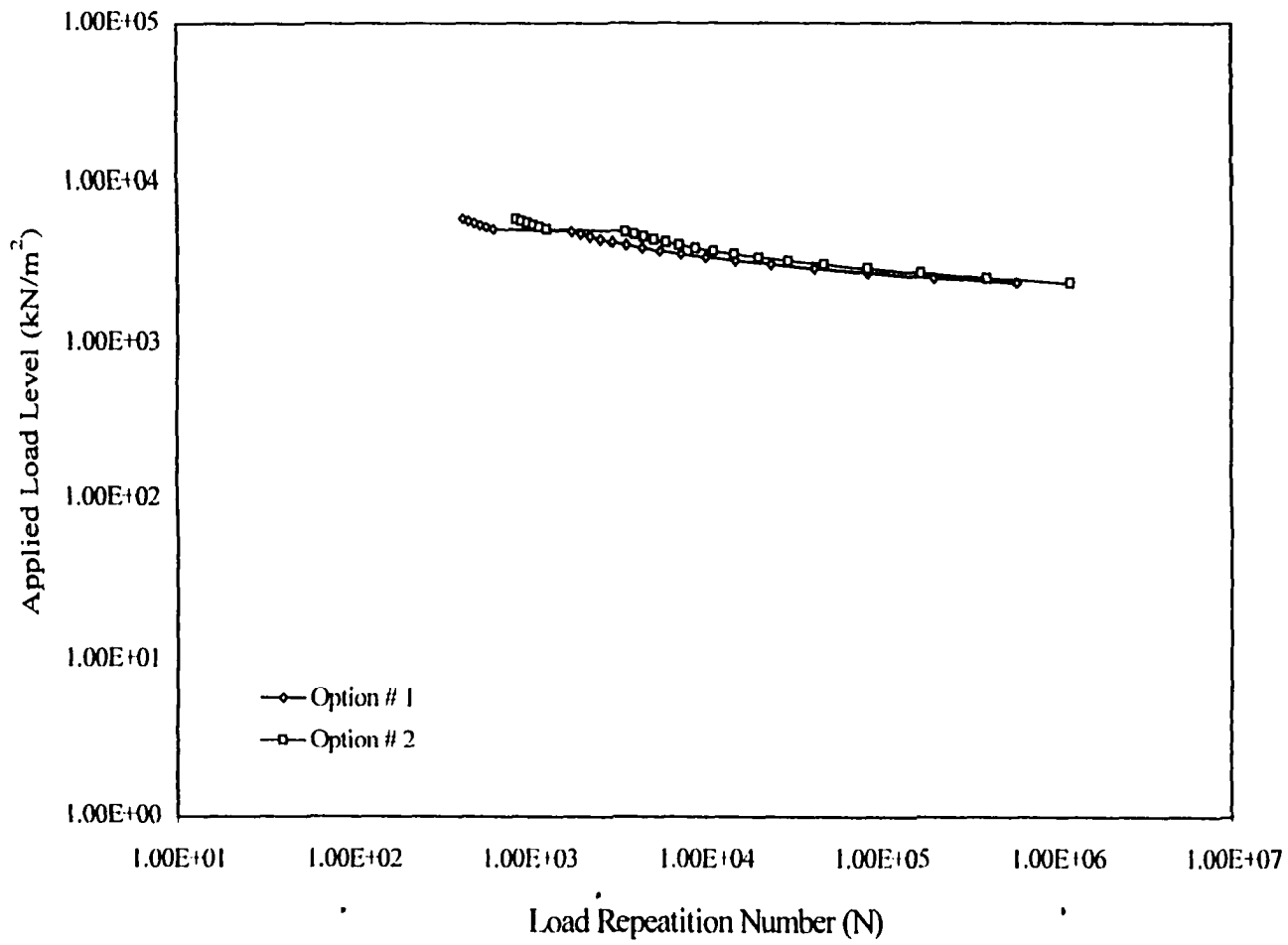


Figure 7.4 Fatigue Life vs. Applied Load Level Curve for Two-Layered Pavement System. (1) without Modification of da/dN . (2) with Modification of da/dN By Considering Crack Tip Deformation.

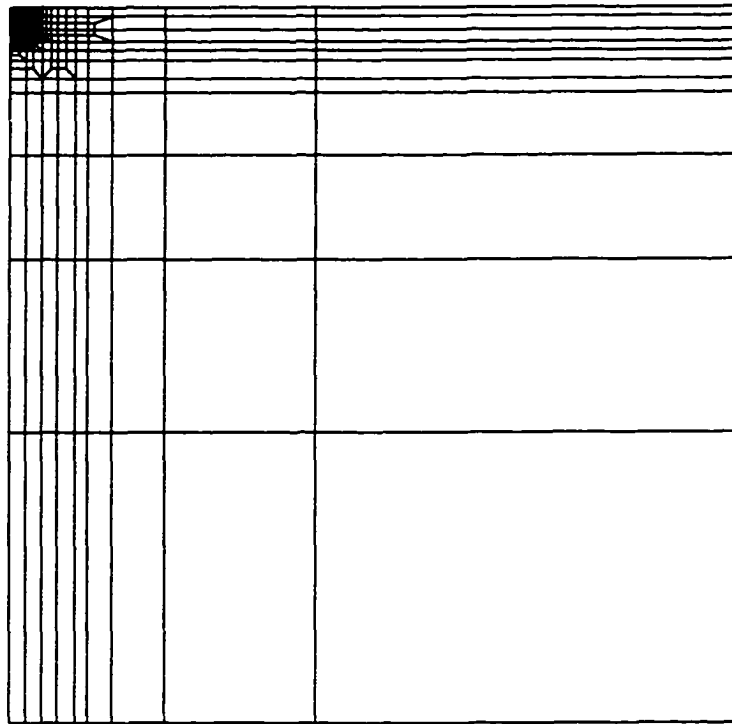


Figure 7.5(a): Finite Element Mesh of Two-Layered Pavement System in Shakedown Analysis.

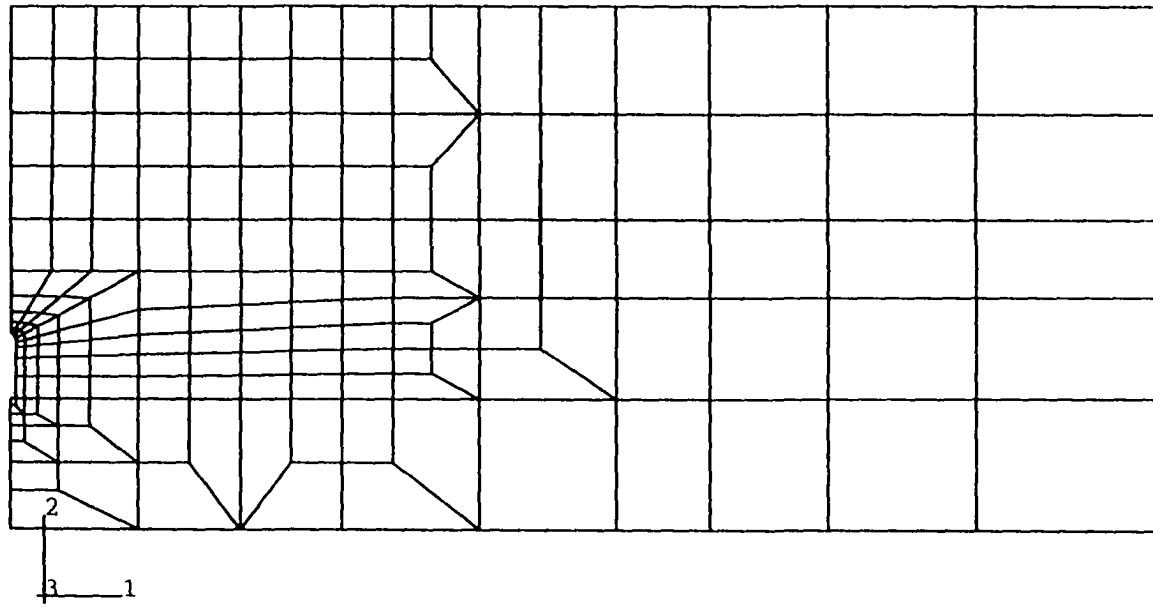


Figure 7.5(b): Notch Tip Finite Element Mesh of Two-Layered Pavement System in Shakedown Analysis.

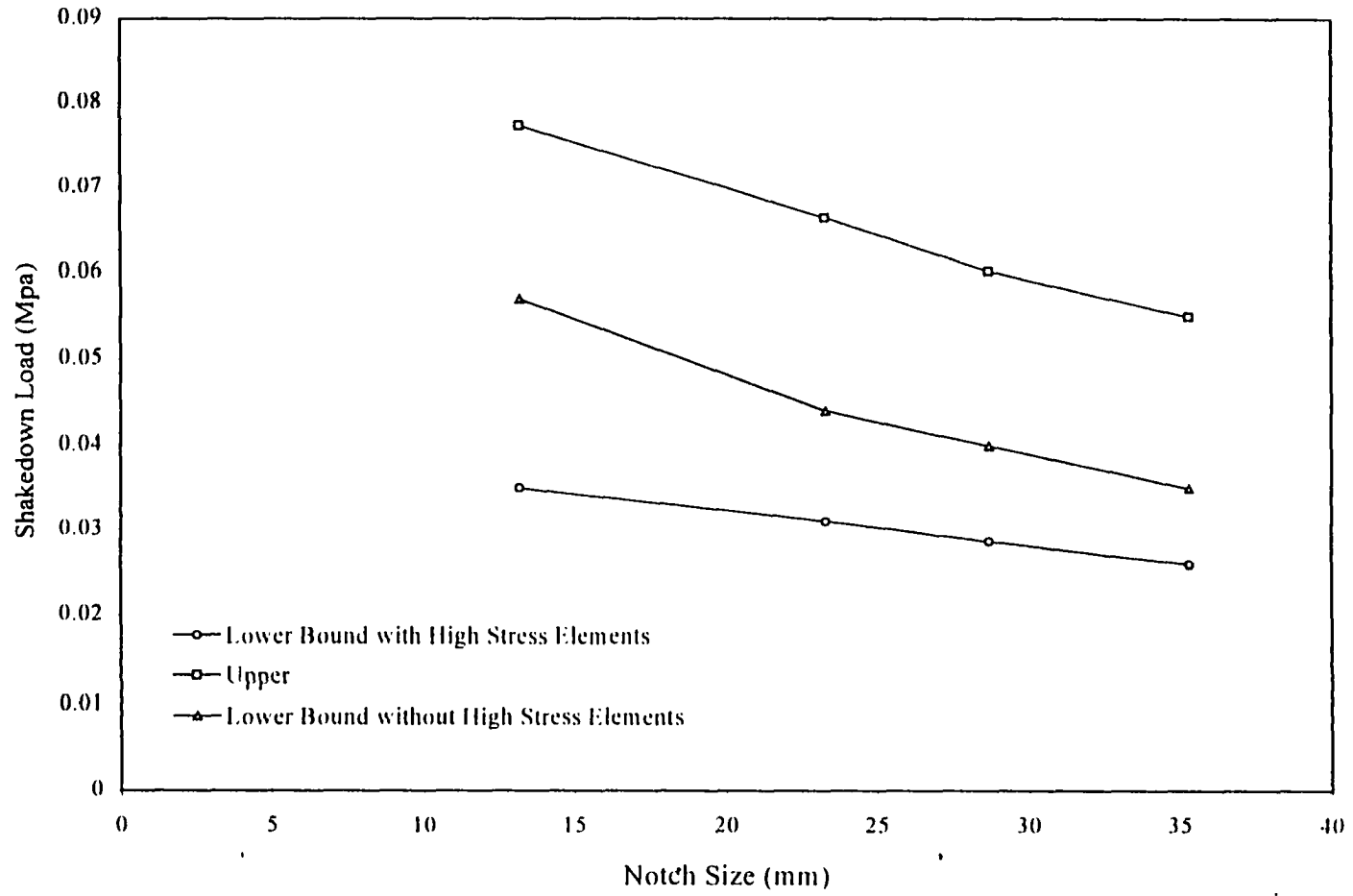


Figure 7.6 Shakedown Load Variation with Notch Size of Two-Layered Pavement System.

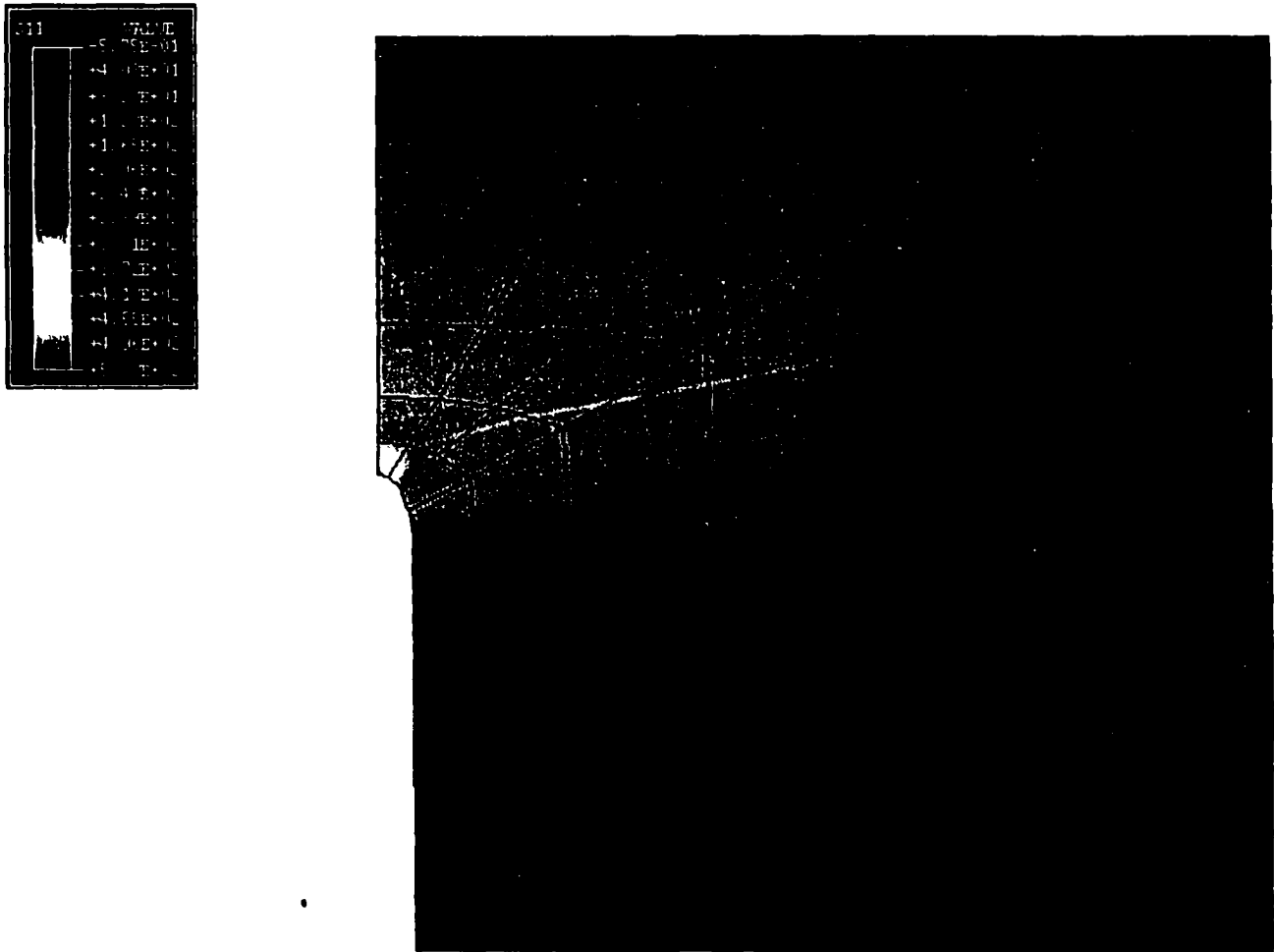


Figure 7.7 Stress (σ_{xx}) Distribution around Notch Tip of Two-Layered Pavement System.

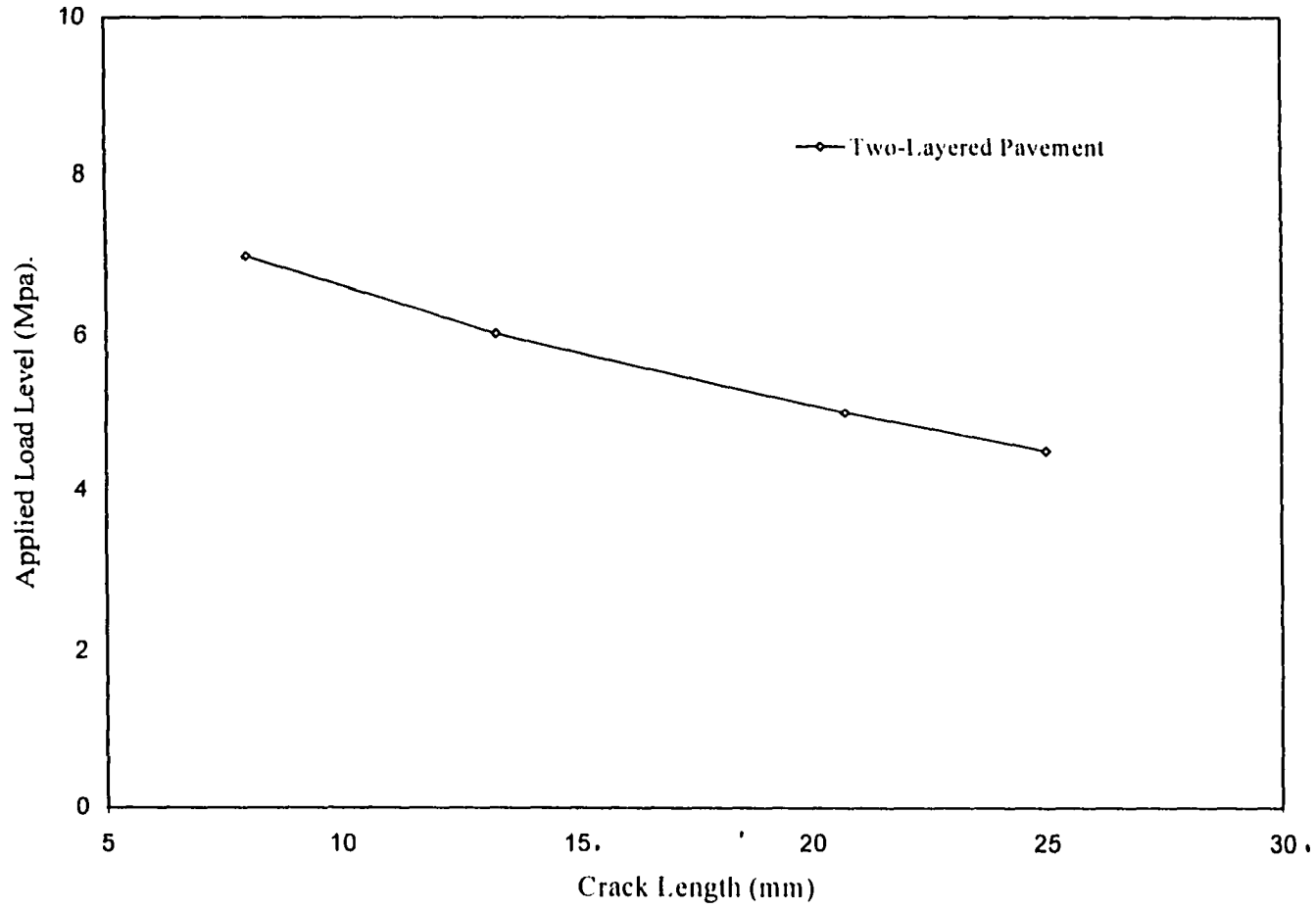


Figure 7.8 Fatigue Failure Load Variation with Crack Lengths of Two-Layered Pavement System.

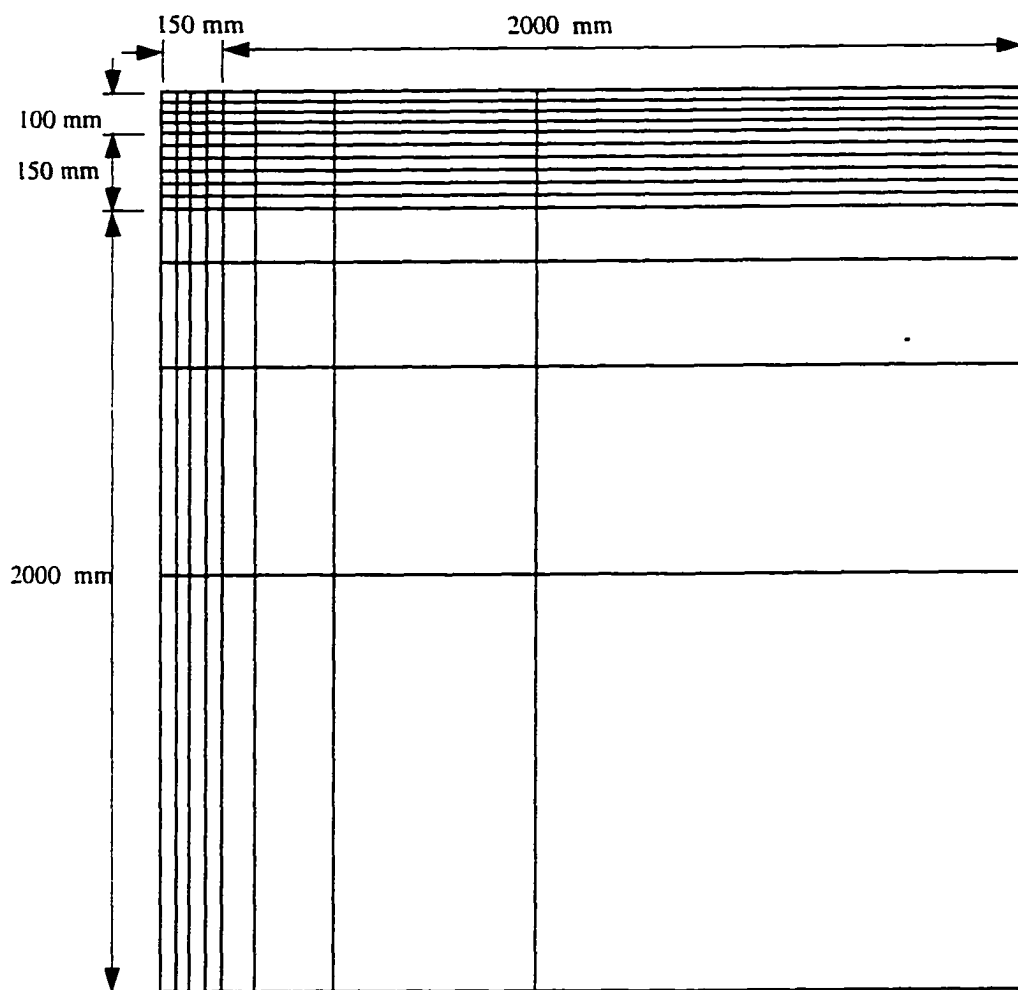


Figure 7.9: Dimension and Finite Element Mesh of Three-Layered Pavement System in Shakedown Analysis.

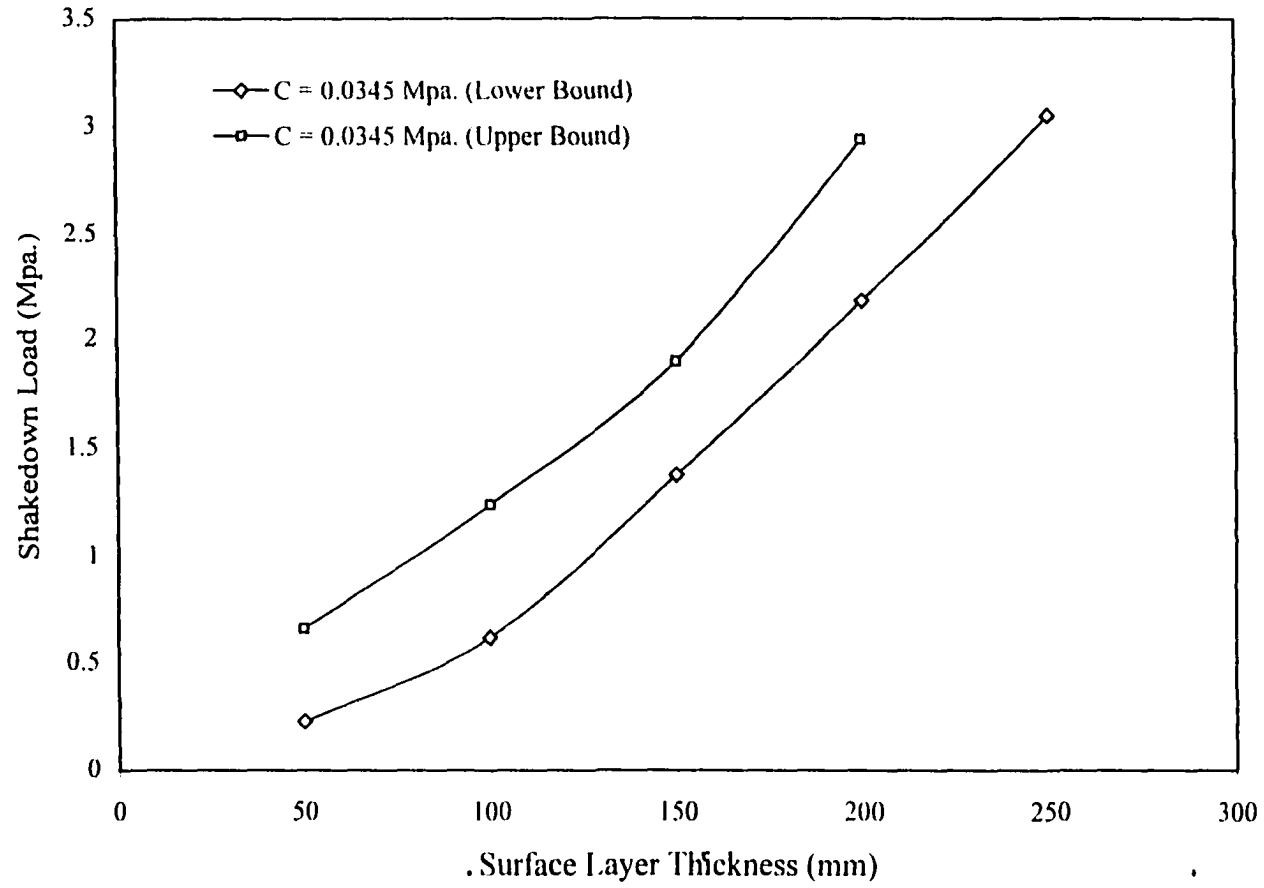


Figure 7.10 Shakedown Load Variation with Different Thickness of Surface Layer of Three-Layered Pavement System.

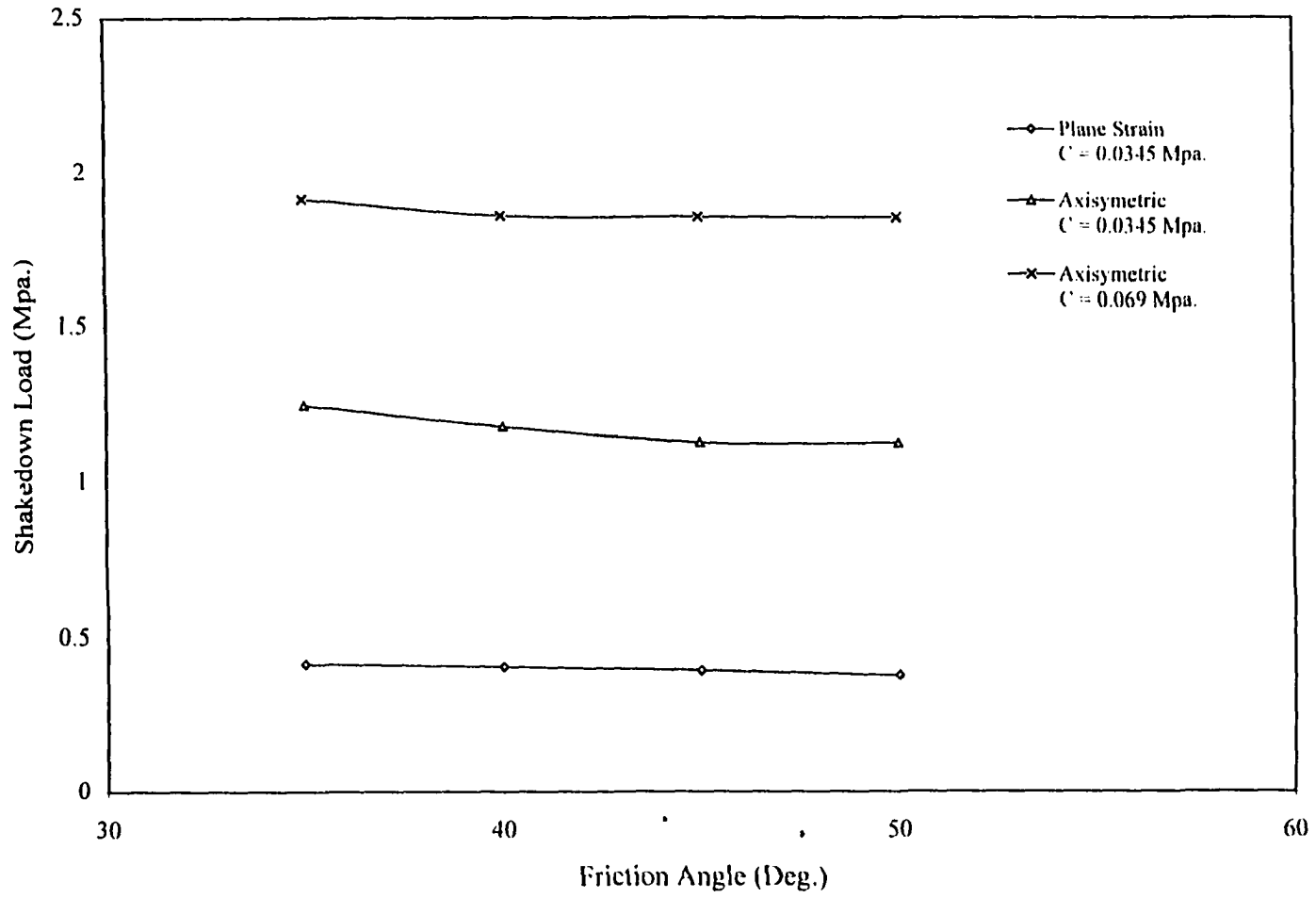


Figure 7.11 Lower Bound Shakedown Load Variation with Base Layer Friction Angle for Three-Layered Pavement System.

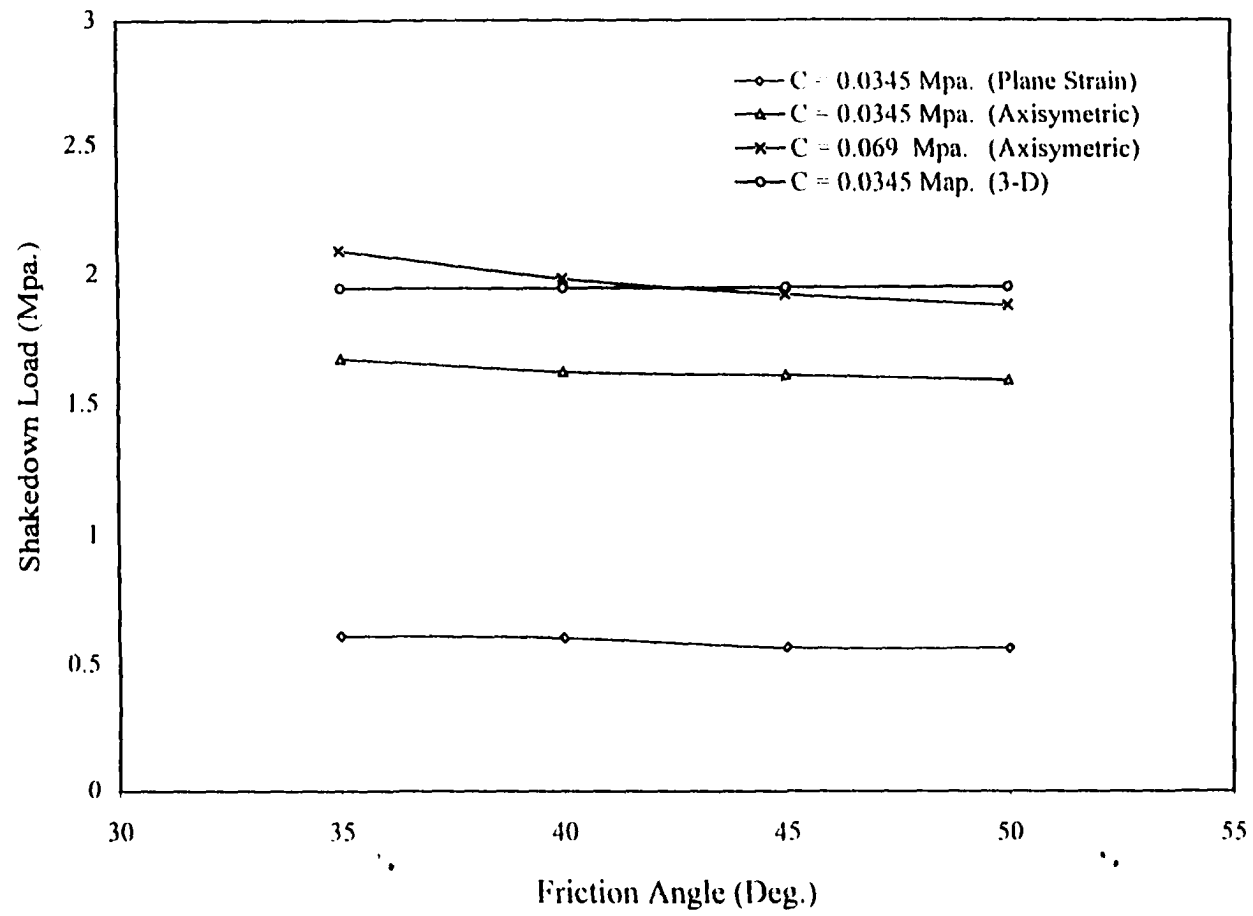


Figure 7.12 Upper Bound Shakedown Load Variation with Base Layer Friction Angle for Three-Layered Pavement System.

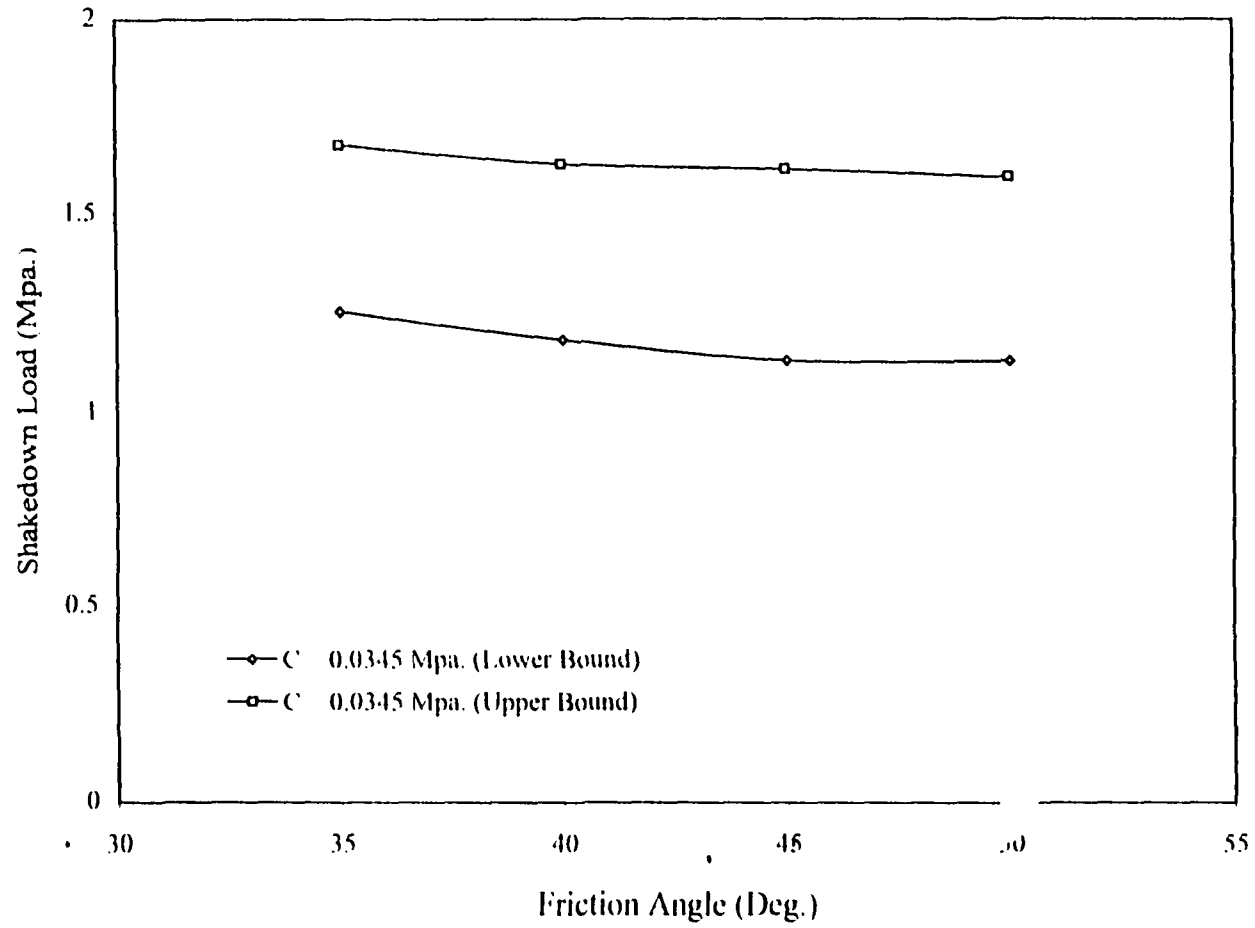


Figure 7.13 Comparison of Shakedown Load Variation with Base Layer Friction Angle for Three-Layered Pavement System between Lower Bound and Upper Bound Value under Axisymmetric Condition with $C' = 0.0345$ Mpa.

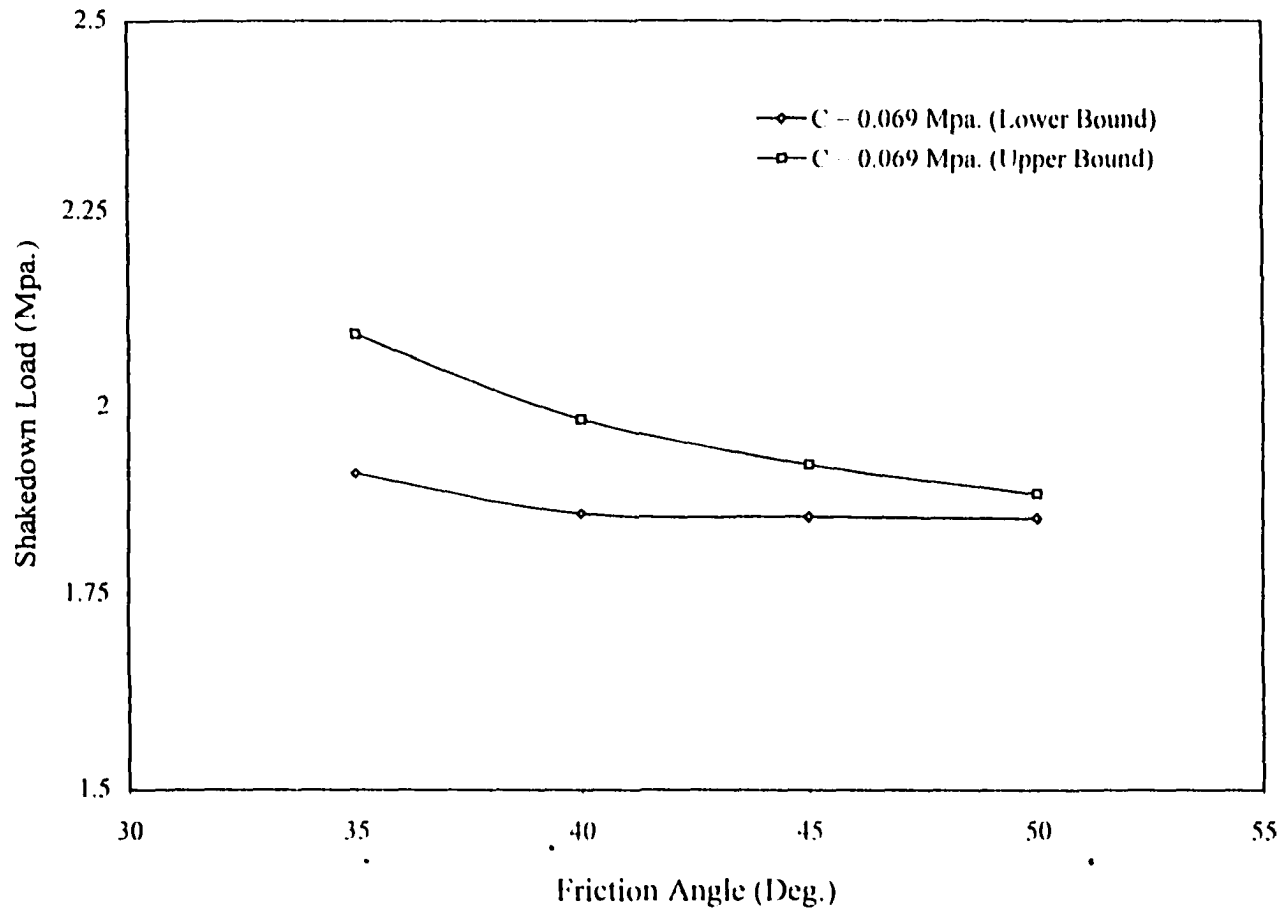


Figure 7.14 Comparison of Shakedown Load Variation with Base Layer Friction Angle for Three-Layered Pavement System between Lower Bound and Upper Bound Value under Axisymmetric Condition with $C = 0.069$ Mpa.

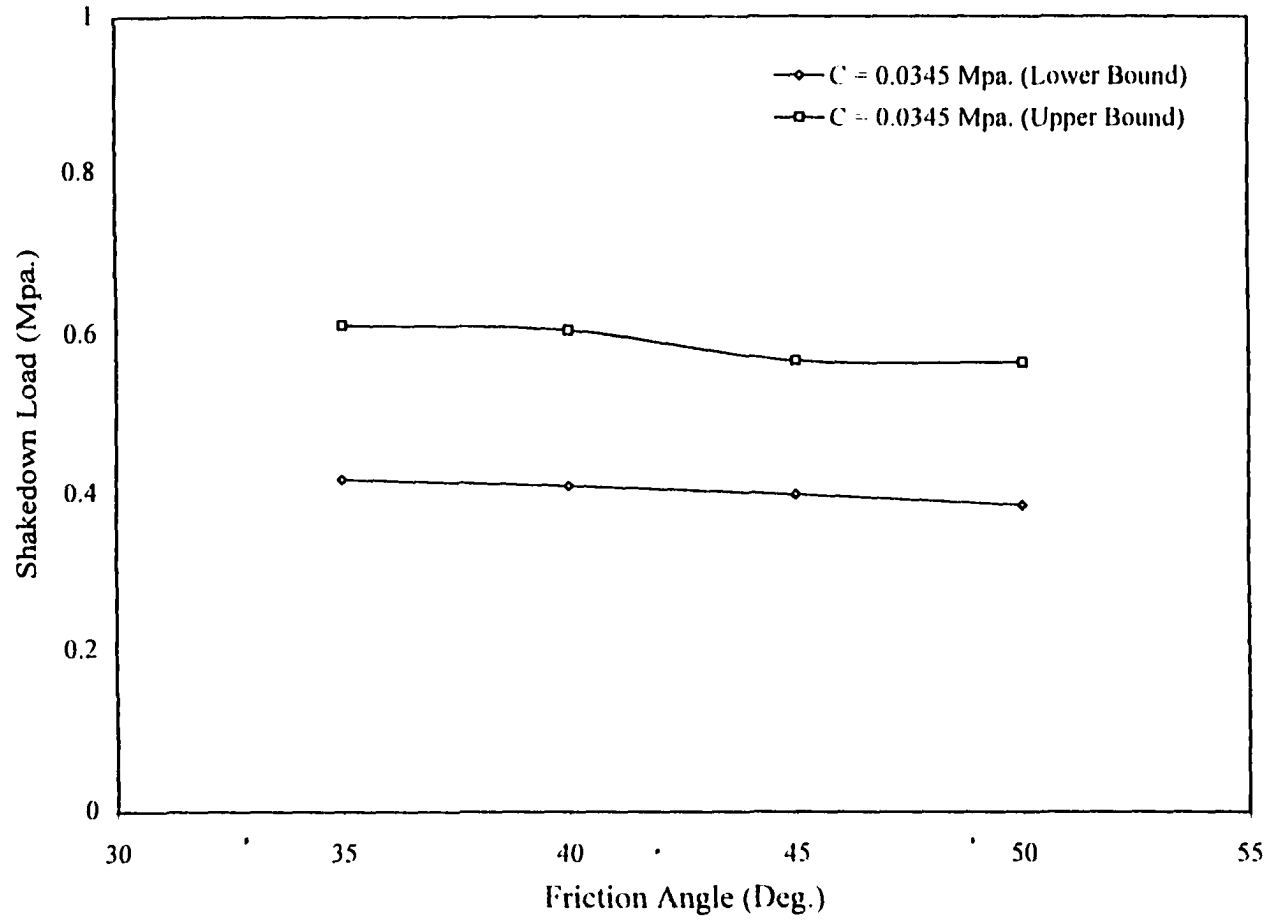


Figure 7.15 Comparison of Shakedown Load Variation with Base Layer Friction Angle for Three-Layered Pavement System between Lower Bound and Upper Bound Value under Plane Strain Condition with $C = 0.0345$ Mpa.

Table 7.1 Material Properties of Three-Layered Pavement System

Layer	Material	Thickness	Elastic Modulus	Possion Ratio	Cohesion	Friction Angle
-	-	(mm)	Mpa	-	Mpa	deg.
Surface	Asphalt Concrete	x	6900	0.3	7.6	35
Base	Gravel	200	200	0.35	0.035	40
Subgrade	Silty	2000	70	0.45	0.04	0

Table 7.2 Shakedown Load for Three-Layered Pavement System

Thickness (mm)			Shakedown Load (Mpa.)	
Surface	Base	Subgrade	Lower Bound	Upper Bound
50	200	2000	0.23	0.66
100	200	2000	0.62	1.24
150	200	2000	1.378	1.9
200	200	2000	2.177	2.94

CHAPTER VIII

SUMMARY AND CONCLUSION

Three numerical algorithms have been proposed and the corresponding computer codes have been developed herein to simulate fatigue crack growth behavior, to predict fatigue life, and to analyze shakedown phenomena of engineering objects and structures subjected to repetitive loading.

Most traditional finite element programs used to simulate fatigue crack growth behavior are unable to establish the fatigue crack growth rate equation. Some have to utilize fatigue test data to obtain fatigue crack growth rate and to predict fatigue life. The proposed numerical algorithm utilized the fracture mechanics parameters, J-integral and R_{curve}, to simulate the crack propagation, to establish the fatigue crack growth rate equation, to determine unstable crack growth, and to predict the fatigue life. Fatigue analyses were conducted for several different materials, such as compact specimen of A533B steel, four-point beam of soil-cement with different material properties (cohesion and friction), and four-point beam of asphalt concrete at 10° F and 68° F, respectively. These numerical results were compared with the available fatigue experimental data and showed very good agreement. The proposed numerical algorithm was also applied to the fatigue analysis of a full-depth two-layered pavement system. The established fatigue crack growth rate was consistent with the data of fatigue test on a four-point beam of the same material.

The applicability of J-integral to a growing crack was checked for every example by satisfying the J-controlled requirements described in chapter IV. For A533B steel (at 200° F), R_{curve} and formulation to calculate J-integral for different crack length were available from the experimental data and were used directly in fatigue analysis by means of the proposed numerical algorithm. For the soil-cement and the asphalt concrete materials, R_{curve} and formulation to calculate J-integral for different crack length were not available and the numerical procedure had to be used to establish R_{curve} and to calculate J-integral value. This step was rather time-consuming and took about 95% of total fatigue analysis time. Further investigation may be needed for this step to reduce the computation efforts.

Application of the shakedown theory to structural engineering has well been developed. For many simple beams and frames, shakedown loads have been calculated and documented [120]. Applications of the shakedown theory to solid mechanics are very limited. Three reasons may be considered for the causes.

- (a) A theoretical elastic solution for general continuum problems, which is needed in a shakedown analysis, is limited, especially for complicated problems.
- (b) Optimization algorithms used in finding optimum shakedown load factor is rather time-consuming, especially for large problems.
- (c) There is no a simple approach to construct the arbitrary admissible plastic paths available in solving upper bound shakedown load problems.

Based on the available numerical algorithms in the shakedown analysis, a very general numerical algorithm was formulated in this study for the lower bound shakedown analysis. For the kinematic shakedown analysis, an eigen-vector technique was proposed and used to construct the arbitrary admissible plastic paths in searching for the upper bound shakedown load. A multidimensional optimization search algorithm was employed in searching for the optimum in both the lower and upper bound shakedown analysis.

Several examples were analyzed using the proposed numerical algorithms. These included a fixed end beam, a plane stress plate with a circular hole and subjected to uniformly distributed tensile stress along the edges, a stratum under uniformly distributed foundation loading, and a full-depth two-layered pavement system under traffic load. The numerical results were compared with the available analytical and numerical data and they showed very good agreement.

The proposed numerical algorithms were also applied to the shakedown analysis of a full-depth three-layered pavement system under consideration of plane strain, axisymmetric, and three-dimensional conditions. The results for plane strain condition yielded rather conservative shakedown load values, when compared to the results of axisymmetric and three-dimension conditions. The results for axisymmetric and three-dimensional condition were very close.

In the lower bound shakedown analysis, it was found that the optimization search basically goes around several critical check points, while most part of the body remains at its initial state. Therefore, deduction of the search variables and limiting the search within sub-region will greatly reduce the computation efforts in the optimization search process.

In the kinematic shakedown analysis(upper bound analysis), the eigen-vectors for each eigen-value of a given system were used to construct the arbitrary admissible plastic fields. The numbers of eigen-value increase with the size of the considered problems. When the problem becomes large, the time needed to obtain the eigen-value and the eigen-vector increases. Furthermore, the optimization search is also dependent on the dimension of the eigen-vector. When the dimension of the eigen-vector increases, the

time spent on the optimization search will also increase. Therefore, further investigation to reduce the dimension of the eigen-vector may be necessary to reduce computation time.

The influence of the finite element mesh on the shakedown load was also investigated in the current study. The numerical results showed that coarse mesh yielded higher shakedown load values. When the mesh became finer, the shakedown load approached a constant value. Therefore, it is recommended that a reasonable finite element mesh has to be used in the shakedown analysis. To ground the comparison of the results from different numerical algorithms on a common condition, a reasonable and a similar finite element mesh, element size ratio, and element type should be used for each algorithm.

REFERENCES

1. Huang, Y. H., *Pavement Analysis and Design*, Prentice Hall, Englewood Cliffs, New Jersey, 1993.
2. Peterson, W. and A. Chesher, *Application of Failure-Time Theory to the Prediction of Surfacing Distress*. Paper Presented at the 65th TRB Conference, January 1986.
3. The Asphalt Institute, *Research and Development of the Asphalt Institute's Thickness Design Manual (MS-1)*, Ninth Edition, Research Report No. 82-2 (RR-82-2). The Asphalt Institute, College Park, Maryland, August 1982.
4. Hveem, F. N., *Pavement Deflections and Fatigue Failures*, in *Design and Testing of Flexible Pavements*, Highway Research Board Bulletin 114, 1955.
5. Monismith, C. L., *Flexibility Characteristics of Asphalt Paving Mixtures*, Proceedings AAPT, vol. 27, 1958.
6. Pell, P. S., *Fatigue Characteristics of Bitumen and Bituminous Mixes*, Proceedings, First International Conference on the Structural Design of Asphalt Pavements, University of Michigan, Ann Arbor, 1962.
7. Deacon, J. A., *Fatigue of Asphalt Concrete*, D. Eng. Thesis, University of California, Berkeley, 1965.
8. Majidzadeh, K., *Analysis of Fatigue and Fracture of Bituminous Paving Mixtures*, Final Report of Project RF 2845, Phase 1. The Ohio State University Research Foundation, Columbus, Ohio, May, 1970.
9. Bazin, P. and J. B. Saunier, *Deformability, Fatigue and Healing Properties of Asphalt Mixes*, Proceedings, Second International Conference on the Structural Design of Asphalt Pavements, University of Michigan, 1967.
10. Savin, G.N., *Stress Concentration Around Holes*, Pergamon Press, New York, 1961.
11. Coffman, Bounner S., Ilves, G. J., and Edwards, W. F., *The Fatigue of Flexible Pavements*, Engineering Experiment Station, The Ohio State University, Report EES 296B-1, February 1971.
12. Franchen, L. and J. Verstraeten, *Methods for Predicting Modulus and Fatigue Laws of Bituminous Mixes under Repeated Bending*, Transportation Research Record 515, Transportation Research Board, pp. 114-123, 1974.
13. Jimenez, R. A. and B. M. Gallaway, *Behavior of Asphalt Concrete Diaphragms to Repetitive Loading*, Proceedings, 1st International Conference on the Structural Design of Asphalt Pavements, pp. 339-344, 1962.
14. Jimenez, R. A., *Fatigue Testing of Asphaltic Concrete Slabs*, STP 508, American Society for Testing and Materials, pp. 3-17, 1972.
15. Mendelson, Alexander, *Plasticity: Theory and Application*, The MacMillan Company, New York, 1968.
16. Monismith, C. L., K. E. Secor, and E. W. Blackmer, *Asphalt Mixture Behavior in Repeated Flexure*, Proceedings, Association of Asphalt Paving Technologists, Vol. 30, 1961.

17. Barksdale, Richard R., Compressive Stress Pulse Times in Flexible Pavements⁶ for Use in Dynamic Testing, HRB Record 345, Highway Research Board, 1971.
18. Pell, P. S., Keynote Lecture-Pavement Materials, Sixth International Conference on the Structural Design of Asphalt Pavements, Vol. 2, pp. 36-70, 1987.
19. Bonnaure, F. A., A. Gravois and J. Udron, A New Method for Predicting the Fatigue Life of Bituminous Mixes, Proceedings, Association of Asphalt Paving Technologists, Vol. 49, pp. 499-524, 1980.
20. Deacon, J. A. and C. L. Monismith, Laboratory Flexural Fatigue Testing of Asphalt Concrete with Emphasis on Compound Loading Tests, in Bituminous Concrete Mixes, HRR No. 158, Washington, D. C., 1967.
21. Raithby, K. D. and A. B. Sterling, The Effect of Rest Periods of Fatigue Performance of a Hot Rolled Asphalt Under Reversed Axial Loading, Proceedings, Association of Asphalt Paving Technologists, Vol. 39, 1970.
22. Raithby, K. D. and A. B. Sterling, Some Effects of Loading History on the Fatigue Performance of Rolled Asphalt, Great Britain, Transport and Road Research Laboratory, TRRL Report LR 496, 1972.
23. Majidzadeh, K., E. M. Kauffman, and C. W. Chang, Verification of Fracture Mechanics Concepts to Predict Cracking of Flexible Pavements, The Ohio State University Research Foundation Final Report, Project RF 2873, March 1971.
24. Salam, Y. M., Characterization of Deformation and Fracture of Asphalt Concrete, Ph. D. Dissertation, Institute of Transportation and Traffic Engineering UCB, 1971.
25. Majidzadeh, K., D. V. Ransamooj, and T. A. Fletcher, Analysis of Fatigue of a Sand Asphalt Mixture, Proceedings, Association of Asphalt Paving Technologists, Vol. 30, 1969.
26. Majidzadeh, K., D. V. Ransamooj, Development of Testing Procedures and a Method to Predict Fatigue Failures of Asphalt Concrete Pavement Systems, The Ohio State University Research Foundation Final Report, Project RF 3200, June 1973.
27. Ransamooj, D. V., Analysis and Design of the Flexibility of Pavements, Ph. D. Thesis, The Ohio State University, 1970.
28. NCHRP 1-26, Calibrated Mechanistic Structural Analysis Procedures for Pavements, vol. II, University of Illinois at Urbana-Champaign Construction Technology Laboratories, Mar. 1990.
29. Grüning, M., Die Tragfähigkeit statisch unbestimmter Tragwerke aus Stahl bei beliebig häufig wiederholter Belastung, Springer, Berlin 1926.
30. Bleich, H., Über die Bemessung statisch unbestimmter Stahlwerke unter der Berücksichtigung des elastisch-plastischen Verhaltens des Baustoffes, Bauingenieur 13, 261-267, 1932.
31. Melan, E., Theorie Statisch unbestimmter Systeme, Proc. Second Congr. IABSE, Berlin, 43, 1936.
32. Koiter, W. T., A New General Theorem on Shakedown of Elastic-Plastic Structures, Proc. Konk. Ned. Akad. Wett. 1359, 14-34, 1956.

33. Prager, W., Shakedown in Elastic-Plastic media subjected to cycles of load and Temperature, *Proceedings, Symp. Plasticita Nella Scienza dille Construzioni*, Bologna 1956, 239-244.
34. Rozenblum, V. I., O Prispoblyayemost neravnomierno nagretykh uprugo-plasicheskikh tel (On Shakedown of Uneven Heated Elastic-Plastic Bodies) *Izv. Akad. Nauk SSSR. OTN, Mekh. Mash.*, No. 7, pp. 136-138, 1957.
35. De Donato, O., Second Shakedown Theorem Allowing for Cycles of Both Loads and Temperature, *Ist. Lombardo di Scienza e Lettere A104*, pp. 265-277, 1970.
36. Maier, G., Shakedown Theory in Perfect Elastoplasticity with Associated and non-associated Flow-laws, *Meccanica* 6, pp. 250-260, 1969.
37. König, J. A. and G. Maier, Shakedown Analysis of Elastoplastic Structures: A review of recent developments, *Nucl. Engng, Design* 66, 81-95.
38. Cazzani, A., R. Contro and L. Corradi, On the Evaluation of the Shakedown Boundary for Temperature-dependent Elastic Properties, *Eur. J. Mech. A/Solids*, 11, n 4, 539-550, 1992.
39. Ceradini, G., Dynamic Shakedown in Elastic-Plastic Bodies, *J. Engng. Mech. Div. Proc. ASCE* 106(3) 481-498, June 1980.
40. Neal, B. G., Plastic Collapse and Shakedown Theorems for Structures of Strain-hardening Material, *J. Aero.Sci.*, 17, 297, 1950.
41. Masing, G., Zur Heyn'schen Theorie der Verfestigung der Metalle Durch Verborgene Elastische Spannungen, *Wissenschaftliche Veröffentlichungen aus dem Siemens-Konzern*, 3, 231, 1924.
42. Stein, E. G. Zhang and J. A. König, Shakedown with Nonlinear Strain-Hardening Including Structural Computation Using Finite Element Method, *Int. J. Plasticity*, vol. 8, pp. 1-31, 1992.
43. Maier, G., A Shakedown Matrix Theory Allowing for Workhardening and Second-order Geometric Effects, *Foundations in Plasticity*, (Cohn, M. Z. and Maier, G., eds), North-Holland, Amsterdam, 417, 1979.
44. Weichert, D., On the Influence of Geometrical Nonlinearities on the Shakedown of Elastic-plastic Structures, *Int. J. of Plasticity*, Vol. 2, No. 2, pp. 135-148, 1986.
45. Polizzotto, C., G. Borino, S. Caddemi and P. Fuschi, Shakedown Problems for Material Models with Internal Variables, *Eur. J. Mech. A/Solids*, 10, n 6, 621-639, 1991.
46. Nayroles, B. and D. Weichert, The Concept of Elasticity Sanctuary and Structural Shakedown, *C. R. Acad. Sci. Paris*, 316, Serie 11, 1493, 1993.
47. Maier, G., Shakedown Theory in Perfect Elastoplasticity with Associated and Nonassociated Flow-laws: A Finite Element Linear Programming Approach, *Meccanica* IV, n. 3, 1969.
48. Belytschko, T., Plane Stress Shakedown Analysis by Finite Elements, *Int. J. Mech. Sci.* 14, 1972.
49. Corradi, L. and A. Zavelani, A Linear Programming Approach to Shakedown Analysis of Structures, *Computer Methods in Applied Mechanics and Engineering* 3, 37-53, 1974.

50. Hung, N. D. and J. A. König, A Finite Element Formulation for Shakedown Problems Using A Yield Criterion of the Mean, *Computer Methods in Applied Mechanics and Engineering* 8, 179-192, 1976.
51. Rowe, P. W., Displacement and Failure Modes of Model Offshore Gravity Platforms Founded on Clay, *Conf. Offshore Europe 75*, Pub. Spearhead Publications.
52. Zienkiewicz, O. C., R. W. Lewis, V. A. Norris, and C. Humpherson, Numerical Analysis for Foundation of Offshore Structures with Special Reference to Progressive Deformation, *Society of Petroleum Eng. of AIME. SPE 5760*.
53. Aboustit, B. L. and D. V. Reddy, Finite Element Linear Programming Approach to Foundation Shakedown. *Proceedings, Int. Symp. On Soils under Cyclic and Transient Loading, Swansea, England* 1, Vol. 2, pp. 727-738, January 1980.
54. Sharp, R. W., Shakedown Analysis and the Design of Pavements, Ph. D. Thesis, University of Sydney, Sydney, 1983.
55. Sharp, R. W. and J. R. Booker, Shakedown of Pavements Under Moving Surface Loads, *J. of Trans. Engng.*, 110, pp. 1-14, 1984.
56. Raad, L., D. Weichert and A. Haidar, Stability of Multi-layer Systems Under Repeated Loads, *TRR*, 1207, pp. 181-186, 1988.
57. Raad, L., D. Weichert and A. Haidar, Shakedown and Fatigue of Pavements with Granular Bases, *TRR*, 1227, pp. 159-172, 1989.
58. Raad, L., D. Weichert and A. Haidar, Analysis of Full-depth Asphalt Concrete Pavements Using Shakedown Theory, *TRR*, 1227, pp. 53-65, 1989.
59. Hooke, R. and T. A. Jeeves, Direct Search Solution of Numerical and Statistical Problems, *J. of the Association for Computing Machinery*, Vol. 8, pp. 212-229, 1961.
60. Collins, I. F. and P. F. Cliffe, Shakedown in Frictional Materials Under Moving Surface Loads, *Int. J. Numerical and Analytical Methods in Geomechanics*, 11, No. 4, pp. 409-420, 1987.
61. Collins, I. F. and A. P. Wang, Shakedown Analysis of Layered Pavements, University of Auckland School of Engineering Report No. 505, 1992.
62. Collins, I. F. and L. R. Saunders, Shakedown in Layered Pavements Under Moving Surface Loads, *Int. J. Numerical and Analytical Methods in Geomechanics*, 11, No. 3, pp. 165-174, 1993.
63. Westergaard, H. M., Bearing Pressures and Cracks, *J. Appl. Mech.*, 6, A 49-53, 1939.
64. Knott, J. F., *Fundamentals of Fracture Mechanics*, John Wiley and Sons, New York - Toronto, 1973.
65. Griffith, A. A., The Phenomena of Rupture and Flow in Solids, *Phil. Trans. R. Soc., Lond. A*, 221, 163-197, 1921.
66. Wells, A. A., Unstable Crack Propagation in Metals-Cleavage and Fast Fracture, *Granfield Crack Propagation Symposium*, 1, pp. 210, Sept. 1961.
67. Irwin, G. R., *Fracture, Handbuch der Physik*, VI, pp. 551-90, Springer-Verlag, Heidelberg, 1958.

68. Parker, A. P., *The Mechanics of Fracture and Fatigue*, London, New York, E. and F. N. SPON LTD, 1981.
69. Dugdale, D. S., *Yielding of Steels Containing Slits*, *J. Mech. Phys. Solids*, **8**, 100-8, 1960.
70. McClintock, F. A., *Plasticity Aspects of Fracture*, *Fracture: An Advanced Treatise*, vol. II, Liebowitz, Ed., Academic Press, New York, pp. 47-225, 1968.
71. Rice, J. R., *A Path Independent Integral and the Approximate Analysis of Strain Concentration by Notches and Cracks*, *J. Appl. Mech.*, pp. 379, June 1968.
72. Rice, J. R., *Fracture: An Advanced Treatise*, vol. II, Liebowitz, Ed., Academic Press, New York, pp. 191-311, 1968.
73. *Standard Test Method for J_{IC} , a Measure of Fracture Toughness*, ASTM E-813-81, vol. 03.01, *Metals-Mechanical Testing*, 1985.
74. Albrecht, P., W. R. Andrews, J. R. Gudas, J. A. Joyce, F. L. Loss, D. E. McCabe, D. W. Schmidt, and W. A. Van DerSluys, *Tentative Test Procedure for Determining the Plane Strain J_1 -R Curve*, *JTVEA, ASTM*, vol. 10, No. 6, 1982.
75. Paris, P. C., H. Tada, A. Zahoor, and H. Ernst, *The Theory of Instability of the Tearing Mode of Elastic-Plastic Crack Growth*, in *Elastic-Plastic Fracture*, ASTM STP 668, pp. 5-36, 1979.
76. Ernst, H. A., P. C. Paris, M. Rossow, and J. W. Hutchinson, *Analysis of Load-Displacement Relationships to Determine J-R Curve and Tearing Instability Material Properties*, *Fracture Mechanics*, ASTM STP 677, C. W. Smith, Ed. American Society for Testing and Materials, pp. 581-599, 1979.
77. Ernst, H. A., P. C. Paris, and J. D. Landes, *Estimations on J-integral and Tearing Modulus T from A Single Specimen Test Record*, *Fracture Mechanics: 13th Conf.* ASTM STP 743, Richard Roberts, Ed., American Society for Testing and Materials, pp. 476-502, 1981.
78. Herrera, R. and J. D. Landes, *A Direct J-R Curve Analysis of Fracture Toughness Tests*, *JTEVA*, vol. 16, No. 5, pp. 427-449, Sept. 1988.
79. Herrera, R. and J. D. Landes, *Direct J-R Curve Analysis: A Guide to the Methodology*, *Fracture Mechanics: 21st Symposium*, ASTM STP 1074, J. P. Gudas, J. A. Joyce, and E. M. Hackett, Eds., American Society for Test of Material, pp. 24-43, 1990.
80. Landes, J. D., Z. Zhou, K. Lee, and R. Herrera, *Normalization Method for developing J-R Curves with the LMN Function*, *JTEVA*, vol. 19, No. 4, pp. 305-311, 1991.
81. Orange, T. W., in *Fracture Mechanics, 21st Symposium*, ASTM STP 1074, J. P. Gudas, J. A. Joyce, and E. M. Hackett, Eds., American Society for Testing of Material, 1990.
82. Paris, P. C. and F. Erdogan, *A Critical Analysis of Crack Propagation Laws*, *J Bas. Engng* **85**, 528-534, 1963.
83. Shanely, F. R., *A Proposed Mechanism of Fatigue Failure*, *Colloquium on Fatigue*, Stockholm, Sweden, 1955.

84. Head, A. K., The Propagation of Fatigue Cracks, *J. of Applied Mechanics* 23, 1956.
85. Frost, N. E. and Dugdale, D. S., The Propagation of Fatigue Cracks in Sheet Specimens, *J. of the Mech. and Physics of Solids*, Vol. 6, No. 2, 1958.
86. Liu, H. W., Crack Propagation in Thin Metal Sheet Under Repeated Loading, *Tran. ASME, J. of Basic Engng.*, vol. 83, March, 1961.
87. Liu, H. W., Fatigue Crack Propagation and Applied Stress Range: An Energy Approach, *Trans. ASME, J. of Basic Engng.* Vol. 85, 1963.
88. McEvily, A. J. and Illg, W., The Rate of Crack Propagation in Two Aluminum Alloys, *NACA Technical Note 4394*, 1958.
89. Forman, R. G., Kearney, V. E. and R. M. Engle, Numerical analysis of Crack Propagation in Cyclic-Loaded Structure, *ASME, Paper No. 66-WA/Met-4*, 1967.
90. Pearson, S. The Effect of Mean Stress on Fatigue Crack Propagation in Half Inch Thick Specimens of Aluminum Alloys of High and Low Fracture Toughness, *Engng. Fract. Mech.* vol. 4, pp. 9, 1972.
91. Hudson, C. M., Effect of Stress Ratio on Fatigue-Crack Growth in 7075-T6 and 2024-T3 Aluminum-Alloy Specimens, *NASA TN D-5390*, 1969.
92. Elber, W., The significance of Fatigue Crack Closure, *Damage Tolerance in Aircraft Structures*, *ASTM STP 486*, 230-242, 1971.
93. Dowling, N. E. and J. A. Begley, Fatigue Crack Growth During Gross Plastic and the J-integral, *Mechanics of Crack Growth*, *ASTM STP 590*, American Society for Testing and Materials, pp.82-103, 1976.
94. El Haddad, M. H. and B. Mukherjee, Elastic-Plastic Fracture Mechanics Analysis of Fatigue Crack Growth, *Elastic-Plastic Fracture: 2nd Symposium*, vol. II, *ASTM STP 803*, C. F. Shih and J. P. Gudas, Ed., American Society for Testing of Materials, pp. II-689-II-707.
95. Tanaka, K., T. Hoshide and M. Nakata, Elastic-Plastic Crack Propagation Under High Cyclic Stresses, *Elastic-Plastic Fracture: Second Symposium, Volume II-Fracture Resistance Curves and Engineering Applications*, *ASTM STP 803*, C. F. Shih and J. P. Gudas, Eds., American Society for Testing of Materials, 1983.
96. Newman, J. C. Jr., Finite Element Analysis of Fatigue Crack Propagation Including the Effects of Crack Closure, Ph. D. Thesis, Virginia Polytechnic Institute and State University, Blacksburg, VA, 1974.
97. Budiansky, B. and J. W. Hutchinson, Analysis of Closure in Fatigue Crack Growth, Division of Applied Science, DAS M-1. Harvard University, Cambridge, Mass., June 1977.
98. Fühning, H. and T. Seeger, *Engineering Fracture Mechanics*, vol. 11, No. 1, pp. 99-122, 1979.

99. Führung, H. and T. Seeger. in *Fracture Mechanics*. ASTM STP 677. C. W. Smith, Ed., American Society for Testing of Materials. 1979. pp. 144-167.
100. Dill, H. D. and Saff, C. R. in *Fatigue Crack Growth Under Spectrum Loads*. ASTM STP 595. American Society for Testing of Materials. pp. 306-319, 1976.
101. Hardrath, H. F., Newman, J. C., Jr., Elba, W., and Poe, C. C., Jr., in *Fracture Mechanics*, N. Perrone, Ed., University Press of Virginia, pp. 347-364, 1978.
102. Bleackley, M. H., A. R. Luxmoore and J. Sumpter, *Evaluation of the J-integral by Analytical and Finite Element Methods*.
103. Ohji, K. K. Ogura and Y. Ohkubo. *On the Closure of Fatigue Crack under Cyclic Tensile Loading*. *Int. J. Fracture* 10, 123-124, 1974.
104. Ohji, K., K. Ogura and Y. Ohkubo. *Cyclic Analysis of a Propagating Crack and Its Correlation with Fatigue Crack Growth*. *Engng Fracture Mech* 7, 457-464, 1975.
105. Newman, J. C. Jr. and H. Armen, Jr., *Elastic-Plastic Analysis of a Propagating Crack Under Cyclic Loading*. *AIAA J.* 13, 1017-1023, 1975.
106. Newman, J. C. Jr., *Finite-Element Analysis of Crack Growth Under Monotonic and Cyclic Loading, Cyclic Stress-Strain and Plastic Deformation Aspects of Fatigue Crack Growth*. ASTM STP 637. 56-80. 1977.
107. Newman, J. C., Jr., *A Crack-Closure Model for Predicting Fatigue Crack Growth under Aircraft Spectrum Loading*. *Methods and Models for Predicting Fatigue Crack Growth under Random Loading*. ASTM STP 748. J. B. Chang and C. M. Hudson, Eds., American Society for Testing of Materials. pp. 53-84. 1981.
108. Chermahini, R. G., K. N. Shivakumar, and J. C. Newman, Jr., *Three-Dimension Finite Element Simulation of Fatigue Crack Growth and Closure*. *Mechanics of Fatigue Crack Closure*. ASTM STP 982. J. C. Newman, Jr. and W. Elba, Ed., American Society for Testing of Materials. pp. 398-413, 1988.
109. Nakagaki, M. and S. N. Atluri. *Elastic-plastic Analysis of Fatigue Crack Closure in Modes I and II*. *AIAA J.* 18, pp. 1110-1117, 1980.
110. Newman, J. C. Jr., *Fatigue Life Prediction Methodology Using a Crack-Closure Model*. *J. Engng. Material and Technology*, vol. 117, pp. 433, 1995.
111. Newman, J. C. Jr., *A Crack Opening Stress Equation for Fatigue Crack Growth*. *Int. J. Fracture*. 24, R131-R135, 1984.
112. McClung, R. C. and H. Sehitoglu. *On the Finite Element Analysis of Crack Closure –I Basic Modeling Issues*. *Engng. Fracture Mech.* 33, 253-272, 1989.
113. McClung, R. C. and H. Sehitoglu. *On the Finite Element Analysis of Crack Closure –II Numerical Results*. *Engng. Fracture Mech.* 33, 253-272, 1989.
114. Lalor, P. L. *Mechanics Aspects of Crack Closure*. M. S. Thesis, Department of Mechanical and Industrial Engineering, Univ. of Illinois at Urbana-Champaign, 1986.

115. Lalor, P. L and H. Sehitoglu, Fatigue Crack Closure outside Small Scale Yielding Regime, *Mechanics of Fatigue Crack Closure*, ASTM STP 982, American Society for Testing of Materials, 342-360, 1988.
116. Lalor, P. L., H. Sehitoglu and R. C. McClung, *Mechanics Aspects of Small Crack Growth from Notches – the Role of Crack Closure*, The Behavior of Short Fatigue Cracks, EGF1, 369-386, Mechanical Engineering Publications, London, 1986.
117. Zhang, X., A. S. L. Chan and G. A. O. Davies, Numerical Simulation of Fatigue Crack Growth Under Complex Loading Sequences, *Engng. Fracture Mech.* vol. 42, No. 2, pp. 305-321, 1992.
118. Melan, E. . *Der Spannungszustand eines Mises-Henckyschen Kontinuums bei veraderlicher Belastung*, Sitzber. Akad. Wiss. Wien Ila 147 73-87, 1938.
119. König , J. A., On A New Method of Shakedown Analysis, *Appl. Mechanics, Bulletin De L'academie Polonaise Des Sciences Série des Sciences Technieqs* vol. XXVI, No. 4, 1978.
120. König , J. A., *Shakedown of Elastic-Plastic Structures*, Elsevier & PWN-Polish Scientific Publishers, Warsaw, 1987.
121. König , J. A., On Upper Bounds to Shakedown Loads, *Z. Angew. Math. Mech.* 59, 349-354, 1979.
122. König , J. A., A Shakedown Theorem for Temperature Dependent Elastic Moduli, *Bulletin De L'Academic Polonaise Des Sciences Serie des sciences Techniques* vol. XVII, No. 3, 1969.
123. Stein, E., G. Zhang and Y. Huang, Modeling and Computation of Shakedown Problems for Nonlinear Hardening Material, *Computer Method. in Applied Mech. and Engng.*, 103, 247-272, 1993.
124. Barsom, John M., *Fracture and Fatigue Control in Structures: Applications of Fracture Mechanics*, 2nd Edition, Prentice-Hall, Inc., Englewood Cliffs, New Jersey, 1987.
125. Schwalbe, K. -H., Approximate Calculation of Fatigue Crack Growth, *Int. J. Fracture* 9, 381, 1973.
126. Schwalbe K. -H., Influence of Stress State on Static Crack Growth in AlZuMgCu 0.5, *Engng Fracture Mech.* 9, 557, 1977.
127. Schwalbe, K. -H., Some Properties of Stable Crack Growth, *Engng Fracture Mech.* 11, 331, 1979.
128. Musuva , J. K. and J. C. Radon. An Elastic-Plastic Crack Growth Analysis Using the J-integral Concept.
129. Miyamoto, H. T. Miyashi and S. Fukuda, An analysis of crack propagation in Welded Structures, Significance of Defects in Welded Structures, Proc. Of Japan-U.S. Seminar, Tokyo, University of Tokyo presses, 189-202, 1973.
130. Blom, A. F. and D. K. Holm, An Experimental and Numerical Study of Crack Closure, *Engng Fracture Mech.* 22, 997-1011, 1985.
131. Fleck, N. A., Finite Element Analysis of Plasticity-induced Crack Closure under Plane Strain Conditions, *Engng Fracture Mech.* 25, 441-449, 1986.
132. Fleck, N. A. and J. C. Newman, Jr., Analysis of Crack Closure under Plane Strain Conditions, *Mechanics of Fatigue Crack Closure*, ASTM STP 982, 319-341, 1988.

133. Zhang, X, Numerical Simulation of Fatigue Crack Propagation under Variable Amplitude Loading, Ph. D. Thesis, Imperial College of Science, Technology and Medicine, University of London, 1990.
134. Rice, J. R., Elastic-Plastic Models for Stable Crack Growth, in Mechanics and Mechanisms of Crack Growth (Proceedings, Conference at Cambridge, England, April, 1973) N. J. May, Ed., British Steel Corporation Physical Metallurgy Center Publication, pp. 14-39, 1975.
135. Hutchinson, J. W. and P. C. Paris, Stability Analysis of J-controlled Crack Growth, Elastic-Plastic Fracture, ASTM STP 668, J. P. Landes, J. A. Begley, and G. A. Clarke, Eds., American Society for Testing and Materials, pp. 37-64, 1979.
136. Shih, C. F., H. G. deLorenzi and W. R. Andrews, Studies on Crack Initiation and Stable Crack Growth, Elastic-Plastic Fracture, ASTM STP 668, J. P. Landes, J. A. Begley, and G. A. Clarke, Eds., American Society for Testing and Materials, pp. 65-120, 1979.
137. Joyce, J. A., H. A. Ernst, and P. C. Paris, Direct Evaluation of J-Resistance Curves from Load Displacement Records, Fracture Mechanics: Twelfth Conference, ASTM STP 700, American Society for Testing and Materials, pp. 222-236 and pp. 13-31, 1980.
138. Hutchinson, J. W., Singular Behavior at the End of a Tensile Crack in a Hardening Material, Mech. Phys. Solids, vol. 16, pp. 13-31, 1968.
139. Rice, J. R., P. C. Paris, and J. G. Merkle, Some Further Results of J-integral Analysis and Estimates, Progress in Flaw Growth and Fracture Toughness Testing, ASTM STP 536, American Society for Testing and Materials, pp. 23- 245, 1973.
140. Begley, J. A. and J. D. Landes, The J-integral as a Fracture Criterion, Fracture Toughness, Proceedings of the 1971 National Symposium on Fracture Mechanics, Part II, ASTM STP 514, American Society for Testing of Materials, pp. 1-20, 1972.
141. Sharobeam, M. H. and J. D. Landes, The Load Separation Criterion and Methodology in Ductile Fracture Mechanics, Int. J. of Fracture vol. 47, pp. 81-104, 1991.
142. Rice, J. R., Mechanics of Crack Tip Deformation and Extension by Fatigue, Fatigue Crack Propagation, ASTM STP 415, American Society for Testing and Materials, pp. 247-311, 1967.
143. Shih, C. F., et al, Methodology for Plastic Fracture, 1st through 5th Quarterly Reports, General Electric Co., Schenectady, N. Y., Sept. 1976 - Dec. 1977.
144. Shih, C. F., in Fracture Analysis, ASTM STP 560, American Society for Testing and Materials, pp. 187-210, 1974.
145. Anderws, W. R. And C. F. Shih, Thickness and Side-Groove Effects on J and δ Resistance Curves for A533B Steel at 93° C, in Elastic-Plastic Fracture, ASTM STP 668, J. P. Landes, J. A. Begley, and G. A. Clarke, Eds., American Society for Testing and Materials, pp. 65-120, 1979.
146. Kumar, V. M. D. German and C. F. Shih, A Engineering Approach for Elastic-Plastic Fracture Analysis. Research Project 1237-1, General Electric Co., 1981.
147. Kumar, V. and C. F. Shih, Fully Plastic Crack Solutions, Estimation Scheme and Stability Analysis for Compact Specimen, in Fracture Mechanics, ASTM Special Technical Publication 700, pp. 406-438, 1980.

148. ABAQUS, Hibbitt, Karlsson and Sorensen, Inc.
149. Pretorius, D. C., Design Considerations for Pavements Containing Soil-Cement Bases, Ph. D. Dissertation, University of California, Berkeley, 1970.
150. George, K. P., Theory of Brittle Fracture Applied to Soil Cement, J. Of Soil Mechanics and Foundations Division, Proc. Of the American Society of Civil Engineers, Vol. 96, No. SM3, May 1970.
151. Crockford, W. W. and D. N. Little, Tensile Fracture and Fatigue of Cement-Stabilized Soil, J. of Transportation Engineering, Vol. 113, No. 5, Sept., 1987.
152. Rice, J. R. and D. M. Tracy, in Numerical and Computer Methods in Structural Mechanics, S. J. Fenves et al, Eds., Academic Press, New York, pp. 585-623, 1973.
153. Grundy, P., Shakedown of Bars in Bending and Tension, Proc. ASCE, J. of Eng. Mech. Div. 1969.
154. Lechkie, F. A. and R. K. Penny, Shakedown as a Guide to the Design of Pressure Vessels, J. Eng. Ind., A.S.M.E. 1969.
155. Maier, G., A Shakedown Matrix Theory Allowing for Workhardening and Second Order Geometrical Effects, Symp. On Foundations of Plasticity, Warsaw, 1972.
156. Hung, N. D., Direct Limit Analysis via Rigid-Plastic Finite Elements, Computer Methods in Appl. Mech. Eng., Vol. 8, pp. 81-116, 1976.
157. Haldar, A. K., D. V. Reddy and M. Arockiasamy, Shakedown Analysis of Fluid-Saturated Foundation Soil, Proc. The Fourth Int. Conf. on Num. Meth. In Geomechanics, pp. 965-973, 1982.
158. Boulbibane, M., D. Weichert and L. Raad, Shakedown Analysis of Anisotropical Soils Using Finite Elements and Mathematical Programming, (in process of publishing) 1996.
159. Fiacco, A. V. and G. P. McCormick, Nonlinear Programming: Sequential Unconstrained Minimization Techniques, John Wiley and Sons, New York, 1968.
160. Torczon, V., Multi-Directional Search: A Direct Search Algorithm for Parallel Machines, Ph. D. thesis, Department of Mathematical Sciences, Rice University, Houston, TX, 1989.
- 161.()
162. Koiter, W. T., General Theorems for Elastic-Plastic Bodies, in Progress in Solid Mechanics, Sneddon, I. and Hill, R. (eds.), Vol. 1, North Holland, Amsterdam, 1960.
163. Gokhfeld, D. A. and O. F. Cherniavsky, Limit Analysis of Structures at Thermal Cycling, Sijthoff and Nordthoff, Alphen au den Rejn, The Netherlands, 1980.
164. Gokhfeld, D. A., Some Problems of Plates and Shells, Proc. VI-th Soviet Conf. Plates and Shells, Baku, 1966, Izd. Nauka, Moscow, 1966.
165. Sawczuk, A., Evaluation of Upper Bounds to Shakedown Loads for Shells, J. Mech, Phys. Solids 17, 291-301, 1969.

166. Smith, D. L. (ed.), *Mathematical Programming Methods in Structural Plasticity*, Springer-Verlag, New York, 1990.
167. Pham, D. C. And Stumpf, H., Kinematical Approach to the Shakedown Analysis of Some Structures, *Quarterly of Applied Mathematics*, vol. 52, No. 4, pp. 707-719, Dec. 1994.
168. Kamenjarzh, J. and Weichert, D., On Kinematic Upper Bounds for the Safety Factor in Shakedown Theory, *Int. J. Plasticity*, 8, 827, 1992.
169. Kamenjarzh, J. and Merzljakov, A., On Dual Extremum Problems in Shakedown Theory, *Sov. Phys. Dokl.* 325., 1992.
170. Kamenjarzh, J., Extremum Problems in Shakedown Theory, in *Inelastic Behavior of Structures under Variable Loads*, Z. Mroz al. (eds.), 219-236, 1995.
171. Hurty, W. C. and M. F. Rubinstein, *Dynamic of Structures*, Prentice-Hall, Inc. Englewood Cliffs, New Jersey, 1964.
172. Höeg, K., Christian, J. T., and Whitman, R. V., Settlement of Strip Load on Elastic-Plastic Soil, *J. Soil Mech. Found. Div. ASCE*, 94(SM2), 431-445, 1968.
173. Chen, W. F., *Limit Analysis and Soil Plasticity*, Elsevier Scientific Publishing Company, Amsterdam, Oxford and New York, 1975.
174. Valliappan, S., Discussion, *J. Soil Mech. Found. Div., ASCE*, 95(SM2), 676-678, 1969.
175. Private Communication with Prof. Jonah Lee. January, 1998.
176. Huang, Y. J. and E. Stein, Prediction of the Fatigue Threshold for a Cracked Body Using Shakedown Theory, *Fatigue Fracture Engng. Mater. Struct.* Vol. 18, No. 3, pp. 363-370, 1995.
177. Huang, Y. J. and E. Stein, Shakedown of a CT Specimen with St52 Steel – Experimental, Analytical and Numerical Investigations, *J. Strain Analysis*, vol. 30 No. 4, 1995.
178. Huang, Y. J. and E. Stein, Shakedown of a Cracked Body Consisting of Kinematic Hardening Material, *Engineering Fracture Mechanics* vol. 54, No. 1, pp.107-112, 1996.

APPENDICES

.

.

.

AAPENDIX A
TABLE USED IN CHAPTER IV

Table A.1: Function h_I for the Compact Specimen in Plane Strain Case

a/b	Hardening parameter n								
	1	2	3	5	7	10	13	16	20
1/4	2.23	2.05	1.78	1.48	1.33	1.26	1.25	1.32	1.57
3/8	2.15	1.72	1.39	0.97	0.693	0.443	0.276	0.176	0.098
1/2	1.94	1.51	1.24	0.919	0.685	0.461	0.314	0.216	0.132
5/8	1.76	1.45	1.24	0.974	0.752	0.602	0.459	0.347	0.248
3/4	1.71	1.42	1.26	1.033	0.864	0.717	0.575	0.448	0.345
1	1.57	1.45	1.35	1.18	1.08	0.95	0.85	0.73	0.63

Table A.2: J_curve Data in Fatigue Analysis

Crack Length	J-integral value at Different Load Levels (M)				
(M)	241.32(MN)	258.56(MN)	275.8(MN)	293.04(MN)	310.28(MN)
0.11722	0.01375	0.02878	0.05744	0.10994	0.20276
0.11798	0.01698	0.03553	0.07092	0.13573	0.25034
0.11875	0.02099	0.04394	0.08770	0.16785	0.30958
0.11951	0.02600	0.05442	0.10862	0.20790	0.38345
0.12027	0.03225	0.06752	0.13476	0.25793	0.47573
0.12103	0.04008	0.08390	0.16746	0.32054	0.59120
0.12179	0.04989	0.10444	0.20846	0.39902	0.73594
0.12256	0.06221	0.13023	0.25995	0.49757	0.91772
0.12332	0.07771	0.16269	0.32473	0.62157	1.14642
0.12408	0.09725	0.20359	0.40638	0.77787	1.43471
0.12484	0.12193	0.25526	0.50951	0.97527	1.79879
0.12560	0.15315	0.32063	0.64000	1.22506	2.25951
0.12637	0.19274	0.40352	0.80546	1.54178	2.84368
0.12713	0.24299	0.50873	1.01547	1.94377	3.58511
0.12789	0.30663	0.64196	1.28141	2.45283	4.52404
0.12865	0.38773	0.81175	1.62033	3.10159	5.72062
0.12941	0.49130	1.02860	2.05320	3.93018	7.24889
0.13018	0.62389	1.30619	2.60729	4.99081	9.20514
0.13094	0.79399	1.66231	3.31817	6.35155	11.71492
0.13170	1.01272	2.12027	4.23231	8.10138	14.94235
0.13246	1.29467	2.71058	5.41064	10.35692	19.10252
0.13322	1.65899	3.47334	6.93320	13.27138	24.47802
0.13399	2.13091	4.46138	8.90545	17.04661	31.44114
0.13475	2.74376	5.74448	11.46667	21.94925	40.48368
0.13551	3.54170	7.41508	14.80140	28.33252	52.25713
0.13627	4.58337	9.59599	19.15477	36.66566	67.62696
0.13703	5.94694	12.45083	24.85339	47.57384	87.74627
0.13780	7.73683	16.19825	32.33370	61.89251	114.15596
0.13856	10.09302	21.13132	42.18072	80.74149	148.92145
0.13932	13.20374	27.64411	55.18105	105.62647	194.81989

Table A.3: R curve Data in Fatigue Analysis

Crack Length (m)	0.117221	0.117602	0.117983	0.118364	0.118745	0.119126	0.119507	0.119888	0.120269	0.12065
J-Integral (MN/M)	0	0.225715	0.4172875	0.58086	0.72163	0.84392	0.951335	1.046815	1.13274	1.2110525
Crack Length (in.)	4.615	4.63	4.645	4.66	4.675	4.69	4.705	4.72	4.735	4.75
J-Integral (in.-kips/in ²)	0	1.2898	2.3845	3.3192	4.1236	4.8224	5.4362	5.9818	6.4728	6.9203

Crack Length (m)	0.121031	0.121412	0.121793	0.122174	0.122555	0.122936	0.123317	0.123698	0.124079	0.12446
J-Integral (MN/M)	1.283345	1.3508425	1.41456	1.4753025	1.5337	1.59026	1.648885	1.6796325	1.7264275	1.754375
Crack Length (in.)	4.765	4.78	4.795	4.81	4.825	4.84	4.855	4.87	4.885	4.9
J-Integral (in.-kips/in ²)	7.3334	7.7191	8.0832	8.4303	8.764	9.0872	9.4222	9.5979	9.8653	10.025

Crack Length (m)	0.125603	0.124841	0.125222	0.125984	0.126365	0.126746	0.127127	0.127508	0.127889	0.12827
J-Integral (MN/M)	1.886675	1.798475	1.842575	1.930775	1.974875	2.018975	2.063075	2.107175	2.151275	2.195375
Crack Length (in.)	4.945	4.915	4.93	4.96	4.975	4.99	5.005	5.02	5.035	5.05
J-Integral (in.-kips/in ²)	10.781	10.277	10.529	11.033	11.285	11.537	11.789	12.041	12.293	12.545

Crack Length (m)	0.128651	0.129032	0.129413	0.129794	0.130175	0.130556	0.130937	0.131318	0.131699	0.13208
J-Integral (MN/M)	2.239475	2.283575	2.327675	2.371775	2.415875	2.459975	2.504075	2.548175	2.592275	2.636375
Crack Length (in.)	5.065	5.08	5.095	5.11	5.125	5.14	5.155	5.17	5.185	5.2
J-Integral (in.-kips/in ²)	12.797	13.049	13.301	13.553	13.805	14.057	14.309	14.561	14.813	15.065

Crack Length (m)	0.132461	0.132842	0.133223	0.133604	0.133985	0.134366	0.134747	0.135128	0.135509	0.13589
J-Integral (MN/M)	2.680475	2.724575	2.768675	2.812775	2.856875	2.900975	2.945075	2.989175	3.033275	3.077375
Crack Length (in.)	5.215	5.23	5.245	5.26	5.275	5.29	5.305	5.32	5.335	5.35
J-Integral (in.-kips/in ²)	15.317	15.569	15.821	16.073	16.325	16.577	16.829	17.081	17.333	17.585

Crack Length (m)	0.136271	0.136652	0.137033	0.137414	0.137795	0.138176	0.138557	0.138938	0.139319	0.1397
J-Integral (MN/M)	3.121475	3.165575	3.209675	3.253775	3.297875	3.341975	3.386075	3.430175	3.474275	3.518375
Crack Length (in.)	5.365	5.38	5.395	5.41	5.425	5.44	5.455	5.47	5.485	5.5
J-Integral (in.-kips/in ²)	17.837	18.089	18.341	18.593	18.845	19.097	19.349	19.601	19.853	20.105

Table A.4: Crack Increments Data in Fatigue Analysis

Crack Tip Location (M)	Crack Increment at Different Load Levels (M)				
	241.32(MN)	258.56(MN)	275.8(MN)	293.04(MN)	310.28(MN)
0.117221	0.000059	0.000171	0.000046	0.000047	0.000022
0.117983	0.000466	0.000235	0.000118	0.000058	0.000028
0.118745	0.000601	0.000296	0.000148	0.000072	0.000034
0.119507	0.000792	0.000376	0.000185	0.00009	0.000042
0.120269	0.001079	0.000483	0.000233	0.000113	0.000053
0.121031		0.00063	0.000296	0.000141	0.000066
0.121793		0.000839	0.000378	0.000178	0.000082
0.122555		0.001165	0.000489	0.000225	0.000103
0.123317			0.000642	0.000287	0.00013
0.124079			0.000865	0.000369	0.000165
0.124841			0.001221	0.00048	0.00021
0.125603				0.000634	0.000269
0.126365				0.00086	0.000347
0.127127				0.001225	0.000453
0.127889					0.000601
0.128651					0.000818
0.129413					0.001166

Table A.5: Crack Increments Data in Fatigue Analysis

Crack Tip Location (M)	Modified Crack Increment at Different Load Levels (M)				
	241.32(MN)	258.56(MN)	275.8(MN)	293.04(MN)	310.28(MN)
0.117221	0.000029	0.000085	0.000323	0.000023	0.000011
0.117983	0.000233	0.000117	0.000059	0.000029	0.000014
0.118745	0.000301	0.000148	0.000074	0.000036	0.000017
0.119507	0.000396	0.000188	0.000093	0.000045	0.000021
0.120269	0.000539	0.000242	0.000117	0.000056	0.000026
0.121031		0.000315	0.000148	0.000071	0.000033
0.121793		0.00042	0.000189	0.000089	0.000041
0.122555		0.000583	0.000244	0.000113	0.000052
0.123317			0.000321	0.000143	0.000065
0.124079			0.000432	0.000184	0.000082
0.124841			0.00061	0.00024	0.000105
0.125603				0.000317	0.000134
0.126365				0.00043	0.000174
0.127127				0.000613	0.000227
0.127889					0.000301
0.128651				-	0.000409
0.129413					0.000583

Table A.6: J-integral Increments Data in Fatigue Analysis

Crack Tip Location (M)	J-integral at Different Load Levels (M)				
	241.32(MN)	258.56(MN)	275.8(MN)	293.04(MN)	310.28(MN)
0.117221	0.072255	0.206883	0.722013	0.057979	0.027599
0.117983	0.53688	0.281371	0.14444	0.071709	0.034101
0.118745	0.677455	0.351275	0.179448	0.088874	0.04221
0.119507	0.862807	0.440524	0.223591	0.110391	0.052348
0.120269	1.114895	0.55558	0.279528	0.137452	0.06505
0.121031		0.705938	0.350843	0.171606	0.081008
0.121793		0.906586	0.442479	0.214899	0.101114
0.122555		1.184748	0.561463	0.270056	0.126526
0.123317			0.718266	0.340777	0.158765
0.124079			0.929789	0.432195	0.199843
0.124841			1.228067	0.551662	0.252455
0.125603				0.710236	0.320273
0.126365				0.925827	0.408389
0.127127				1.231725	0.523855
0.127889					0.677239
0.128651					0.886581
0.129413					1.185502

Table A.8: Crack Increment Data in Fatigue Analysis

Crack Tip Location (MM)	Crack Increments at Different Load Levels (MM)											
	734.2(N)	700.8(N)	667.5(N)	634.1(N)	600.8(N)	567.4(N)	534(N)	467.2(N)	433.8(N)	400.5(N)	333.8(N)	233.6(N)
3.2992	0.000807	0.000719	0.000635	0.000567	0.000498	0.000437	0.000383	0.000285	0.000244	0.000204	0.000139	0.000067
3.31524	0.001019	0.000906	0.000806	0.000713	0.00062	0.000543	0.000476	0.000352	0.000299	0.000253	0.000173	0.000083
4.1239		0.001069	0.000948	0.000838	0.000736	0.00064	0.00056	0.000417	0.000353	0.0003	0.000206	0.000098
4.9486				0.000967	0.000848	0.000738	0.000647	0.000483	0.000408	0.000345	0.000235	0.000113
5.7733					0.000964	0.00084	0.00073	0.000543	0.000462	0.00039	0.000266	0.000128
6.598						0.000944	0.000828	0.00061	0.000522	0.000435	0.000301	0.000144
7.4227						0.001045	0.000909	0.000671	0.000571	0.000482	0.000329	0.000159
8.2474							0.001	0.000736	0.000629	0.00053	0.000362	0.000174
9.0721								0.000804	0.000695	0.00059	0.000395	0.000189
9.8968								0.000874	0.000744	0.000632	0.000431	0.000204
10.7215								0.000946	0.000799	0.000679	0.000463	0.000222
11.5462									0.000877	0.000738	0.000502	0.000238
12.3709									0.000931	0.000783	0.000542	0.000255
13.1956									0.001	0.000848	0.000571	0.000274
14.0203										0.000897	0.000605	0.000294
14.845										0.000955	0.000644	0.000311

Table A.9: Modified Crack Increment Data in Fatigue Analysis

Crack Tip Location (MM)	Modified Crack Increments at Different Load Levels (10**(-3)MM)											
	734.2(N)	700.8(N)	667.5(N)	634.1(N)	600.8(N)	567.4(N)	534(N)	467.2(N)	433.8(N)	400.5(N)	333.8(N)	233.6(N)
3.2992	0.4035	0.3595	0.3175	0.2835	0.249	0.2185	0.1915	0.1425	0.122	0.102	0.07	0.034
3.31524	0.5095	0.453	0.403	0.3565	0.31	0.2715	0.238	0.176	0.1495	0.1265	0.086	0.042
4.1239		0.5345	0.474	0.419	0.368	0.32	0.28	0.2085	0.1765	0.15	0.103	0.049
4.9486				0.4835	0.424	0.369	0.3235	0.2415	0.204	0.1725	0.1175	0.056
5.7733					0.482	0.42	0.365	0.2715	0.231	0.195	0.133	0.064
6.598						0.472	0.414	0.305	0.261	0.2175	0.1505	0.072
7.4227						0.5225	0.4545	0.3355	0.2855	0.241	0.1645	0.08
8.2474							0.5	0.368	0.3145	0.265	0.181	0.087
9.0721								0.402	0.3475	0.295	0.1975	0.094
9.8968								0.437	0.372	0.316	0.2155	0.102
10.7215								0.473	0.3995	0.3395	0.2315	0.111
11.5462									0.4385	0.369	0.251	0.119
12.3709									0.4655	0.3915	0.271	0.1275
13.1956									0.5	0.424	0.2855	0.137
14.0203										0.4485	0.3025	0.147
14.845										0.4775	0.322	0.1555

Table A.10: Cyclic J-integral Data in Fatigue Analysis

Crack Tip Location (MM)	Cyclic J-integral at Different Load Levels (Mpa-MM)											
	734.2(N)	700.8(N)	667.5(N)	634.1(N)	600.8(N)	567.4(N)	534(N)	467.2(N)	433.8(N)	400.5(N)	333.8(N)	233.6(N)
3.2992	0.00156	0.00145	0.00135	0.00126	0.00118	0.0011	0.00104	0.00092	0.00087	0.00082	0.00074	0.00065
3.31524	0.00181	0.00168	0.00155	0.00144	0.00133	0.00123	0.00115	0.001	0.00094	0.00088	0.00078	0.00067
4.1239		0.00187	0.00173	0.00159	0.00147	0.00135	0.00125	0.00108	0.001	0.00094	0.00082	0.00069
4.9486				0.00175	0.0016	0.00147	0.00136	0.00116	0.00107	0.00099	0.00086	0.00071
5.7733					0.00175	0.00159	0.00146	0.00123	0.00113	0.00105	0.00089	0.00073
6.598						0.00172	0.00158	0.00131	0.00121	0.0011	0.00094	0.00075
7.4227						0.00185	0.00168	0.00139	0.00127	0.00116	0.00097	0.00076
8.2474							0.00179	0.00147	0.00134	0.00122	0.00101	0.00078
9.0721								0.00155	0.00142	0.00129	0.00105	0.0008
9.8968								0.00164	0.00148	0.00134	0.0011	0.00082
10.7215								0.00172	0.00155	0.0014	0.00114	0.00084
11.5462									0.00164	0.00147	0.00118	0.00086
12.3709									0.00171	0.00153	0.00123	0.00088
13.1956									0.00179	0.00161	0.00127	0.0009
14.0203										0.00166	0.00131	0.00093
14.845										0.00174	0.00136	0.00095

Table A.11: Pretorius Fitting Equations of Fatigue Test

Dependent Variable	Fatigue Equation	Standard Error in Independent Variable N_f	Number of Data Points
Initial Strain	$\log N_f = 9.110 - 0.0578\epsilon_i$	7.24	31
Initial Stress	$\log N_f = 7.481 - 0.0162\sigma_i$	14.2	25
Initial Radius of Curvature Ratio	$\log N_f = 10.281 - 11.280 \frac{R_c}{R}$	9.12	23

Table A.12: Asphalt Cement Material Mechanical Properties

Temperature (F)	Elastic Modulus (MPa)	Poison Ratio (MPa)	Cohesion -	Friction Angle degree
10°	$2.21 * 10^4$	0.35	7.584	48°
68°	$2.48 * 10^3$	0.35	4.551	17°

Table A.13: Crack Increment Data in Fatigue Analysis

Crack Tip Location (MM)	Crack Increments at Different Load Levels (MM)											
	1668.8(N)	1585.3(N)	1501.8(N)	1418.4(N)	1335(N)	1251.6(N)	1168.1(N)	1084.7(N)	917.8(N)	834.4(N)	801(N)	767.6(N)
3.2992	0.00107	0.00095	0.00085	0.00074	0.00065	0.00056	0.00049	0.00042	0.00029	0.00024	0.00022	0.0002
3.300314	0.00132	0.00118	0.00104	0.00092	0.00081	0.0007	0.00061	0.00051	0.00036	0.0003	0.00027	0.00025
4.1239	0.00157	0.0014	0.00124	0.00109	0.00095	0.00083	0.00071	0.00061	0.00043	0.00035	0.00033	0.0003
4.9486	0.00182	0.00161	0.00142	0.00126	0.0011	0.00095	0.00082	0.0007	0.0005	0.00041	0.00037	0.00034
5.7733			0.00161	0.00142	0.00124	0.00108	0.00093	0.0008	0.00056	0.00046	0.00042	0.00039
6.598				0.00159	0.00139	0.00121	0.00104	0.00089	0.00063	0.00051	0.00047	0.00043
7.4227						0.00133	0.00115	0.00099	0.00069	0.00057	0.00052	0.00048

Table A.14: Modified Crack Increment Data in Fatigue Analysis

Crack Tip Location (MM)	Modified Crack Increment at Different Load Levels (MM)											
	1668.8(N)	1585.3(N)	1501.8(N)	1418.4(N)	1335(N)	1251.6(N)	1168.1(N)	1084.7(N)	917.8(N)	834.4(N)	801(N)	767.6(N)
3.2992	0.00053	0.00048	0.00042	0.00037	0.00032	0.00028	0.00024	0.00021	0.00015	0.00012	0.00011	0.0001
3.300314	0.00066	0.00059	0.00052	0.00046	0.0004	0.00035	0.0003	0.00026	0.00018	0.00015	0.00014	0.00013
4.1239	0.00078	0.0007	0.00062	0.00054	0.00048	0.00041	0.00036	0.0003	0.00022	0.00018	0.00016	0.00015
4.9486	0.00091	0.0008	0.00071	0.00063	0.00055	0.00048	0.00041	0.00035	0.00025	0.0002	0.00019	0.00017
5.7733			0.0008	0.00071	0.00062	0.00054	0.00047	0.0004	0.00028	0.00023	0.00021	0.00019
6.598				0.00079	0.00069	0.0006	0.00052	0.00044	0.00031	0.00026	0.00024	0.00022
7.4227						0.00067	0.00058	0.00049	0.00035	0.00028	0.00026	0.00024

Table A.15: Cyclic J-integral Data in Fatigue Analysis

Crack Tip Location (MM)	Cyclic J-integral at Different Load Levels (Mpa - MM)											
	1668.8(N)	1585.3(N)	1501.8(N)	1418.4(N)	1335(N)	1251.6(N)	1168.1(N)	1084.7(N)	917.8(N)	834.4(N)	801(N)	767.6(N)
3.2992	0.006246	0.005898	0.005577	0.005255	0.004973	0.004711	0.004479	0.004264	0.003893	0.003732	0.003672	0.003613
3.300314	0.007025	0.006598	0.00617	0.005802	0.005451	0.005131	0.004842	0.004563	0.004103	0.003903	0.003833	0.003764
4.1239	0.007759	0.007244	0.006756	0.006305	0.005895	0.005513	0.005166	0.004847	0.004308	0.004077	0.00399	0.003904
4.9486	0.008529	0.007881	0.007317	0.006816	0.00633	0.005891	0.005495	0.005132	0.004506	0.004239	0.004136	0.004046
5.7733			0.007887	0.007309	0.006773	0.00628	0.005828	0.005417	0.004701	0.004402	0.004287	0.004183
6.598				0.007815	0.007218	0.006672	0.00617	0.0057	0.004903	0.004564	0.004439	0.004318
7.4227						0.007051	0.006504	0.005994	0.005099	0.004725	0.004588	0.004457

Table A.16: Crack Increment Data in Fatigue Analysis

Crack Tip Location (MM)	Crack Increments at Different Load Levels (MM)											
	600.8(N)	567.4(N)	534(N)	500.6(N)	467.2(N)	433.8(N)	400.5(N)	367.1(N)	333.75(N)	300.4(N)	267(N)	233.6(N)
3.2992	0.00095	0.00085	0.00075	0.00066	0.00057	0.00049	0.00042	0.00035	0.00029	0.00024	0.00019	0.00015
3.300314	0.00118	0.00105	0.00093	0.00082	0.00071	0.00061	0.00052	0.00044	0.00036	0.00029	0.00023	0.00018
4.1239	0.0014	0.00125	0.0011	0.00097	0.00084	0.00073	0.00062	0.00052	0.00043	0.00035	0.00028	0.00021
4.9486	0.00161	0.00144	0.00127	0.00112	0.00098	0.00084	0.00072	0.0006	0.0005	0.0004	0.00032	0.00025
5.7733	0.00183	0.00163	0.00144	0.00127	0.0011	0.00095	0.00081	0.00068	0.00056	0.00046	0.00036	0.00028
6.598		0.00182	0.00161	0.00142	0.00123	0.00106	0.00091	0.00076	0.00063	0.00051	0.0004	0.00031
7.4227		0.00202	0.00178	0.00157	0.00136	0.00117	0.001	0.00084	0.0007	0.00056	0.00045	0.00034

Table A.17: Modified Crack Increment Data in Fatigue Analysis

Crack Tip Location (MM)	Modified Crack Increments at Different Load Levels (MM)											
	600.8(N)	567.4(N)	534(N)	500.6(N)	467.2(N)	433.8(N)	400.5(N)	367.1(N)	333.75(N)	300.4(N)	267(N)	233.6(N)
3.2992	0.00048	0.00042	0.00038	0.00033	0.00029	0.00025	0.00021	0.00018	0.00015	0.00012	9.4E-05	7.3E-05
3.300314	0.00059	0.00053	0.00047	0.00041	0.00036	0.00031	0.00026	0.00022	0.00018	0.00015	0.00012	9E-05
4.1239	0.0007	0.00062	0.00055	0.00048	0.00042	0.00036	0.00031	0.00026	0.00022	0.00017	0.00014	0.00011
4.9486	0.00081	0.00072	0.00064	0.00056	0.00049	0.00042	0.00036	0.0003	0.00025	0.0002	0.00016	0.00012
5.7733	0.00091	0.00082	0.00072	0.00063	0.00055	0.00047	0.00041	0.00034	0.00028	0.00023	0.00018	0.00014
6.598		0.00091	0.00081	0.00071	0.00062	0.00053	0.00045	0.00038	0.00031	0.00025	0.0002	0.00016
7.4227		0.00101	0.00089	0.00078	0.00068	0.00059	0.0005	0.00042	0.00035	0.00028	0.00022	0.00017

Table A.18: Cyclic J-integral Data in Fatigue Analysis

Crack Tip Location (MM)	Cyclic J-integral at Different Load Levels (Mpa - MM)											
	600.8(N)	567.4(N)	534(N)	500.6(N)	467.2(N)	433.8(N)	400.5(N)	367.1(N)	333.75(N)	300.4(N)	267(N)	233.6(N)
3.2992	0.00405	0.0037	0.00336	0.00305	0.00276	0.00248	0.00224	0.00201	0.0018	0.00161	0.00144	0.00129
3.300314	0.00483	0.00439	0.00398	0.00359	0.00323	0.00289	0.00259	0.0023	0.00204	0.00181	0.0016	0.00141
4.1239	0.00557	0.00506	0.00457	0.00411	0.00368	0.00328	0.00292	0.00257	0.00227	0.00199	0.00174	0.00153
4.9486	0.00631	0.00571	0.00515	0.00462	0.00413	0.00366	0.00325	0.00285	0.0025	0.00217	0.00189	0.00164
5.7733	0.00704	0.00637	0.00572	0.00513	0.00457	0.00404	0.00357	0.00312	0.00273	0.00236	0.00203	0.00175
6.598		0.00702	0.0063	0.00563	0.00501	0.00442	0.00389	0.00338	0.00295	0.00254	0.00218	0.00186
7.4227		0.00768	0.00687	0.00614	0.00545	0.00481	0.00422	0.00366	0.00318	0.00272	0.00232	0.00197

APPENDIX B

Variable Definition of Fatigue Life Analysis Program (FLAP)

The fatigue life analysis program conducts fatigue analysis by using R_curve and J-integral curve. R_curve can be constructed by using load-displacement curves as described in chapter IV. Currently, load-displacement curves and J-integral-displacement curves are obtained by means of elastic-plastic analysis using ABAQUS [1]. FLAP then reads in the load-displacement and J-integral-displacement data and constructs R_curves and J-integral curves. The R_curve and J-integral curves are then used to establish a fatigue crack growth rate equation. From this equation, fatigue life for the considered system can be predicted. The definition of the variables used in the program are defined and explained in the followings.

Elastic-plastic Analysis

Elastic-plastic analysis is conducted by using ABAQUS to obtain load-displacement and J-integral-displacement data. This step is necessary in fatigue analysis. The input data can be stored in a file with extension .inp. ABAQUS can read these data from the file and conduct elastic-plastic analysis.

Input data:

The input data to ABAQUS usually includes node numbers and their coordinates, element numbers and their nodes, material properties, boundary conditions and applied loads. For a detailed description about how to use ABAQUS, refer to the ABAQUS user's manual [1].

Output data:

The output data from ABAQUS are very flexible and usually dependent on the user's requirements. For fatigue life analysis, only load, displacement and J-integral values are needed and saved to a separated file, femdx.m, which will interface with the fatigue analysis program, FLAP. Each file corresponds to a specific initial crack length. Therefore, the number of load – displacement files is equal to the number of different crack lengths.

Fatigue Analysis

Input data:

HED (12A6)	Title of the job, which characterizes the problem you are running.
NUMLD (I4)	Total number of load displacement curves corresponding to different crack lengths..
NUMDX (I4)	Total number of crack increments used in constructing R_curve.
NUMLL (I4)	Total number of load levels in fatigue analysis. For each load level, the program will compute fatigue life.
NUMDS (I4)	The number of the displacement levels. It is not used currently.

DX(F8.4)	Displacement increments used in constructing R _{curve} .
ALPHA(F8.4)	0.0. Currently is not used.
BETA(F8.4)	0.0. Currently is not used.
COHEN(F8.4)	Material cohesion used for each layer for a layered system.
PHI(F8.4)	Material internal friction angle used for each layer for a layered system.
POW(F8.4)	1.0. Currently is not used.
HARDING(F8.4)	This is a correlation factor that will correlate the fatigue crack growth rate obtained by a numerical method to best represent experimental data. The value is within 0.0001 – 0.001.

The following variables are input in free format.

B0	Remaining ligament i. e. WIDTH – C0.
C0	Crack length.
WIDTH	Width of a specimen.
THICK	Thickness of a specimen.
DICK0	Crack increment.
DIS0	Displacement increment. It is not used currently.
ALEN	Length of a Specimen.
E0	Elastic modulus of a specimen.

Output data:

The output data from FLAP basically contains the following information:

- (1) Fatigue crack growth increment at each given load level. The data are arranged in columns from the highest load level down to the lowest load level.
- (2) Cyclic J-integral values corresponding to fatigue crack growth increment at each load level.
- (3) Fatigue crack growth rate obtained by fitting fatigue crack growth increment and cyclic J-integral values.
- (4) Predicted fatigue life for each load level.

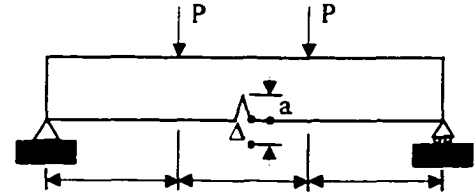
All of these output data are stored in the file, fatig.out.

The flow chart is provided on page 249. The listing of the program (FLAP) is stored on the enclosed diskette.

EXAMPLE FOR INPUT DATA

A simple supported beam as shown in the figure below is given as an example to display how to input data for fatigue analysis using FLAP. The dimension and material properties are:

Length	L = 457.2 MM,		
Width	W = 76.2 MM,		
Thickness	T = 76.2 MM,		
Initial crack length	C0 = 3.2992 MM,		
Ligament	B0 = 72.9008 MM,		
Elastic modulus	E = 17300.0 Mpa,		
Poisson ratio	$\nu = 0.15$,		
Cohesion	C = 2.586 Mpa,	Friction angle	$\phi = 42^\circ$.



The input data to ABAQUS are data defining the finite element model and material properties. The finite element model used in this example is the same as in Fig. 4.3. The elastic material properties are described as above. The parameters of plastic properties of Mohr-columb material model, C and ϕ , have to be converted to the parameters of Drucker-Prager material model, K, β , and σ_c^0 . The formulations to convert these parameters are detailed in the ABAQUS user's manual [1]. In this example they are given by K=1.0, $\beta = 47^\circ$, and $\sigma_c^0 = 4.85$ Mpa. Static analysis procedure was used. Prescribed displacement was given to obtain load displacement data and J-integral displacement data. The output of load displacement data and J-integral displacement data are saved in the files. femdx.m.

The input data for fatigue analysis is given in the following:

```

/*Job title */
FATIGUE ANALYSIS FOR SIMPLE SUPPORTED BEAM
/* Control data as defined above */
20 20 15 15 0.0050 0.00 0.00 2.586 42.0 1.0 0.00057
72.9008,3.2992,76.2,76.2,0.8247,0.030,457.2,17300.0
/* Load levels used in fatigue analysis */
801.0,767.625,734.25,700.875,667.5,634.125
600.75,567.375,534.0,467.25,433.88,400.5
333.75,267.0,233.625
/*Displacement levels. Currently not used */
0.06647,0.06268,0.0592,0.05572,0.05224,0.04875
0.04527,0.04179,0.03831,0.03482,0.03134,0.02785

```

0.02437,0.02089,0.01742

/* Data in the CF array. Currently not used */

3.2992,5.7733,8.2474,9.0721,9.8968

11.5462,13.1956,14.0203,14.0203,14.0203,14.0203

14.0203,14.0203,14.0203,14.0203,14.0203,14.0203

14.0203,14.0203,14.0203

/*Crack increments */

0.8247 0.8247,0.8247,0.8247,0.8247,0.8247,0.8247

0.8247,0.8247,0.8247,0.8247,0.8247,0.8247,0.8247

0.8247,0.8247,0.8247,0.8247,0.8247,0.8247

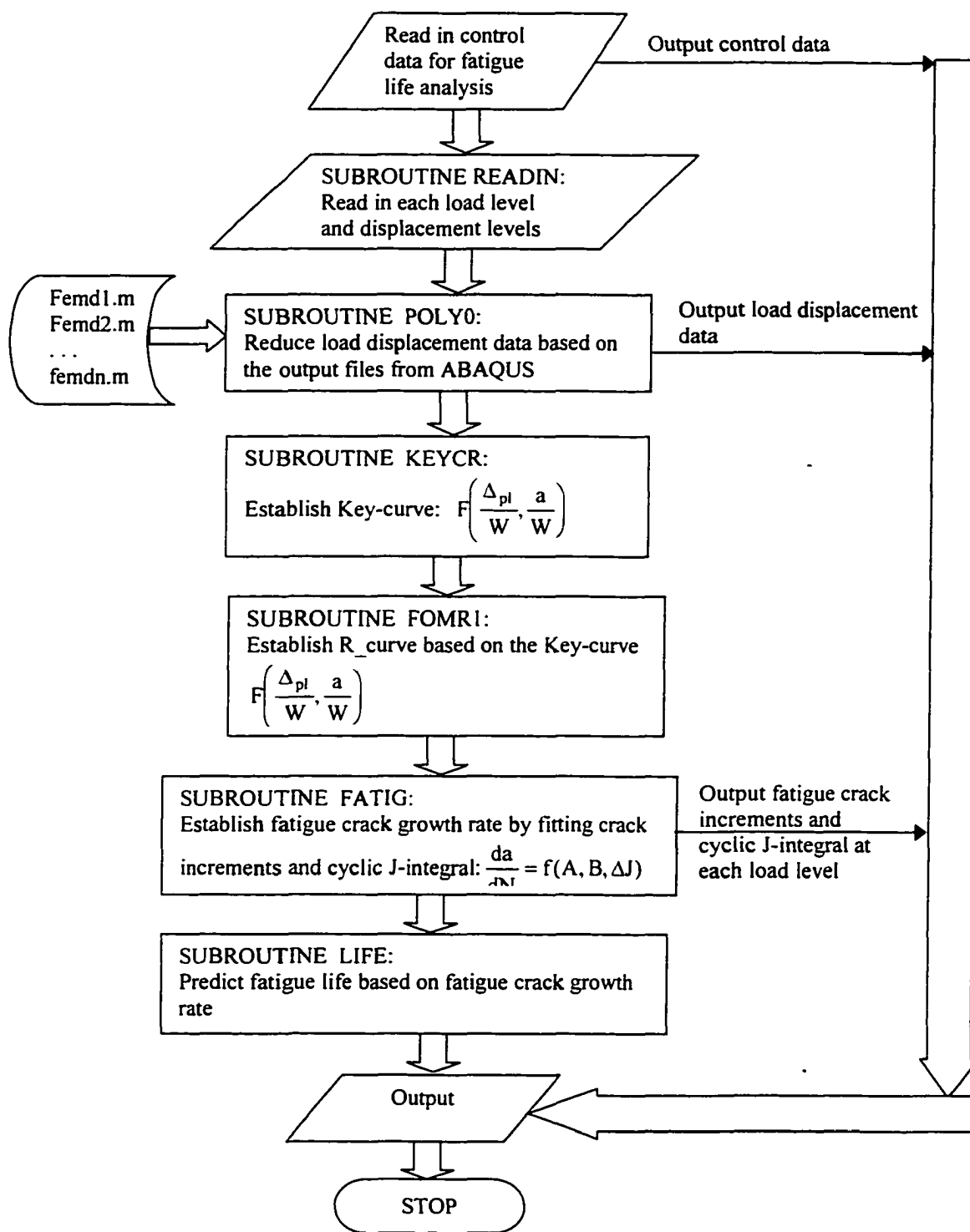
/* Remaining ligaments corresponding to each crack increment */

72.9008,72.0761,71.2514,70.4267,69.602,68.7773,67.9526

67.1279,66.3032,65.4785,63.8291,63.0044,62.1797,61.3550

60.5303,59.7056,58.8809,58.0562,57.2315,56.4068,55.5821

54.7574,53.9327,53.108,52.2833



Output from FLAP:

IFATIGUE ANALYSIS FOR BEAM STRUCTURE

LOAD DISPLACEMENT CURVE NUMBER = 20
 CRACK INCREMENTAL NUMBER = 20
 LOAD LEVEL NUMBER = 15
 DISPLACEMENT LEVEL NUMBER = 15
 DISPLACEMENT DIVISION = 0.0050
 MODIFICATION COEFFICIENT = 0.0000
 MODIFICATION COEFFICIENT = 0.0000
 COHENSIVE COEFFICIENT = 2.5860
 FRACTION COEFFICIENT = 42.0000
 POWER OF FITTING FUNCTION = 1.0000
 POWER OF FITTING FUNCTION = 0.000570

LOAD MATRIX

0.000000E+00	0.647766E+02	0.129505E+03	0.194287E+03	0.258949E+03
0.323600E+03	0.388202E+03	0.452670E+03	0.517020E+03	0.581232E+03
0.645210E+03	0.708918E+03	0.772331E+03	0.835073E+03	0.835073E+03
0.835073E+03	0.835073E+03	0.835073E+03	0.835073E+03	0.835073E+03
0.000000E+00	0.643809E+02	0.128776E+03	0.193055E+03	0.257332E+03
0.321579E+03	0.385680E+03	0.449627E+03	0.513416E+03	0.577047E+03
0.640121E+03	0.702941E+03	0.765253E+03	0.765253E+03	0.765253E+03
0.765253E+03	0.765253E+03	0.765253E+03	0.765253E+03	0.765253E+03
0.000000E+00	0.639635E+02	0.127927E+03	0.191786E+03	0.255608E+03
0.319325E+03	0.382982E+03	0.446408E+03	0.509640E+03	0.572524E+03
0.634939E+03	0.696910E+03	0.696910E+03	0.696910E+03	0.696910E+03
0.696910E+03	0.696910E+03	0.696910E+03	0.696910E+03	0.696910E+03
0.000000E+00	0.635053E+02	0.126945E+03	0.190354E+03	0.253736E+03
0.316946E+03	0.380035E+03	0.442862E+03	0.505477E+03	0.567657E+03
0.629253E+03	0.690331E+03	0.690331E+03	0.690331E+03	0.690331E+03
0.690331E+03	0.690331E+03	0.690331E+03	0.690331E+03	0.690331E+03
0.000000E+00	0.630066E+02	0.125942E+03	0.188899E+03	0.251711E+03
0.314346E+03	0.376819E+03	0.439038E+03	0.500958E+03	0.562348E+03
0.623158E+03	0.623158E+03	0.623158E+03	0.623158E+03	0.623158E+03
0.623158E+03	0.623158E+03	0.623158E+03	0.623158E+03	0.623158E+03
0.000000E+00	0.624744E+02	0.124919E+03	0.187257E+03	0.249536E+03
0.311547E+03	0.373412E+03	0.434930E+03	0.496076E+03	0.556682E+03
0.556682E+03	0.556682E+03	0.556682E+03	0.556682E+03	0.556682E+03
0.556682E+03	0.556682E+03	0.556682E+03	0.556682E+03	0.556682E+03
0.000000E+00	0.619134E+02	0.123809E+03	0.185542E+03	0.247179E+03
0.308681E+03	0.369812E+03	0.430659E+03	0.491131E+03	0.550835E+03
0.550835E+03	0.550835E+03	0.550835E+03	0.550835E+03	0.550835E+03
0.550835E+03	0.550835E+03	0.550835E+03	0.550835E+03	0.550835E+03
0.000000E+00	0.613212E+02	0.122589E+03	0.183775E+03	0.244793E+03
0.305535E+03	0.366006E+03	0.426122E+03	0.485709E+03	0.544677E+03
0.544677E+03	0.544677E+03	0.544677E+03	0.544677E+03	0.544677E+03
0.544677E+03	0.544677E+03	0.544677E+03	0.544677E+03	0.544677E+03
0.000000E+00	0.606917E+02	0.121322E+03	0.181848E+03	0.242146E+03
0.302207E+03	0.361986E+03	0.421243E+03	0.480181E+03	0.538220E+03

0.538220E+03	0.538220E+03	0.538220E+03	0.538220E+03	0.538220E+03
0.538220E+03	0.538220E+03	0.538220E+03	0.538220E+03	0.538220E+03
0.000000E+00	0.600424E+02	0.120016E+03	0.179880E+03	0.239495E+03
0.298861E+03	0.357885E+03	0.416376E+03	0.474368E+03	0.474368E+03
0.474368E+03	0.474368E+03	0.474368E+03	0.474368E+03	0.474368E+03
0.474368E+03	0.474368E+03	0.474368E+03	0.474368E+03	0.474368E+03
0.000000E+00	0.593572E+02	0.118634E+03	0.177787E+03	0.236692E+03
0.295354E+03	0.353611E+03	0.411305E+03	0.468385E+03	0.468385E+03
0.468385E+03	0.468385E+03	0.468385E+03	0.468385E+03	0.468385E+03
0.468385E+03	0.468385E+03	0.468385E+03	0.468385E+03	0.468385E+03
0.000000E+00	0.586502E+02	0.117210E+03	0.175630E+03	0.233823E+03
0.291674E+03	0.349100E+03	0.405860E+03	0.462156E+03	0.462156E+03
0.462156E+03	0.462156E+03	0.462156E+03	0.462156E+03	0.462156E+03
0.462156E+03	0.462156E+03	0.462156E+03	0.462156E+03	0.462156E+03
0.000000E+00	0.579172E+02	0.115739E+03	0.173435E+03	0.230820E+03
0.287925E+03	0.344334E+03	0.400478E+03	0.400478E+03	0.400478E+03
0.400478E+03	0.400478E+03	0.400478E+03	0.400478E+03	0.400478E+03
0.400478E+03	0.400478E+03	0.400478E+03	0.400478E+03	0.400478E+03
0.000000E+00	0.571637E+02	0.114209E+03	0.171141E+03	0.227710E+03
0.283935E+03	0.339740E+03	0.394708E+03	0.394708E+03	0.394708E+03
0.394708E+03	0.394708E+03	0.394708E+03	0.394708E+03	0.394708E+03
0.394708E+03	0.394708E+03	0.394708E+03	0.394708E+03	0.394708E+03
0.000000E+00	0.563841E+02	0.112677E+03	0.168784E+03	0.224517E+03
0.280015E+03	0.334836E+03	0.388919E+03	0.442397E+03	0.442397E+03
0.442397E+03	0.442397E+03	0.442397E+03	0.442397E+03	0.442397E+03
0.442397E+03	0.442397E+03	0.442397E+03	0.442397E+03	0.442397E+03
0.000000E+00	0.555845E+02	0.111041E+03	0.166318E+03	0.221290E+03
0.275804E+03	0.329830E+03	0.383140E+03	0.383140E+03	0.383140E+03
0.383140E+03	0.383140E+03	0.383140E+03	0.383140E+03	0.383140E+03
0.383140E+03	0.383140E+03	0.383140E+03	0.383140E+03	0.383140E+03
0.000000E+00	0.547579E+02	0.109415E+03	0.163830E+03	0.217920E+03
0.271566E+03	0.324703E+03	0.376976E+03	0.376976E+03	0.376976E+03
0.376976E+03	0.376976E+03	0.376976E+03	0.376976E+03	0.376976E+03
0.376976E+03	0.376976E+03	0.376976E+03	0.376976E+03	0.376976E+03
0.000000E+00	0.539201E+02	0.107761E+03	0.161289E+03	0.214519E+03
0.267303E+03	0.319503E+03	0.370726E+03	0.370726E+03	0.370726E+03
0.370726E+03	0.370726E+03	0.370726E+03	0.370726E+03	0.370726E+03
0.370726E+03	0.370726E+03	0.370726E+03	0.370726E+03	0.370726E+03
0.000000E+00	0.530576E+02	0.106018E+03	0.158722E+03	0.210989E+03
0.262752E+03	0.313962E+03	0.313962E+03	0.313962E+03	0.313962E+03
0.313962E+03	0.313962E+03	0.313962E+03	0.313962E+03	0.313962E+03
0.313962E+03	0.313962E+03	0.313962E+03	0.313962E+03	0.313962E+03
0.000000E+00	0.521794E+02	0.104212E+03	0.156014E+03	0.207412E+03
0.258315E+03	0.308528E+03	0.358036E+03	0.358036E+03	0.358036E+03
0.358036E+03	0.358036E+03	0.358036E+03	0.358036E+03	0.358036E+03
0.358036E+03	0.358036E+03	0.358036E+03	0.358036E+03	0.358036E+03

J-INTEGRAL MATRIX FOR LOAD CONTROL

0.122977E-02	0.109200E-02	0.984308E-03	0.876636E-03	0.774928E-03
0.691242E-03	0.607555E-03	0.532638E-03	0.467330E-03	0.347650E-03
0.298046E-03	0.248428E-03	0.169213E-03	0.107310E-03	0.818201E-04
0.000000E+00	0.139366E-02	0.124257E-02	0.110519E-02	0.983411E-03

0.869957E-03	0.756502E-03	0.663043E-03	0.581177E-03	0.429162E-03
0.364493E-03	0.308706E-03	0.211739E-03	0.133233E-03	0.101048E-03
0.000000E+00	0.000000E+00	0.146402E-02	0.130363E-02	0.115634E-02
0.102175E-02	0.898185E-03	0.780459E-03	0.683493E-03	0.509413E-03
0.430570E-03	0.366396E-03	0.250953E-03	0.157953E-03	0.119745E-03
0.000000E+00	0.000000E+00	0.000000E+00	0.150194E-02	0.133553E-02
0.117861E-02	0.103378E-02	0.900097E-03	0.789567E-03	0.588726E-03
0.498144E-03	0.421541E-03	0.286495E-03	0.180681E-03	0.138321E-03
0.000000E+00	0.000000E+00	0.000000E+00	0.000000E+00	0.000000E+00
0.133496E-02	0.117588E-02	0.102428E-02	0.890362E-03	0.662129E-03
0.563564E-03	0.476441E-03	0.324066E-03	0.206393E-03	0.156530E-03
0.000000E+00	0.000000E+00	0.000000E+00	0.000000E+00	0.000000E+00
0.000000E+00	0.131492E-02	0.115133E-02	0.100991E-02	0.744410E-03
0.637348E-03	0.530254E-03	0.366980E-03	0.230511E-03	0.175358E-03
0.000000E+00	0.000000E+00	0.000000E+00	0.000000E+00	0.000000E+00
0.000000E+00	0.000000E+00	0.127451E-02	0.110838E-02	0.818562E-03
0.696478E-03	0.588040E-03	0.401510E-03	0.252950E-03	0.193859E-03
0.000000E+00	0.000000E+00	0.000000E+00	0.000000E+00	0.000000E+00
0.000000E+00	0.000000E+00	0.139857E-02	0.121902E-02	0.897965E-03
0.767570E-03	0.646469E-03	0.441637E-03	0.279875E-03	0.212319E-03
0.000000E+00	0.000000E+00	0.000000E+00	0.000000E+00	0.000000E+00
0.000000E+00	0.000000E+00	0.000000E+00	0.132917E-02	0.981042E-03
0.847666E-03	0.719911E-03	0.482594E-03	0.303101E-03	0.231275E-03
0.000000E+00	0.000000E+00	0.000000E+00	0.000000E+00	0.000000E+00
0.000000E+00	0.000000E+00	0.000000E+00	0.000000E+00	0.106564E-02
0.907727E-03	0.770493E-03	0.526152E-03	0.329838E-03	0.249319E-03
0.000000E+00	0.000000E+00	0.000000E+00	0.000000E+00	0.000000E+00
0.000000E+00	0.000000E+00	0.000000E+00	0.000000E+00	0.115403E-02
0.974582E-03	0.828070E-03	0.564624E-03	0.357792E-03	0.270865E-03
0.000000E+00	0.000000E+00	0.000000E+00	0.000000E+00	0.000000E+00
0.000000E+00	0.000000E+00	0.000000E+00	0.000000E+00	0.124755E-02
0.106984E-02	0.900281E-03	0.612712E-03	0.382396E-03	0.290606E-03
0.000000E+00	0.000000E+00	0.000000E+00	0.000000E+00	0.000000E+00
0.000000E+00	0.000000E+00	0.000000E+00	0.000000E+00	0.000000E+00
0.113596E-02	0.954630E-03	0.661171E-03	0.411746E-03	0.311201E-03
0.000000E+00	0.000000E+00	0.000000E+00	0.000000E+00	0.000000E+00
0.000000E+00	0.000000E+00	0.000000E+00	0.000000E+00	0.000000E+00
0.121962E-02	0.103465E-02	0.696607E-03	0.434165E-03	0.334364E-03
0.000000E+00	0.000000E+00	0.000000E+00	0.000000E+00	0.000000E+00
0.000000E+00	0.000000E+00	0.000000E+00	0.000000E+00	0.000000E+00
0.130124E-02	0.109409E-02	0.738097E-03	0.464601E-03	0.358784E-03
0.000000E+00	0.000000E+00	0.000000E+00	0.000000E+00	0.000000E+00
0.000000E+00	0.000000E+00	0.000000E+00	0.000000E+00	0.000000E+00
0.000000E+00	0.116452E-02	0.786190E-03	0.497893E-03	0.379777E-03
0.000000E+00	0.000000E+00	0.000000E+00	0.000000E+00	0.000000E+00
0.000000E+00	0.000000E+00	0.000000E+00	0.000000E+00	0.000000E+00
0.000000E+00	0.124269E-02	0.835196E-03	0.528547E-03	0.397166E-03
0.000000E+00	0.000000E+00	0.000000E+00	0.000000E+00	0.000000E+00
0.000000E+00	0.000000E+00	0.000000E+00	0.000000E+00	0.000000E+00
0.000000E+00	0.000000E+00	0.896571E-03	0.558305E-03	0.425387E-03
0.000000E+00	0.000000E+00	0.000000E+00	0.000000E+00	0.000000E+00
0.000000E+00	0.000000E+00	0.000000E+00	0.000000E+00	0.000000E+00
0.000000E+00	0.000000E+00	0.959939E-03	0.602303E-03	0.450973E-03

0.000000E+00	0.000000E+00	0.000000E+00	0.000000E+00	0.000000E+00
0.000000E+00	0.000000E+00	0.000000E+00	0.000000E+00	0.000000E+00
0.000000E+00	0.000000E+00	0.100303E-02	0.640163E-03	0.481196E-03

CRACK GROWTH INCREMENTAL FOR OPTION # 1 (Obtained by Eq. 4.14)

0.000896	0.000807	0.000719	0.000635	0.000567	0.000498	0.000437	0.000383	0.000285	0.000244
0.000204	0.000139	0.000088	0.000067						
0.000000	0.001019	0.000906	0.000806	0.000713	0.000620	0.000543	0.000476	0.000352	0.000299
0.000253	0.000173	0.000109	0.000083						
0.000000	0.000000	0.001069	0.000948	0.000838	0.000736	0.000640	0.000560	0.000417	0.000353
0.000300	0.000206	0.000129	0.000098						
0.000000	0.000000	0.000000	0.000000	0.000967	0.000848	0.000738	0.000647	0.000483	0.000408
0.000345	0.000235	0.000148	0.000113						
0.000000	0.000000	0.000000	0.000000	0.000000	0.000964	0.000840	0.000730	0.000543	0.000462
0.000390	0.000266	0.000169	0.000128						
0.000000	0.000000	0.000000	0.000000	0.000000	0.000000	0.000944	0.000828	0.000610	0.000522
0.000435	0.000301	0.000189	0.000144						
0.000000	0.000000	0.000000	0.000000	0.000000	0.000000	0.001045	0.000909	0.000671	0.000571
0.000482	0.000329	0.000207	0.000159						
0.000000	0.000000	0.000000	0.000000	0.000000	0.000000	0.000000	0.001000	0.000736	0.000629
0.000530	0.000362	0.000229	0.000174						
0.000000	0.000000	0.000000	0.000000	0.000000	0.000000	0.000000	0.000000	0.000804	0.000695
0.000590	0.000395	0.000248	0.000189						
0.000000	0.000000	0.000000	0.000000	0.000000	0.000000	0.000000	0.000000	0.000874	0.000744
0.000632	0.000431	0.000270	0.000204						
0.000000	0.000000	0.000000	0.000000	0.000000	0.000000	0.000000	0.000000	0.000946	0.000799
0.000679	0.000463	0.000293	0.000222						
0.000000	0.000000	0.000000	0.000000	0.000000	0.000000	0.000000	0.000000	0.000000	0.000877
0.000738	0.000502	0.000313	0.000238						
0.000000	0.000000	0.000000	0.000000	0.000000	0.000000	0.000000	0.000000	0.000000	0.000931
0.000783	0.000542	0.000337	0.000255						
0.000000	0.000000	0.000000	0.000000	0.000000	0.000000	0.000000	0.000000	0.000000	0.001000
0.000848	0.000571	0.000356	0.000274						
0.000000	0.000000	0.000000	0.000000	0.000000	0.000000	0.000000	0.000000	0.000000	0.000000
0.000897	0.000605	0.000381	0.000294						
0.000000	0.000000	0.000000	0.000000	0.000000	0.000000	0.000000	0.000000	0.000000	0.000000
0.000955	0.000644	0.000408	0.000311						

CRACK GROWTH INCREMENTAL FOR OPTION # 2 (Obtained by Eq. 4.22b)

0.000000	0.000448	0.000404	0.000359	0.000318
0.000283	0.000249	0.000218	0.000191	0.000142
0.000122	0.000102	0.000069	0.000044	0.000034
0.000000	0.000000	0.000510	0.000453	0.000403
0.000357	0.000310	0.000272	0.000238	0.000176
0.000149	0.000126	0.000087	0.000055	0.000041
0.000000	0.000000	0.000000	0.000535	0.000474
0.000419	0.000368	0.000320	0.000280	0.000209
0.000176	0.000150	0.000103	0.000065	0.000049
0.000000	0.000000	0.000000	0.000000	0.000000

0.000483 0.000424 0.000369 0.000324 0.000241
 0.000204 0.000173 0.000117 0.000074 0.000057
 0.000000 0.000000 0.000000 0.000000 0.000000
 0.000000 0.000482 0.000420 0.000365 0.000271
 0.000231 0.000195 0.000133 0.000085 0.000064
 0.000000 0.000000 0.000000 0.000000 0.000000
 0.000000 0.000000 0.000472 0.000414 0.000305
 0.000261 0.000217 0.000150 0.000094 0.000072
 0.000000 0.000000 0.000000 0.000000 0.000000
 0.000000 0.000000 0.000523 0.000454 0.000336
 0.000285 0.000241 0.000164 0.000104 0.000079
 0.000000 0.000000 0.000000 0.000000 0.000000
 0.000000 0.000000 0.000000 0.000500 0.000368
 0.000315 0.000265 0.000181 0.000115 0.000087
 0.000000 0.000000 0.000000 0.000000 0.000000
 0.000000 0.000000 0.000000 0.000000 0.000402
 0.000347 0.000295 0.000198 0.000124 0.000095
 0.000000 0.000000 0.000000 0.000000 0.000000
 0.000000 0.000000 0.000000 0.000000 0.000437
 0.000372 0.000316 0.000216 0.000135 0.000102
 0.000000 0.000000 0.000000 0.000000 0.000000
 0.000000 0.000000 0.000000 0.000000 0.000473
 0.000400 0.000339 0.000231 0.000147 0.000111
 0.000000 0.000000 0.000000 0.000000 0.000000
 0.000000 0.000000 0.000000 0.000000 0.000000
 0.000439 0.000369 0.000251 0.000157 0.000119
 0.000000 0.000000 0.000000 0.000000 0.000000
 0.000000 0.000000 0.000000 0.000000 0.000000
 0.000466 0.000391 0.000271 0.000169 0.000127
 0.000000 0.000000 0.000000 0.000000 0.000000
 0.000000 0.000000 0.000000 0.000000 0.000000
 0.000500 0.000424 0.000285 0.000178 0.000137
 0.000000 0.000000 0.000000 0.000000 0.000000
 0.000000 0.000000 0.000000 0.000000 0.000000
 0.000000 0.000449 0.000302 0.000190 0.000147
 0.000000 0.000000 0.000000 0.000000 0.000000
 0.000000 0.000000 0.000000 0.000000 0.000000
 0.000000 0.000477 0.000322 0.000204 0.000156

J-INTEGRAL INCREMENTAL

0.001662 0.001555 0.001447 0.001345 0.001261 0.001178 0.001103 0.001037 0.000918 0.000868
 0.000818 0.000739 0.000677 0.000652
 0.000000 0.001813 0.001675 0.001554 0.001440 0.001327 0.001233 0.001151 0.000999 0.000935
 0.000879 0.000782 0.000703 0.000671
 0.000000 0.000000 0.001874 0.001727 0.001592 0.001468 0.001351 0.001254 0.001079 0.001001
 0.000936 0.000821 0.000728 0.000690
 0.000000 0.000000 0.000000 0.000000 0.001749 0.001604 0.001470 0.001360 0.001159 0.001068
 0.000992 0.000857 0.000751 0.000708
 0.000000 0.000000 0.000000 0.000000 0.000000 0.001746 0.001594 0.001460 0.001232 0.001134
 0.001046 0.000894 0.000776 0.000727
 0.000000 0.000000 0.000000 0.000000 0.000000 0.000000 0.001721 0.001580 0.001314 0.001207
 0.001100 0.000937 0.000801 0.000745

0.000000 0.000000 0.000000 0.000000 0.000000 0.000000 0.001845 0.001678 0.001389 0.001267
 0.001158 0.000972 0.000823 0.000764
 0.000000 0.000000 0.000000 0.000000 0.000000 0.000000 0.000000 0.001789 0.001468 0.001338
 0.001217 0.001012 0.000850 0.000782
 0.000000 0.000000 0.000000 0.000000 0.000000 0.000000 0.000000 0.000000 0.001551 0.001418
 0.001290 0.001053 0.000873 0.000801
 0.000000 0.000000 0.000000 0.000000 0.000000 0.000000 0.000000 0.000000 0.001636 0.001478
 0.001341 0.001096 0.000900 0.000819
 0.000000 0.000000 0.000000 0.000000 0.000000 0.000000 0.000000 0.000000 0.001724 0.001545
 0.001398 0.001135 0.000928 0.000841
 0.000000 0.000000 0.000000 0.000000 0.000000 0.000000 0.000000 0.000000 0.000000 0.001640
 0.001470 0.001183 0.000952 0.000861
 0.000000 0.000000 0.000000 0.000000 0.000000 0.000000 0.000000 0.000000 0.000000 0.001706
 0.001525 0.001231 0.000982 0.000881
 0.000000 0.000000 0.000000 0.000000 0.000000 0.000000 0.000000 0.000000 0.000000 0.001790
 0.001605 0.001267 0.001004 0.000904
 0.000000 0.000000 0.000000 0.000000 0.000000 0.000000 0.000000 0.000000 0.000000 0.000000
 0.001664 0.001308 0.001035 0.000929
 0.000000 0.000000 0.000000 0.000000 0.000000 0.000000 0.000000 0.000000 0.000000 0.000000
 0.001735 0.001356 0.001068 0.000950

FATIGUE LIFE FOR LOAD CASE 4 WITH CRITICAL CRACK LENGTH 2.4741 ARE

0.4917E+04

REPETITION FOR EACH CRACK INCREMENTAL

0.214488E+04
 0.369954E+04
 0.491675E+04

FATIGUE LIFE FOR LOAD CASE 5 WITH CRITICAL CRACK LENGTH 2.4741 ARE

0.6120E+04

REPETITION FOR EACH CRACK INCREMENTAL

0.270606E+04
 0.462935E+04
 0.611966E+04

FATIGUE LIFE FOR LOAD CASE 6 WITH CRITICAL CRACK LENGTH 3.2988 ARE

0.9072E+04

REPETITION FOR EACH CRACK INCREMENTAL

0.335573E+04
 0.574813E+04
 0.759744E+04
 0.907155E+04

FATIGUE LIFE FOR LOAD CASE 7 WITH CRITICAL CRACK LENGTH 4.1235 ARE

0.1312E+05

REPETITION FOR EACH CRACK INCREMENTAL

0.433712E+04

0.741313E+04

0.975530E+04

0.116103E+05

0.131158E+05

FATIGUE LIFE FOR LOAD CASE 8 WITH CRITICAL CRACK LENGTH 5.7729 ARE

0.1962E+05

REPETITION FOR EACH CRACK INCREMENTAL

0.549274E+04

0.941133E+04

0.124141E+05

0.147856E+05

0.167009E+05

0.182849E+05

0.196231E+05

FATIGUE LIFE FOR LOAD CASE 9 WITH CRITICAL CRACK LENGTH 6.5976 ARE

0.2718E+05

REPETITION FOR EACH CRACK INCREMENTAL

0.730915E+04

0.124721E+05

0.163914E+05

0.194791E+05

0.219594E+05

0.239935E+05

0.257135E+05

0.271752E+05

FATIGUE LIFE FOR LOAD CASE 10 WITH CRITICAL CRACK LENGTH 9.0717 ARE

0.5799E+05

REPETITION FOR EACH CRACK INCREMENTAL

0.146770E+05

0.247929E+05

0.322410E+05

0.380183E+05

0.426342E+05

0.463947E+05

0.495371E+05

0.521789E+05

0.544207E+05

0.563397E+05

0.579899E+05

FATIGUE LIFE FOR LOAD CASE 11 WITH CRITICAL CRACK LENGTH 11.5458 ARE

0.8678E+05

REPETITION FOR EACH CRACK INCREMENTAL

0.207216E+05

0.351455E+05

0.457707E+05

0.539340E+05

0.603633E+05

0.655825E+05

0.699446E+05

0.735514E+05

0.766100E+05

0.792823E+05

0.815652E+05

0.835285E+05

0.852590E+05

0.867754E+05

FATIGUE LIFE FOR LOAD CASE 12 WITH CRITICAL CRACK LENGTH 12.3705 ARE

0.1391E+06

REPETITION FOR EACH CRACK INCREMENTAL

0.351137E+05

0.584133E+05

0.752236E+05

0.880131E+05

0.980885E+05

0.106195E+06

0.112796E+06

0.118161E+06

0.122622E+06

0.126484E+06

0.129776E+06

0.132614E+06

0.135076E+06

0.137211E+06

0.139102E+06

FATIGUE LIFE FOR LOAD CASE 13 WITH CRITICAL CRACK LENGTH 12.3705 ARE

0.5642E+06

REPETITION FOR EACH CRACK INCREMENTAL

0.174381E+06

0.278385E+06

0.348622E+06

0.399308E+06

0.436341E+06

0.464393E+06

0.486590E+06
0.504150E+06
0.518208E+06
0.529705E+06
0.539195E+06
0.546957E+06
0.553537E+06
0.559262E+06
0.564175E+06

FATIGUE LIFE FOR LOAD CASE 14 WITH CRITICAL CRACK LENGTH 12.3705 ARE

0.7947E+07

REPETITION FOR EACH CRACK INCREMENTAL

0.327310E+07
0.492315E+07
0.588906E+07
0.650059E+07
0.690095E+07
0.718240E+07
0.738497E+07
0.753290E+07
0.764479E+07
0.772903E+07
0.779427E+07
0.784568E+07
0.788691E+07
0.792055E+07
0.794718E+07

FATIGUE LIFE FOR LOAD CASE 15 WITH CRITICAL CRACK LENGTH 12.3705 ARE

0.8378E+08

REPETITION FOR EACH CRACK INCREMENTAL

0.412285E+08
0.593608E+08
0.686633E+08
0.739413E+08
0.771529E+08
0.792022E+08
0.805756E+08
0.815264E+08
0.822055E+08
0.826962E+08
0.830519E+08
0.833186E+08
0.835182E+08
0.836667E+08
0.837804E+08

FATIGUE LIFE FOR LOAD CASE 4 WITH CRITICAL CRACK LENGTH 2.4741 ARE
0.9834E+04

REPETITION FOR EACH CRACK INCREMENTAL

0.428975E+04
0.739908E+04
0.983350E+04

FATIGUE LIFE FOR LOAD CASE 5 WITH CRITICAL CRACK LENGTH 2.4741 ARE
0.1224E+05

REPETITION FOR EACH CRACK INCREMENTAL

0.541213E+04
0.925871E+04
0.122393E+05

FATIGUE LIFE FOR LOAD CASE 6 WITH CRITICAL CRACK LENGTH 3.2988 ARE
0.1814E+05

REPETITION FOR EACH CRACK INCREMENTAL

0.671146E+04
0.114963E+05
0.151949E+05
0.181431E+05

FATIGUE LIFE FOR LOAD CASE 7 WITH CRITICAL CRACK LENGTH 4.1235 ARE
0.2623E+05

REPETITION FOR EACH CRACK INCREMENTAL

0.867423E+04
0.148263E+05
0.195106E+05
0.232205E+05
0.262315E+05

FATIGUE LIFE FOR LOAD CASE 8 WITH CRITICAL CRACK LENGTH 5.7729 ARE
0.3925E+05

REPETITION FOR EACH CRACK INCREMENTAL

0.109855E+05
0.188227E+05
0.248283E+05
0.295712E+05
0.334018E+05
0.365697E+05
0.392463E+05

FATIGUE LIFE FOR LOAD CASE 9 WITH CRITICAL CRACK LENGTH 6.5976 ARE

0.5435E+05

REPETITION FOR EACH CRACK INCREMENTAL

0.146183E+05
 0.249442E+05
 0.327828E+05
 0.389582E+05
 0.439188E+05
 0.479871E+05
 0.514270E+05
 0.543504E+05

FATIGUE LIFE FOR LOAD CASE 10 WITH CRITICAL CRACK LENGTH 9.0717 ARE

0.1160E+06

REPETITION FOR EACH CRACK INCREMENTAL

0.293540E+05
 0.495859E+05
 0.644819E+05
 0.760366E+05
 0.852685E+05
 0.927894E+05
 0.990741E+05
 0.104358E+06
 0.108841E+06
 0.112679E+06
 0.115980E+06

FATIGUE LIFE FOR LOAD CASE 11 WITH CRITICAL CRACK LENGTH 11.5458 ARE

0.1736E+06

REPETITION FOR EACH CRACK INCREMENTAL

0.414433E+05
 0.702910E+05
 0.915413E+05
 0.107868E+06
 0.120727E+06
 0.131165E+06
 0.139889E+06
 0.147103E+06
 0.153220E+06
 0.158565E+06
 0.163130E+06
 0.167057E+06
 0.170518E+06
 0.173551E+06

FATIGUE LIFE FOR LOAD CASE 12 WITH CRITICAL CRACK LENGTH 12.3705 ARE

0.2782E+06

REPETITION FOR EACH CRACK INCREMENTAL

0.702275E+05
 0.116827E+06
 0.150447E+06
 0.176026E+06
 0.196177E+06
 0.212389E+06
 0.225592E+06
 0.236323E+06
 0.245244E+06
 0.252968E+06
 0.259552E+06
 0.265227E+06
 0.270152E+06
 0.274423E+06
 0.278205E+06

FATIGUE LIFE FOR LOAD CASE 13 WITH CRITICAL CRACK LENGTH 12.3705 ARE

0.1128E+07

REPETITION FOR EACH CRACK INCREMENTAL

0.348761E+06
 0.556771E+06
 0.697245E+06
 0.798617E+06
 0.872682E+06
 0.928786E+06
 0.973180E+06
 0.100830E+07
 0.103642E+07
 0.105941E+07
 0.107839E+07
 0.109391E+07
 0.110707E+07
 0.111852E+07
 0.112835E+07

FATIGUE LIFE FOR LOAD CASE 14 WITH CRITICAL CRACK LENGTH 12.3705 ARE

0.1589E+08

REPETITION FOR EACH CRACK INCREMENTAL

0.654620E+07
 0.984631E+07
 0.117781E+08
 0.130012E+08
 0.138019E+08
 0.143648E+08
 0.147699E+08
 0.150658E+08

0.152896E+08
 0.154581E+08
 0.155885E+08
 0.156914E+08
 0.157738E+08
 0.158411E+08
 0.158944E+08

FATIGUE LIFE FOR LOAD CASE 15 WITH CRITICAL CRACK LENGTH 12.3705 ARE

0.1676E+09

REPETITION FOR EACH CRACK INCREMENTAL

0.824570E+08
 0.118722E+09
 0.137327E+09
 0.147883E+09
 0.154306E+09
 0.158404E+09
 0.161151E+09
 0.163053E+09
 0.164411E+09
 0.165392E+09
 0.166104E+09
 0.166637E+09
 0.167036E+09
 0.167333E+09
 0.167561E+09

FATIGUE LIFE FOR LOAD CASE 4 WITH CRITICAL CRACK LENGTH 2.4741 ARE

0.2950E+04

REPETITION FOR EACH CRACK INCREMENTAL

0.106224E+04
 0.203725E+04
 0.295004E+04

FATIGUE LIFE FOR LOAD CASE 5 WITH CRITICAL CRACK LENGTH 2.4741 ARE

0.3128E+04

REPETITION FOR EACH CRACK INCREMENTAL

0.113077E+04
 0.216362E+04
 0.312778E+04

FATIGUE LIFE FOR LOAD CASE 6 WITH CRITICAL CRACK LENGTH 3.2988 ARE

0.4279E+04

REPETITION FOR EACH CRACK INCREMENTAL

0.119890E+04
 0.229470E+04
 0.331697E+04
 0.427858E+04
 FATIGUE LIFE FOR LOAD CASE 7 WITH CRITICAL CRACK LENGTH 4.1235 ARE
 0.5539E+04

REPETITION FOR EACH CRACK INCREMENTAL

0.128552E+04
 0.245823E+04
 0.354813E+04
 0.457146E+04
 0.553875E+04
 FATIGUE LIFE FOR LOAD CASE 8 WITH CRITICAL CRACK LENGTH 5.7729 ARE
 0.7833E+04

REPETITION FOR EACH CRACK INCREMENTAL

0.137058E+04
 0.262313E+04
 0.378897E+04
 0.488279E+04
 0.591526E+04
 0.689612E+04
 0.783326E+04
 FATIGUE LIFE FOR LOAD CASE 9 WITH CRITICAL CRACK LENGTH 6.5976 ARE
 0.9378E+04

REPETITION FOR EACH CRACK INCREMENTAL

0.148071E+04
 0.283041E+04
 0.408342E+04
 0.525853E+04
 0.636573E+04
 0.741554E+04
 0.841861E+04
 0.937849E+04
 FATIGUE LIFE FOR LOAD CASE 10 WITH CRITICAL CRACK LENGTH 9.0717 ARE
 0.1425E+05

REPETITION FOR EACH CRACK INCREMENTAL

0.178847E+04
 0.340737E+04
 0.489838E+04
 0.629101E+04
 0.760140E+04

0.884144E+04
 0.100226E+05
 0.111495E+05
 0.122274E+05
 0.132609E+05
 0.142529E+05

FATIGUE LIFE FOR LOAD CASE 11 WITH CRITICAL CRACK LENGTH 11.5458 ARE

0.1863E+05

REPETITION FOR EACH CRACK INCREMENTAL

0.196436E+04
 0.374693E+04
 0.538865E+04
 0.691794E+04
 0.835133E+04
 0.970680E+04
 0.109977E+05
 0.122237E+05
 0.133966E+05
 0.145273E+05
 0.156103E+05
 0.166505E+05
 0.176554E+05
 0.186251E+05

FATIGUE LIFE FOR LOAD CASE 12 WITH CRITICAL CRACK LENGTH 12.3705 ARE

0.2193E+05

REPETITION FOR EACH CRACK INCREMENTAL

0.226380E+04
 0.429298E+04
 0.615208E+04
 0.787915E+04
 0.949861E+04
 0.110254E+05
 0.124698E+05
 0.138348E+05
 0.151340E+05
 0.163834E+05
 0.175796E+05
 0.187290E+05
 0.198346E+05
 0.208987E+05
 0.219282E+05

FATIGUE LIFE FOR LOAD CASE 13 WITH CRITICAL CRACK LENGTH 12.3705 ARE

0.3082E+05

REPETITION FOR EACH CRACK INCREMENTAL

0.348623E+04
 0.652650E+04
 0.926452E+04
 0.117716E+05
 0.140740E+05
 0.162117E+05
 0.182177E+05
 0.201004E+05
 0.218731E+05
 0.235522E+05
 0.251458E+05
 0.266551E+05
 0.280989E+05
 0.294891E+05
 0.308227E+05

FATIGUE LIFE FOR LOAD CASE 14 WITH CRITICAL CRACK LENGTH 12.3705 ARE

0.5787E+05

REPETITION FOR EACH CRACK INCREMENTAL

0.768269E+04
 0.140941E+05
 0.196556E+05
 0.245691E+05
 0.289560E+05
 0.329471E+05
 0.365958E+05
 0.399501E+05
 0.430590E+05
 0.459379E+05
 0.486257E+05
 0.511445E+05
 0.535188E+05
 0.557645E+05
 0.578722E+05

FATIGUE LIFE FOR LOAD CASE 15 WITH CRITICAL CRACK LENGTH 12.3705 ARE

0.1007E+06

REPETITION FOR EACH CRACK INCREMENTAL

0.151970E+05
 0.274347E+05
 0.376791E+05
 0.464836E+05
 0.541857E+05
 0.610123E+05
 0.671411E+05
 0.726902E+05
 0.777588E+05
 0.823975E+05
 0.866520E+05

0.905869E+05
0.942237E+05
0.975808E+05
0.100705E+06

.

APPENDIX C

Variable Definition of Static Shakedown Analysis Program (SSAP)

Static shakedown analysis program (SSAP) consists of two functional parts. The first part conducts static analysis by means of the finite element method. This part currently is carried out by ABAQUS. The stress distribution under reference loads for a given problem is written to an ABAQUS interface file, abafil1.fil, which will interface with the second part of the program. If, in addition to repeated load program, a static load (time-independent) such as geostatic load in pavements and foundation problem, is also applied to a system, the second file, abafil2.fil also has to be provided. The second part of the program is to search for a shakedown load by using a multidirectional direct search algorithm. The source code of the second part of the program has been developed according to the algorithm discussed in chapter V. This program is coded with two kinds of material models. One is a pressure-dependent elastic-perfectly plastic material that obeys Mohr-Columb yield criterion. The other is a pressure-independent elastic-perfectly plastic material that follows Von-Mises yield criterion. Static shakedown load of two dimensional problem (plane stress, plane strain, and axisymmetric) can be analyzed. Up to a three-layer pavement system with different materials can be modeled in the program. The input data definition and format are described below.

Static Analysis

Input data:

The input data to ABAQUS usually includes node numbers and their coordinates, element numbers and their nodes, material properties, boundary conditions and applied loads. For detailed description about how to use ABAQUS, refer to the ABAQUS user's manual [1]. This step is necessary in the shakedown analysis. The input data can be saved to a file with extension .inp. ABAQUS can read these data in the file.

Output data:

The output data from ABAQUS are very flexible and usually dependent on the user's requirements. For static shakedown analysis, stresses at each integral point under reference load are required and saved to ABAQUS output file, called abafil1.fil, which will interface with shakedown analysis program, SSAP. If static loads (time-independent) are also applied to the system, the stresses at each integral point under these loads are also required and saved to another ABAQUS output file, abafil2.fil.

Static Shakedown Analysis

Input data:

HED (12A6) Title of the job, which characterizes the problem you are running.

- NUMNP (I4) Total number of nodal points of a finite element model for a considered problem.
- NUMEL (I4) Total number of elements used in a finite element model of a considered problem.
- NS (I4) Column dimension of a strain matrix(B-matrix). It is usually dependent on the number of the integral points used in an element and the dimensions of a problem. In a two dimensional case, for 1 integral point, $NS = 1*4 = 4$; for 2 integral points, $NS = 2*4 = 8$; for 4 integral points, $NS = 4*4 = 16$. This is same for axisymmetric problem.
- ND (I4) The Number of the degrees of freedom of an element in a finite element model. It is the degree of freedom times the number of nodes in an element.
- NFILE(I4) Total number of interface files. If only abafil1.fil is used, NFILE = 1. If both abafil1.fil and abafil2.fil are used, NFILE = 2.

The following input data are in free format.

- LAY[3] For a layered system, it defines element numbers within each layer. Up to a three-layer system with different materials can be analyzed by the program.
- LAY[1] - defines the ending element number of the first layer. The element within this layer should be numbered in the following format: e_1, e_2, \dots, e_{L1} .
- LAY[2] - defines the ending element number of the second layer. The element within this layer should be numbered in the following format: $e_{L1+1}, e_{L1+2}, \dots, e_{L1+L2}$.
- LAY[3] - defines the ending element number of the third layer. The element within this layer should be numbered in the following format: $e_{L1+L2+1}, e_{L1+L2+2}, \dots, e_{L1+L2+L3}$.
- E[3] Defines elastic moduli used for each layer for a layered system.
- ANU[3] Poisson ratio used for each layer for a layered system.
- COHN[3] Material cohesion used for each layer for a layered system.
- PHI[3] Material internal friction angle used for each layer for a layered system.
- THICK Thickness used for a plane stress condition in the analysis. For a plane strain condition, THICK=1.0. For an axisymmetric problem, THICK can set to 0.0.
- YIELD Material yield stress used for Von-Mises failure criterion.
- MATYPE Material type used in the analysis. EQ. 1 for metal material and Von-Mises yield criterion is Used. EQ. 2 for pressure dependent material and Mohr-columb yield criterion is used.
- FRF1 Square of material yield stress σ_0 . For Von -Mises material, $FRF1 = \sigma_0^2$. For Mohr-Columb material, $FRF1 = \left[\frac{2C \cos \phi}{1 + \sin \phi} \right]^2$.

RF2 Inverse of the square of reference load level, p_o , i. e. $RF2 = 1/p_o^2$, where p_o is the load used in static analysis to obtain stresses at every integral point.

Two convergence criteria were coded in the program, which can only be changed by changing the code. One criterion is that the current objective function minus previous objective function has to be less than $\epsilon = 10^{-3}$. The other is the shakedown load factor increment, $\Delta\lambda$ is less than $\epsilon_o = 10^{-5}$.

Output data:

Static shakedown load parameter. The shakedown is the reference load multiplied by the shakedown load parameter.

The listing of the program (SSAP) is stored on the enclosed diskette. Because SSAP includes ABAQUS user's subroutines, it has to be linked with ABAQUS utility subroutine libraries when it is used. The ABAQUS user's manual [1] gives detailed descriptions about how to compile and link the user's program and subroutines with ABAQUS utility subroutine libraries. After the program is linked with the ABAQUS utility subroutine libraries, it can be executed like other programs. The flow chart of the program is provided on the following page.

EXAMPLE FOR DATA INPUT

Consider a beam fixed at one end and supported at the other end as shown in the figure. The dimension and material properties are:

Span Length $L = 12.0$ in.(304.8 mm).

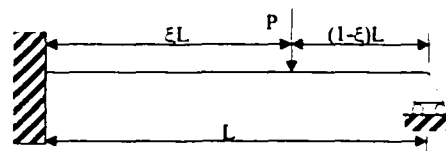
Height $H = 3.0$ in.(76.2 mm).

Thickness $T = 1.0$ in.(25.4 mm).

Elastic modulus $E = 3.5 \times 10^7$ psi. (24.1×10^4 Mpa.)

Poisson ratio $\nu = 0.15$

Yield stress $\sigma_o = 500.0$ psi.(3.45 Mpa.).

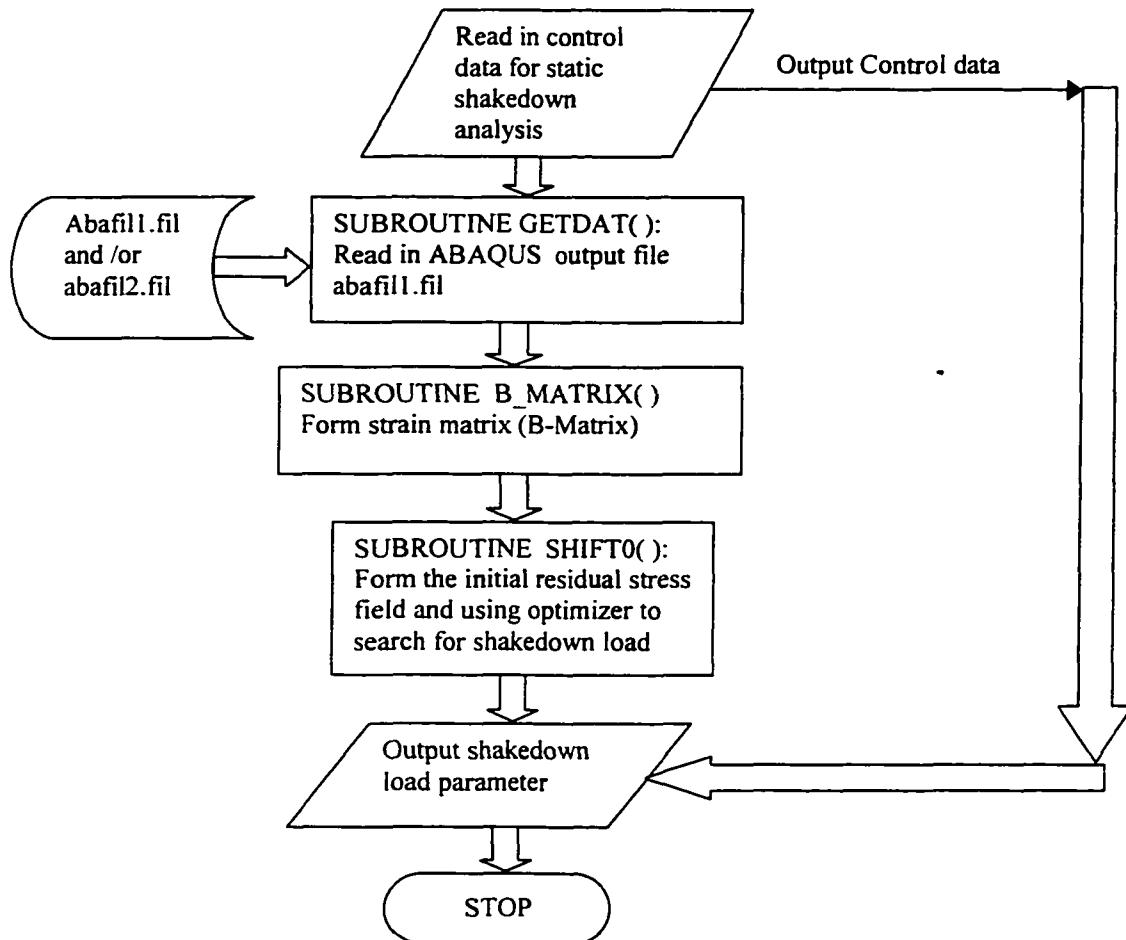


The input data to ABAQUS are data defining the finite element model and material elastic properties. The beam is divided into 36 elements with 52 nodes as shown in Fig. 5.4. The material elastic properties are described as above. Point load, $P = 100$ bl.(444 N), is applied at node 28. The output file is saved in the ABAQUS output file, abafill.fil. The input data for shakedown analysis program are:

```
/* Job title */
SHAKEDOWN ANALYSIS DATA FOR A BEAM
/* Control data */
  52  36  16   8   1
/* The following data format is designed for three-layer system. For non-layered problem, only one value is
used and the other two values can be assigned to any arbitrary values, as in this example. If the two-layer
system is considered, the first two values are used and the third one can be any value */
/* Ending element number for each layer. Here only one layer is defined */
36,81,117
/* Elastic modulus for each layer */
3.0e7,1.0e4,1.0e4
/* Poisson ratio for each layer */
0.15,0.45,0.45
/* Cohesion for each layer */
500.,6.,6.
/* Internal friction angle for each layer */
42.0,5.0,5.0
/* Yield stress and material type */
1.0,500.0,2
/* Square of yield stress and inverse square of reference load */
2.5E5,1.0E-4
```

Output data:

Static shakedown load parameter: 5.399



APPENDIX D

Variable Definition of Kinematic Shakedown Analysis Program (KSAP)

The kinematic shakedown analysis program (KSAP) consists of two functional parts. The first part is to find the stress distribution under the reference load and eigen-vectors for a given system by means of the finite element method. This part currently is carried out by ABAQUS. The static and eigen-value analysis provides two output files that interface with the second part of the program. The first file contains stress distribution under the reference load. The second file contains eigen-vectors for each eigen-value of the system. The second part of the program is to search for the kinematic shakedown load by using a nonlinear programming technique. The source code is developed based on the algorithm provided in Chapter VI. The second part of the program reads two groups of input data. One is control data that defines finite element model and material properties used for a given system. The other that is needed in searching for the shakedown load is the stresses and eigen-vectors generated from the static and eigen-value analysis by using ABAQUS. This program is coded with two kinds of material models. One is pressure-dependent elastic-perfectly plastic material that obeys Mohr-Columb yield criterion. The other is pressure-independent elastic-perfectly plastic material that follows Von-Mises yield criterion. The shakedown loads of two dimensional problems (plane stress, plane strain, and axisymmetric) and three dimensional problems can be calculated. Up to three-layer pavement systems with different materials can be analyzed. The definition of the input data and their format are described in the following.

Static and Eigen-value Analysis

Input data:

The input data to ABAQUS usually includes node numbers and their coordinates, element numbers and their nodes, material properties, boundary conditions and applied loads. For detailed description about how to use ABAQUS, refer to the ABAQUS user's manual [1]. The static analysis and eigen-value analysis are conducted separately with two different input files.

Output data:

The output data from ABAQUS are very flexible and usually dependent on user's requirements. For kinematic shakedown analysis, we need to run ABAQUS twice. From static analysis, stresses at every integral point are obtained and saved to ABAQUS output file abafil1.fil. From eigen-value analysis, the eigen-modes corresponding each eigen-value are obtained and saved to ABAQUS output file abafil2.fil. These two files will interface with kinematic shakedown analysis program, KASP.

Kinematic Shakedown Analysis

Input data:

- HED (12A6) Title of the job, which characterizes the problem you are running.
- NUMNP (I4) Total number of nodal point of a finite element model for a considered problem.
- NUMEL (I4) Total number of elements used in a finite element model of a considered problem.
- NS (I4) Column dimension of a strain matrix(B-matrix). It is usually dependent on the number of the integral points used in an element and the dimensions of a problem. In two dimensional case for 1 integral point, $NS = 1*4 = 4$; for 2 integral points, $NS = 2*4 = 8$; for 4 integral points $NS = 4*4 = 16$. This is same as in axisymmetric condition. In three-dimensional case, for 1 integral point, $NS = 1*6 = 6$; for 2 integral points, $NS = 2*6 = 12$; for 4 integral points $NS = 4*6 = 24$.
- ND (I4) The Number of the degree of freedom of an element in a finite element model. It is the degree of freedom times the number of nodes in an element.
- NGEV (I4) Total number of eigen-vectors of the system used in shakedown analysis.

The convergence criterion is coded in the program, which can only be changed through the source code. The convergence is defined as the value of the current shakedown load factor minus the previous one is less than $\varepsilon = 10^{-5}$.

The following input data are in free format.

- LAY[3] (3I4) For a layered system, it defines element numbers within each layer. Up to three layer Systems with different materials can be analyzed by the program.
- LAY[1] - defines the ending element number of the first layer. The element within this layer should be numbered in the following format: e_1, e_2, \dots, e_{L1} .
- LAY[2] - defines the ending element number of the second layer. The element within this layer should be numbered in the following format: $e_{L1+1}, e_{L1+2}, \dots, e_{L1+L2}$.
- LAY[3] - defines the ending element number of the third layer. The element within this layer should be numbered in the following format: $e_{L1+L2+1}, e_{L1+L2+2}, \dots, e_{L1+L2+L3}$.
- E[3] Defines elastic moduli used for each layer for a layered system.
- ANU[3] Poisson ratio used for each layer for a layered system.
- COHN[3] Material cohesion used for each layer for a layered system.
- PHI[3] Material internal friction angle used for each layer for a layered system.
- THICK Thickness used for plane stress conditions in the analysis. For plane strain condition,

- THICK=1.0. For axisymmetric and three dimensional problem, THICK can set to 0.0.
- YIELD** Material yield stress used for Von-Mises failure criterion.
- MATYPE** Material type used in the analysis. EQ. 1 for metal material with Von-Mises yield criterion. EQ. 2 for pressure dependent material with Mohr-columb yield criterion.

Output data:

Kinematic shakedown load parameter. The shakedown is the reference load multiplied by the shakedown load parameter.

The program (KSAP) is on the enclosed diskette. Because KSAP includes ABAQUS user's subroutines, it has to be linked with ABAQUS utility subroutine libraries when it is used. The ABAQUS user's manual [1] gives detailed descriptions about how to compile and link user's program and subroutines with ABAQUS utility subroutine libraries. After the program is linked with ABAQUS utility subroutine libraries, it can be executed like other regular programs. The flow chart of the program is provided in the following page.

EXAMPLE FOR DATA INPUT

Consider a beam fixed at one end and supported at another end as shown in the figure. The dimension and material properties are:

Span Length $L = 12.0$ in.(304.8 mm).

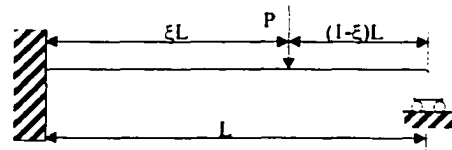
Height $H = 3.0$ in.(76.2 mm).

Thickness $T = 1.0$ in.(25.4 mm).

Elastic modulus $E = 3.5 \cdot 10^7$ psi.(24.1 $\cdot 10^4$ Mpa.)

Poisson ratio $\nu = 0.15$

Yield stress $\sigma_0 = 500.0$ psi.(3.45 Mpa.)



The input data to ABAQUS are data defining the finite element model and material elastic properties. The beam is divided into 36 elements with 52 nodes as shown in Fig. 6.4. Static analysis gives stresses at every integral point and saved in the file abafil1.fil. 95 Eigen-vectors are obtained from eigen-value analysis and stored in the file abafil2.fil. These two files will interface with KSAP. The input data for upper shakedown analysis are:

/* Job title */

SHAKE DOWN ANALYSIS DATA FOR A BEAM (UPPER)

/* Control data for the analysis */

52 36 16 8 95

/* The following data format is designed for a three-layer system. For non-layered problems, only the first one value is used and the other two values can be assigned to any arbitrary values, as in this example. If the two-layer system is considered, the first two values are used and the third one can be any value */

/* Ending element number for each layer */

36, 81, 117

/* Elastic modulus for each layer */

3.0e7, 1.0e4, 1.0e4

/* Poisson ratio for each layer */

0.15, 0.45, 0.45

/* Cohesion for each layer */

500., 6., 6.

/* Internal friction angle for each layer */

42.0, 5.0, 5.0

/* Yield stress and material type */

1.0, 500.0, 2

Output data:

Kinematic shakedown load: 5.724.

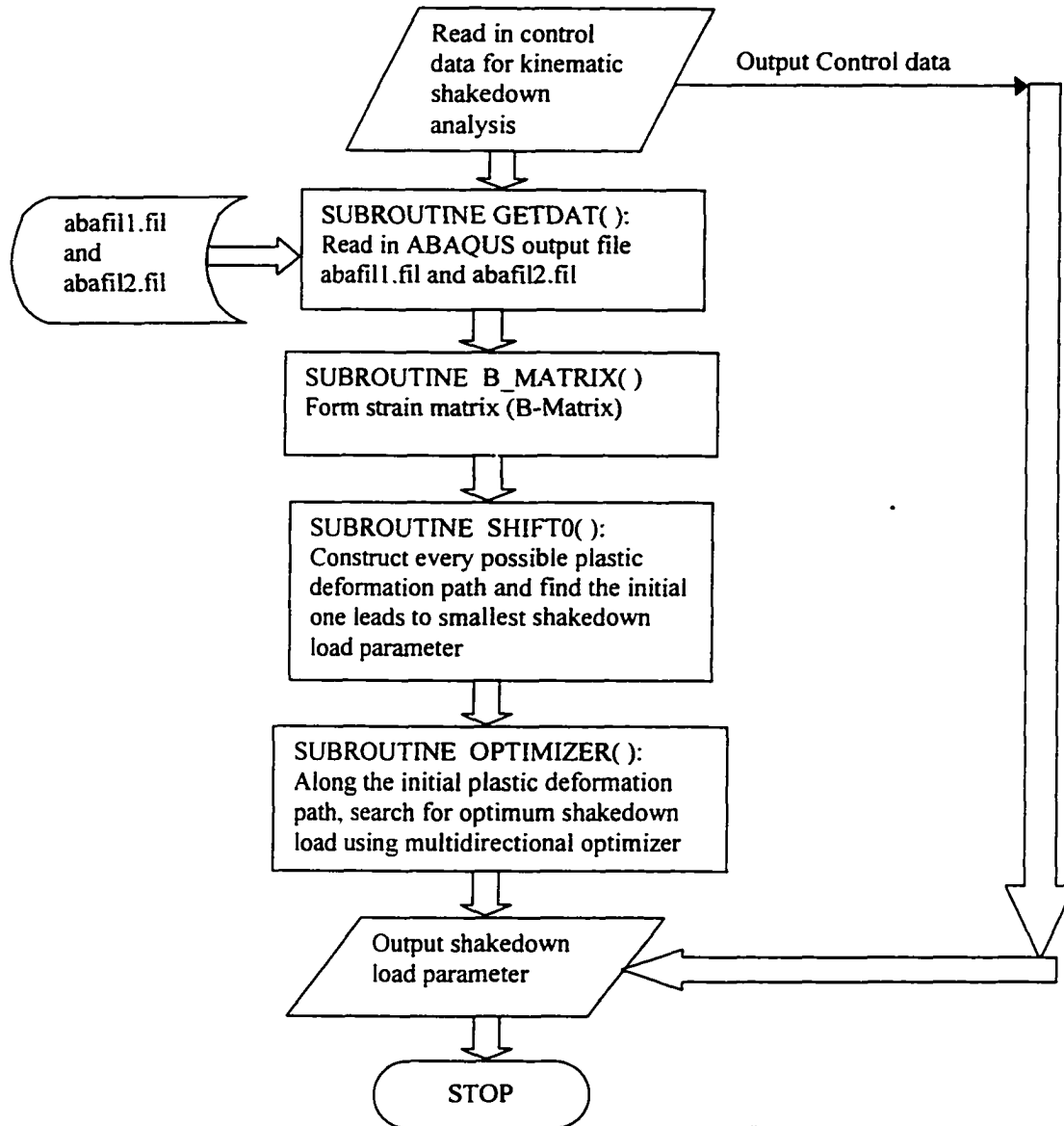
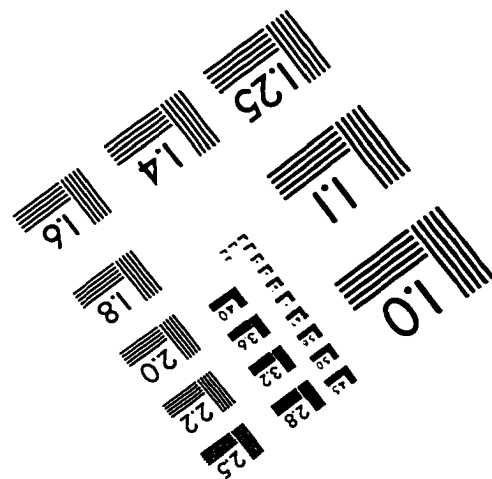
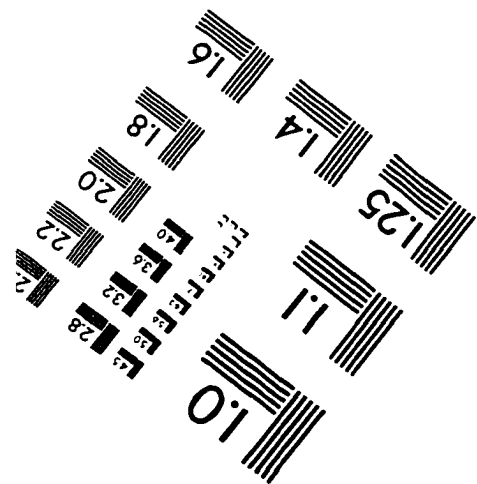
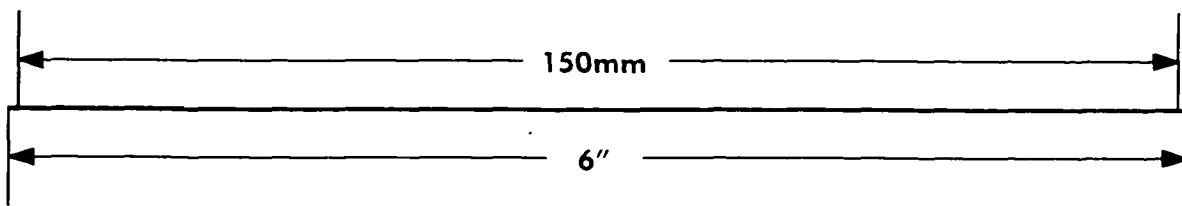
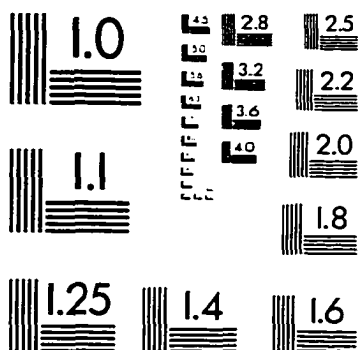
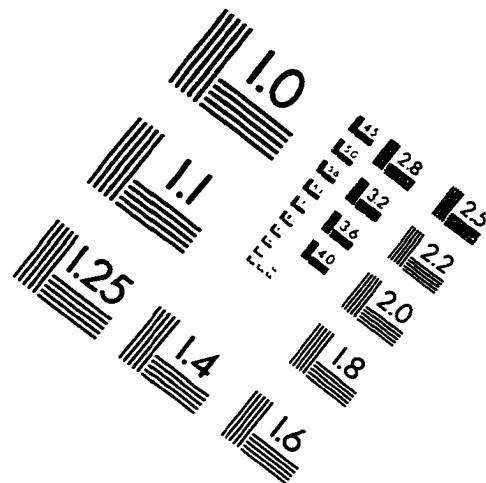
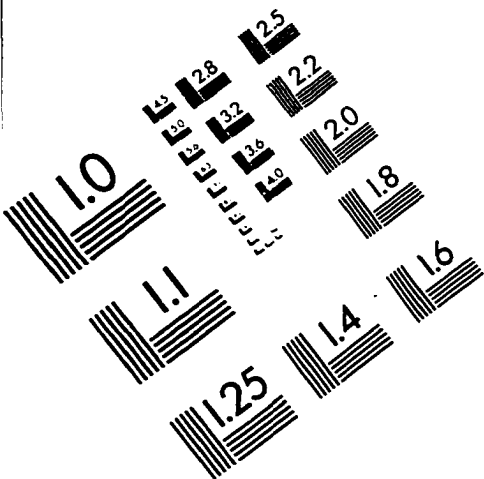


IMAGE EVALUATION TEST TARGET (QA-3)



APPLIED IMAGE, Inc
 1653 East Main Street
 Rochester, NY 14609 USA
 Phone: 716/482-0300
 Fax: 716/288-5989

© 1993, Applied Image, Inc., All Rights Reserved